

REPORT DOCUMENTATION PAGE

AFRL-SR-BL-TR-01-

0570

Public reporting burden for this collection of information is estimated to average 1 hour per response, including the time for reviewing instructions, data needed, and completing and reviewing this collection of information. Send comments regarding this burden estimate or any other aspect of this collection of information, including suggestions for reducing burden, to Department of Defense, Washington Headquarters Services, Directorate for Information Operations and Reports (0704-0188), 121 Gould Street, Washington, DC 20310-1404. Comments should be submitted within 30 days from the date of this form. This report does not display a currency valid OMB control number. PLEASE DO NOT RETURN YOUR FORM TO THE ABOVE ADDRESS.

1. REPORT DATE (DD-MM-YYYY) 29/09/2001			2. REPORT TYPE Final Report	3. DATES COVERED (From - To) 1/15/98-6/30/01	
4. TITLE AND SUBTITLE A Computational-experimental approach to hierarchical modeling of damage and failure in non-uniform composite materials			5a. CONTRACT NUMBER		
			5b. GRANT NUMBER F49620-98-1-0193		
			5c. PROGRAM ELEMENT NUMBER		
			5d. PROJECT NUMBER		
			5e. TASK NUMBER		
			5f. WORK UNIT NUMBER		
7. PERFORMING ORGANIZATION NAME(S) AND ADDRESS(ES) Department of Mechanical Engineering 2021D Robinson Laboratory 216 W. 18 th Avenue Columbus, OH 43210			8. PERFORMING ORGANIZATION REPORT AIR FORCE OFFICE OF SCIENTIFIC RESEARCH (AFOSR)		
9. SPONSORING / MONITORING AGENCY NAME(S) AND ADDRESS(ES) Dr. H. Thomas Hahn, IPA/Program Manager Air Force Office of Scientific Research 801 N. Randolph St. Room 732 Arlington, VA 22203-1977			NOTICE OF TRANSMITTAL DTIC THIS IS THE SPONSOR/MONITOR'S APPROVAL FOR PUBLIC RELEASE LAW AFR 190-12. DISTRIBUTION IS UNLIMITED.		
13. SUPPLEMENTARY NOTES			20011126 103		
14. ABSTRACT Progress has been made in advancing the state of the art in multiple-scale modeling of damage in composite materials, as delineated below. Interfacial Debonding Analysis in Multiple Fiber Reinforced Composites: Decohesion at multiple fiber interfaces of elastic fiber reinforced composites is modeled by the Voronoi cell finite element model (VCFEM). Interfacial debonding is accommodated by cohesive zone models and simulations are compared with results from experiments, performed using cruciform specimens of fiber polymer-matrix composites. A Multi-level Computational Model for Multi-scale Damage Analysis in Composite and Porous Materials: An adaptive multi-level methodology is developed to create a hierarchy of computational sub-domains with varying resolution for multiple scale problems. It concurrently predicts variables at the structural and microstructural scales and tracks microstructural damage. VCFEM conducts microstructural analysis, while a displacement based FEM code executes the macroscopic analysis. The adaptive process increases efficiency and accuracy. Experimental-Computational Investigation Of Damage Evolution In Discontinuously Reinforced Composite: A combined experimental-computational approach to study the evolution of microscopic damage to cause failure in commercial SiC particle reinforced DRA's. Aspects of microstructural geometry that are most critical for damage nucleation and evolution are accomplished. Micromechanical modeling of 2D micrographs are conducted with VCFEM. Inferences on the initiation and propagation of damage are made from the 2D simulations.					
15. SUBJECT TERMS Composite Materials, Multi-Scale Analysis, Image based microstructural modeling, experimental validation					
16. SECURITY CLASSIFICATION OF: a. REPORT			17. LIMITATION OF ABSTRACT	18. NUMBER OF PAGES	19a. NAME OF RESPONSIBLE PERSON
b. ABSTRACT					a. REPORT
c. THIS PAGE					19b. TELEPHONE NUMBER (include area code)

**A COMPUTATIONAL-EXPERIMENTAL APPROACH TO
HIERARCHICAL MODELING OF DAMAGE AND FAILURE
IN NON-UNIFORM COMPOSITE MATERIALS**

Final Report to

Directorate of Aerospace and Materials Sciences

Mechanics of Materials Program

Dr. H. Thomas Hahn, Program Manager

**AIR FORCE OFFICE OF SCIENTIFIC RESEARCH
801 N. Randolph St., Rm 947
Arlington, VA 22203-1977**

for

Grant # F49620-98-1-0193
to The Ohio State University

by

Somnath Ghosh, Principal Investigator, Professor
Department of Mechanical Engineering
2021D Robinson Laboratory, 206 W. 18th Ave.
The Ohio State University, Columbus, OH 43210

2001

Contents

1 Executive Summary	1
2 List of Publications	3
2.1 Dissertations/Theses Acknowledging this Grant	3
2.2 Refereed Publications Acknowledging this Grant	3
2.3 List of Participating Scientific Personnel	4
3 Interfacial Debonding Analysis in Multiple Fiber Reinforced Composites	5
3.1 Introduction	5
3.2 Interfacial Debonding with the Voronoi Cell FEM	6
3.2.1 Cohesive Zone Models for Interfacial Decohesion	9
3.2.2 Implementation of Cohesive Zone Models in VCFEM	11
3.3 Numerical Examples	12
3.3.1 Comparison with results of Needleman [22]	12
3.3.2 An Experimental-Computational Study	13
3.3.3 Multiple Fibers in the Microstructure	18
3.4 Concluding Remarks	20
4 A Multi-level Computational Model for Multi-scale Damage Analysis in Composite and Porous Materials	46
4.1 Introduction	46
4.2 Two Way Coupling for Multiple Scale Modeling	48
4.3 A Multi Level Model for Coupling Different Scales	49
4.4 Homogenization with Voronoi Cell FEM	50
4.4.1 Asymptotic homogenization with microstructural periodicity	50
4.4.2 The Voronoi Cell FEM for Microstructural Analysis	52
4.4.3 Coupling Asymptotic Homogenization with VCFEM	54
4.5 Computational Subdomain Level-0 in the Hierarchical Model	55
4.5.1 An Elastic-Plastic Constitutive Model	55
4.5.2 Elasto-Plasticity with Anisotropic Yield Function	56
4.5.3 Numerical Implementation of the Constitutive Model	58
4.5.4 Numerical Examples with the Continuum Constitutive Model	59

4.5.5	Level-0/1 Mesh Enrichment by h-Adaptation	61
4.6	Computational Subdomain Level-1 in the Hierarchical Model	62
4.7	Computational Subdomain Level-2 in the Hierarchical Model	62
4.7.1	Damage Criterion for Particle Cracking in Level-2	63
4.8	Coupling the Levels in the Hierarchical FE Model	63
4.9	Adaptation Criteria for Various Levels	65
4.10	Numerical Examples with the Adaptive Multilevel Model	67
4.10.1	Effects of inhomogeneity size (Scale effect)	67
4.10.2	Homogenization vs. multi-level simulation	69
4.10.3	Effect of heterogeneity distribution and shape	69
4.10.4	A heterogeneous plate with a macroscopic holes	70
4.11	An Example on Convergence of the Multi-level Method	70
4.11.1	Microscale VCFEM Simulations	71
4.11.2	Multi-level Simulations	72
4.12	Discussions and Conclusion	73
5	Experimental-Computational Investigation Of Damage Evolution In Discontinuously Reinforced Aluminum Matrix Composite	107
5.1	Introduction	107
5.2	Experiments for Damage Assessment	108
5.2.1	Interrupted tests	108
5.2.2	Damage examination and microscopic analysis	109
5.2.3	Major observations	110
5.3	Equivalent Microstructure & Mesh Generation	110
5.4	Microstructure and Damage Characterization	111
5.5	Damage Simulation by Voronoi Cell FEM	113
5.5.1	Calibration of Weibull parameters σ_0 and m	114
5.6	Characteristic Size of Microstructures	116
5.7	Conclusions	117

Chapter 1

Executive Summary

The project entitled "*A Computational-experimental Approach to Hierarchical Modeling of Damage and Failure in Non-uniform Composite Materials*" began in February 1998. A no-cost extension was granted to continue this project till June 30, 2001. During the period of this grant, substantial progress has been made in advancing the state of the art in multiple scale modeling and damage by interfacial debonding and fiber cracking in composite materials. Research has been conducted in a few distinct areas that are delineated below. A list of publications, acknowledging this grant is provided in chapter 2.

I. Interfacial Debonding Analysis in Multiple Fiber Reinforced Composites

(Details provided in Chapter 3)

Decohesion at multiple fiber interfaces of elastic fiber reinforced composites is modeled by the Voronoi cell finite element model (VCFEM) in this chapter. Interfacial debonding is accommodated by cohesive zone models, in which normal and tangential springs tractions are expressed in terms of interfacial separation. Model simulations are compared with results from experiments, performed using cruciform specimens of single and multiple fiber polymer-matrix composites. An inverse problem is solved to calibrate the cohesive zone parameters. Debonding at fiber matrix interfaces are simulated for different architectures, volume fractions and boundary conditions, to understand the influence of microstructural morphology and boundary conditions on the decohesion process.

II. A Multi-level Computational Model for Multi-scale Damage Analysis in Composite and Porous Materials

(Details provided in Chapter 4)

An adaptive multi-level methodology is developed in this chapter to create a hierarchy of computational sub-domains with varying resolution for multiple scale problems. It is intended to

concurrently predict evolution of variables at the structural and microstructural scales, as well as to track the incidence and propagation of microstructural damage in composite and porous materials. The microstructural analysis is conducted with the Voronoi cell finite element model (VCFEM), while a conventional displacement based FEM code executes the macroscopic analysis. The model introduces three levels in the computational domain which include macro, macro-micro and microscopic analysis. It differentiates between non-critical and critical regions and ranges from macroscopic computations using continuum constitutive relations to zooming in at 'hotspots' for pure microscopic simulations. Coupling between the scales in regions of periodic microstructure is accomplished through asymptotic homogenization. An adaptive process significantly increases the efficiency while retaining appropriate level of accuracy for each region. Numerical examples are conducted for composite and porous materials with a variety of microscopic architectures to demonstrate the potential of the model.

III. Experimental-Computational Investigation Of Damage Evolution In Discontinuously Reinforced Aluminum Matrix Composite

(Details provided in Chapter 5)

This chapter deals with a combined experimental-computational approach to study the evolution of microscopic damage to cause failure in commercial SiC particle reinforced DRA's. Determination of aspects of microstructural geometry that are most critical for damage nucleation and evolution forms a motivation for this work. An interrupted testing technique is invoked where the load is halted in the material instability zone, following necking but prior to fracture. Sample microstructures in the severely necked region are microscopically examined in 3D using a serial sectioning method. The micrographs are then stacked sequentially on a computer to reconstruct 3D microstructures. Computer simulated equivalent microstructures with elliptical or ellipsoidal particles and cracks are constructed for enhanced efficiency, which are followed by tessellation into meshes of 2-D and 3-D Voronoi cells. Various characterization functions of geometric parameters are generated and sensitivity analysis is conducted to explore the influence of morphological parameters on damage. Micromechanical modeling of 2D micrographs are conducted with Voronoi Cell Finite Element Method (VCFEM). Inferences on the initiation and propagation of damage are made from the 2D simulations. Finally, the effect of size and characteristic lengths of representative material element (RME) on the extent of damage in the model systems is investigated.

Chapter 2

List of Publications

2.1 Dissertations/Theses Acknowledging this Grant

1. Y. Ling, "Development of the Voronoi Cell Finite Element Model for Interfacial Debonding in Elastic Composites", M.S. Thesis, The Ohio State University, Winter 2000.
2. J. Fan, "3D Voronoi Cell Finite Element Method for Composite and Porous Materials", M.S. Thesis, The Ohio State University, Autumn 2000.

2.2 Refereed Publications Acknowledging this Grant

Journals

1. M. Li, S. Ghosh and O. Richmond, " An experimental-computational approach to the investigation of damage evolution in discontinuously reinforced aluminum matrix composite", *Acta Materialia*, Vol. 47 No. 12, pp. 3515-3532, 1999.
2. M. Li, S. Ghosh, O. Richmond, H. Weiland and T.N. Rouns, " Three dimensional characterization and modeling of particle reinforced MMCs. Part I: Quantitative description of microstructural morphology", *Materials Science and Engineering A*, Vol. A265, pp. 153-173, 1999.
3. M. Li, S. Ghosh, O. Richmond, H. Weiland and T.N. Rouns, " Three dimensional characterization and modeling of particle reinforced MMCs. Part II: Damage characterization", *Materials Science and Engineering A*, Vol. A266. pp.221-240, 1999.
4. S. Ghosh, K. Lee and P. Raghavan, " A multi-level computational model for multiscale damage analysis in composite and porous materials", *International Journal of Solids and Structures*, Vol. 38 No. 14, pp. 2335-2385, 2001.
5. S. Ghosh, Y. Ling, B. S. Majumdar and R. Kim, "Interfacial debonding in multiple fiber-reinforced composites, *Mechanics of Materials*, Vol. 32 (10), pp. 561 -591, 2000.

6. P. Raghavan, S. Moorthy, S. Ghosh and N. Pagano, "Revisiting the composite laminate problem with an adaptive multi-level computational model, Composites Science and Technology, Vol. 61, pp. 1017-1040, 2001.
7. S. Moorthy and S. Ghosh, "Adaptivity and convergence in the Voronoi cell finite element model for analyzing heterogeneous materials, Computer Methods in Applied Mechanics and Engineering, Vol. 185, pp. 37-74, 2000.
8. S. Ghosh and S. Moorthy, "A three dimensional Voronoi cell finite element model for discretely reinforced composites, (to be submitted for publication).

Proceedings

9. K. Lee, S. Moorthy and S. Ghosh, " Multiple Scale Computational Model for damage in Composite Materials." Modeling and Simulation Based Engineering, S.N. Atluri and P.E. O'Donoghue (eds.), Tech Science Press, pp. 1420-1425, 1998.
10. S. Ghosh and Y. Ling, " A microstructure based computational model for interfacial debonding in fiber reinforced composites, Proceedings of SEM IX International Congress, Orlando, FL, June 2000, pp. 65-68, 2000.
11. S. Ghosh and P. Raghavan, 'An Adaptive Multilevel Computational Model for Composite Laminates', Modeling and Simulation Based Engineering, Proceedings of International Conference on Computational Engineering Science, S. N. Atluri (ed), 2001.

2.3 List of Participating Scientific Personnel

1. **Dr. Somnath Ghosh**, Principal Investigator.
Professor of Mechanical Engineering, The Ohio State University.
2. **Dr. Suresh Moorthy**, Post-Doctoral Fellow 1997-2001.
3. **Mr. Prasanna Raghavan**, Ph.D. July 2002 (expected).
Graduate Research Associate in Mechanical, 1998-present.
4. **Mr. Yong Ling**, M.S. 2000,
Graduate Research Associate in Applied Mechanics. 1998-2000.
5. **Mr. Jian Fan**, M.S. 2000,
Graduate Research Associate in Applied Mechanics. 1998-2000.

Chapter 3

Interfacial Debonding Analysis in Multiple Fiber Reinforced Composites

3.1 Introduction

Affordability issues are gradually shifting design practice away from the assembly of small sub-components towards large unitized structures. In this paradigm shift, greater emphasis is placed on design based on analysis, rather than on laboratory tests. The micro-mechanisms of failure in composite materials, e.g. polymer or organic matrix composites are generally known. They involve either fiber splitting or fiber-matrix interface decohesion, followed by matrix cracking. The damage mechanisms are sensitive to local morphological parameters like volume fraction, size, shape and spatial distribution of reinforcements, interfacial strength and process-related defects. Fibers and interfaces, in regions of clustering or preferential alignment, are subjected to increased local stresses and have a greater propensity to undergo damage nucleation than those in dilute regions. A number of failure prediction models for composite laminates are phenomenological and have been based on empirical methods or ply level fracture mechanics. These macroscopic models are not capable of relating the failure process to local interactions and stress concentrations. Because of limited large-scale tests in the emerging design environment, it is critical that a robust failure analysis model evolve from the details of the microstructure and incorporate the micromechanics of damage modes.

Analysis of damage evolution by decohesion of fiber-matrix interfaces in multiple fiber-reinforced microstructures is the objective of the present study. The effect of weak bonding or debonded interface on the mechanical properties have been studied by several investigators e.g. [4, 13, 26], using simplified models for representing imperfect conditions through traction discontinuities. The propagation of interfacial cracking or decohesion at fiber-matrix interfaces has been successfully modeled by a number of researchers using the cohesive volumetric finite element methods. Among the important contributions to the field of damage evolution by normal and tangential separation are those by Needleman [22, 23, 24], Tvergaard [29, 30], Allen et. al. [2, 18], Lissenden et. al. [17], Geubelle et. al. [9, 15], Walter et. al. [32], among others. A majority of these studies have used unit cell models, which assume that the material is constituted of periodic repetition of single

cells. Displacement based finite element analyses, with the inclusion-matrix interface represented through traction-displacement constitutive models, are used to predict the onset and growth of debonding . While these models provide valuable insights into the microstructural damage processes, the simple microstructure are ineffective in addressing the interaction between fibers, effects of clustering, alignment, relative sizes etc., that are often observed in micrographs. To overcome this limitation, Zhong and Knauss [33] have proposed a hybrid discrete-continuum approach in which discrete particle interactions with damage evolution are modeled, accounting for particle size and spacing.

In this work, decohesion at multiple fiber interfaces is modeled for polymer matrix composites by the Voronoi cell finite element model (VCFEM), developed by Ghosh and coworkers [34]. VCFEM has been established as an effective tool for efficient and accurate modeling of non-uniform microstructures with heterogeneities of arbitrary shapes, sizes or dispersions with perfect interfaces in [35, 34, 21]. In VCFEM, the computational model evolves by tessellation of the microstructure to generate a mesh of multi-sided Voronoi polygons as shown in figure 3.1. The Voronoi cell formulation is augmented in this work to incorporate interfacial debonding through the introduction of cohesive zone models. This is accomplished by permitting the elastic matrix and inclusion phases to be connected at nodes by normal and tangential cohesive springs. The debonding process is assumed to be quasi-static, neglecting inertia. The analysis is assumed to be in-plane and post-debonding friction is neglected in this study. Simulations with the model are compared with results from experiments performed using single and multiple fiber cruciform specimens. An inverse problem is solved, using minimization techniques to calibrate cohesive zone parameters for comparison studies. Finally, debonding at multi-fiber interfaces are simulated for different architectures, volume fractions and boundary conditions to understand their effect on decohesion.

3.2 Interfacial Debonding with the Voronoi Cell FEM

The Voronoi cell finite element model (VCFEM) for a heterogeneous domain with a dispersion of inclusions or voids, implements a mesh of Voronoi polytopes. The Voronoi cells, surrounding each heterogeneity, are generated by a surface based tessellation algorithm [11, 14] to yield multiple edges depending on the number of neighboring heterogeneities. Each element in VCFEM consists of the heterogeneity and its neighborhood region of matrix. No further refinement of the element is required with this formulation. VCFEM has been successfully developed by Ghosh et. al. [35, 34, 21] for accurate stress and deformation analysis of elastic and plastic materials with perfect interfaces. It uses an assumed stress hybrid finite element formulation [35, 21] with specially developed equilibrated stress fields consistent with micromechanics. VCFEM is able to significantly enhance computing efficiency for complex microstructures compared to conventional displacement based FEM packages. Large regions of the microstructure are thereby easily modeled by this method. A brief account of the extension of VCFEM to accommodate the inclusion-matrix interfacial debonding is presented next.

Consider a typical multiphase domain or representative volume element Ω consisting of N in-

clusions (see figure 3.1a), each contained in a Voronoi cell element Ω_e , as shown in figure 3.1b. The matrix and the inclusion or reinforcement phases in each element are denoted by Ω_m and Ω_c respectively, i.e. $\Omega_e = \Omega_m \cup \Omega_c$. Each element boundary $\partial\Omega_e$ is assumed to be comprised of the prescribed traction and displacement boundaries Γ_{tm} and Γ_{um} respectively, and the inter-element boundary Γ_m , i.e. $\partial\Omega_e = \Gamma_{tm} \cup \Gamma_{um} \cup \Gamma_m$. For allowing decohesion of the matrix-inclusion interface, an incompatible displacement field is facilitated across the interface through a set of connected node-pairs. The nodes in each pair belong to the matrix and inclusion boundaries $\partial\Omega_m^c$ and $\partial\Omega_c^m$ respectively. $\partial\Omega_c^m$ has an outward normal \mathbf{n}^c ($= \mathbf{n}^m$), while \mathbf{n}^e is the outward normal to $\partial\Omega_e$. It should be noted that the interfacial zone has zero thickness prior to deformation, but the nodes may separate with progression of deformation and onset of decohesion.

An incremental VCFEM formulation accommodates evolving interfacial damage with changing applied loads, deformation and stress fields. Let σ^m and σ^c be the equilibrated stress fields and ϵ^m and ϵ^c the corresponding strain fields in the matrix and inclusion phases of each Voronoi element respectively. The prefix Δ corresponds to increments. Furthermore, let \mathbf{u} , \mathbf{u}^m and \mathbf{u}^c denote kinematically admissible displacement fields on $\partial\Omega_e$, $\partial\Omega_m^c$ and $\partial\Omega_c^m$ respectively. A complementary energy functional may be expressed for each element in terms of increments of stress and boundary/interface displacement fields as:

$$\begin{aligned} \Pi_e(\sigma, \Delta\sigma, \mathbf{u}, \Delta\mathbf{u}) = & - \int_{\Omega_m} \Delta B(\sigma^m, \Delta\sigma^m) d\Omega - \int_{\Omega_c} \Delta B(\sigma^c, \Delta\sigma^c) d\Omega - \int_{\Omega_m} \epsilon^m : \Delta\sigma^m d\Omega \\ & - \int_{\Omega_c} \epsilon^c : \Delta\sigma^c d\Omega + \int_{\partial\Omega_e} (\sigma^m + \Delta\sigma^m) \cdot \mathbf{n}^e \cdot (\mathbf{u}^m + \Delta\mathbf{u}^m) d\partial\Omega - \int_{\Gamma_{tm}} (\mathbf{t} + \Delta\mathbf{t}) \cdot (\mathbf{u}^m + \Delta\mathbf{u}^m) d\Gamma \\ & - \int_{\partial\Omega_m^c} (\sigma^m + \Delta\sigma^m) \cdot \mathbf{n}^c \cdot (\mathbf{u}^m + \Delta\mathbf{u}^m) d\partial\Omega + \int_{\partial\Omega_c^m} (\sigma^c + \Delta\sigma^c) \cdot \mathbf{n}^c \cdot (\mathbf{u}^c + \Delta\mathbf{u}^c) d\partial\Omega \\ & - \int_{\partial\Omega_m^c / \partial\Omega_c^m} \int_{(u_n^m - u_n^c)}^{(u_n^m + \Delta u_n^m - u_n^c - \Delta u_n^c)} T_n^m d(u_n^m - u_n^c) d\partial\Omega \\ & - \int_{\partial\Omega_m^c / \partial\Omega_c^m} \int_{(u_t^m - u_t^c)}^{(u_t^m + \Delta u_t^m - u_t^c - \Delta u_t^c)} T_t^m d(u_t^m - u_t^c) d\partial\Omega \end{aligned} \quad (3.1)$$

where B is the complementary energy density and the superscripts m and c correspond to variables associated with the matrix and inclusion phases. The different terms in the right hand side of equation (4.21) are included to provide weak forms of essential governing equations of the problem. The fifth term corresponds to inter-element traction reciprocity while the sixth term accounts for the boundary traction. The last two terms provide the work done by the interfacial tractions $\mathbf{T}^m = T_n^m \mathbf{n}^m + T_t^m \mathbf{t}^m$ due to interfacial separation $(\mathbf{u}^m - \mathbf{u}^c)$, where T_n and T_t are the normal and tangential components. The traction on the matrix interface $\partial\Omega_m^c$ is related to the stresses and interface normals as

$$\mathbf{T}^m = \sigma^m \cdot \mathbf{n}^m = -\sigma^m \cdot \mathbf{n}^c = -\sigma^c \cdot \mathbf{n}^c \quad (3.2)$$

The interfacial response is described by constitutive relations that prescribe the dependence of normal and tangential tractions on components of interfacial separation. The total energy for the

entire heterogeneous domain is obtained by adding the energy functionals for N elements

$$\Pi = \sum_{e=1}^N \Pi_e \quad (3.3)$$

Equating the variation of Π_e in equation (4.21) with respect to stress increments $\Delta\sigma^m$ and $\Delta\sigma^c$ to zero, yields the element displacement compatibility relations in each of the phases Ω_m and Ω_c . Furthermore, setting the variation of Π in equation (3.3) with respect to the independent boundary displacements $\Delta\mathbf{u}$, $\Delta\mathbf{u}^m$ and $\Delta\mathbf{u}^c$ to zero, yield the traction reciprocity conditions on the interelement boundaries (Γ_m) and traction boundaries (Γ_{tm}), and fiber-matrix interfaces, $\partial\Omega_m^c$ and $\partial\Omega_c^m$ respectively.

Independent assumptions on stress increments $\Delta\sigma$ are made in the matrix and reinforcement phases to accommodate stress jumps across the interface. In two-dimensional analysis, the Airy's stress function $\Phi(x, y)$ is used as a convenient tool for deriving equilibrated stress increments. An essential micromechanics observation, that interfacial stress concentrations depend on the shape of the inclusion, has been incorporated in the choice of stress functions, by Moorthy and Ghosh [34] through the decomposition of the matrix stress functions into (a) a purely polynomial function Φ_{poly}^m and (b) a reciprocal function Φ_{rec}^m ($\Phi^m = \Phi_{poly}^m + \Phi_{rec}^m$). The inclusion stress functions are admitted as polynomial function Φ_{poly}^c ($\Phi^c = \Phi_{poly}^c$). The pure polynomial function Φ_{poly} accommodates the far field stress in the matrix and inclusion and are written as:

$$\Phi_{poly}^m = \sum_{p,q} x^p y^q \Delta\beta_{pq}^m \quad \text{and} \quad \Phi_{poly}^c = \sum_{p,q} x^p y^q \Delta\beta_{pq}^c \quad (3.4)$$

The reciprocal stress function Φ_{rec}^m in the matrix facilitates stress concentration at the interface accounting for inclusion shape and decays at large distances from the interface.

$$\Phi_{rec}^m = \sum_{p,q} x^p y^q \sum_{i=1}^n \frac{1}{f^{p+q+i-1}} \Delta\beta_{pqi}^m = \sum_{p,q} x^p y^q \left(\frac{\Delta\beta_{pq1}^m}{f^{p+q}} + \frac{\Delta\beta_{pq2}^m}{f^{p+q+1}} + \dots \right) \quad (3.5)$$

The function $f(x, y)$ is a specially mapped radial coordinate that has the properties

$$f(x, y) = 1 \text{ on } \partial\Omega_c^m \quad \text{and} \quad \frac{1}{f(x, y)} \rightarrow 0 \text{ as } (x, y) \rightarrow \infty \quad (3.6)$$

For 2D elliptical heterogeneities, $f(x, y)$ can be constructed by conformal mapping while for 3D, ellipsoidal coordinates can be chosen to represent this function. Stress increments in the matrix and inclusion phases of the Voronoi cell elements may be obtained by differentiating the stress functions with respect to x and y , to yield expressions of the form:

$$\begin{Bmatrix} \Delta\sigma_{xx}^m \\ \Delta\sigma_{yy}^m \\ \Delta\sigma_{xy}^m \end{Bmatrix} = [\mathbf{P}^m]\{\Delta\beta^m\} \quad \text{and} \quad \begin{Bmatrix} \Delta\sigma_{xx}^c \\ \Delta\sigma_{yy}^c \\ \Delta\sigma_{xy}^c \end{Bmatrix} = [\mathbf{P}^c]\{\Delta\beta^c\} \quad (3.7)$$

where $[\mathbf{P}^m]$ and $[\mathbf{P}^c]$ are the stress interpolation matrices in the matrix and inclusion. The boundary displacements are generated by interpolation in terms of nodal displacements on $\partial\Omega_e$, $\partial\Omega_c^m$ and $\partial\Omega_c^c$ using conventional linear or quadratic shape functions.

$$\{\Delta\mathbf{u}\} = [\mathbf{L}^e]\{\Delta\mathbf{q}\} \text{ on } \partial\Omega_e, \quad \{\Delta\mathbf{u}^m\} = [\mathbf{L}^c]\{\Delta\mathbf{q}^m\} \text{ on } \partial\Omega_c^m \text{ and } \{\Delta\mathbf{u}^c\} = [\mathbf{L}^c]\{\Delta\mathbf{q}^c\} \text{ on } \partial\Omega_c^c \quad (3.8)$$

where $\{\Delta\mathbf{q}\}$, $\{\Delta\mathbf{q}^m\}$ and $\{\Delta\mathbf{q}^c\}$ are the generalized nodal displacement vectors. The stress and displacement interpolations are substituted in equations 4.21 and 3.3. Subsequently stationarity conditions of these equations are evaluated with respect to the stress parameters $\Delta\beta^m$ and $\Delta\beta^c$, and displacement parameters $\{\Delta\mathbf{q}\}$, $\{\Delta\mathbf{q}^m\}$ and $\{\Delta\mathbf{q}^c\}$ to yield the stress and displacement solutions in each element. The details of VCFEM formulation and solution methodology are presented in [35, 34] and is not repeated here.

3.2.1 Cohesive Zone Models for Interfacial Decohesion

Modeling the decohesion of matrix-reinforcement interfaces is conveniently accomplished using crack initiation and propagation criteria based on the evaluation of traditional fracture mechanics parameters K and J . An alternative approach has been pioneered by Dugdale [8], Barenblatt [3], Rice [27] and others to avoid crack initiation and growth conditions. This approach uses cohesive zone interfacial models to depict fracture as a phenomenon of progressive separation across an extended crack tip or cohesive zone, that is resisted by cohesive tractions. Traction across the interface reaches a maximum, subsequently decreases and eventually vanishes with increasing interfacial separation, signaling complete decohesion. Dimensional considerations introduce a characteristic length in these models. The interface mechanical response is specified in terms of critical interfacial strength and work of separation per unit area and no additional failure criteria are required. A number of cohesive zone models have been developed to characterize interfacial decohesion at the continuum scale. Needleman [22, 23, 24] has proposed a potential based framework to describe debonding initiation through complete separation in the cohesive zone. A similar potential based model has also been developed by Tvergaard [29, 30]. Cohesive zone models utilizing nonlinear spring models to depict the interfacial failure process have been proposed by Knauss and coworkers [31, 33]. Geubelle et. al. [9, 15]. From thermodynamic considerations, Costanzo and Allen [6, 7] have postulated rate dependent cohesive zone models with internal state variables to represent microscopic dissipation mechanisms. Ortiz et al. [5, 25] have developed a class of irreversible cohesive laws from potential or free energy functions for tracking dynamically growing cracks.

In this work the rate-independent cohesive zone models of Needleman [22, 23, 24] and Geubelle et. al. [9, 15] are incorporated in the Voronoi cell FEM to model initiation and progressive debonding of matrix-inclusion interfaces in composites. The loading portion of the interfacial decohesion is manifested by these laws. In Needleman's model, the normal and tangential components of interfacial traction are derived from a potential, that is expressed in terms of polynomial or exponential functions of displacement jumps or separation across the interface. The potential using polynomial

(cubic) functions is expressed in the form:

$$\phi(u_n, u_t) = \frac{27}{4} \sigma_{max} \delta^* \left\{ \frac{1}{2} \left(\frac{u_n}{\delta^*} \right)^2 \left[1 - \frac{4}{3} \left(\frac{u_n}{\delta^*} \right) + \frac{1}{2} \left(\frac{u_n}{\delta^*} \right)^2 \right] + \frac{1}{2} \alpha \left(\frac{u_t}{\delta^*} \right)^2 \left[1 - 2 \left(\frac{u_n}{\delta^*} \right) + \left(\frac{u_n}{\delta^*} \right)^2 \right] \right\} \\ \forall u_n \leq \delta^* \quad (3.9)$$

where u_n and u_t are the normal and tangential components of displacement jump at the interface. The cohesive zone parameters are σ_{max} , the maximum traction carried by the interface undergoing a purely normal separation i.e. $u_t = 0$, δ^* , a characteristic length and α , the ratio of interface shear to normal stiffness of the interface. The tractions are obtained by differentiating the potential as

$$T_n = -\frac{\partial \phi}{\partial u_n} = -\frac{27}{4} \sigma_{max} \left\{ \left(\frac{u_n}{\delta^*} \right) \left[1 - 2 \left(\frac{u_n}{\delta^*} \right) + \left(\frac{u_n}{\delta^*} \right)^2 \right] + \alpha \left(\frac{u_t}{\delta^*} \right)^2 \left[\left(\frac{u_n}{\delta^*} \right) - 1 \right] \right\} \quad (3.10)$$

$$T_t = -\frac{\partial \phi}{\partial u_t} = -\frac{27}{4} \sigma_{max} \left\{ \alpha \left(\frac{u_t}{\delta^*} \right) \left[1 - 2 \left(\frac{u_n}{\delta^*} \right) + \left(\frac{u_n}{\delta^*} \right)^2 \right] \right\}$$

For $u_n > \delta^*$, the traction components T_n and T_t are zero in this model. In an alternative form, the potential is expressed using exponential functions of the separation as:

$$\phi(u_n, u_t) = \frac{9}{16} \sigma_{max} \delta^* \times \left\{ 1 - \left[1 + z \left(\frac{u_n}{\delta^*} \right) - \frac{1}{2} \alpha z^2 \left(\frac{u_t}{\delta^*} \right)^2 \right] e^{-z \left(\frac{u_n}{\delta^*} \right)} \right\} \quad (3.11)$$

where $z = \frac{16\epsilon}{9}$. Thus the interfacial traction components are

$$T_n = -\frac{\partial \phi}{\partial u_n} = -\sigma_{max} e \left\{ z \left(\frac{u_n}{\delta^*} \right) - \frac{1}{2} \alpha z^2 \left(\frac{u_t}{\delta^*} \right)^2 \right\} e^{-z \left(\frac{u_n}{\delta^*} \right)} \quad (3.12)$$

$$T_t = -\frac{\partial \phi}{\partial u_t} = -\sigma_{max} e \left\{ \alpha z \left(\frac{u_n}{\delta^*} \right) \right\} e^{-z \left(\frac{u_n}{\delta^*} \right)}$$

Coupling between normal and tangential components is achieved through the functions of u_n and u_t .

The cohesive failure model by Geubelle et. al. [9, 15] incorporates a bilinear form of the traction-displacement jump relation for mode mixity of applied tractions. The traction-separation law is expressed as

$$T_n = \begin{cases} \frac{\sigma_{max}}{\delta_{max}} \delta_n & \text{for } \delta \leq \delta_{max} \\ \frac{\sigma_{max}}{\delta} \frac{1-\delta}{1-\delta_{max}} \delta_n & \text{for } \delta > \delta_{max} \end{cases}$$

$$T_t = \begin{cases} \frac{\sigma_{max}}{\delta_{max}} \frac{u_n^c}{u_t^c} \delta_t & \text{for } \delta \leq \delta_{max} \\ \frac{\sigma_{max}}{\delta} \frac{1-\delta}{1-\delta_{max}} \frac{u_n^c}{u_t^c} \delta_t & \text{for } \delta > \delta_{max} \end{cases} \quad (3.13)$$

where u_n and u_t are the normal and tangential components of interfacial displacement jump and δ_n , δ_t and δ are the corresponding non-dimensional variables, defined as

$$\delta_t = \frac{u_t}{u_t^c}, \quad \delta_n = \frac{u_n}{u_n^c}, \quad \delta = \sqrt{\delta_t^2 + \delta_n^2} \quad (3.14)$$

The parameters u_n^c and u_t^c are critical values of normal and tangential separation, for which complete debonding is assumed to occur. The parameter σ_{max} corresponds to the maximum value of normal traction T_n for a normal displacement jump of $u_n = \delta_{max} u_n^c$. The maximum absolute value of $|T_t|$ is $\tau_{max} = \sigma_{max} \frac{u_n^c}{u_t^c}$ which occurs at $|u_t| = \frac{1}{2} \delta_{max} u_t^c$. Since the work of separation per unit area on the interface in the normal and tangential directions, are expressed as

$$\Gamma_n = \frac{1}{2} \sigma_{max} u_n^c, \quad \text{and} \quad \Gamma_t = \frac{1}{2} \tau_{max} u_t^c \quad (3.15)$$

The maximum tangential traction expression implies that $\Gamma_n = \Gamma_t$, or that the critical energy release rates are the same for mode I and mode II. This constraint, in a sense, creates an equivalence between the potential based models and the non-linear spring relations. Parameters in both classes of models may be adjusted, so that they possess the same essential features, e.g. the fracture energy or the area under the cohesive law, the peak cohesive traction etc.. The parameters u_n^c, u_t^c or δ^* typically introduce a characteristic length of the material microstructure. A major difference between the two models is that the Geubelle's model admits a jump in the slope of the traction-displacement curve, while the Needleman's polynomial and exponential models have continuous slopes.

Both of these laws are reversible i.e., they retrace the traction-displacement curve upon unloading. It has been argued (see Ortiz et. al. [25, 5]) that the decohesion process is expected to exhibit some irreversibility. Following their models, irreversibility is incorporated in the present work by allowing the cohesive surfaces to linearly unload to and reload from the origin.

3.2.2 Implementation of Cohesive Zone Models in VCFEM

For implementing the interfacial constitutive relations in VCFEM, the last two terms in equation 4.21 are replaced with traction-separation relations of the cohesive zone model. For Needleman's models this takes the form

$$\begin{aligned} & - \int_{\partial\Omega_m^c / \partial\Omega_c^c} \int_{u_n}^{u_n + \Delta u_n} T_n^m du_n d\partial\Omega - \int_{\partial\Omega_m^c / \partial\Omega_c^c} \int_{u_t}^{u_t + \Delta u_t} T_t^m du_t d\partial\Omega \\ & = \int_{\partial\Omega_m^c / \partial\Omega_c^c} [\phi(u_n + \Delta u_n, u_t + \Delta u_t) - \phi(u_n, u_t)] d\partial\Omega \end{aligned} \quad (3.16)$$

where the potentials $\phi(u_n, u_t)$ are stated in equations (3.9.3.11). For Geubelle's model the work of separation becomes

$$- \int_{\partial\Omega_m^c / \partial\Omega_c^c} \int_{u_n}^{u_n + \Delta u_n} T_n^m du_n d\partial\Omega$$

$$\begin{aligned}
& - \int_{\partial\Omega_m^c / \partial\Omega_\xi^c} \int_{u_t}^{u_t + \Delta u_t} T_t^m du_t d\partial\Omega \\
& = (1 - \Psi) \int_{\partial\Omega_m^c / \partial\Omega_\xi^c} \frac{1}{2} \frac{\sigma_{max} u_n^c}{\delta_{max}} ((\delta_n + \Delta\delta_t)^2 + (\delta_t + \Delta\delta_t)^2) d\partial\Omega + \\
& \quad \Psi \int_{\partial\Omega_m^c / \partial\Omega_\xi^c} \frac{\sigma_{max} u_n^c}{1 - \delta_{max}} [\sqrt{\delta_t^2 + (\delta_n + \Delta\delta_n)^2} + \sqrt{\delta_n^2 + (\delta_t + \Delta\delta_t)^2}] \\
& \quad - \frac{1}{2} ((\delta_n + \Delta\delta_n)^2 + (\delta_t + \Delta\delta_t)^2) d\partial\Omega
\end{aligned} \tag{3.17}$$

where Ψ is a step function defined as

$$\Psi = \begin{cases} 0 & \text{for } \delta \leq \delta_{max} \\ 1 & \text{for } \delta > \delta_{max} \end{cases}$$

The normal and tangential separation at the interface may be expressed in terms of the nodal displacements using the interpolated forms of equation 4.22 as:

$$\begin{aligned}
u_n &= u_n^m - u_n^c = \{\mathbf{n}^c\}^T [\mathbf{L}^c] \{\mathbf{q}^m - \mathbf{q}^c\} \\
u_t &= u_t^m - u_t^c = \{\mathbf{t}^c\}^T [\mathbf{L}^c] \{\mathbf{q}^m - \mathbf{q}^c\}
\end{aligned} \tag{3.18}$$

Here $\{\mathbf{n}^c\}$ and $\{\mathbf{t}^c\}$ are arrays containing direction cosines of unit outward normal and unit tangent vectors to the interface. The resulting weak forms of the element kinematic relations and traction reciprocity conditions are nonlinear due to the nonlinear traction-displacement relation in the cohesive zone models. A Newton-Raphson method iteration method is consequently employed to solve for the stresses and displacements. In the event of unloading in an increment due to reduction of interfacial separation (crack closure), an unloading algorithm to approach the origin, is activated.

3.3 Numerical Examples

The numerical examples are divided into three categories. In the first example, VCFEM results with the cohesive zone model are compared with results in Needleman [22]. The second set of examples is aimed at the evaluation of cohesive parameters by comparison of VCFEM simulations with experimental results and further validation. In the final set, VCFEM simulations are used to make predictions of damage and overall mechanical behavior for fiber reinforced composite microstructures with different morphologies. The stress functions in the inclusion phase of each Voronoi Cell element is generated using 33 terms (7-th order polynomial stress function, i.e. $p+q=2..7$) for the polynomial function in equation (3.4). The matrix stress function has an additional 36 reciprocal terms due to the reciprocal terms in equation 3.5 (3 reciprocal terms for each polynomial exponent from 2 to 4, i.e. $i = p + q..p + q + 2 \forall p + q \in [2..4]$). Displacement fields on the element boundary and on the matrix and inclusion parts of the interface are represented using linear interpolations $[\mathbf{L}^e]$ and $[\mathbf{L}^c]$ in equation (4.22). The number of node-pairs on the interface is set to 16. This is consistent with the requirements of stability and rank sufficiency of the assumed stress hybrid FEM, as discussed in [34, 21]. The initial locations of interfacial nodes, prior to debonding,

are determined by an adaptation procedure that is detailed in [21]. In this process, nodes are added or positioned to minimize the error in inter-element and interfacial traction continuity. It results in optimization of the virtual work with respect to traction discontinuity across boundaries. The node-pairs are moved in the direction of the debond once debonding sets in, to accurately capture the crack tip stress concentration.

3.3.1 Comparison with results of Needleman [22]

In [22], the cohesive zone model of equations (3.11) has been used for simulating debonding of an elastic-plastic matrix from rigid spherical reinforcements. The reinforcements of 1.04% volume fraction are arranged in a cylindrical periodic array. Consequently, an axisymmetric analysis of a square unit cell with periodic boundary conditions is conducted. In Needleman's analysis [22], the matrix is modeled as rate dependent elastic-viscoplastic material with isotropic hardening, with the effective plastic strain rate $\dot{\epsilon}$ being expressed in terms of the effective stress $\bar{\sigma}$ as

$$\dot{\epsilon} = \dot{\epsilon}_0 \left[\frac{\bar{\sigma}}{g(\bar{\epsilon})} \right]^{\frac{1}{m}}, \quad g(\bar{\epsilon}) = \sigma_0 (1 + \bar{\epsilon}/\epsilon_0)^N, \quad \epsilon_0 = \frac{\sigma_0}{E} \quad (3.19)$$

where m and N are the strain rate hardening and strain hardening exponents and σ_0 is a reference strength. The matrix material properties are assumed to be $E_m = 500\sigma_0$, $\nu_m = 0.3$ and $\sigma_0 = 400 MPa$. The current version of VCFEM formulation can only support rate independent plasticity. It is deemed that the small value of the exponent ($m = 0.01$) in [22] would agree (at least qualitatively) with the VCFEM results using rate independent plasticity ($m = 0$). The inclusion is modeled as elastic with very high stiffness. The cohesive zone parameters in equations (3.11) are taken as $\sigma_{max} = 3\sigma_0$, $\delta/r_0 = 0.01$, and $\alpha = 10.0$. The stress triaxiality parameter ρ , is set to 0.5. The VCFEM model consists of a single element with periodic boundary conditions imposed as

$$\begin{aligned} \dot{u}_x = 0, \quad \dot{T}_y = 0, & \quad \text{on } x = 0 \quad \dot{u}_x = \dot{U}_x = \dot{\epsilon}_\infty b_0, \quad \dot{T}_y = 0, \quad \text{on } x = R_0 \\ \dot{u}_y = \dot{U}_y, \quad \dot{T}_x = 0, & \quad \text{on } y = R_0 \end{aligned} \quad (3.20)$$

Here, \dot{u}_x and \dot{u}_y , and \dot{T}_x and \dot{T}_y are the velocities and traction rates, in the radial and axial directions respectively. The macroscopic effective stress $\Sigma_e = |\Sigma_x - \Sigma_y|$ is plotted as a function of the axial strain $\epsilon_a = \ln(1 + U_x/b_0)$ in figure 3.2. The onset of debonding is signaled by the sudden drop in stress level and its arrest is indicated by the resumption of monotonic increase of flow stress. The results of VCFEM simulation agree rather well with those in [22]. The slightly higher stress values can be attributed to the small deformation rate independent plasticity with exponent $m = 0$ in VCFEM formulation.

3.3.2 An Experimental-Computational Study

Prior to predicting the interfacial debonding phenomena for multiple-fiber reinforced composites with the computational model, limited comparisons with experiments are conducted with model composite systems with two objectives. The first is to ascertain the material parameters in the cohesive zone model, viz. σ_{max} , δ^* and α in Needleman's models [24] and σ_{max} , δ_{max} , u_n^c and

u_t^c in Geubelle's model [15]. The parameters are evaluated by solving inverse problems in which the difference between critical experimental observations and results of VCFEM simulations are minimized. The second objective is to validate the predictions of VCFEM against experimental observations for composites with different microscopic architectures.

The experimental procedure

The debonding experiments are conducted with model single and multiple fiber specimens in the form of a cruciform as shown in figure 3.3a. The cruciform shape has been developed in [12, 19, 28] to avoid the development of stress singularity at the intersection of fiber-matrix interface and free surface, with conventional uniform width specimens. Such stress singularities promote interfacial separation near the free surface and results in invalid interface strength data. The most significant advantage of the cruciform geometry is that it forces debond failure to initiate in the central region of the specimen.

The model composite specimens are fabricated by casting in a cruciform-shaped silicone rubber mold to specimen dimensions shown in figure 3.3 and table 1. The circular fillets at the cross junctions reduce stress concentration in the matrix at these locations. The reinforcing fibers in the composite system are stainless steel filaments. The fibers of predetermined length are positioned in the mold and the matrix material is cast around them. Larger diameters are helpful in detecting the debond initiation process and are chosen for the single fiber cruciforms. The matrix is an epoxy resin (Epon 828 manufactured by Shell Chemical Co.), that is cured with a polyetheramine (Jeffamine D-230 manufactured by Texaco Inc.) for 3 days at ambient temperature.

Room-temperature curing reduces residual thermal stresses in the matrix, due to mismatch in the fiber and matrix thermal properties, to a minimum. The epoxy matrix is transparent and allows visualization of the debonding process at the fiber-matrix interface. Preliminary experiments with no interfacial coating, indicate that the bond strength is high and interface failure progresses rapidly to cause immediate catastrophic rupture. Consequently, the steel filaments are cleaned and polished with acetone and coated with a very thin film of freekote ($< 0.1 \mu m$) prior to casting the specimens. The freekote imparts a weak strength to the steel-epoxy interface. This allows a somewhat stable growth of the debond crack, thereby permitting determination of the parameters in interfacial cohesive zone models.

In the experimental set up, three strain gages (A, B and C) are affixed on faces of the specimen as shown in figure 3.3a. Two gages (A and B) are located in the central portion of the cruciform in vicinity of potential debond sites. Thus their readings are assumed to correspond to the debonding strains in the specimen. The third gage C is mounted on the limb, away from the fibers and represents the far-field strain. Furthermore, to prevent specimen failure in the grip region, fiberglass/epoxy end tabs are adhesive bonded on the upright portion of the specimen. Four different microstructural architectures are considered for the experiments. They are:

- Specimen # 1 containing a single circular fiber.

- Specimen # 2 containing a single elliptical fiber with major axis along the loading direction ($\alpha_{maj} = 0^\circ$),
- Specimen # 3 containing a single elliptical fiber with major axis perpendicular to the loading direction ($\alpha_{maj} = 90^\circ$),
- Specimen # 4 containing 5 identical circular fibers.

These are schematically illustrated in figure 3.3 and the geometric details on location, size etc. are given in table 1. The area fraction in the table are for the cross-section at the outer edge. The elastic material properties for the reinforcing steel fibers and epoxy matrix are experimentally determined as:

Young's modulus $E_{steel} = 210$ GPa, Poisson's ratio $\nu_{steel} = 0.3$; Young's modulus $E_{epoxy} = 4.6$ GPa, Poisson's ratio $\nu_{epoxy} = 0.4$.

The cohesive properties of the debonding material are evaluated by solving the inverse problem mentioned in section 3.3.2.

The model specimens are loaded in tension on a servo-hydraulic testing machine. The readings from the strain gages are recorded continuously and the onset of fiber-matrix debonding is interpreted from a sharp change in the slope of the stress-strain curve based on gage readings at the cruciform center. Acoustic emission sensors are also employed to confirm the onset of debonding. In figure 3.5, the abrupt change in slope at B corresponds to debond initiation, and the relatively flat portion BC corresponds to the strain jump. Subsequent loading (CD) proceed with a lower stress-strain slope, due to a reduced load carrying capability of the partially debonded fiber. Unloading along DA and subsequent reloading along ACD indicate no further change in slope, i.e. no additional debonding. Matrix cracks always initiate at the fiber-matrix debond site and grow rapidly to cause specimen failure. A few specimens are not loaded to fracture, to allow observation of the partially debonded interface.

Following interface failure, some of the cruciform specimens are sectioned along the center, parallel to the loading direction. A drop of a fluorescent dye penetrant is positioned above the sectioned fiber and vacuum infiltration is used to force the penetrant into the debonded interface. The sectioned face is then polished to remove traces of the dye from the original drop. Thereby, only the dye that has penetrated along the interface crack will remain. The fiber is then viewed under an ultraviolet light, which causes the regions containing the dye to remain bright in an otherwise dark background. Figure 3.4a shows the debond under oblique incidence, where the fiber surface is visible through the transparent matrix. The bright regions correspond to locations of debond and they are concentrated on the fiber surface in the direction of the loading axis. Also, note that they are generally absent in the wing region, which experience significantly lower loads than the cruciform center. Figure 3.4b shows the cross section of the fiber at a higher magnification, and the debonded region is the thin bright strip along the fiber periphery. The ends of the debond are highlighted by the arrows, and the loading direction is horizontal in the figure. Figure 3.4b also shows that the total angle of debonding was approximately 85° .

Evaluation of a Conversion Factor for Stress 3-D to 2D Stresses

The experimental results are compared with results of simulations by a 2-D (plane strain) Voronoi cell finite element model for validation and damage prediction. While the fiber-reinforced cruciform specimen represents a 3-D problem in actuality, the stresses and displacements at the center of the cruciform can be well approximated by two 2-D solutions for a reasonably slender geometry. Prior to comparison of the results, a conversion factor is established for predicting the 3-D stress state from 2-D simulations. A full 3-D analysis of the cruciform specimen and a plane strain analysis of the section containing a single circular fiber are conducted using the commercial finite element package ANSYS. Perfect interface with no debonding is assumed in these analyses. Figure 3.6 shows comparison of the radial stress σ_{rr} and tangential stress $\sigma_{r\theta}$ along the interface for the two analyses. A stress concentration factor is defined as the ratio of the maximum radial stress along the tensile axis at the pole of the fiber-matrix interface (angle=0 in the figure) to the far-field stress. This factor is computed to be $k_{2D} = 1.349$ for 2D analysis and $k_{3D} = 1.139$ for 3-D. By multiplying the plane strain results with a factor $k = \frac{k_{2D}}{k_{3D}} = 0.844$ enables a very good match with the 3-D solution, as shown in the stress plots of figure 3.6. Consequently, the 2-D stresses from VCFEM analysis are multiplied by the factor $k = 0.844$ for comparison with 3-D experimental results. The 2-D sections analyzed, corresponds to rectangular vertical sections through the center of the cruciform specimen, shown in figure 3.3a. The sections have dimensions of $33\text{ mm} \times y_e$ with the fiber cross-sections in the central region, and where y_e is given in table 1. A total of $(n + 2)$ Voronoi cell elements, where n correspond to the fibers and two additional elements for the limb portions, are used to perform this 2-D analysis.

Evaluation of cohesive zone parameters

Cohesive zone parameters for the models proposed by Needleman [22, 23] and Geubelle et. al. [9, 15] are calibrated by solving an inverse problem using the VCFE model and comparing with experimental results. The computational model analyzes the 2-D cross-sections shown in figure 3.3b under plane strain conditions and loaded axially. In Geubelle's model, the parameters to be determined are δ_{max} , σ_{max} , u_f^c and u_n^c , while in Needleman's model the parameters are σ_{max} , δ^* and α . Their evaluation for a given bonding material (freeskote in this problem) follows a multi-variable optimization process, in which, four key variables are chosen for minimizing the difference between experimental and computational results. These effective values are marked in figure 3.5 and are: (i) the strain at which debonding initiates (S_I), (ii) the strain (S_{II}) at which debonding arrests, (iii) the stress (S_{III}) at which debonding arrests, and (iv) post debonding slope of the stress-strain plot (S_{IV}). The major steps in this evaluation process are:

1. For each of the models in equations 3.11, 3.13 and 3.13, the overall stress-strain response with debonding behavior is first determined (similar to figure 3.5) for a range of candidate values of cohesive parameters. These parameters are chosen from an estimated range of possible values. For each set of parameters, e.g. $(\delta_{max}, \sigma_{max}, u_f^c, u_n^c)$ or $(\sigma_{max}, \delta^*, \alpha)$, an independent VCFEM simulation of the microstructure with debonding in simple tension, is performed.
2. The key variables $S_i (i = I \dots IV)$ are represented as polynomial functions of the cohesive zone

parameters. This produces continuous functions for gradient based optimization methods, necessary in parameter evaluation. For Geubelle's model [15, 9], these are written as

$$S_i = (a_{i0} + a_{i1}\delta_{max} + a_{i2}\delta_{max}^2 + \dots) + (b_{i0} + b_{i1}\sigma_{max} + b_{i2}\sigma_{max}^2 + \dots) \\ + (c_{i0} + c_{i1}u_t^c + c_{i2}u_t^{c2} + \dots) + (d_{i0} + d_{i1}u_n^c + d_{i2}u_n^{c2} + \dots) \quad (3.21)$$

while for Needleman's model [22, 23], these are

$$S_i = (a_{i0} + a_{i1}\sigma_{max} + a_{i2}\sigma_{max}^2 + \dots) + (b_{i0} + b_{i1}\delta^* + b_{i2}\delta^{*2} + \dots) + (c_{i0} + c_{i1}\alpha + c_{i2}\alpha^2 + \dots) \quad (3.22)$$

3. To evaluate the coefficients of the polynomial expansions i.e. $a_{i0}, a_{i1}, \dots, b_{i0}, b_{i1}, \dots, c_{i0}, c_{i1}, \dots, d_{i0}, d_{i1}, \dots$, approximately 150 VCFEM simulations are conducted with different parameter sets. For each simulation with a set of values e.g. $(\delta_{max}, \sigma_{max}, u_t^c, u_n^c)$ or $(\sigma_{max}, \delta^*, \alpha)$, the computed values of $S_i, i = I..IV$ are recorded from the stress-strain plots. The minimum number of simulations correspond to the total number of unknown coefficients. However, a higher number is performed in this study to accommodate a larger range of cohesive parameters.
4. The coefficients $a_{i0}, a_{i1}, \dots, b_{i0}, b_{i1}, \dots, c_{i0}, c_{i1}, \dots, d_{i0}, d_{i1}, \dots$ are evaluated by a least square based minimization process using MATLAB. This enables explicit construction of the functions $S_i, i = I..IV$.
5. The parameters of cohesive zone models in Geubelle and Needleman are finally obtained by minimizing the difference between experimental and simulated values of the key variables S_i in the stress-strain plots of figure 3.5 or 3.10. A multi-parameter optimization problem is solved as :

$$\text{Minimize} \left[\sum_{i=1}^4 w_i (S_i^{\text{simulation}} - S_i^{\text{experiment}})^2 \right] \\ \text{w.r.t. } \sigma_{max}, \delta_{max}, u_n^c \text{ and } u_t^c \\ \text{OR} \\ \text{w.r.t. } \sigma_{max}, \delta^* \text{ and } \alpha \quad (3.23)$$

The weights w_i may be suitably chosen to impart preferential importance to the key variables. Equal weights are chosen for this analysis.

Two sets of resulting values of the cohesive zone parameters are presented in table 2. The first set correspond to values that are evaluated by comparison with the results of experiments with specimen 1. When these parameters are used to simulate the other specimens 2, 3 and 4, it is seen that the maximum difference between experiments and simulations occur for specimen 3. A second set of parameters are consequently derived using the key variables S_i for both specimens 1 and 3, shown in figures 3.5 and 3.10. A small difference is noted in table 2, between the values of the two sets. The results shown in the following sections are with the second set of cohesive parameters.

Comparison of VCFEM and experimental results

Results of VCFEM simulations for the four different microstructures of specimens 1, 2, 3 and 4 are compared with experiments, macroscopically in figures 3.5, 3.10 and 3.15 and microscopically in figure 3.4. The abscissa in figures 3.5, 3.10 and 3.15, is the gage strain recorded by 0.8 mm strain gages mounted on the specimen surface (A in figure 3.3a). The corresponding strains in VCFEM analyses are calculated from the change in length of a 0.8 mm segment, located on the 2D specimen boundary, closest to the fiber. In table 3, the simulated gage strains and the area-averaged strains are tabulated. There is a small difference between the two strains. This may be attributed to the fact that the edge along which the gage strain is measured is sufficiently close to the fibers for local effects of the interface to prevail. The ordinate in the plots of figures 3.5, 3.10 and 3.15 are the area-averaged macroscopic stresses in the direction of loading. The stress-strain plots for all three decohesion models (Geubelle, Needleman-polynomial and Needleman-exponential) in figure 3.5 show good agreement with the experimental stress-strain behavior. The onset of debond, signaled by a sharp reduction of slope, is also predicted quite well. However, the arrest of debond, as indicated by an increase in the post-decohesion stiffness, is more gradual for the simulations than for experiments.

The experimentally determined debonding angle by dye injection is evaluated in figure 3.4 to be approximately 85° . The corresponding simulated value is found to be 91° (see table 3). This corresponds to a 6.6% deviation from experiments. Table 3 also presents the overall stiffness values before and after debonding and the total debonding angle along the interface, using Geubelle's model [15]. The undamaged overall stiffness K_{ud} is the slope of the area averaged tensile stress-strain plots in the loading direction, for the rectangular section through the cruciform center. The highest K_{ud} is observed for specimen 2 with $\alpha_{maj} = 0^\circ$, while the lowest is that for specimen 4 with a lower volume fraction. The maximum drop in stiffness occurs with specimen 3 ($\alpha_{maj} = 90^\circ$) since this interface undergoes the largest debonding angle ($\theta_d=134^\circ$). The minimum drop is for the multiple fiber specimen even with considerable interfacial debonding ($\theta_d=87^\circ$), mainly due to the small area fraction. The increase in debonding angle, as functions of the averaged strain, are plotted in figures 3.7 and 3.16. For specimen 1, the response of the three interfacial decohesion models are extremely close. The debonding angle increases rapidly after initiation with little additional strain, and then tapers off asymptotically to a stable value. The initiation strains for specimens 1 and 3 are quite close, while that for the specimen 2 is significantly lower. Also the smallest stable debond angle occurs with the specimen 2 and the largest for specimen 3 with specimen 1 in the middle. The stable debonding angle for both specimens 1 and 4 with circular fibers are quite close.

To understand the effects of stress distribution on the debonding process, the normal and tangential interfacial stresses σ_{nn} and σ_{nt} are plotted from $\phi = 0^\circ$ (the loading direction) to $\phi = 180^\circ$, in figures 3.8, 3.9, 3.11, 3.12, 3.13 and 3.14. The peak stress at the tip of the crack or debond is obtained from the spring tractions at the node-pair, just ahead of the debonded nodes where the condition $\delta = 1$ in equation (3.14) is satisfied. The normal stress plots are symmetric about the angular position $\phi = 90^\circ$, while the tangential stresses are antisymmetric about this angle. Prior to debonding, the normal stress is maximum at $\phi = 0^\circ$, while the shear stress peaks out at

$\phi = 45^\circ$. Once debonding initiates, the peaks occurs at the crack tip and subsides monotonically till it reaches the pole at $\phi = 90^\circ$, where σ_{nn} is mildly compressive. With progressive debonding, the peak tensile stress σ_{nn} initially increases in magnitude but subsequently decreases. This behavior may be explained as a consequence of two competing phenomena, viz. an increase in average stress due to increasing debond length and a decrease in the normal component of stress with increasing angular orientation, especially as $\phi \rightarrow 90^\circ$. The compressive region also increases with increasing decohesion. Similar observations have also made in [1]. For the tangential stress σ_{nt} , the maximum value at the crack tip is also found to first increase slightly and then decrease with progressive debonding. From these plots, it is easy to explain the reasons for the nucleation and progress in decohesion, as depicted in figures 3.7 and 3.16.

Through a combination of experimental and computational simulations, these examples establish considerable confidence in the model for understanding the behavior of the interfacial debonding phenomena.

3.3.3 Multiple Fibers in the Microstructure

In this final set of examples, computational analyses are conducted to understand the effect of morphology and applied boundary conditions on the initiation and progress of debonding induced damage in microstructures containing multiple fibers. The microstructure in these examples contain 100 circular fibers in a square region. To investigate the role of fiber interaction due to different spatial dispersions, two distributions viz. a uniform distribution and a random distribution are considered. For comprehending the role of boundary conditions on the damage evolution process, two in-plane conditions viz. (a) periodic conditions and (b) displacement (non-periodic) boundary conditions, are specified. The periodicity boundary conditions are imposed by requiring edges to remain straight and parallel to the original direction throughout deformation. This may be achieved through the following conditions.

$$\begin{aligned} u_x &= 0 \text{ (on } x = 0\text{)} , u_y = 0 \text{ (on } y = 0\text{)} , u_x = u_{ap} \text{ (on } x = L_x\text{)} , u_y = D_y^* \text{ (on } y = L_y\text{)} \\ T_y &= 0 \text{ (on } x = 0 \text{ and } x = L_x\text{)} , T_x = 0 \text{ (on } y = 0 \text{ and } y = L_y\text{)} \end{aligned} \quad (3.24)$$

where u_{ap} is a monotonically increasing applied displacement and D_y^* is determined from the average force condition $\int_X T_x dx = 0$ on $y = L_y$. For the displacement boundary conditions, $y = L_y$ is a traction free-edge. The elastic material properties for the reinforcing steel fibers and epoxy matrix are the same as in the previous section, i.e. Young's modulus $E_{steel} = 210$ GPa, Poisson's ratio $\nu_{steel} = 0.3$; Young's modulus $E_{epoxy} = 4.6$ GPa. Poisson's ratio $\nu_{epoxy} = 0.4$. The interface is represented by the cohesive zone model of Geubelle et. al. [15] with the same parameters, i.e. $\delta_{max} = 0.9347$, $\sigma_{max} = 0.012570$ GPa, $u_t^c = 0.00007217$ mm and $u_n^c = 0.00006395$ mm. The plane strain Voronoi cell finite element model is used in this analysis, with a tessellated mesh of 100 Voronoi elements each containing a fiber. For the uniform distribution, the tessellation process yields square elements, while for the random distribution the cells have variable number of edges. The two meshes with boundary conditions are shown in figures 3.17 a and b.

The macroscopic or area-averaged stress-strain response for the two architectures are plotted for the two boundary conditions in figure 3.18a. Prior to debonding, the stiffness of the random microstructure is marginally higher than that for the uniform one. For each microstructure, the behavior with periodicity is stiffer than that without. This is due to the additional displacement constraint imposed by the periodicity condition, which raises stresses in the microstructure. Appreciable debonding in fibers is signaled by an abrupt change in slope of the stress-strain curve. This is noticed at a significantly smaller strain for the random microstructure. However, the ultimate loss of stiffness is higher for the uniform microstructure. The number of debonded fibers as a function of increasing strain is plotted in figure 3.18b. The rate of damage growth is more gradual for the random microstructure. This rate is initially low, but increases considerably with straining in the intermediate region and finally tapers off at higher values of strain. This is because, initial stages of debonding are influenced by the inter-fiber spacing. Interfaces of fibers that are in close proximity are damaged early. The subsequent stages of damage also depend on the overall strain state. In the uniform model, the initiation takes place later but the growth of damage by interfacial decohesion occurs rapidly. This is particularly true for the periodic boundary condition. With the displacement boundary conditions, the growth is slow in the beginning but increases substantially with straining.

A clear delineation of the debonding process is obtained from the contour plots of the tensile stress σ_{xx} in figures 3.19 and 3.20. The figures show the debonds on the interfaces, as well as locations of stress concentrations. For the uniform microstructure with displacement boundary conditions (non-periodic), debonding starts at the fiber in the upper right corner and propagates down along the diagonal to create a dominant damage path. The reason for the damage propagation along a distinct path is explained from the radial stress σ_{rr} plots along the interfaces, in figures 3.21. The fiber numbers 1, 2, 3, and 4 are delineated in figure 3.17a. At a macroscopic strain value of $\epsilon = 1.31 \times 10^{-4}$, just before initiation, the radial stress at the interface of the corner fiber #2 is higher at the poles along to the loading axis (i.e. $\theta = 0^\circ, 180^\circ$). This causes the fiber #2 to debond first. Following this, the radial stress in fiber #3 exceeds that of others at the poles and hence debonds. This pattern is observed for the entire load cycle. Finally, all fibers debond at higher values of the applied strain. In contrast, all fibers debond simultaneously for the periodic boundary conditions, with no apparent dominant path. A single unit cell with these periodic boundary conditions also produce identical results. It is clear from this example, that even though the microstructure may have geometric periodicity, the evolution of damage to cause failure is likely to follow a non-periodic and dominant local path. This makes the application of the conventional unit cell analysis to problems with evolving damage, inappropriate.

For the random microstructure, the difference in debond initiation and growth behavior with different boundary conditions is not as prominent. In contrast, the effect of local morphology is much more dominant. This is observed in figures 3.18b and 3.20. Debonding initiates in fibers that are in close proximity with other fibers and evolves randomly with increased straining. The relation between damage evolution and the local dispersion for the random microstructure, is better understood from the histograms of figures 3.22 and 3.23. In these histograms, the relative spacing and proximity among fibers is characterized by two spatial functions viz. (a) local area fraction (LAF)

and (b) the nearest neighbor distance (NND). The local area fraction (LAF) is measured as the ratio of the fiber area to the area of the Voronoi cell containing it. The nearest neighbor distance (NND) is measured as the smallest surface to surface distance between neighbors that share common Voronoi cell edges. The ordinate of the histograms represents the total number, as well as the number of debonded fibers as functions of the characterization functions LAF and NND. Different shades are used to delineate additionally debonded fibers with increasing strain. The LAF function has a bell shaped distribution whereas the NND function is clearly monotonically decreasing for the total number (debonded+intact) fibers. Debonding initiates at the higher values of LAF and lower values of NND. There is a monotonic decrease of debonded fibers with decreasing LAF and increasing NND. The monotonicity is particularly obvious for the latter function. The low NND represents closely packed fibers which are more likely to debond early, in the loading cycle. Similar responses are obtained for both periodic and displacement boundary conditions. The statistics of debonding are also tabulated in table 4.

The effect of volume or area fractions are also investigated through a second area fraction of $v_f = 10\%$. Both constant and randomly varying sizes of randomly dispersed fibers are considered for the 10% microstructure. The macroscopic responses for these models are plotted in the figures 3.18. As long as the volume fraction is the same, the overall stiffness is not very sensitive to the size distribution, i.e. it is quite close for both the constant and the randomly varying diameters. However, the dependence of damage on the size distribution is considerable and occurs earlier for the variable size. The onset of debonding is considerably delayed for the lower volume fraction, due to increased average spacing between fibers which result in lower stress concentration. In summary, the process of initiation and growth of damage by interfacial debonding depends on several competing factors such as morphology, fiber interaction, load and boundary conditions. It is important to include large portions of the microstructure to capture the different effects, which is a major shortcoming of unit cell analyses.

3.4 Concluding Remarks

The initiation and growth of damage by interfacial decohesion in multiple-fiber polymer matrix composites is analyzed with in-plane loading in this work. The fiber and matrix phases are modeled with elastic properties. The progress of interfacial debonding with quasi-static loading is modeled by cohesive zone constitutive relations in terms of normal and tangential tractions and interfacial separation. In these relations, the traction increases with separation, reaches a maximum and subsequently subsides to zero traction, signaling debonding. The stress and damage analyses is conducted with the Voronoi cell finite element model, that has been established as an effective tool for modeling of non-uniform microstructures. VCFEM has been developed (see [34, 21]) to yield high computational efficiency with good accuracy for modeling large heterogeneous microstructures.

The VCFC model for interfacial debonding has been compared with a variety of established results in literature, the details of which are reported in the M.S. thesis of Ling [16]. Only a single satisfactory comparison of macroscopic results with those in [22] are presented in this work. A com-

bined experimental-computational study is conducted for specimens of polymer matrix composites in this work. An inverse methodology is developed for calibrating the cohesive model parameters from simple experimental results. It is based on minimizing the difference in the macroscopic stress-strain plots with damage, obtained by VCFE simulations and experiments. For the experiments, single and multiple fiber cruciforms specimens of circular and elliptical shapes, are fabricated to avoid stress concentrations at the edges. Results are considered from more than one experimental specimens, to account for the variability between experiments in the calibration process. VCFE debonding analyses are subsequently conducted to simulate experiments with other specimens. The microscopic debonding angle in experiments is estimated by a dye penetration technique. Good agreement is obtained between experiments and the simulations, both with respect to macroscopic (averaged stress-strain behavior) and microscopic (debond angle) observations.

In numerical simulations of multiple fibers microstructures, different morphologies and boundary conditions are analyzed to understand their influence on the decohesion process. Different architectures include uniform and random dispersions, different volume fractions and different size distributions. The boundary conditions include imposed periodicity and prescribed displacement conditions. For the uniform microstructure, the path of growing damage is found to be very sensitive to the boundary conditions. Even with periodic geometric features, a distinct non-periodic and dominant damage path evolves with increasing strain, for non-periodic boundary conditions. This effect is significant at higher volume fractions. Periodic damage is only observed with periodic conditions. An important conclusion that can be derived from this example is that unit cells with periodic boundary conditions are inadequate for properly predicting the expected local nature of damage growth. For random microstructures, the debond induced damage is found to be more sensitive to the local morphology e.g. inter-fiber spacing than to the boundary conditions. The damage growth process is observed to take place gradually over a longer range of increasing strain for the random microstructures.

This study reveals the significance of analyzing large regions of the microstructure and proves the effectiveness of the VCFEM analysis for the same. The Voronoi cells also play an important role in developing geometric descriptors for quantitative characterization (e.g. LAF, NND) since they represent regions of immediate influence for each fiber and also delineate neighbors. It provides the essential link between the microstructural features and response, that is important in damage analysis.

Bibliography

- [1] Achenbach, J.D., Zhu, H., 1990. Effect of Interphases on Micro and Macromechanical Behavior of hexagonal-Array Fiber Composites. *J. Appl. Mech.*, 57, 956-963.
- [2] Allen, D.H., Jones, R.H., Boyd, J.G., 1994. Micro-mechanical analysis of continuous fiber metal matrix composite including the effects of matrix visco-plasticity and evolving damage. *J. Mech. Phys. Solids*, 42 502-529.
- [3] Barenblatt, G.I., 1962. The mathematical theory of equilibrium of cracks in brittle fracture. *Adv. Appl. Mech.*, 7, 55-129.
- [4] Benveniste, Y., 1984. On the effect of debonding on the overall behavior of composite materials. *Mech. Mater.*, 3, 349-358.
- [5] Camacho, G.T., Ortiz, M., 1996. Computational modelling of impact damage in brittle materials. *Int. J. Solids Struct.*, 33(20-22), 2899-2938.
- [6] Costanzo, F., Allen, D.H., 1995. A Continuum Thermodynamic Analysis of Cohesive Zone Models. *Int. J. Engrg. Sci.* 33, 2197-2219.
- [7] Costanzo, F., Walton, J.R., 1997. A Study of Dynamic Crack Growth in Elastic Materials Using a Cohesive Zone Model. *Int. J. Engrg. Sci.* 35, 1085-1114.
- [8] Dugdale, D.S., 1960. Yielding of steel sheets containing clits. *J. Mech. Phys. Solids*, 8, 100-104.
- [9] Geubelle, P.H., (1995). Finite deformation effects in homogeneous and interfacial fracture, *Int. J. Solids Struct.*, 32, 1003-1016.
- [10] Ghosh, S., Moorthy S., 1995. Elastic-plastic Analysis of Arbitrary Heterogeneous Materials with the Voronoi Cell Finite Element Method. *Comp. Meth. Appl. Mech. Engrg.*, 121, 373-409.
- [11] Ghosh, S., Mukhopadhyay, S.N., 1991. A two dimensional automatic mesh generator for finite element analysis of randomly dispersed composites. *Comput. and Struct.*, 41, 245-256.
- [12] Gundel, D.B., Majumdar, B.S., Miracle, D.B., 1995. Evaluation of the intrinsic transverse response of fiber reinforced composites using a cross-shaped sample geometry. *Scripta Metall.*, 33, 2057-.

- [13] Hashin, Z., 1990. Thermoelastic properties of fiber composites with imperfect interface. *Mech. Mater.*, 8, 333-348.
- [14] Li, M., Ghosh, S., Richmond, O., Weiland, H., Rouns, T.N., 1999. Three dimensional characterization and modeling of particle reinforced metal matrix composites: Part I, Quantitative description of microstructural morphology, *Mater. Sci. Engng.*, A265, 153-173.
- [15] Lin, G., Geubelle, P.H., Scottos, N.R., in press. Simulation of fiber debonding and frictional sliding in a model composite pushout test. *Int. J. Solids Struct.*, (in press).
- [16] Ling, Y., 2000. Development of the Voronoi cell finite element model for interfacial debonding in elastic composites, M.S. Thesis, The Ohio State University.
- [17] Lissenden, C.J., 1990. Fiber-matrix interfacial constitutive relations for metal-matrix composites. *Composites B*, 30, 267-278.
- [18] Lo, D.C., Allen, D.H., 1994. Modeling of delamination damage evolution on laminated composites subjected to low velocity impact. *Int. J. Damage*, 3, 378-407.
- [19] Majumdar, B.S., Gundel, D.B., Dutton, R., Warrier, S.G., Pagano, N.J., 1998. Evaluation of the tensile interface strength in brittle matrix composite systems. *J. Amer. Cer. Soc.*, 81, No.6, 1600-1610.
- [20] Moorthy, S., Ghosh, S., 1996. A Model for Analysis of Arbitrary Composite and Porous Microstructures with Voronoi Cell Finite Elements. *Int. J. Numer. Meth. Engng.*, 39, 2363-2398.
- [21] Moorthy, S., Ghosh, S., 2000. Adaptivity and convergence in the Voronoi cell finite element model for analyzing heterogeneous materials. *Comp. Meth. Appl. Mech. Engin.*, (in press).
- [22] Needleman, A., 1987. A continuum model for void nucleation by inclusion debonding. *J. Appl. Mech.*, 54, 525-531.
- [23] Needleman, A., 1990. An analysis of decohesion along an imperfect interface. *Int. J. Fracture*, 42, 21-40.
- [24] Needleman, A., 1992. Micromechanical modeling of interfacial decohesion. *Ultramicroscopy*, 40, 203-214.
- [25] Ortiz, M., Pandolfi, A., 1999. Finite-Deformation Irreversible Cohesive element for Three-dimensional Crack-Propagation Analysis. *Int. J. Numer. Meth. in Engng.*, 44, 1267-1282.
- [26] Pagano, N.J., and Tandon, G.P., 1990. Modeling of imperfect bonding in fiber reinforced brittle matrix composites. *Mech. Mater.*, 9, 49-64.
- [27] Rice, J.R., 1968. Mathematical analysis in the mechanics of fracture, in H. Liebowitz (ed.), *Fracture*, Academic Press, New York, 191-311.

- [28] Tandon, R., Kim, R., Warrier, S.G., Majumdar, B.S., 1998. Influence of edge effects in estimating interfacial normal strength in model unidirectional composites. Composites, Part B, 30, 115-134.
- [29] Tvergaard, V., 1995. Fiber debonding and breakage in a whisker reinforced metal. Mater. Sci. Engng., A190, 215-222.
- [30] Tvergaard, V., 1990. Effect of fiber debonding in a whisker-reinforced metal. Mater. Sci. Engng., A125, 203-213.
- [31] Ungsuwarungsri, T., and Knauss, W.G., 1987. The role of damage-softened material behavior in the fracture of composites and adhesives. Int. Jour. Fracture, 35, 221-241.
- [32] Walter, M.E., Ravichandran, G., Ortiz, M., 1997. Computational modeling of damage evolution in unidirectional fiber-reinforced ceramic-matrix composites. Comput. Mech., 20(1-2), 192-198, 1997.
- [33] Zhong, X.A., Knauss, W.G., 1997. Analysis of interfacial failure in particle filled elastomers. J. Eng. Mater. Tech., 119(3), 198-204.

Specimen #	# fibers	Shape	x_c, y_c (mm)	x_e, y_e (mm)	a, b (mm)	$A_f\%$	α_{maj}^o
1	1	Circular	3.41,3.0	6.82,6.0	2.36,2.36	10.69	-
2	1	Elliptic	3.88,2.74	7.21,5.92	3.71,1.52	10.37	0
3	1	Elliptic	3.78,3.02	7.21,5.59	3.71,1.52	10.99	90
4	5	Circular	2.89,2.23	7.65,5.69	0.355,0.355	1.14	-
4	5	Circular	4.31,2.23	7.65,5.69	0.355,0.355	1.14	-
4	5	Circular	4.22,3.47	7.65,5.69	0.355,0.355	1.14	-
4	5	Circular	2.94,3.37	7.65,5.69	0.355,0.355	1.14	-
4	5	Circular	3.68,2.78	7.65,5.69	0.355,0.355	1.14	-

Table 3.1: Statistics of geometrical parameters in the experimental specimens: (a) specimen number, (b) number of fibers, (c) fiber cross-section, (d) fiber centroidal coordinates (x_c, y_c), (e) size of the cross-section shown in figure 3.1b (x_e, y_e), (f) fiber major and minor axes (a, b), (g) cross-sectional area fraction (A_f) and (h) major axis angle with the loading direction (α_{maj}).

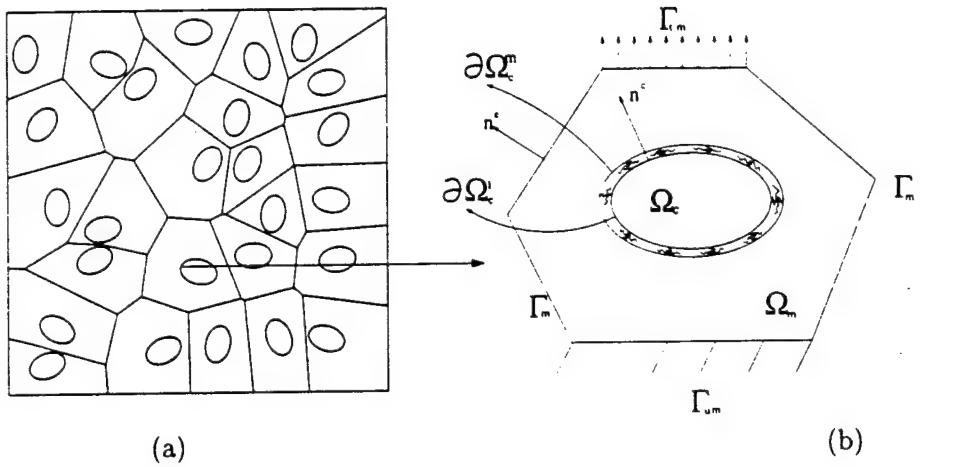


Figure 3.1: (a) A mesh of Voronoi cell elements generated by tessellation of the heterogeneous microstructural domain (b) A typical Voronoi cell element with delineation of the phases and interface region.

Model	Specimen #	δ_{max}	σ_{max}	u_t^c	u_n^c
Geubelle.	1 only	0.9412	0.012846 GPa	0.00007392 mm	0.00006407 mm
Geubelle	1 & 3	0.9347	0.012570 GPa	0.00007217 mm	0.00006395 mm
Model	Specimen #	σ_{max}	δ^*	α	
Needleman(poly)	1 only	0.014613 GPa	0.00004837 mm	0.7104	
Needleman(poly)	1 & 3	0.014428 GPa	0.00004889 mm	0.7116	
Needleman(expo)	1 only	0.014980 GPa	0.00005019 mm	0.6841	
Needleman(expo)	1 & 3	0.014831 GPa	0.00005007 mm	0.6887	

Table 3.2: Cohesive zone parameters for the three models evaluated from the specimen 1 only and specimens 1 and 3 combined.

Specimen #	K_{ud} (MPa)	K_d (MPa)	$\Delta K\%$	Averaged $\epsilon_{in}^a \%$	Gage $\epsilon_{in}^g \%$	θ_d^o
1	4974	4265	14.25	0.140	0.141	91
2	5249	4621	11.96	0.066	0.063	46
3	5163	3581	30.64	0.145	0.111	134
4	4821	4682	2.88	0.139	0.138	87 (all)

Table 3.3: Results of VCFEM simulation with Geubelle's model: (i) the overall undamaged stiffness K_{ud} for the 2-D section, (ii) the damaged overall stiffness K_d , (iii) the change in overall stiffness, (iv) the averaged tensile strain at the onset of debonding ϵ_{in}^a , (v) the corresponding gage strain ϵ_{in}^g and (vi) the final debonded angle θ_d^o .

fiber #	LAF	NND (mm)	$\epsilon = 0.96$		$\epsilon = 1.04$		$\epsilon = 1.12$	
			Di	Pe	Di	Pe	Di	Pe
1	34.26%	0.819	D	D	D	D	D	D
2	25.75%	2.388	B	B	D	D	D	D
3	25.76%	0.916	B	B	B	D	D	D
4	25.12%	1.336	B	B	B	B	D	D
5	21.30%	2.390	B	B	B	B	B	D
6	11.01%	6.453	B	B	B	B	B	B

Table 3.4: The relation between quantitative descriptors of the microstructure and the damage propagation for displacement (Di) and periodic (Pe) boundary conditions. Values of strain should be read as $\epsilon \times 10^{-4}$. D stands for debonded and B is for bonded at a particular strain.

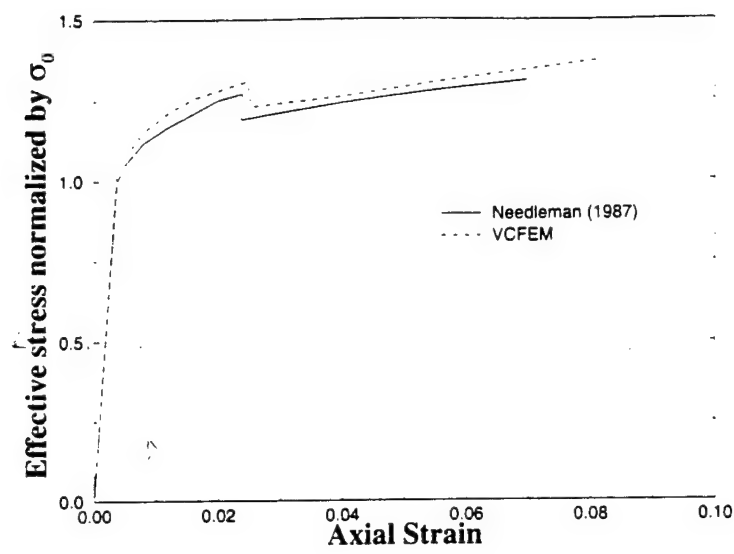


Figure 3.2: Plot of the effective stress Σ_e as a function of axial strain ϵ_a for comparison with results in [22].

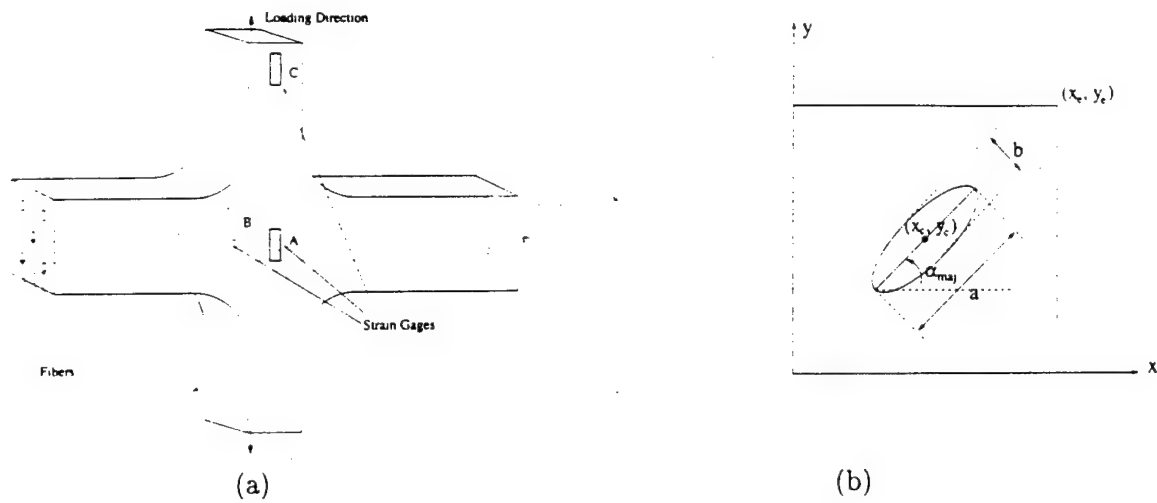
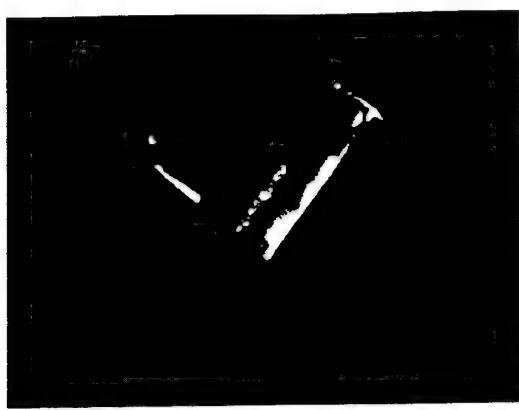


Figure 3.3: (a) A schematic diagram of the cruciform specimen with reinforced fibers and applied loading, (b) a typical cross-section delineating critical geometric parameters.



(a)



(b)

Figure 3.4: (a) Faceview of the debonded cruciform specimen showing dye penetration, (b) the cross section indicating debonding angle as the limits of the dye penetrated region.

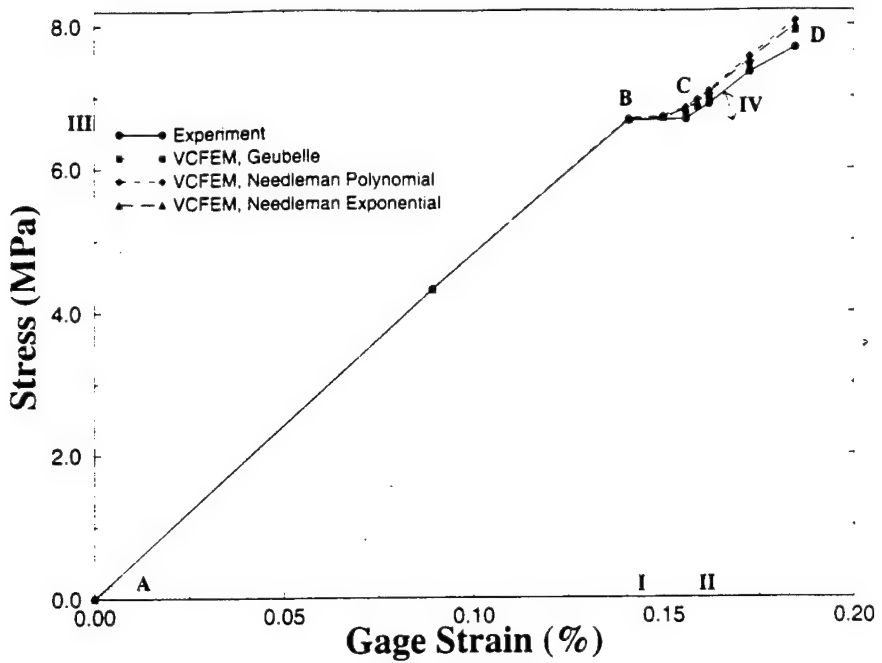


Figure 3.5: Macroscopic pre- and post debonded stress-strain response of the specimen with a single reinforced circular fiber. The roman numerals (I, II, III and IV) correspond to critical property values used to calibrate the cohesive zone model.

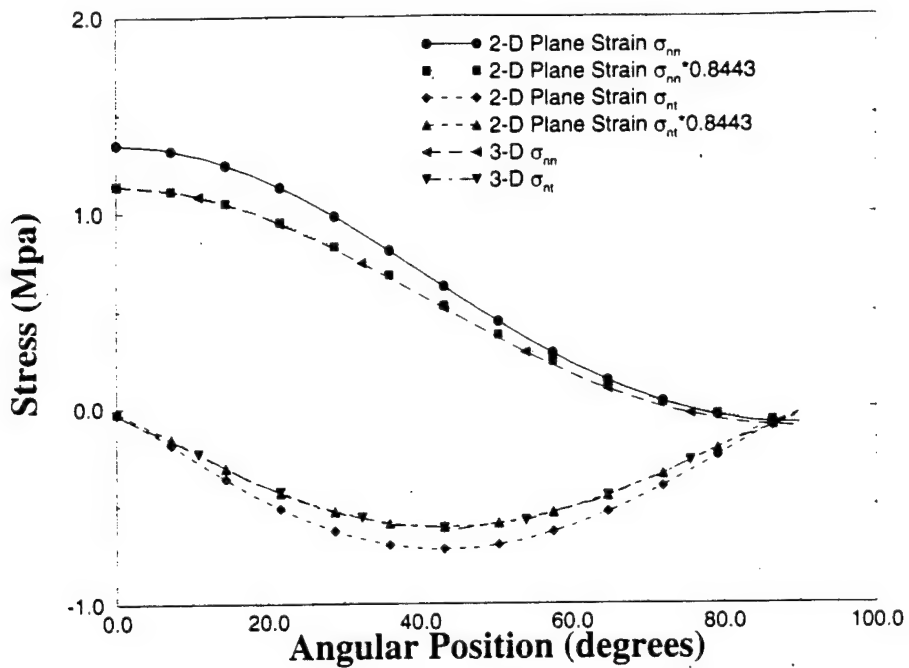


Figure 3.6: A plot of the normal and tangential stresses at a perfect interface by ANSYS, for obtaining the conversion factor between 3-D and 2-D analysis.

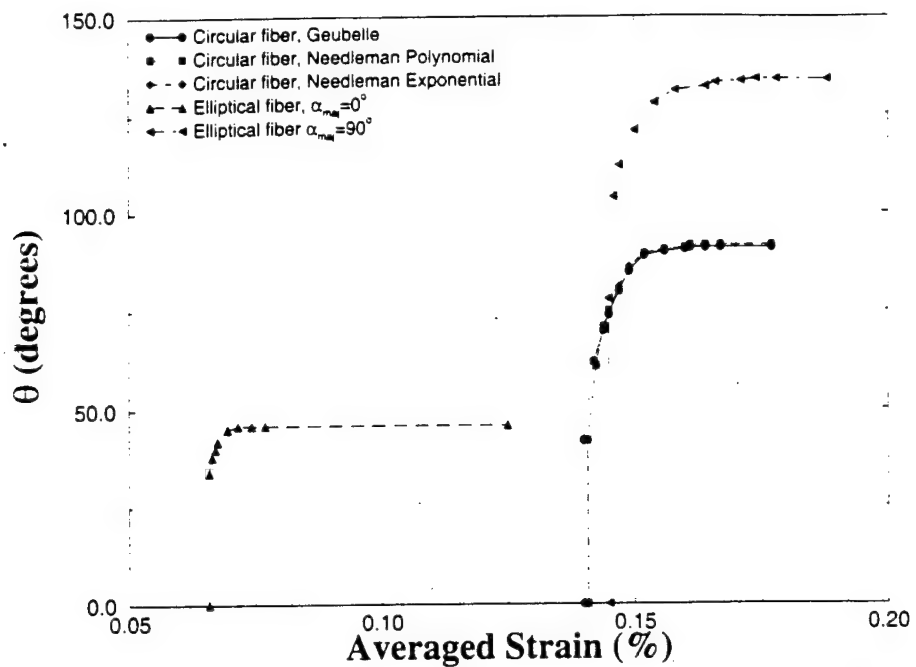


Figure 3.7: Plot of the debonding angle θ_d as a function of average strain with different cohesive zone models

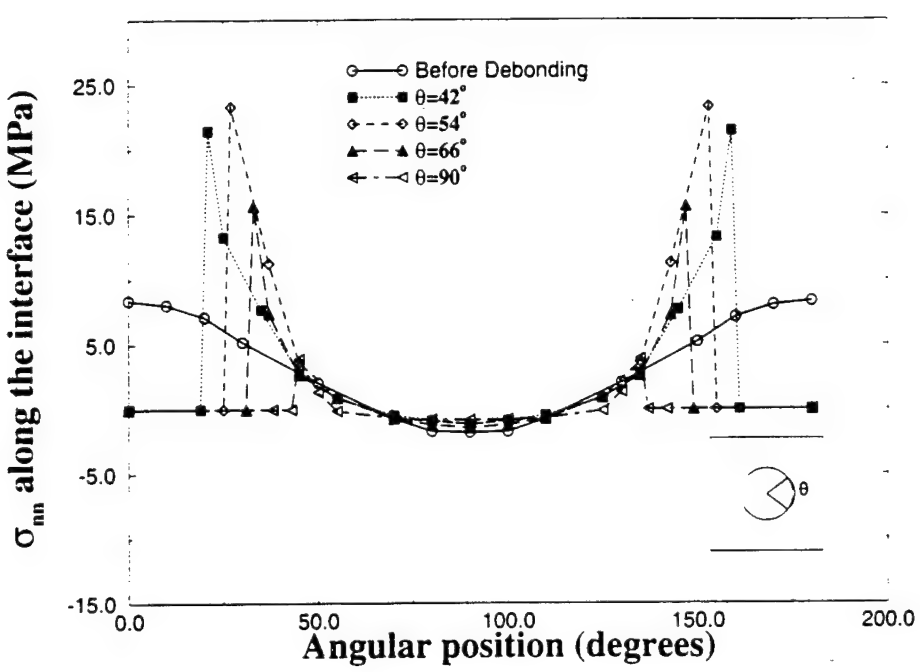


Figure 3.8: Distribution of the normal stress σ_{nn} along the circular interface for increasing values of the debonded angle θ_d .

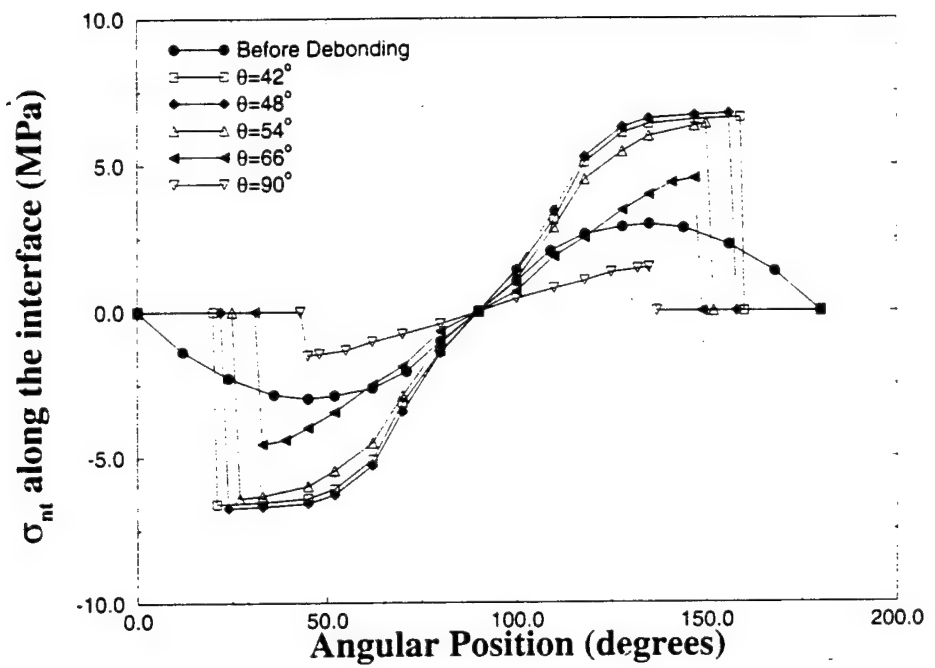


Figure 3.9: Distribution of the tangential stress σ_{nt} along the circular interface for increasing values of the debonded angle θ_d .

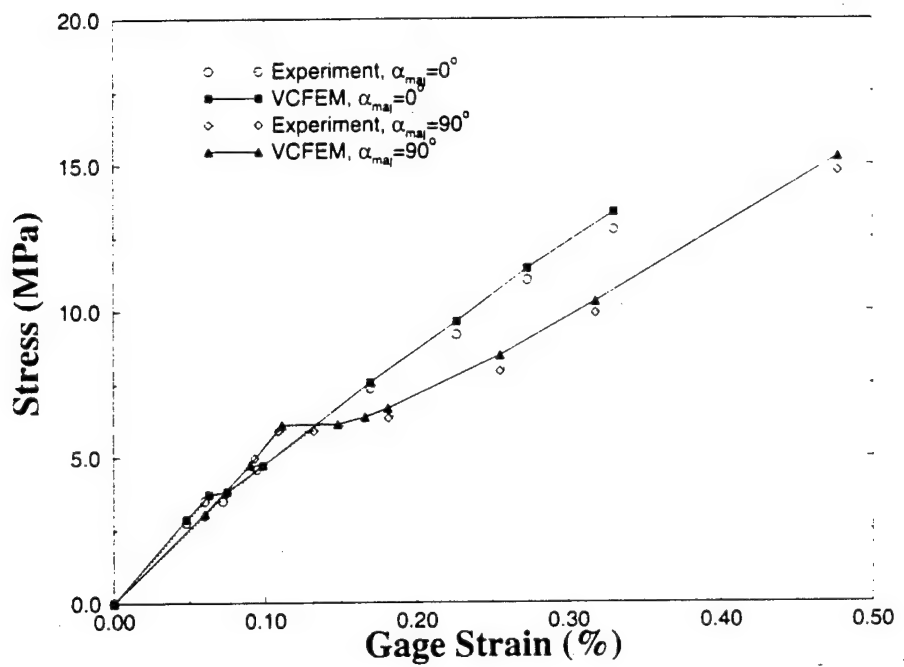


Figure 3.10: Macroscopic pre- and post debonded stress-strain response of the specimen with a single reinforced elliptical fiber, oriented along and perpendicular to the loading axis.

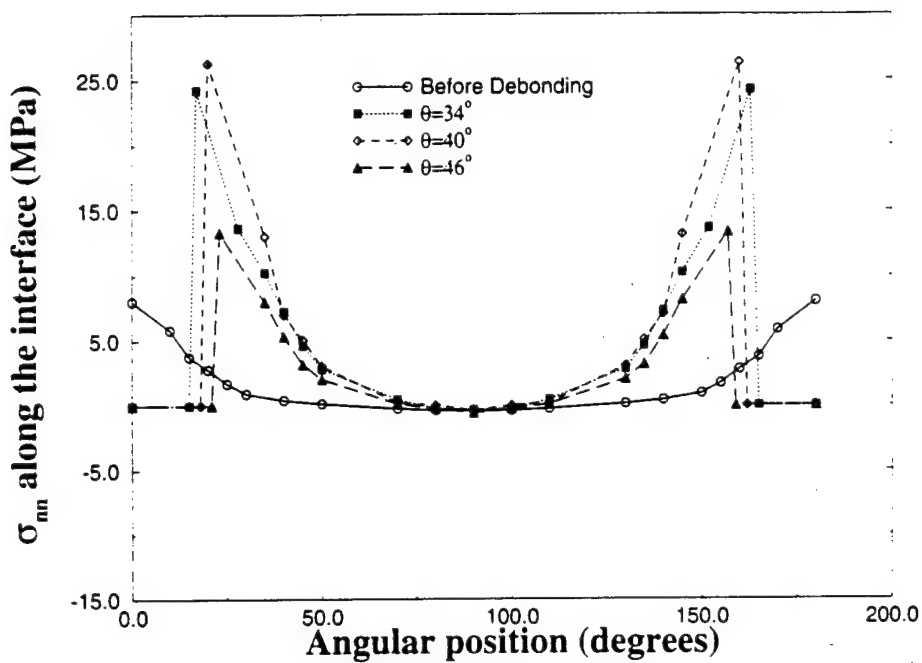


Figure 3.11: Distribution of the normal stress σ_{nn} along the elliptical interface for increasing values of the debonded angle θ_d , ($\alpha_{maj} = 0^\circ$).

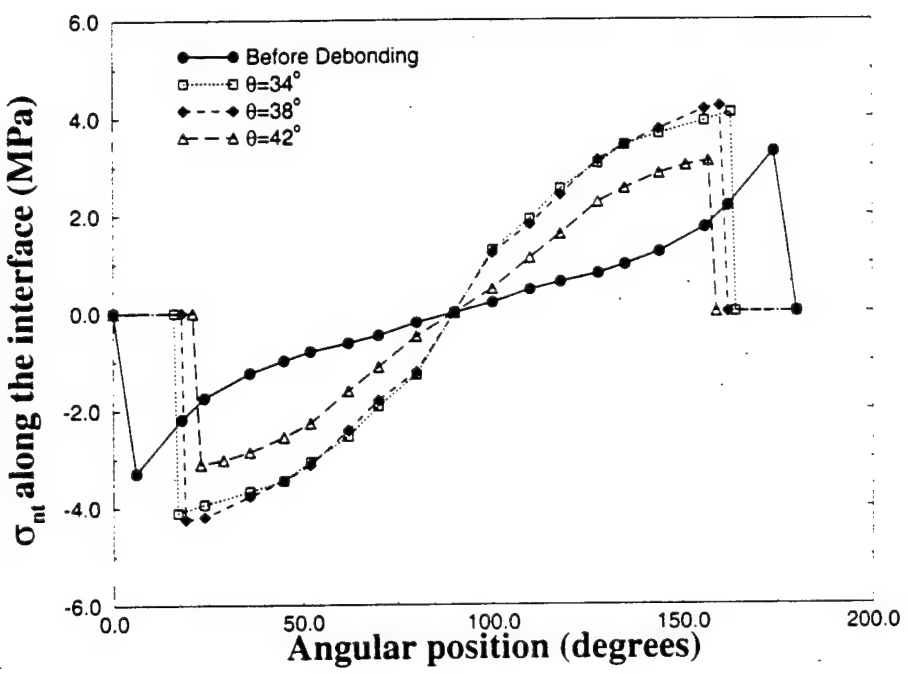


Figure 3.12: Distribution of the tangential stress σ_{nt} along the elliptical interface for increasing values of the debonded angle θ_d , ($\alpha_{maj} = 0^\circ$).

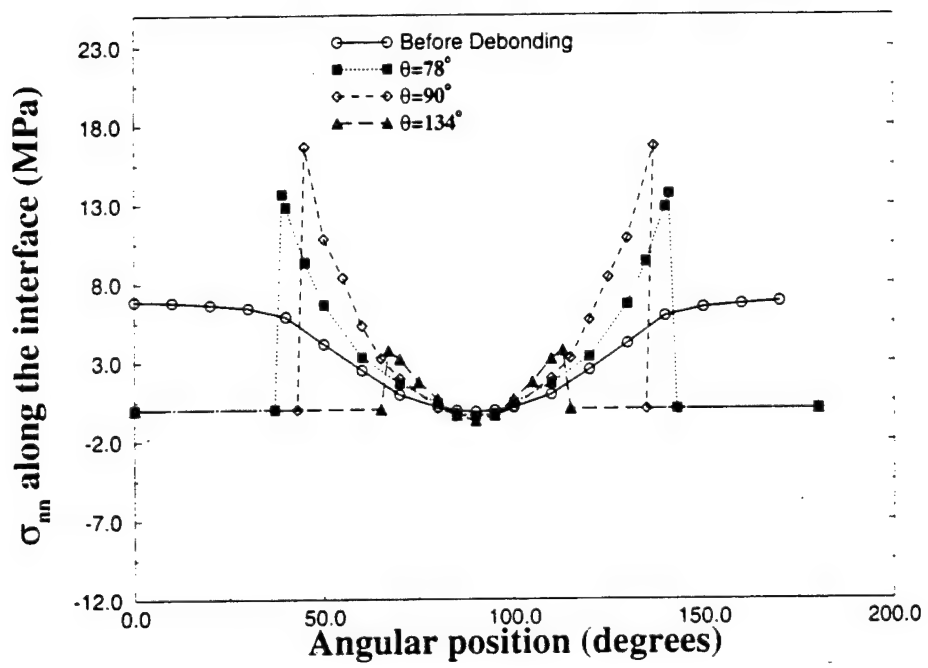


Figure 3.13: Distribution of the normal stress σ_{nn} along the elliptical interface for increasing values of the debonded angle θ_d , ($\alpha_{maj} = 90^\circ$).

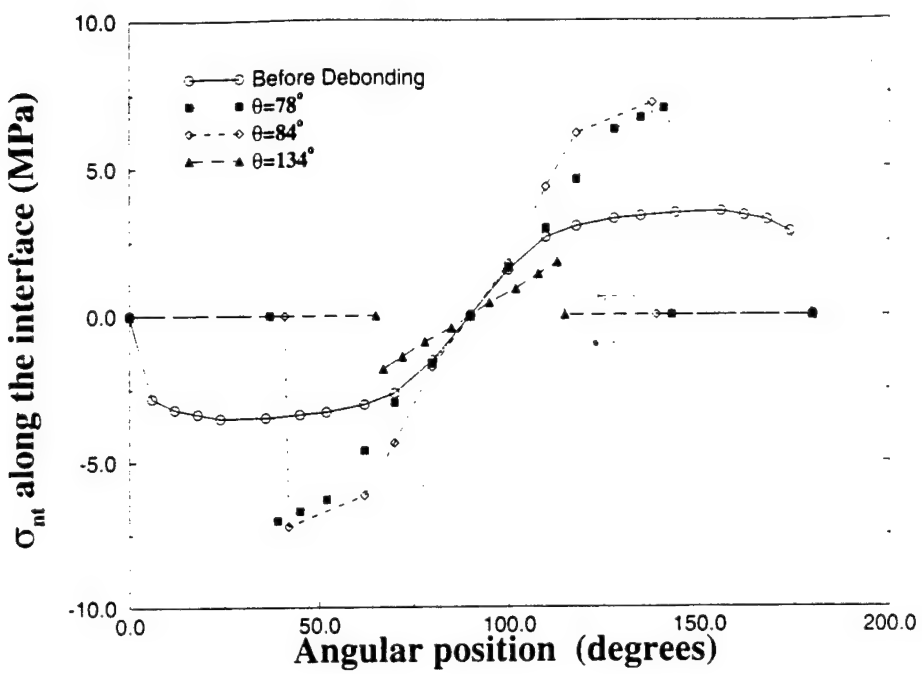


Figure 3.14: Distribution of the tangential stress σ_{nt} along the elliptical interface for increasing values of the debonded angle θ_d , ($\alpha_{maj} = 90^\circ$).

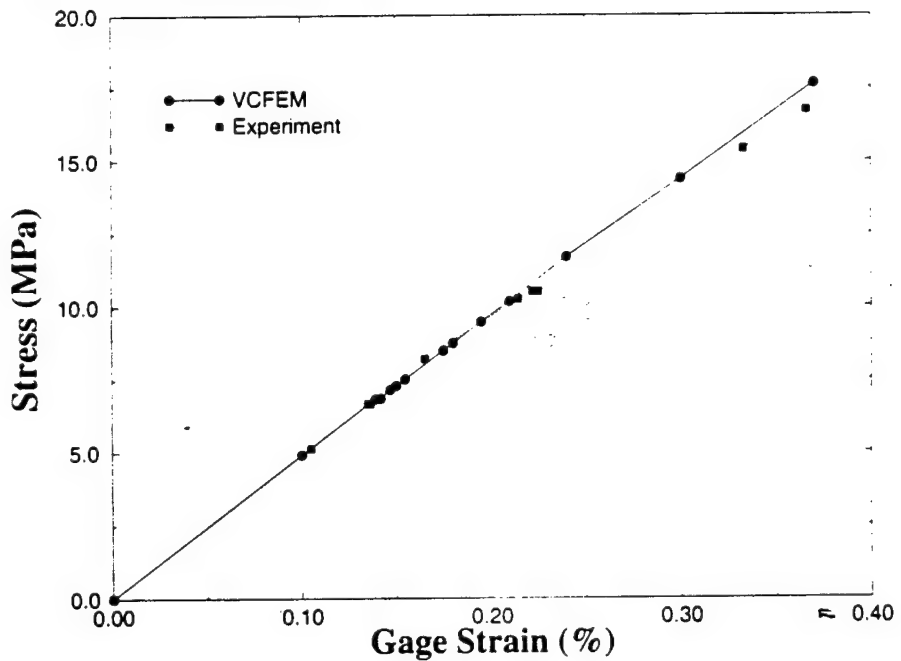


Figure 3.15: Macroscopic pre- and post debonded stress-strain response of the specimen with five circular fibers.

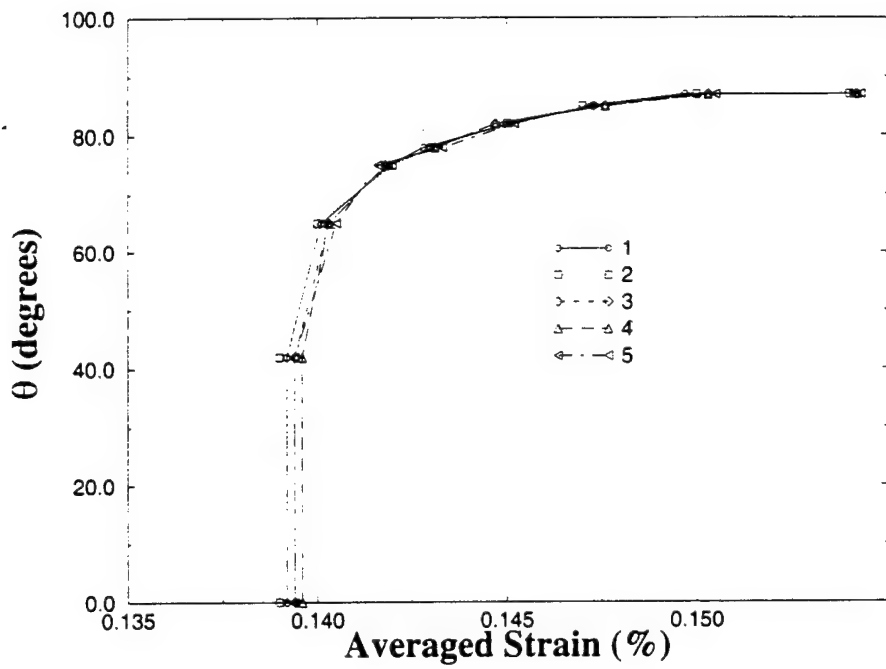
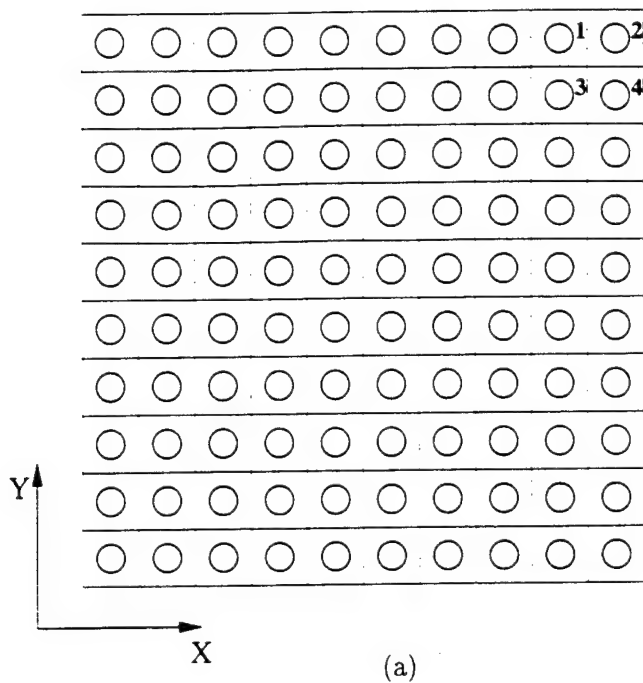
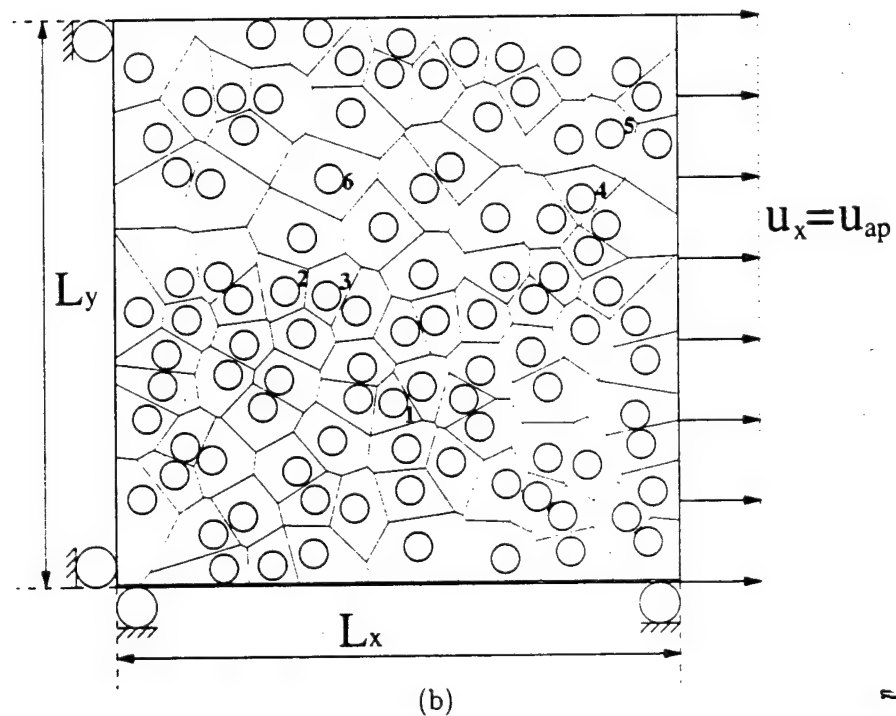


Figure 3.16: Plot of the debonding angle θ as a function of strain, for each fiber in the multi-fiber specimen.



(a)



(b)

Figure 3.17: Tessellated mesh of Voronoi elements for microstructures containing 100 fibers with area fraction=20%, (a) Uniform distribution (b) Random distribution.

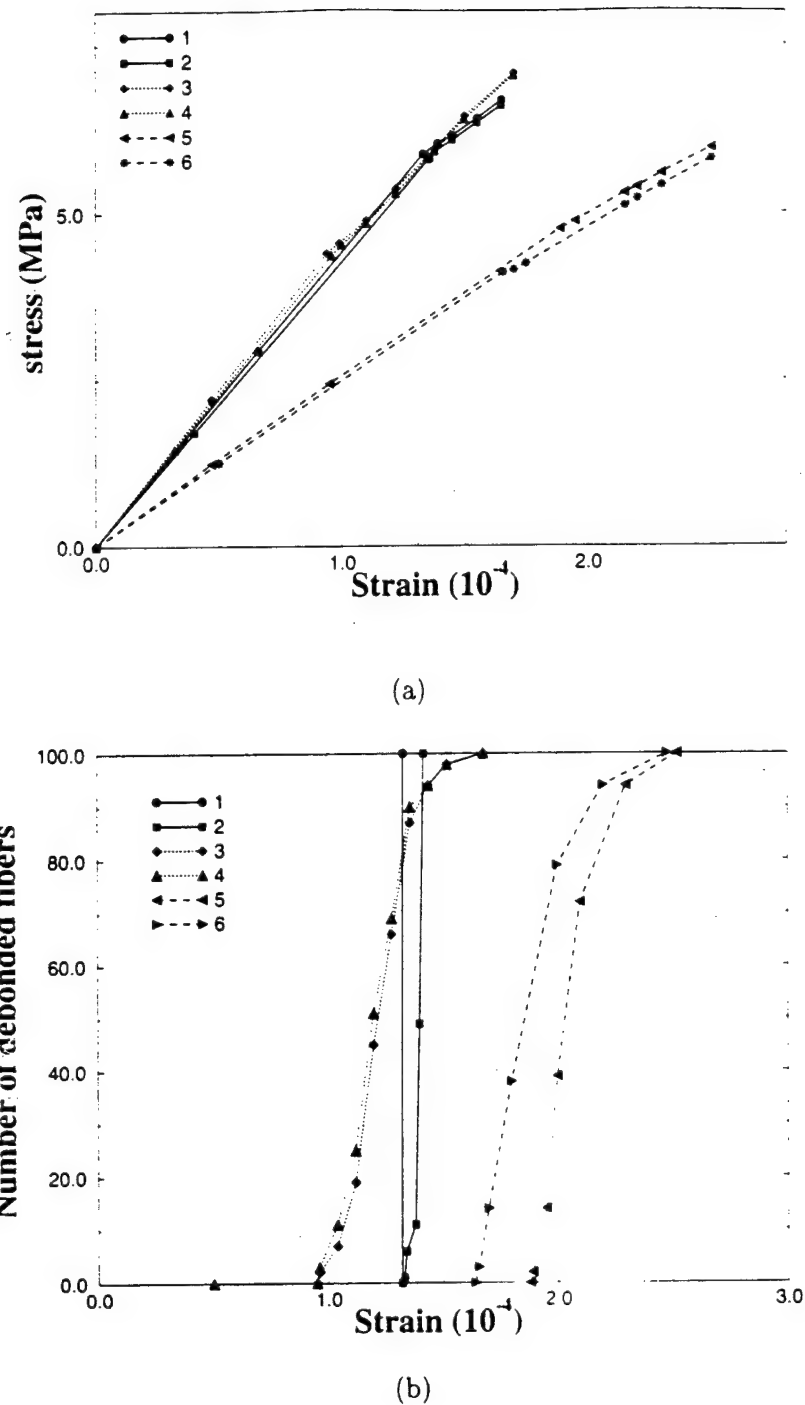
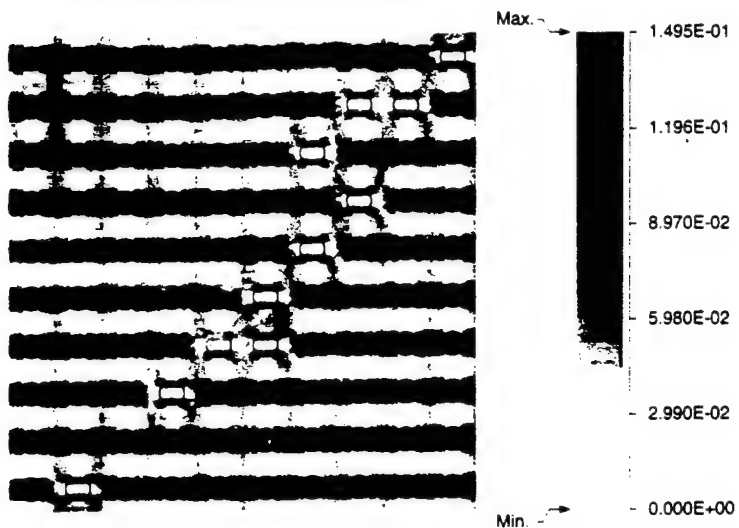
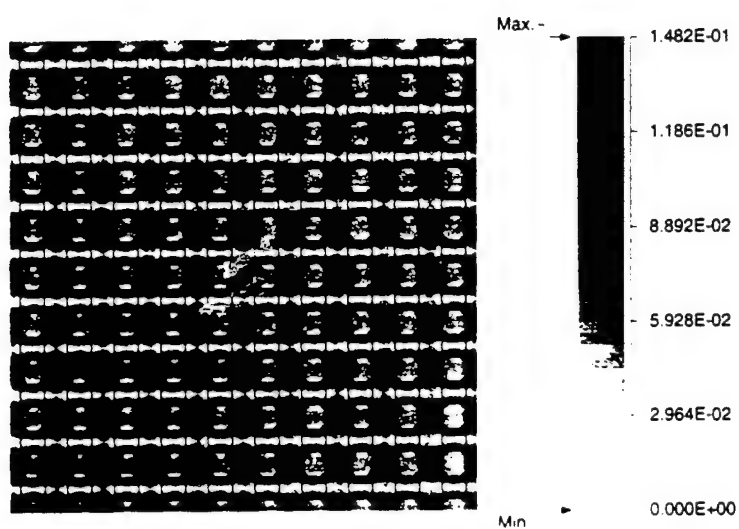


Figure 3.18: (a) Macroscopic pre- and post debonded stress-strain response of the microstructures containing 100 circular fibers and (b) microscopic plot of the number of debonded fibers as a function of strain. The 6 plots in each figure correspond to: (1) $vf=20\%$, uniform dispersion-uniform size-periodic boundary, (2) $vf=20\%$, uniform dispersion-uniform size-displacement boundary, (3) $vf=20\%$, random dispersion-uniform size-displacement boundary, (4) $vf=20\%$, random dispersion-uniform size-periodic boundary, (5) $vf=10\%$, random dispersion-uniform size-displacement boundary and (6) $vf=10\%$, random dispersion-random size-displacement boundary.

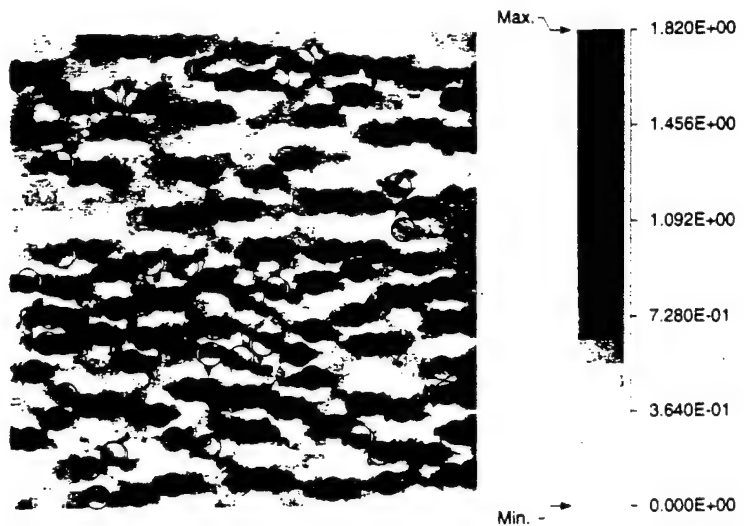


(a)

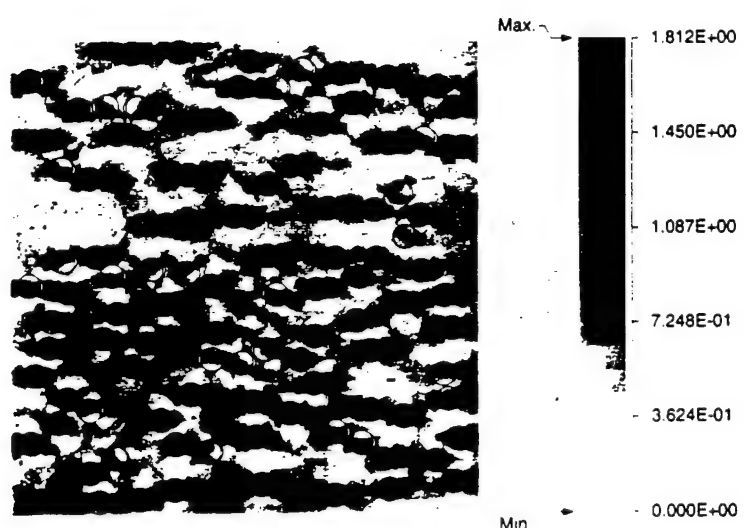


(b)

Figure 3.19: Contour plots of the microscopic axial stress σ_{xx} for the uniformly dispersed microstructure ($vf=20\%$) at $\epsilon = 1.34 \times 10^{-4}$; (a) without periodicity and (b) with periodicity.

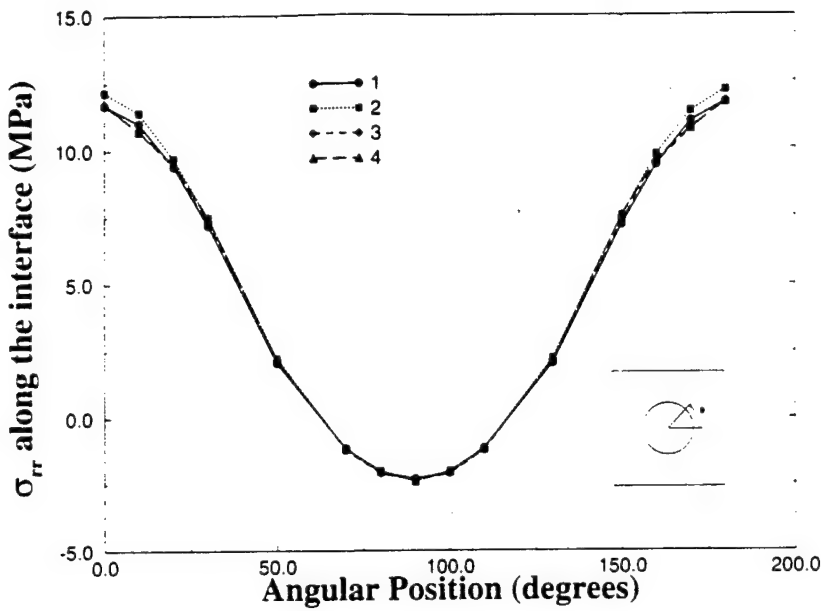


(a)

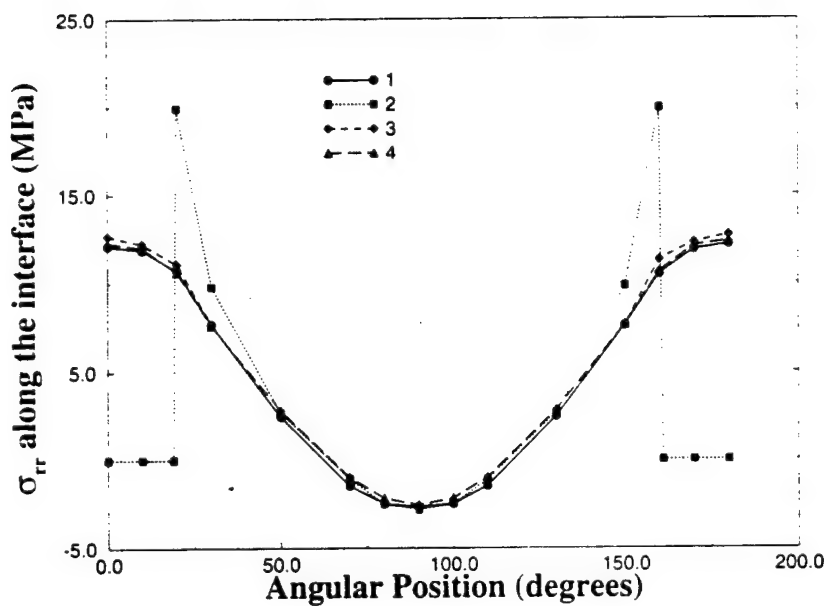


(b)

Figure 3.20: Contour plots of the microscopic axial stress σ_{xx} for the randomly dispersed microstructure ($vf=20\%$) at $\epsilon = 1.12 \times 10^{-4}$; (a) without periodicity and (b) with periodicity.

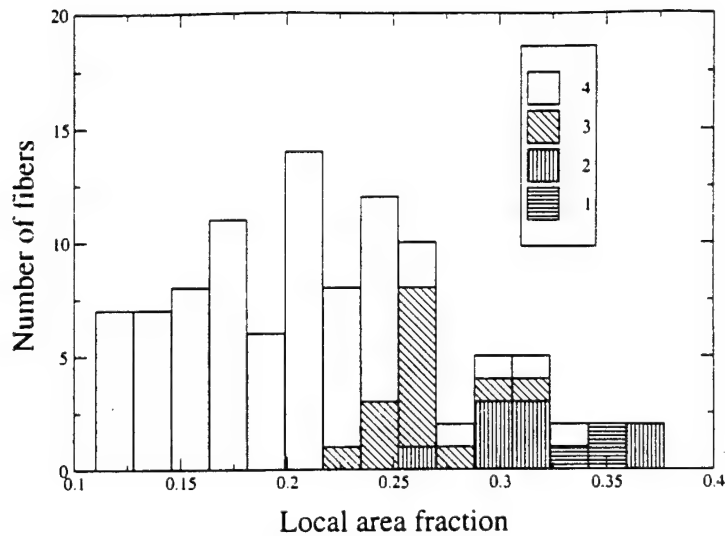


(a)

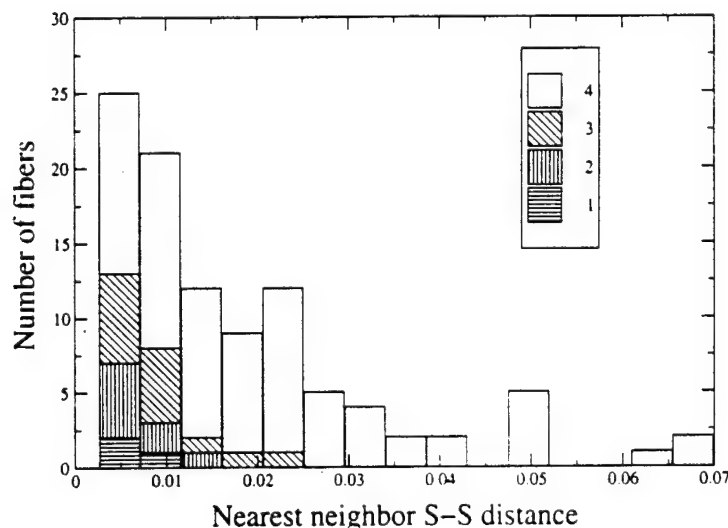


(b)

Figure 3.21: Distribution of the radial stress σ_{rr} along the interface for different fibers (1, 2, 3 and 4 in figure 3.17a) of the uniform microstructure with displacement boundary conditions for (a) $\epsilon = 1.31 \times 10^{-4}$ and (b) $\epsilon = 1.33 \times 10^{-4}$

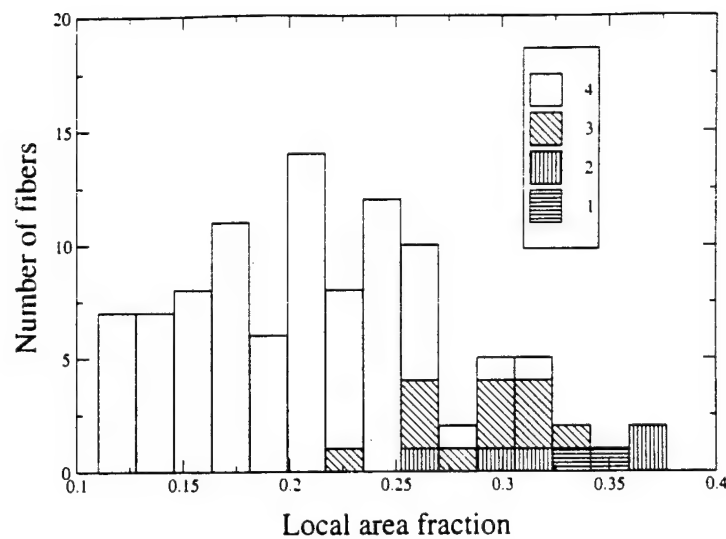


(a)

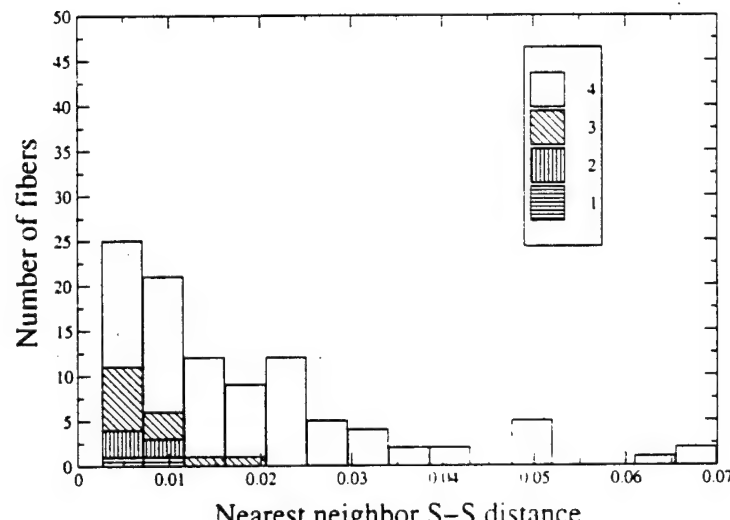


(b)

Figure 3.22: Histograms showing the number of debonded and bonded fibers as functions of (a) local area fraction (LAF) (b) nearest neighbor surface to surface distance (NND), with periodicity boundary conditions. 1, 2, 3 in the legend correspond to increasing strain levels $\epsilon = 0.96 \times 10^{-4}$, $\epsilon = 1.04 \times 10^{-4}$ and $\epsilon = 1.12 \times 10^{-4}$, while 4 in the legend corresponds to undamaged interfaces.



(a)



(b)

Figure 3.23: Histograms showing the number of debonded and bonded fibers as functions of (a) local area fraction (LAF) (b) nearest neighbor surface to surface distance (NND), with **displacement** boundary conditions. 1, 2, 3 in the legend correspond to increasing strain levels $\epsilon = 0.96 \times 10^{-4}$, $\epsilon = 1.04 \times 10^{-4}$ and $\epsilon = 1.12 \times 10^{-4}$, while 4 in the legend corresponds to undamaged interfaces.

Chapter 4

A Multi-level Computational Model for Multi-scale Damage Analysis in Composite and Porous Materials

4.1 Introduction

Heterogeneous structures with second phase inclusions or voids in the microstructure are conventionally analyzed with macroscopic properties obtained from homogenization of response at smaller (meso-, micro-) length scales. The mathematical homogenization theory, which uses asymptotic expansions of displacement, strain and stress fields about macroscopic values, has been used as a tool for analyzing multiple scale responses in Benssousan et. al. (1978), Sanchez-Palencia (1980), Parton and Kudryavtsev (1993), Bakhvalov and Panasenko (1984). The method is based on assumptions of spatial periodicity of microscopic representative volume elements (RVE) and local uniformity of macroscopic fields within each RVE. It decomposes the multiscale boundary value problem into a decoupled set of micro-scale RVE problem and a macro-scale problem. Concurrent finite element analyses are executed at the each scale for information transfer between the scales. Multiple scale analysis of linear elastic reinforced composites by this method have been conducted by Fish and Belsky (1995), Fish and Wagiman (1993), Guedes and Kikuchi (1991) and Hollister and Kikuchi (1992). For nonlinear materials, the homogenization methods have been extended by Suquet (1985), Fish et.al. (1997), Guedes (1990) and Cheng (1992). The method has also been implemented to simulate damage by fiber-matrix debonding in linear elastostatics by Lene (1986) and fiber rupture using a phenomenological damage model by Devries et. al. (1989).

Despite its advantages, asymptotic homogenization has suffered shortcomings arising from efficiency and accuracy considerations. Enormous computational efforts can result with this method due to the fact that at each integration point in the macroscopic model, boundary value problems of the microstructural RVE should be solved twice. To economize computations, many studies have assumed simple unit cells models of the microscopic RVE. Such idealizations may however be unrealistic for deformation and failure analysis of many materials. The homogenization method

has another major limitation stemming from its basic assumptions, viz. (a) uniformity of the macroscopic fields within each RVE and (b) spatial periodicity of the RVE. The uniformity assumption is not appropriate in critical regions of high gradients, where the macroscopic fields can vary considerably. Free edges, interfaces, macrocracks, neighborhood of material discontinuities and most importantly in the regions of evolving microscopic damage and instability are potential sites of nonuniformity. Furthermore, statistical periodicity implies that the RVE may be repeated to represent the entire neighborhood of a macroscopic point. For non-uniform microstructures sufficiently large portions should be considered as RVE for homogenization analysis. Unit cell models are severely limited in this respect. Even higher order theories of homogenization may be computationally unviable. A few effective global-local techniques based on hierarchical decomposition and superposition of field variables have been proposed by Belytschko et. al. (1994), Robbins and Reddy (1996) and Hughes (1995). Pagano and Rybicki (1974) had discussed the breakdown of effective modulus theory for composite laminates with free edges and the need for global-local techniques. Fish and Belsky (1995) and Fish et. al. (1994) have used global-local techniques with multigrid methods to extend the multiple scale modeling to non-periodic materials. Zohdi et. al. (1996), Oden and Zohdi (1997) and Oden et. al. (1999) have developed a homogenized Dirichlet projection method (HDPM), which resolves the microstructural effects at different scales on the macroscopic response of heterogeneous structures.

Adaptivity in the computational modules for multiple scale problems entails minimizing two types of errors, viz. the discretization error and the modeling error due to homogenized material properties as discussed in Oden et. al. (1997,1999). In the present work, an adaptive multi-level method is proposed in to address the latter type of modeling error. It is aimed at improving the accuracy of analyses of elastic-plastic composite and porous structures with microstructural damage. The model uses computational hierarchy to concurrently predict the evolution of variables at structural and microstructural scales, as well as to track the incidence and propagation of microstructural damage. Analysis of microstructural response with arbitrary distributions, shapes and sizes of heterogeneities is conveniently done by the Voronoi Cell finite element model (VCFEM) (see e.g. Moorthy and Ghosh (1996,1998), Ghosh et. al. (1997)). A high level of computational efficiency with sufficient accuracy and resolution has been achieved for elastic and elastic-plastic materials by this method. Progressive damage by particle cracking has been done in Moorthy and Ghosh (1998). Recently, an adaptive VCFEM has been successfully proposed by Moorthy and Ghosh (1999), where element adaptation is executed in two consecutive stages based on a-posteriori evaluation of error measures. In the first stage, displacement function adaptations are carried out by a h -refinement and p -enrichment strategy, which is followed by an enrichment of stress functions to reduce the error in kinematic relations.

For periodic representative volume elements (RVE) of elastic and elastic-plastic materials, the microstructural VCFEM has been coupled with structural analysis codes by using asymptotic homogenization in Ghosh, Lee and Moorthy (1995,1996). This method fails for problems where assumptions of macroscopic uniformity and statistical periodicity are questionable. Consequently, it becomes necessary to implement a combination of homogenization and global-local methods, which

is a nontrivial undertaking due to lack of apriori knowledge of regions that require differential resolution. The multi-level methodology developed in this work addresses this issue by differentiating between non-critical and critical regions and ranging from macroscopic computations using continuum constitutive relations to zooming in at ‘hotspots’ for pure microscopic simulations. The zoom-in is accomplished by a mesh-enrichment technique or h -adaptation, where macroscopic elements are successively dissected in regions of steep solution gradients. Also the adaptations are based on local estimates of ‘error’ or solution gradients. The work introduces three levels of the computational domain, for (a) fully macroscopic analysis with homogenized material parameters, (b) macro-microscopic analysis for periodic RVE’s and (c) fully microscopic analysis. Additionally a new way of developing a piecewise continuous elastic-plastic constitutive model is presented in this work. This model accounts for the details of microstructural morphology and variables. A number of numerical examples are solved with various microscopic architectures to support the development of this multi-level model.

4.2 Two Way Coupling for Multiple Scale Modeling

Multiple scale modeling of heterogeneous materials is necessary to concurrently account for spatial variability at the macro- and micro-scales. An effective model of this class requires two-way coupling for efficient computing, as well as for accurate representation of the necessary variables at different scales. The first is a ‘bottom up’ coupling for determination of equivalent homogeneous behavior at a macroscopic point \mathbf{x} , as a function of the microstructural geometry and behavior of the constitutive phases, but independent of applied loads to the structure. In the homogenization procedure, an isolated representative volume element (RVE) $Y(\mathbf{x}) \subset \mathbb{R}^3$ is identified at microstructural scale of heterogeneities (figure ??b). The scale \mathbf{y} of the RVE domain $Y(\mathbf{x})$ is large with respect to the characteristic length l of microscopic heterogeneities, but is significantly small compared to the macroscopic length scale \mathbf{L} of the structure and applied loads. Homogenized variables at the macroscopic scale are obtained by volume averaging of variables in the RVE, following the definition

$$\langle f \rangle_{Y(\mathbf{x})} = \frac{1}{|Y|} \int_Y f(y) dy \quad \text{where } |Y| = \int_Y dY \quad (4.1)$$

The condition for macroscopic homogeneity, according to the Hill-Mandel hypothesis (see e.g. Hill (1965)), assumes equivalence of strain energy for the actual and equivalent homogenized media. Thus for a statically admissible stress field $\sigma(\mathbf{y})$ and kinematically admissible strain field $\epsilon(\mathbf{y})$,

$$\langle \sigma : \epsilon \rangle_Y = \langle \sigma \rangle_Y : \langle \epsilon \rangle_Y \quad \forall \mathbf{y} \in Y \quad (4.2)$$

The microscopic stress $\sigma(\mathbf{y})$ and strain $\epsilon(\mathbf{y})$ fields satisfying the homogeneity condition (4.2) may be obtained by solving boundary value problems for the RVE Y with prescribed homogeneous stress/strain or periodicity boundary conditions, stated as:

$$\mathbf{T}^b = \langle \sigma \rangle_Y \cdot \mathbf{n}(\mathbf{y}) = \sigma \cdot \mathbf{n}(\mathbf{y}) \quad \text{on } \partial Y : \quad \text{Uniform Traction} \quad (a)$$

$$\mathbf{u}^b = \langle \epsilon \rangle_Y \cdot \mathbf{y} \quad \text{on } \partial Y : \quad \text{Uniform Strain} \quad (b)$$

$$\mathbf{u}^b = \langle \boldsymbol{\epsilon} \rangle_Y \cdot \mathbf{y} + \hat{\mathbf{u}}(\mathbf{y}) = \langle \boldsymbol{\epsilon} \rangle_Y \cdot \mathbf{y} + \hat{\mathbf{u}}(\mathbf{y} + \mathbf{k}\hat{\mathbf{Y}}) \text{ on } \partial Y : \text{ Y-Periodicity } \quad (c) \quad (4.3)$$

where \mathbf{k} is an 3×3 array of integers and $\hat{\mathbf{Y}}$ is the period of Y -periodic displacement functions $\hat{\mathbf{u}}$, interpreted as local perturbations to macroscopic strain based displacement fields. The macroscopic constitutive equations are obtained by solving a boundary value problem of the RVE Y with any one of the three sets of boundary conditions in equation (4.3), followed by the averaging process in equation (4.1). For linear elastic constituent phases in Y , the relation between the strain energy functions has been established in Suquet (1987) as:

$$\langle \boldsymbol{\epsilon} \rangle : \mathbf{E}_{tr}^h : \langle \boldsymbol{\epsilon} \rangle \leq \langle \boldsymbol{\epsilon} \rangle : \mathbf{E}_{per}^h : \langle \boldsymbol{\epsilon} \rangle \leq \langle \boldsymbol{\epsilon} \rangle : \mathbf{E}_{str}^h : \langle \boldsymbol{\epsilon} \rangle \quad \forall \mathbf{E} \subset \mathbb{R}^9 \quad (4.4)$$

where \mathbf{E}_{tr}^h , \mathbf{E}_{per}^h , \mathbf{E}_{str}^h are respectively the homogenized stiffness tensors evaluated with uniform traction, periodicity and uniform strain boundary conditions, and $\langle \boldsymbol{\epsilon} \rangle$ is the macroscopic (applied or averaged) strain field. The difference in stiffnesses with the kinematic and kinetic boundary conditions, reduce with decreasing size of Y . It is generally concluded by Hollister and Kikuchi (1992) that for the same RVE size, the periodicity boundary conditions are expected to yield more accurate statistically homogenized constitutive parameters and macroscopic properties.

The other coupling is the ‘top down’ where the evolution of variables are evaluated in the microstructure from known macroscopic variables, by a process termed as *localization*. In those regions, where the microstructure may admit a RVE Y , the microscopic variables can be evaluated by solving a boundary value problem with imposed macroscopic strains and the local periodicity condition in equation 4.3c. In other regions, where assumptions of local periodicity of the RVE may be unrealistic, the localization process will entail direct interfacing of the microstructural and macroscopic regions.

4.3 A Multi Level Model for Coupling Different Scales

In the spirit of true two way coupling of multiple scale problems, the computational domain in this work is adaptively decomposed into three levels of hierarchy based on requirements of resolution. Such hierarchy is intended to increase computational efficiency as well as accuracy in concurrent prediction of variables at the continuum and microstructural scales. As proposed in Lee et. al. (1999), the model uses homogenization of microstructural RVE solutions to evaluate homogenized properties and cascades down the scales at hotspots of evolving damage. The three levels of hierarchy with requirements of increasing resolution (figure 4.2) are as follows.

i. Computational Subdomain Level-0:

These correspond to non-critical macroscopic regions in figure 4.2a, where deformation variables are relatively uniform and periodicity conditions may be assumed for the underlying material RVE. Scale effects are negligible in this region and local constitutive relations may be derived from postulates of the RVE approaching zero volume. Continuum level anisotropic plasticity constitutive relations, that are consistent with the actual microstructural constitution, are developed for macroscopic modeling of these regions.

The *level-0* macroscopic simulations are accompanied by element refinement or *h-adaptation* for two reasons. The first is to identify and reduce a chosen ‘error measure’ in the macroscopic computational model. A second attribute is that it enables the computational model to ‘zoom in’ on regions of evolving nonuniformity due to microscopic non-homogeneity. This reduces the disparity in size of the macro- and micro- scale elements by successive refinement of macroscopic elements in the critical regions as shown in figure 4.2a.

- ii. **Computational Subdomain Level-1:** These are regions that face imminent microscopic non-homogeneity and resulting macroscopic nonuniformities (figure 4.2a,b). Though the computations are still macroscopic, concurrent monitoring of the development of damage and instabilities in the RVE is possible in this level. For concurrent macro- and micro- scale analyses the asymptotic homogenization methods, which is based on the existence of an RVE, is used. Macroscopic element refinement by h-adaptation continues for this level.

- iii. **Computational Subdomain Level-2:** These critical regions materialize with the evolution of microstructural damage in the form of evolved microcracks or instabilities (figure 4.2b), leading to high macroscopic field gradients. The assumptions of macroscopic uniformity and local periodicity are unrealistic. To realize scale effects, it is required that the level-1 macro-micro computational model switch to a completely microscopic model, encompassing large portions of the microstructure. A detailed flow chart of the adaptive hierarchical process is depicted in figure 4.3.

The substructured computational domain is delineated as an elastic-plastic body of material domain Ω_{MAT} that consists of regions $\Omega_{MAT(p)}$ for which the RVE is repeated periodically, and also of regions $\Omega_{MAT(np)}$ where the periodicity assumptions do not hold, i.e.

$$\Omega_{MAT}(\mathbf{x}, \mathbf{u}) = \Omega_{MAT(p)}(\mathbf{x}, \mathbf{u}) \cup \Omega_{MAT(np)}(\mathbf{x}, \mathbf{u}) \quad (4.5)$$

The macroscopic regions of periodicity are further constituted of repeating a large number of RVE’s Y , i.e.

$$\Omega_{MAT(p)} = \bigcup_{k=1}^{N(p)} \bar{Y}_k^{MAT(p)} \quad \text{where} \quad \bar{Y}_k^{MAT(p)} = \bigcup_{l=1}^{\infty} Y_k^l \quad (4.6)$$

Here $N(p)$ corresponds to the number of different RVE’s Y_k^l in the periodic regions, and for all practical purposes, ∞ corresponds to a sufficiently large number. The non-periodic region $\Omega_{MAT(np)}$ is defined as the set of all microstructural regions for which the $N(np)$ RVE’s are not repeated, i.e.

$$\Omega_{MAT(np)} = \bigcup_{k=1}^{N(np)} Y_k^{MAT(np)} : Y_k \cap Y_l = 0 \quad \forall k \neq l \quad (4.7)$$

The level-0 and level-1 of the computational domain Ω correspond to the periodic regions, while the level-2 belongs to the non-periodic regions as

$$\Omega_{l0} \cup \Omega_{l1} \subset \Omega_{MAT(p)} : \Omega_{l2} \subset \Omega_{MAT(np)} \quad (4.8)$$

4.4 Homogenization with Voronoi Cell FEM

4.4.1 Asymptotic homogenization with microstructural periodicity

Consider a heterogeneous structure occupying a region $\Omega_{structure}$ (figure ??a), for which the heterogeneous microstructure constitutes of spatially repeated RVE's $Y(\mathbf{x})$ about a macroscopic point \mathbf{x} as shown in figure ??b. The RVE is discretized into a mesh of Voronoi cells, which naturally evolve from the microstructure by Dirichlet tessellation. In the Voronoi cell FEM (VCFEM), each Voronoi cell represents a basic structural element (BSE) which is the neighborhood of a heterogeneity in the microstructure. The dimensions of the $Y(\mathbf{x})$ are typically very small in comparison with the structural dimensions L , i.e. $\frac{L}{\epsilon}$ is a very small positive number ϵ . Due to variation of evolutionary variables in a small neighborhood ϵ of the macroscopic point \mathbf{x} , all variables are assumed to exhibit dependence on both length scales i.e. $\Phi^\epsilon = \Phi(\mathbf{x}, \frac{\mathbf{x}}{\epsilon})$, where $\mathbf{y} = \frac{\mathbf{x}}{\epsilon}$. The superscript ϵ denotes association of the function with the two length scales and hence Ω^ϵ corresponds to a connected structural and microstructural domain. The assumption of periodic repetition of the microstructure about \mathbf{x} makes the dependence of the function on $\mathbf{y} (= \frac{\mathbf{x}}{\epsilon})$, Y -periodic (see e.g. Bakhvalov and Panasenko (1984), Guedes and Kikuchi (1991), Hollister and Kikuchi (1992), Devries (1989)). For small deformation elasto-plasticity, the rate forms of the equilibrium, kinematic and constitutive relations are given as:

$$\begin{aligned} \text{Equilibrium : } \dot{\sigma}_{ij,j}^\epsilon &= -\dot{f}_i, & \text{Kinematics : } \dot{e}_{kl}^\epsilon &= \frac{1}{2} \left(\frac{\partial \dot{u}_k^\epsilon}{\partial x_l^\epsilon} + \frac{\partial \dot{u}_l^\epsilon}{\partial x_k^\epsilon} \right) \\ \text{Constitutive : } \dot{\sigma}_{ij}^\epsilon &= E_{ijkl}^\epsilon \dot{e}_{kl}^\epsilon & \text{in } \Omega^\epsilon \end{aligned} \quad (4.9)$$

where $\dot{\sigma}_{ij}^\epsilon(\mathbf{x}, \mathbf{y})$, $\dot{e}_{ij}^\epsilon(\mathbf{x}, \mathbf{y})$ and $\dot{u}_i^\epsilon(\mathbf{x}, \mathbf{y})$ are Y -periodic rates of stress, strain and displacement fields respectively. Furthermore the periodic boundary conditions may be specified as

$$\begin{aligned} \dot{u}_i^\epsilon(\mathbf{x}, \mathbf{y}) &= \dot{u}_i^\epsilon(\mathbf{x}, \mathbf{y} + \mathbf{kY}) \quad \text{on RVE boundary } \partial Y \\ \text{and } \dot{\sigma}_{ij}^\epsilon &\text{ is continuous across } \partial Y \end{aligned} \quad (4.10)$$

The Y -periodic displacement rate field is approximated by an asymptotic expansion about \mathbf{x} with respect to the parameter ϵ :

$$\dot{u}_i^\epsilon(\mathbf{x}) = \dot{u}_i^0(\mathbf{x}, \mathbf{y}) + \epsilon \dot{u}_i^1(\mathbf{x}, \mathbf{y}) + \epsilon^2 \dot{u}_i^2(\mathbf{x}, \mathbf{y}) + \dots, \quad \mathbf{y} = \frac{\mathbf{x}}{\epsilon} \quad (4.11)$$

Noting that the spatial \mathbf{x}^ϵ derivative of any function depends on the two length scales and is given as:

$$\frac{\partial}{\partial x_i^\epsilon} \left(\Phi(\mathbf{x}, \mathbf{y} = \frac{\mathbf{x}}{\epsilon}) \right) = \frac{\partial \Phi}{\partial x_i} + \frac{1}{\epsilon} \frac{\partial \Phi}{\partial y_i} \quad (4.12)$$

the stress rate tensor $\dot{\sigma}_{ij}^\epsilon$ can be expressed as

$$\dot{\sigma}_{ij}^\epsilon = \frac{1}{\epsilon} \dot{\sigma}_{ij}^0 + \dot{\sigma}_{ij}^1 + \epsilon \dot{\sigma}_{ij}^2 + \epsilon^2 \dot{\sigma}_{ij}^3 \dots \quad (4.13)$$

where

$$\dot{\sigma}_{ij}^0 = E_{ijkl}^\epsilon \frac{\partial \dot{u}_k^0}{\partial y_l} , \quad \dot{\sigma}_{ij}^1 = E_{ijkl}^\epsilon \left(\frac{\partial \dot{u}_k^0}{\partial x_l} + \frac{\partial \dot{u}_k^1}{\partial y_l} \right) , \quad \dot{\sigma}_{ij}^2 = E_{ijkl}^\epsilon \left(\frac{\partial \dot{u}_k^1}{\partial x_l} + \frac{\partial \dot{u}_k^2}{\partial y_l} \right) \quad (4.14)$$

From equations 4.9 and 4.13, and using the periodicity condition on the RVE boundary $\int_{d\Gamma_Y} f d\Gamma_Y = 0$, it can be proved (see e.g. Ghosh et. al. (1995,1996)) that

$$\dot{\sigma}_{ij}^0 = 0, \quad \dot{u}_i^0 = \dot{u}_i^0(\mathbf{x}) \quad \text{and} \quad \frac{\partial \dot{\sigma}_{ij}^1}{\partial y_j} = \frac{\partial}{\partial y_j} [E_{ijkl}^\epsilon \{ \frac{\partial \dot{u}_k^0}{\partial y_l} + \frac{\partial \dot{u}_k^1}{\partial y_l} \}] = 0 \quad (4.15)$$

By neglecting the terms associated with ϵ or higher in equation (4.13), the constitutive relation in the Y -domain is expressed as

$$\dot{\sigma}_{ij}^\epsilon = \dot{\sigma}_{ij}^1 = E_{ijkl}^\epsilon \dot{e}_{kl}^\epsilon = E_{ijkl}^\epsilon \left(\frac{\partial \dot{u}_k^0}{\partial x_l} + \frac{\partial \dot{u}_k^1}{\partial y_l} \right) \quad (4.16)$$

Here \dot{e}_{kl}^ϵ is the microstructural strain rate tensor, for which $e_{kl} = \frac{1}{2} (\frac{\partial \dot{u}_k^0}{\partial x_l} + \frac{\partial \dot{u}_k^0}{\partial x_k})$ is an averaged macroscopic part and $e_{kl}^1 = \frac{1}{2} (\frac{\partial \dot{u}_k^1}{\partial y_l} + \frac{\partial \dot{u}_k^1}{\partial y_k})$ is denoted as a fluctuating strain rate tensor (see e.g. Suquet (1985)). Due to linearity of the rate problem, $\dot{\sigma}_{ij}^1$, \dot{u}_i^1 and the microscopic equilibrium condition can be expressed as

$$\dot{\sigma}_{ij}^1 = \hat{\sigma}_{ij}^{kl}(\mathbf{y}) \frac{\partial \dot{u}_k^0}{\partial x_l}, \quad \dot{u}_i^1 = \chi_i^{kl}(\mathbf{y}) \frac{\partial \dot{u}_k^0}{\partial x_l}, \quad \frac{\partial \hat{\sigma}_{ij}^{kl}(\mathbf{y})}{\partial y_j} = 0 \quad (4.17)$$

In equation (4.17), $\hat{\sigma}_{ij}^{kl}$ is a Y -antiperiodic function and χ_i^{kl} is a Y -periodic function representing characteristic modes of the deformation in the RVE. Substituting equation (4.17) in the constitutive relations of equation (4.9) yields the microscopic constitutive relations as:

$$\hat{\sigma}_{ij}^{kl}(\mathbf{y}) = E_{ijpm}^\epsilon [\delta_{kp} \delta_{lm} + \frac{\partial \chi_p^{kl}}{\partial y_m}] \quad (4.18)$$

where δ_{ij} is Kronecker delta. The mean of equation (4.18) yields the homogenized elastic-plastic tangent modulus for use in the macroscopic analysis, in the form

$$E_{ijkl}^H = < \hat{\sigma}_{ij}^{kl} >_Y = \frac{1}{|Y|} \int_Y \hat{\sigma}_{ij}^{kl} dY = \frac{1}{|Y|} \int_Y E_{ijpm}^\epsilon (\delta_{kp} \delta_{lm} + \frac{\partial \chi_p^{kl}}{\partial y_m}) dY \quad (4.19)$$

The macroscopic stress and strain relation can thus be stated as

$$\dot{\Sigma}_{ij}(\mathbf{x}) = < E_{ijkl}^\epsilon (\delta_{km} \delta_{ln} + \frac{\partial \chi_k^{mn}}{\partial y_l}) \frac{\partial \dot{u}_m^0}{\partial x_n} >_Y = E_{ijmn}^H \dot{e}_{mn}(\mathbf{x}) \quad (4.20)$$

where the homogenized variables are $\Sigma(\mathbf{x}) = < \sigma^\epsilon(\mathbf{x}, \mathbf{y}) >_Y$ and $\mathbf{e}(\mathbf{x}) = < \mathbf{e}^\epsilon(\mathbf{x}, \mathbf{y}) >_Y$. The incremental small deformation analysis for elastic-plastic materials can be conducted with the homogenized modulus at the macroscopic level and by using the Voronoi cell finite element model (VCFEM) for solving the microscopic problem.

4.4.2 The Voronoi Cell FEM for Microstructural Analysis

The Voronoi cell finite element model (VCFEM) has been successfully developed for composite and porous materials in Moorthy and Ghosh (1996,1998,1999). Arbitrary dispersion patterns, shapes and sizes of heterogeneities are readily modeled by VCFEM. The computational model naturally evolves by Dirichlet tessellation of the microstructure as shown in figure ??b. Each Voronoi cell with the embedded inclusion or void is treated as an element in this formulation. In Moorthy and Ghosh (1998) and Ghosh and Moorthy (1998), the VCFEM formulation has been extended to include damage evolution in the form of particle cracking, where the crack is realized as an elliptical void. Each Voronoi cell element is amenable to change in topology from two constituent phases (matrix and inclusions) in undamaged cells, to three phases (matrix, inclusion and crack) in damaged cells. Complete particle cracking or splitting is assumed to occur at the very onset of damage.

The VCFS formulation constructs a hybrid element by combining the aspects of finite element methods with important micromechanics considerations. Use of a hybrid stress based formulation results in a high level of accuracy with a significantly reduced degree of freedom, compared to displacement based FEM models. Consider a typical representative volume element Y consisting of N undamaged and/or damaged particles, that are contained in each of the N Voronoi cell elements, as shown in figure ??(b). In VCFEM, the RVE Y is comprised of the Voronoi cell elements Y_e , i.e. $Y = \cup_{e=1}^N Y_e$. The assumed stress hybrid formulation in VCFEM requires independent assumptions of an equilibrated stress field (σ) in each of the matrix and inclusion phases of each element $Y_e = Y_e^m \cup Y_e^c$, and compatible displacement fields \mathbf{u} on the element boundary ∂Y_e , \mathbf{u}' on the matrix-inclusion interface ∂Y_c and \mathbf{u}'' on the crack boundary ∂Y_{cr} . In an incremental formulation for elasto-plasticity, the incremental variational formulation introduces an element energy functional,

$$\begin{aligned} \Pi_e^C(\Delta\sigma, \Delta\mathbf{u}) = & - \int_{Y_e} \Delta B(\sigma, \Delta\sigma) dY - \int_{Y_e} \epsilon : \Delta\sigma dY \\ & + \int_{\partial Y_e} (\sigma + \Delta\sigma) \cdot \mathbf{n}^e \cdot (\mathbf{u} + \Delta\mathbf{u}) d\partial Y \quad (\text{Inter-element Traction Reciprocity}) \\ & - \int_{\Gamma_{im}} (\bar{\mathbf{t}} + \Delta\bar{\mathbf{t}}) \cdot (\mathbf{u} + \Delta\mathbf{u}) d\Gamma \quad (\text{Boundary Traction}) \\ & - \int_{\partial Y_c} (\sigma^m + \Delta\sigma^m - \sigma^c - \Delta\sigma^c) \cdot \mathbf{n}^c \cdot (\mathbf{u}' + \Delta\mathbf{u}') dY \quad (\text{Matrix-Inclusion Interface Traction}) \\ & - \int_{\partial Y_{cr}} (\sigma^c + \Delta\sigma^c) \cdot \mathbf{n}^{cr} \cdot (\mathbf{u}'' + \Delta\mathbf{u}'') dY \quad (\text{Crack Boundary Traction}) \end{aligned} \quad (4.21)$$

where ΔB is the increment of complimentary energy density. Variables (σ, \mathbf{u}) correspond to values at the beginning of an increment, while variables $(\Delta\sigma, \Delta\mathbf{u})$ are the corresponding increments in a load increment or step. Outward normals on ∂Y_e , ∂Y_c and ∂Y_{cr} are denoted by \mathbf{n}^e , \mathbf{n}^c and \mathbf{n}^{cr} respectively. Superscripts m , c and cr are associated with the matrix, inclusion and crack phases respectively in each Voronoi cell element. The total energy for the entire RVE of N Voronoi cells is obtained as $\Pi^C = \sum_{e=1}^N \Pi_e^C$. Setting the first variation of Π_e^C in equation (4.21) with respect to stress increments $\Delta\sigma$ to zero yields the element compatibility as the Euler equation,

while setting the first variations of Π^C with respect to the independent boundary displacements $\Delta\mathbf{u}$, $\Delta\mathbf{u}'$ and $\Delta\mathbf{u}''$ to zero, yield the inter-element boundary traction reciprocity, matrix-inclusion interface traction reciprocity and zero traction crack boundary condition respectively. Independent assumptions on stress increments $\Delta\sigma$ are made in the matrix and inclusion phases in each element, thus allowing stress discontinuities across the interface. In this process special forms of the Airy's stress function $\Phi(x, y)$ to enhance computational efficiency, has been developed in Moorthy and Ghosh (1996, 1998) for equilibrated stress fields. The functions facilitate stress concentration near the interface and crack boundary, accounting for the shape of the inclusion and crack and also help satisfy traction reciprocity at the interfaces ∂Y_e and ∂Y_{cr} . Furthermore, they decay at large distances from the interfaces. Compatible displacement increments are generated on each of the boundaries/interfaces ∂Y_e , ∂Y_c and ∂Y_{cr} by interpolating nodal displacements using polynomial shape functions. The stress and displacement interpolations may be expressed as:

$$\begin{aligned}\{\Delta\sigma^m\} &= [\mathbf{P}^m(x, y)]\{\Delta\beta^m\} \text{ (in matrix) and } \{\Delta\sigma^c\} = [\mathbf{P}^c(x, y)]\{\Delta\beta^c\} \text{ (in inclusion)} \\ \{\Delta\mathbf{u}\} &= [\mathbf{L}^e]\{\Delta\mathbf{q}\} \text{ (on element boundary)}, \quad \{\Delta\mathbf{u}'\} = [\mathbf{L}^c]\{\Delta\mathbf{q}'\} \text{ (on interface), and} \\ \{\Delta\mathbf{u}''\} &= [\mathbf{L}^{cr}]\{\Delta\mathbf{q}''\} \text{ (on crack face)}\end{aligned}\quad (4.22)$$

where $\{\Delta\mathbf{q}\}$, $\{\Delta\mathbf{q}'\}$ and $\{\Delta\mathbf{q}''\}$ are the nodal displacement increment vectors, and $[\mathbf{L}^e]$, $[\mathbf{L}^c]$ and $[\mathbf{L}^{cr}]$ are the corresponding interpolation matrices.

4.4.3 Coupling Asymptotic Homogenization with VCFEM

In the incremental formulation, the equilibrated microscopic stress increment corresponds to $\Delta\sigma^1 (= \Delta\sigma^\epsilon)$ in equation (4.17) and the microstructural strain increments are designated as $\Delta\epsilon^\epsilon$ in equation (4.16). Similarly, the increments in microscopic displacements on the cell boundaries ∂Y_e are identified with $\Delta\mathbf{u}^1$ in equation (4.17) and those on the interface and crack surface are denoted by $\Delta\mathbf{u}^{1'}$ and $\Delta\mathbf{u}^{1''}$ respectively. In the absence of explicit traction boundaries due to periodicity conditions on the boundary, the incremental energy functional for each Voronoi cell element in equation (4.21) is modified for the asymptotic homogenization process as:

$$\begin{aligned}\Pi_e^C &= - \int_{Y_e} \frac{1}{2} S_{ijkl}^\epsilon \Delta\sigma_{ij}^\epsilon \Delta\sigma_{kl}^\epsilon dY - \int_{Y_e} \epsilon^\epsilon : \Delta\sigma^\epsilon dY + \\ \int_{\partial Y_e} (\sigma^\epsilon + \Delta\sigma)^\epsilon \cdot \mathbf{n}^e \cdot (\mathbf{u}^1 + \Delta\mathbf{u}^1) d\partial Y &- \int_{\partial Y_c} (\sigma^{\epsilon m} + \Delta\sigma^{\epsilon m} - \sigma^{\epsilon c} - \Delta\sigma^{\epsilon c}) \cdot \mathbf{n}^c \cdot (\mathbf{u}^{1'} + \Delta\mathbf{u}^{1'}) d\partial Y \\ - \int_{\partial Y_{cr}} (\sigma^{\epsilon c} + \Delta\sigma^{\epsilon c}) \cdot \mathbf{n}^{cr} \cdot (\mathbf{u}^{1''} + \Delta\mathbf{u}^{1''}) d\partial Y &+ \int_{Y_e} (\mathbf{e} + \Delta\mathbf{e}) \Delta\sigma^\epsilon dY\end{aligned}\quad (4.23)$$

where S_{ijkl}^ϵ is an instantaneous elastic-plastic compliance tensor. The last term in equation (4.23) incorporates the effect of macroscopic strains \mathbf{e} in the microstructure. The stationary condition of Π_e^C with respect to stress increment $\Delta\sigma_{ij}^\epsilon$ yields as Euler's equations, the incremental form of kinematic relations

$$e_{ij}^\epsilon + \Delta e_{ij}^\epsilon = e_{ij} + \Delta e_{ij} + \frac{\partial(u_i^1 + \Delta u_i^1)}{\partial y_j} \quad \text{in the element matrix and inclusion phases} \quad (4.24)$$

Stationarity of the total energy functional $\Pi^C = \sum_{e=1}^N \Pi_e^C$ with respect to displacement increments Δu_i^1 , $\Delta u_i^{1'}$ and $\Delta u_i^{1''}$, result in the inter-element, interface and crack boundary traction reciprocity conditions respectively.

$$\begin{aligned} (\sigma_{ij}^\epsilon + \Delta\sigma_{ij}^\epsilon) \cdot n_j^{e+} &= -(\sigma_{ij}^\epsilon + \Delta\sigma_{ij}^\epsilon) \cdot n_j^{e-} && \text{on } \partial Y_e \\ (\sigma_{ij}^{\epsilon c} + \Delta\sigma_{ij}^{\epsilon c}) \cdot n_j^c &= (\sigma_{ij}^{\epsilon m} + \Delta\sigma_{ij}^{\epsilon m}) \cdot n_j^c && \text{on } \partial Y_c \\ (\sigma_{ij}^{\epsilon c} + \Delta\sigma_{ij}^{\epsilon c}) \cdot n_j^{cr} &= 0 && \text{on } \partial Y_{cr} \end{aligned} \quad (4.25)$$

The microscopic VCFEM module is executed for two purposes in each increment of the macroscopic module. The first is to evaluate the microscopic stress increments $\Delta\sigma^\epsilon$ from given values of the macroscopic strain $\bar{\epsilon}$ at the beginning of the step, and its increment $\Delta\bar{\epsilon}$. The second is to calculate the instantaneous homogenized tangent modulus E_{ijkl}^H at the end of the increment in the macroscopic module. The details of the calculation of microscopic stress and homogenized tangent modulus calculation procedure are given in Ghosh et. al. (1995,1996). The Voronoi cell finite element module is incorporated in a macroscopic analysis module with the interface being created by the homogenization procedure. The macroscopic analysis is performed using a displacement based finite element code with plane strain QUAD4 elements. Numerical integration in these elements uses one-point reduced integration and hourglass control (see Koh and Kikuchi (1987)). Material constitutive relations at each integration point of elements are obtained from homogenization of microscopic VCFEM results. Microscopic stresses σ_{ij}^ϵ are averaged to yield macroscopic stresses Σ_{ij} . The microscopic VCFEM is also invoked to evaluate the homogenized elastic-plastic tangent modulus \mathbf{E}^H by applying unit components of macroscopic strain.

4.5 Computational Subdomain Level-0 in the Hierarchical Model

Level-0 corresponds to macroscopic regions ($\Omega_{l0} \subset \Omega_{MAT(p)}$) in figure 4.2a, where deformation variables like stresses and strains are relatively uniform in their macroscopic behavior. Scale effects are negligible and local constitutive relations may be derived from postulates of zero RVE volume in the limit and periodicity. It is assumed that macroscopic analyses with homogenized constitutive relations are sufficient for these regions. Anisotropic constitutive relations with varying parameters are developed for continuum analysis of heterogeneous microstructures with elastic-plastic constituent phases. To account for details of microstructural morphology, the constitutive model is based on two scale analysis using the asymptotic homogenization method and microstructural analysis by VCFEM. A continuum constitutive model can greatly enhance computational efficiency over two-scale analysis.

4.5.1 An Elastic-Plastic Constitutive Model

Various continuum constitutive models have been proposed, based on unit cell analyses of composite and porous microstructures. One parameter plastic potential functions with assumptions of anisotropy have been introduced in Sun and Chen (1991) and Xie and Adams (1995) for composite materials, where the parameter is determined by least squares fitting of unit cell characteristic

responses. Bao et. al. (1991) have used the same hardening exponent for the composite as for the matrix material. A widely used continuum constitutive model for porous materials is that of Gurson (1977), which has been modified by Tvergaard (1982) with unit cell analysis to incorporate the effects of void growth and coalescence. Besides the limitations in representing actual microstructural heterogeneities, a number of these constitutive models do not adequately accommodate variations in constitutive parameters with evolving deformation and do not account for post-yield anisotropy. Terada and Kikuchi (1995) have tried to overcome this by using the asymptotic homogenization to develop an extensive numerical response database in the strain space. Instantaneous overall composite properties are determined from discrete values of homogenized stress-strain values at points of this database. This approach, however leads to huge database to cover all possible deformation paths and requires solving an inordinately large number of RVE boundary value problems. Fish et. al. (1997) have used the idea of transformation strain fields, introduced by Dvorak and Benveniste (1992), to develop a two point averaging scheme based on the mathematical homogenization theory with piecewise constant transformation fields. However, approximating the eigen-strains with low order polynomial functions may not be able to fully account for large gradients in stresses and strains between phases.

Motivated by two considerations, a piecewise continuous elastic-plastic constitutive model with an anisotropic yield function is developed in this work. The first is an accuracy consideration, in that it should account for the microstructural morphology, e.g. spatial distributions, shapes, sizes and properties of the individual phases, phase interactions, as well as the evolving stress and strain fields. This can be achieved if the model is developed from detailed finite element analyses of the RVE (e.g. VCFEM analysis), subjected to a wide variety of loading conditions. The second is an efficiency consideration, since the creation of a prohibitively large numerical database with a very large number of numerical experiments is of no consequence. The efficient development of a constitutive model, accounting for underlying evolution of state variables, is accomplished by generating piecewise continuous model parameters from data in a discretized strain space (see figure 4.4). Numerical data points in the strain space are systematically created through a sequence of computational RVE analyses subject to an ordered set of macroscopic strains and strain paths. The strain space in figure 4.4 is discretized into cubic elements, each containing 32 nodes or data points. From the computational RVE analysis, constitutive parameters like yield function coefficients and plastic work are generated for each nodal point. The constitutive relation at any point in the strain space are then obtained by interpolating nodal values using conventional shape functions. Elastic-plastic models developed in the ensuing sections are for plane strain assumptions.

Linear Elasticity

Orthotropic homogenized elastic material properties are obtained by asymptotic homogenization in conjunction with the VCCE analysis of the composite and porous microstructures from equation (4.19) as explained in Ghosh et. al. (1995). With plane strain assumptions, three separate VCCE analyses are conducted, each corresponding to an independent component of the macroscopic strain $\{e_{xx}, e_{yy}, e_{xy}\}$. The orthotropic elasticity tensor is stored for macroscopic analysis.

4.5.2 Elasto-Plasticity with Anisotropic Yield Function

The inclusion phase in composites are assumed to be linear elastic, while the matrix phase is assumed elastic-plastic for both composite and porous materials. In plane strain modeling, an assumption that the total plastic strain in the out of plane or ‘third’ direction is zero, is made. The yield function can then be described in terms of the macroscopic in-plane stress components (Σ_{xx} , Σ_{yy} and Σ_{xy}). The yield function for porous and composite are written using Hill’s 1948 anisotropic yield function (see e.g. Hill (1965), Xie and Adams (1995)) in conjunction with the hydrostatic stress dependent models of the Tvergaard-Gurson (see e.g. Gurson (1977), Tvergaard (1982)) as:

$$\Phi = \frac{C(\Sigma_{xx} - \Sigma_{yy})^2 + 3\Sigma_{xy}^2}{Y_f^2(W_p)} + H \cosh\left(\frac{\sqrt{3}}{2} \frac{(\Sigma_{xx} + \Sigma_{yy})}{Y_f(W_p)}\right) - 1 = 0 \quad (4.26)$$

where e_{xx}, e_{yy}, e_{xy} are the macroscopic in-plane strains, $C(e_{xx}, e_{yy}, e_{xy}, W_p)$ is a strain dependent yield surface parameter and $Y_f(W_p)$ is the flow stress in shear. For the composite materials the dependence of pressure on yielding is deemed negligible and the hydrostatic stress coefficient H is ignored. Coefficients $C(e_{xx}, e_{yy}, e_{xy}, W_p)$, $Y_f(W_p)$ and H are determined from computational experiments detailed next. The increment of plastic strain is obtained from the yield function Φ by using the associated flow rule for hardening materials, i.e. $\dot{e}_{ij}^p = \lambda \frac{\partial \Phi}{\partial \Sigma_{ij}}$.

Coefficient Evaluation

A. H and $Y_f(W_p)$

Computational exercises indicate that the variation of H with increasing hydrostatic loading is not significant. It is therefore assumed to be a constant for all load histories. This assumption is consistent with the Tvergaard-Gurson models, where H is determined in terms of the initial void volume fraction. The constitutive parameters H and $Y_f(W_p)$ are evaluated in a coupled manner by solving the microstructural RVE boundary value problems with two distinct loading conditions viz. (i) biaxial tension loading ($\Sigma_{xx} = \Sigma_{yy} = \Sigma_{hyd}$, $\Sigma_{xy} = 0$) and (ii) pure shear loading ($\Sigma_{xy} = \Sigma_{sh}$, $\Sigma_{xx} = \Sigma_{yy} = 0$). For load condition (i), equation (4.26) becomes:

$$\Phi(\Sigma_{hyd}, \Sigma_{hyd}, 0, W_p) = H \cosh\left(\sqrt{3} \frac{\Sigma_{hyd}}{Y_f(W_p)}\right) - 1 = 0 \quad (4.27)$$

and for load condition (ii), it becomes:

$$\Phi(0, 0, \Sigma_{sh}, W_p) = \frac{3 \Sigma_{sh}^2}{Y_f^2(W_p)} + H - 1 = 0 \quad \text{or} \quad Y_f(W_p) = \sqrt{\frac{3 \Sigma_{sh}^2}{1 - H}} \quad (4.28)$$

The values of H and $Y_f(W_p)$ are determined iteratively from equation (4.28) and further validated against equation (4.27). The steps are as follows.

1. Solve a macro-micro boundary value problem with RVE homogenization, with incremental pure shear loading. Obtain macroscopic plastic work by averaging the the microstructural

plastic work ($\dot{W}_p = \frac{1}{V_{RVE}} \int_{\Omega} \sigma_{ij} \dot{\epsilon}_{ij}^p d\Omega$) and plot the macroscopic shear stress as a function of plastic work W_p .

2. Assume a starting value for H (e.g. $3*f_0$ as in Gurson (1977), Tvergaard (1982) and evaluate $Y_f(W_p)$ from equation (4.28).
3. Solve a pure macroscopic boundary value problem with incremental biaxial loading, using the homogenized elastic-plastic constitutive relation and associated flow rule with yield function (4.26).
4. Plot the $e_{xx} - \Sigma_{hyd}$ and $e_{yy} - \Sigma_{hyd}$ curves for the entire history of biaxial loading.
5. Solve a macro-micro boundary value problem with RVE homogenization with the same incremental biaxial loading as in the previous step. Plot the $\Sigma_{hyd} - e_{xx}$ and $\Sigma_{hyd} - e_{yy}$ curves for the entire history of loading.
6. Compare the results of steps 4 and 5. If the two curves from both methods are within a preset tolerance everywhere, then the process is terminated and value of H in step 2 is accepted. Otherwise, the entire sequence is repeated with a different value of H .

B. $C(e_{ij}, W_p)$

The coefficient C in equation (4.26) is found to vary considerably with evolution of plastic deformation and examples of its variation with straining and plastic work are shown in figures 4.5. While it is assumed to be a function of the total strain and plastic work, its dependence on load history is assumed to be negligible. In the discretized strain space of figure 4.4, the value of a piecewise continuous C at any point may then be obtained by interpolation from nodal values according to

$$C(e_{xx}, e_{yy}, e_{xy}, W_p) = \sum_{\alpha=1}^{32} C_{\alpha}(W_p) N_{\alpha}(e_{xx}, e_{yy}, e_{xy}) \quad (4.29)$$

where C_{α} are the nodal values and N_{α} are shape functions for a 32-noded brick element.

Generation of Discretized Strain Space and Nodal Parameters

The nodal values of macroscopic stresses ($\Sigma_{xx}, \Sigma_{yy}, \Sigma_{xy}$) and the corresponding plastic work W_p are first evaluated at each nodal point in a subspace of the $e_{xx} - e_{yy} - e_{xy}$ space by solving incremental macro-microscopic boundary value problems with VCFEM and asymptotic homogenization. In this process, macroscopic strain increments are applied to the RVE subjected to periodic boundary conditions (see e.g. Ghosh et. al. (1996,1997)). Strain increments are applied along a radial line in the strain space, such that a constant ratio between strain components is maintained, i.e. $\Delta e_{xx} : \Delta e_{yy} : \Delta e_{xy} = 1 : \tan\theta : (1 + \tan^2\theta)\tan\phi$, where θ and ϕ are the angular coordinates in the strain space of figure 4.4. The flow stress $Y_f(W_p)$ at each node in figure 4.4 can be obtained from the shear stress-plastic work plot and equation (4.28). From the values of macroscopic variables ($\Sigma_{xx}, \Sigma_{yy}, \Sigma_{xy}, Y_f(W_p)$) at a node corresponding to the end of an increment, the coefficient

$C(e_{xx}, e_{yy}, e_{xy}, W_p)$ is calculated using equation (4.26).

From the symmetry conditions, only a quarter of the $e_{xx} - e_{yy} - e_{xy}$ strain space is considered for loading such that $0^\circ \leq \theta \leq 180^\circ$ in the $e_{xx} - e_{yy}$ plane and $0^\circ \leq \phi \leq 90^\circ$ outside of this plane. This is indicated in figure 4.4. This chosen subspace of the strain space is divided into 16 cubic brick element with 32 nodal points each. The location of elements in the strain space are selected to optimally account for the variations in C . These variations in C with the coordinate angle θ (location in the $e_{xx} - e_{yy}$ plane) and the plastic work W_p for the different microstructures are plotted in figure 4.5. The parabolic form of C in figure 4.5a is consistent with the quadratic term $(\Sigma_{xx} - \Sigma_{yy})^2$ in the yield function. The minimum values occur near $\theta = 135^\circ$ corresponding to a pure deviatoric state. The coefficient subsequently increases to account for the increase in plastic work in the yield function Φ . In figure 4.5b, the coefficient C as a function of the plastic work, which corresponds to the radial direction in the strain space, is plotted. The value of C stabilizes beyond a value of the plastic work, which is used as the outer boundary of the strain space envelope in figure 4.4.

4.5.3 Numerical Implementation of the Constitutive Model

The elastic-plastic constitutive model for composite and porous materials is derived from the anisotropic yield function (4.26) with associated flow rule and isotropic hardening. In an incremental form, the stress increments $\Delta\Sigma_{ij}$ are related to elastic increments of strains $(\Delta e_{kl} - \Delta e_{kl}^p)$ admitting additive decomposition, as

$$\Delta\Sigma_{ij} = E_{ijkl}^H (\Delta e_{kl} - \Delta e_{kl}^p) \quad (4.30)$$

where E_{ijkl}^H is the homogenized elasticity tensor. Using associated flow rule, components of the plastic strain increment are obtained as:

$$\Delta e_{ij}^p = \Delta\lambda \frac{\partial\Phi}{\partial\Sigma_{ij}} \quad (4.31)$$

Elimination of the flow parameter $\Delta\lambda$ from the above equations results in the two equations

$$\Delta e_{xx}^p \left(\frac{\partial\Phi}{\partial\Sigma_{yy}} \right) - \Delta e_{yy}^p \left(\frac{\partial\Phi}{\partial\Sigma_{xx}} \right) = 0 \quad , \quad \Delta e_{xx}^p \left(\frac{\partial\Phi}{\partial\Sigma_{xy}} \right) - \Delta e_{xy}^p \left(\frac{\partial\Phi}{\partial\Sigma_{xx}} \right) = 0 \quad (4.32)$$

These equations are solved using the backward Euler integration method, with gradients evaluated at the end of the increment. With known increments of strain, the resulting set of equations (4.32) together with the yield function (4.26) are solved iteratively by using the Newton-Raphson method. The stress increments are obtained by the following steps.

1. Initialize values of $\Delta\Sigma_{xx}$, $\Delta\Sigma_{yy}$ and $\Delta\Sigma_{xy}$.
2. Calculate the gradient $\left(\frac{\partial\Phi}{\partial\Sigma_{ij}}\right)$ of the yield function and solve for the increments of plastic strain Δe_{xx}^p , Δe_{yy}^p and Δe_{xy}^p from equations (4.30) and (4.32). Update the stresses and plastic work using the relation $\Delta W_p = \Sigma_{xx}\Delta e_{xx}^p + \Sigma_{yy}\Delta e_{yy}^p + \Sigma_{xy}\Delta e_{xy}^p$.

3. If $\Phi \leq tol_1$ and correction to plastic strain increment $\delta e_{ij}^p \leq tol_2$, where tol_1 and tol_2 are prescribed tolerances, then stop. Otherwise go to step 2.

The parameter C is then obtained from the interpolation equation (4.29).

4.5.4 Numerical Examples with the Continuum Constitutive Model

The elastic-plastic constitutive model is validated by comparing the results of macroscopic numerical simulations with those generated by macro-micro scale analysis using asymptotic homogenization. Examples are conducted for both composite and porous materials with different microstructure morphologies, viz. different shapes, sizes and spatial distributions of the heterogeneities.

Analysis of Composite Microstructures

Six microstructural RVE's of 20% V_f Alumina-aluminum composite with Alumina fiber in aluminum matrix, as shown in figure 4.6, are analyzed. The RVE's are classified as:

- (a): Square edge pattern with a circular inclusion (C1)
- (b): Square edge pattern with an elliptical inclusion (aspect ratio $\frac{a}{b} = 3$) (C2)
- (c): Random pattern with 25 identical circular inclusions (C3)
- (d): Horizontally aligned random pattern with 25 identical elliptical inclusions (C4)
- (e): Randomly oriented random pattern with 25 identical elliptical inclusions (C5)
- (f): Random pattern with 17 random shape and size inclusions (C6)

The material properties for the elastic Alumina fiber are:

Young's Modulus (E_c)= 344.5GPa, Poisson Ratio (ν_c)= 0.26;

and for the elastic-plastic Aluminum matrix are:

Young's Modulus (E_m)= 68.3 GPa, Poisson Ratio (ν_m)=0.30, Initial Yield Stress (Y_0): 55 MPa, and Post Yield hardening law: $\sigma_{eqv} = Y_0 + 2.08\epsilon_{eqv}^{pl}$.

The RVE's are subjected to four different types of loading viz.

- L1: Pure shear loading with increments($\Delta\Sigma_{xx} = \Delta\Sigma_{yy} = 0, \Delta\Sigma_{xy} = \Delta\Sigma$)
- L2: Uniaxial tension loading with increments ($\Delta\Sigma_{xx} = \Delta\Sigma, \Delta\Sigma_{yy} = \Delta\Sigma_{xy} = 0$)
- L3: Biaxial tension loading with increments ($\Delta\Sigma_{xx} = \Delta\Sigma_{yy} = \Delta\Sigma, \Delta\Sigma_{xy} = 0$)
- L4: Biaxial tension-compression loading with increments ($\Delta\Sigma_{xx} = -\Delta\Sigma_{yy} = \Delta\Sigma, \Delta\Sigma_{xy} = 0$)

The stress-strain response of the six composite microstructural RVE's with the four loading conditions are conducted and the results for simple tension (L1) are depicted in figure 4.7. The results by the constitutive model and two-scale asymptotic homogenization approach are generally found to agree very well for the entire range of loading upto fairly high level of straining. The only discrepancy is found with the biaxial tension loading condition (L3), for which the deviation strains are shown in table 1. However the deviations occurs at high strains levels, for which the stresses are nearly twice the matrix yield stress. It is important to note that the deviation of continuum model response from the two-scale asymptotic homogenization response can be used

as a signal for switching from the former to the latter type of analysis in a multiple scale simulation.

As an example of a structural analysis with the two approaches, a square plate with a square hole is solved with tension loading on two opposite faces. A quarter of the plate with symmetry and loading conditions is shown in figure 4.8a. A total traction of 55 MPa is applied in 10 equal increments. The material is a 20 % V_f Alumina-aluminum composite with the microstructural RVE consisting of 15 identical circular inclusions dispersed randomly in the matrix (figure 4.8b). The material properties are the same as in the previous example. Comparison of the results are made through contour plots of the macroscopic stress Σ_{xx} (shown in figure 4.9) and macroscopic plastic work W_p (not shown). The figures reveal that at all locations the difference in the two approaches is less than 1%. However, the computational efficiency of the macroscopic analysis with the continuum constitutive model is far superior than the two scale analysis. The scale up in efficiency for this problem is approximately 75000%, and is therefore very desirable when only macroscopic results are of interest.

Analysis of Porous Microstructures

The six microstructural RVEs are analyzed again for porous materials, with voids replacing the inclusions in figure 4.6. The material considered is an aluminum alloy with 20% void volume fraction and the following elastic-plastic properties:

Young's Modulus (E_m)= 68.3 GPa, Poisson Ratio (ν_m)= 0.30, Initial Yield Stress (Y_0)= 55 MPa, and Post Yield hardening law: $\sigma_{eqv} = Y_0 + 2.08\epsilon_{eqv}^{pl}$. The same four load histories (L1,L2,L3,L4) are applied. An important difference between the composite and porous microstructures, is that in the latter plastic strain localization in small regions is a common occurrence depending on the void morphology and the nature of loading. Such nonhomogeneous distribution of plastic strains is a major source of discrepancies between responses by the two approaches and act as 'limiters' for the range of application of the continuum model. Microstructures with homogeneous and nonhomogeneous distributions of plastic strain are shown in figure 4.10. For the microstructure V1 (square edge pattern with a circular void) the strain distribution is quite uniform in pure shear loading, while for the microstructure V2 (square edge with an elliptical void) there is intense localization with narrow ligaments. Consequently the continuum model ceases to be effective.

As in the case with composites, the main challenge for the homogenized constitutive model is encountered during simulations with biaxial tension loading, i.e. ($\Delta\Sigma_{xx} = \Delta\Sigma_{yy} = \Delta\Sigma_b$ and $\Delta\Sigma_{xy} = 0$). The first term in the yield function (4.26) drops out for this loading and the model delivers the same amounts of plastic strains in the x and y directions. Due to the lack of anisotropy in the hydrostatic term in the yield function, the continuum model is effective only for those microstructures that exhibit near-isotropic plastic behavior for this loading. Microstructures V2 (square edge with elliptical void) and V4 (horizontally aligned elliptical voids with random spatial distribution) shows very different strain responses for each direction with biaxial loading. Thus the continuum constitutive model is largely ineffective for these RVE's. The microstructures V5 (randomly oriented identical elliptical voids with random spatial distribution) and V6 (random spatial distribution with random shape and size) also show significant plastically induced directional effects

and the constitutive models are therefore restricted to the elastic range. The list of performance and strain ranges of all the microstructures with the different loading are given in table 2. The microstructures V1 and V3 exhibit relatively isotropic responses and yield satisfactory agreement between responses by the constitutive model and the two-scale asymptotic homogenization. Comparisons of stress-strain responses for biaxially and uniaxially loaded RVE's are made in figures 4.11. These show very good agreement. The RVE's V2 and V4 exhibit intense localization early on in the straining, while the RVE's V5 and V6 exhibit marked anisotropy with biaxial loading. Plastic flow predictions for these RVE's with the continuum model are therefore not reliable.

4.5.5 Level-0/1 Mesh Enrichment by h-Adaptation

The transition between various levels in this model is augmented by an adaptive mesh refinement involving element subdivision or *h-refinement* in the level-0 and level-1 regions. This local mesh enrichment is intended to serve two purposes, viz. (a) to identify and reduce discretization error in the computational model and (b) to reduce modeling error by zooming in on regions of evolving localization due to microscopic non-homogeneity. The latter is also effective in bridging the gap between the macro- and micro- scale elements by successive element refinement in critical regions, as shown in figures (4.2a and 4.16). The adaptive h-refinement has been extensively discussed in literature (see e.g. Zhu and Zienkiewicz (1988,1992), Melosh and Marcal (1977), Demkowicz et. al. (1985), Bass and Oden (1987)) and the latest advances in adaptive methods in mechanics have been presented in a compilation by Ladev'eze and Oden (1998). Within the category of h-adaptive procedures, two methods, viz. the mesh enrichment or refinement methods (e.g. Zhu and Zienkiewicz (1988), Bass and Oden (1987)) and mesh regeneration methods (e.g. Zhu, Hinton and Zienkiewicz (1993), Paulino et. al. (1999)) have evolved. While the mesh regeneration methods have been preferred for their relatively higher efficiency, the enrichment method is deemed more suitable for the present work. This is due to the fact that the regeneration method alters element locations with respect to the underlying material RVE and will necessitate cumbersome mapping.

Following procedures outlined in Bass and Oden (1987), the mesh refinement procedure entails subdividing each quadrilateral QUAD4 element into four smaller elements, thus adding four new nodes on the boundary and one in the center. For compatibility with the displacement fields on the boundary of larger adjacent elements, linear constraint relations are imposed on the new boundary nodes of the subdivided element. A static condensation process is then used to eliminate the explicit inclusion of the new nodes in the global stiffness and load vectors (see Bass and Oden (1987) for details). Numerical integration in each QUAD4 element after adaptation is performed by one point reduced integration with hourglass control (Koh and Kikuchi (1987)).

4.6 Computational Subdomain Level-1 in the Hierarchical Model

The level-1 regions ($\Omega_{l1} \subset \Omega_{MAT(p)}$) in the computational domain are intended as 'swing' or 'transition' regions, where microscopic information in the RVE is used to decide whether microscopic computations are necessary for these regions. They are identified by locally high gradients of macro-

scopic variables e.g. stresses, strains strain energy etc. that are indicators of imminent damage evolution or localization in the microstructure. Computations in these regions are still based on assumptions of macroscopic uniformity and periodicity of the RVE. Concurrent with macroscopic simulations, computations are necessary in the the microstructure to monitor the initiation and growth of damage. The RVE response for level-1 elements is explicitly calculated using asymptotic homogenization and VCFEM analysis. The computations in elements belonging to the level-1 domain undergo a sequence of finite element analyses as follows.

(a) Microstructural analysis of the RVE, subjected to the sequence of unit macroscopic strains or increments with periodicity boundary conditions to generate homogenized tangent modulus (E_{ijkl}^H).

(b) Macroscopic analysis of the structure using (E_{ijkl}^H) of step (a), to evaluate macroscopic variables e.g. stresses and strains due to applied loads.

(c) Microstructural analysis of the RVE at each sampling point (e.g. integration point) of macroscopic elements. with actual macroscopic strains and increments obtained from step (b) and periodicity conditions on the RVE boundary. Microscopic stresses and strains ($\sigma^\epsilon, \epsilon^\epsilon$) are thus calculated in the RVE's of each element. For linear elastic constituent phases, the microstructural stress recovery process can be achieved by using a linear combination of solutions with unit strains from step (a). However, explicit solution of nonlinear equations are required for problems with nonlinearity. This is executed in an iterative manner in this work.

Computational requirements of elements in this level are considerably higher than that for level 0. At each integration point in the macroscopic computational mesh, a complete microstructural analysis of the RVE problem is done several times (at least 3 times for step (a) and once for step (c) in the present case) within each iteration loop. Thus the level-1 elements are computationally more expensive compared to level-0 elements. It is therefore important to design robust criteria to avoid redundant element transition from level-0 to level-1. It is also critical that this level be discontinued once the microstructural damage or instability evolved beyond pre-determined threshold values.

4.7 Computational Subdomain Level-2 in the Hierarchical Model

Level-2 regions (figure 4.2b) are classified as those with severe microstructural nonuniformities in the form of evolving damage. This results in loss of statistical periodicity of the assumed RVE and these regions may be identified with $\Omega_{MAT(np)}$ in equation (4.5). In the computational model, the level-2 elements ($\Omega_{l2} \subset \Omega_{MAT(np)}$) materialize from the microstructure of level-1 elements. It is assumed that prior to this transition, the level-1 elements have been refined to reach sufficiently high spatial resolution. In Ω_{l2} , the macro-micro model of level-1 switches to a completely microscopic model.

The method of generating the level-2 microstructure in each element is illustrated in figure (4.12). An extended microstructure is first created by repeating RVE's in succession, to cover the entire region of the macroscopic level-1 elements in transition to level-2. In equation (4.7), a local

non-periodic region is created as :

$$Y_k^{MAT(np)} = \cup_{l=1}^{N^\infty} Y_k^l \quad (4.33)$$

where Y_k^l corresponds to the RVE's in a periodic domain, adjusted for microscopic evolution. This is then overlayed by the macroscopic elements to accurately encase the level-2 region with clearly delineated boundaries. Each level-2 element now contains a heterogeneous material distribution (Y_k^e) that is defined as the intersection of the non-periodic material region $Y_k^{MAT(np)}$ and the element domain Ω_{l2}^e

$$Y_k^e = Y_k^{MAT(np)} \cap \Omega_{l2}^e \quad (4.34)$$

This region is subsequently tessellated into a mesh of Voronoi cell elements (figure 4.12b). Traction continuity between level-2 microstructural region and neighboring level-0/level-1 elements is incorporated through a layer of transition elements.

4.7.1 Damage Criterion for Particle Cracking in Level-2

The level-2 VCFEM modeling consist of brittle reinforcing particles and a ductile matrix material. For the brittle particulate materials, microstructural damage initiation is assumed to be governed by a maximum principal stress based criterion. In this criterion, a crack is initiated when the maximum principal stress in tension exceeds a critical fracture stress σ^{cr} at a point. In the computational procedure, complete particle splitting is assumed to occur in the form of an elliptical void, normal to the principal direction, as soon as the principal tensile stress reaches σ^{cr} . In the case of particle splitting, the crack tip extends nominally into the matrix. In the incremental computational procedure, more than one point may exceed the critical σ^{cr} value during increment. The location of a single crack is determined by a weighted averaging method as:

$$x_{damage} = \frac{\sum x \frac{\sigma_i^c(x,y)}{\sigma^{cr}}}{\sum \frac{\sigma_i^c(x,y)}{\sigma^{cr}}} \quad , \quad y_{damage} = \frac{\sum y \frac{\sigma_i^c(x,y)}{\sigma^{cr}}}{\sum \frac{\sigma_i^c(x,y)}{\sigma^{cr}}} \quad \forall \quad [\sigma_i^c(x,y) \geq \sigma^{cr}] \quad (4.35)$$

where $\sigma_i^c(x,y)$ corresponds to all values of maximum tensile principal stress larger than σ^{cr} in the particle. The crack is oriented at right angles to the principal stress directions at (x_{damage}, y_{damage}) and extends to the interface on both sides.

4.8 Coupling the Levels in the Hierarchical FE Model

While level-0 elements ($E_{l0} \in \Omega_{l0}$) and level-1 elements ($E_{l1} \in \Omega_{l1}$) are coupled naturally through the familiar assembly process, the interfacing of level-2 ($E_{l2} \in \Omega_{l2}$) elements with either of the first two requires more attention. The mismatch in the number of boundary nodes in these elements necessitate the introduction of transition elements ($E_{tr} \in \Omega_{l2}$), acting as buffer zones as shown in figure 4.13. Both E_{l2} and E_{tr} elements employ VCFEM for setting up the element Stiffness matrices and load vectors. The entire computational domain is thus comprised of

$$\Omega^e = \{\Omega_{l0} \cup \Omega_{l1} \cup \Omega_{l2} : \Omega_{l0} = \cup_{k=1}^{N_{l0}} E_{l0}; \Omega_{l1} = \cup_{k=1}^{N_{l1}} E_{l1}; \Omega_{l2} = \cup_{k=1}^{N_{l2}} E_{l2} \cup \cup_{k=1}^{N_{tr}} E_{tr}\}$$

for which the nodes are differentiated as (see figure 4.13):

- (i) ($\text{nd}^{l2/1}$) or internal level-2 Voronoi cell element nodes that are not on any interface or boundary,
- (ii) ($\text{nd}^{l2/2}$) or Voronoi cell element nodes on the E_{l2} - E_{l2} interface,
- (iii) ($\text{nd}^{l2/tr}$) or Voronoi cell element nodes on E_{l2} - E_{tr} interface,
- (iv) ($\text{nd}^{l01/tr}$) or nodes on $E_{l0/1}$ - E_{tr} interface that belong to E_{l0} and E_{l1} elements,
- (v) (nd^{sc}) or Voronoi cell element nodes on $E_{l0/1}$ - E_{tr} interface that do not belong to E_{l0} and E_{l1} and need to be statically condensed. In an incremental analysis for elasto-plasticity, the principle of virtual work for the computational domain at the end of the $n - th$ increment may be written as a scalar valued function G in terms of variables at different levels as:

$$\begin{aligned} G^{n+1}(\Delta \mathbf{u}, \delta \mathbf{u}) &= \int_{\Omega_{l0}^{n+1}} \sum_{ij} (\mathbf{u}^n + \Delta \mathbf{u}) \frac{\partial \delta u_i}{\partial x_j} d\Omega - \int_{\Omega_{l0}^{n+1}} f_i \delta u_i d\Omega \\ &\quad + \int_{\Omega_{l1}^{n+1}} \sum_{ij} (\mathbf{u}^n + \Delta \mathbf{u}) \frac{\partial \delta u_i}{\partial x_j} d\Omega - \int_{\Omega_{l1}^{n+1}} f_i \delta u_i d\Omega \\ &\quad + \int_{\Omega_{l2}^{n+1}} \sigma_{ij} (\mathbf{u}^n + \Delta \mathbf{u}) \frac{\partial \delta u_i}{\partial x_j} d\Omega - \int_{\Omega_{l2}^{n+1}} f_i \delta u_i d\Omega \\ &\quad - \int_{\Gamma_{l0}^{n+1}} t_i \delta u_i d\Gamma - \int_{\Gamma_{l1}^{n+1}} t_i \delta u_i d\Gamma - \int_{\Gamma_{l2}^{n+1}} t_i \delta u_i d\Gamma \end{aligned} \quad (4.36)$$

In an iterative solution process with the Newton-Raphson method, a consistent linearization by taking the directional derivative of G^{n+1} along incremental displacement vector $\Delta \mathbf{u}$, yields the tangent stiffness matrix. For the $i - th$ iteration, the assembled equations have the following structure.

$$\begin{bmatrix} K^{l0/1, l0/1} & K^{l0/1, l2} \\ K^{l2, l0/1} & K^{l2, l2} \end{bmatrix}^i \begin{Bmatrix} \Delta U^{l0/1} \\ \Delta U^{l2B} \end{Bmatrix}^i = \begin{Bmatrix} \Delta F^{l0/1} \\ \Delta F^{l2} \end{Bmatrix}^i \quad (4.37)$$

Here $\Delta U^{l0/1}$ corresponds to displacements at nodes ($\text{nd}^{l0/1}$) that belong to elements E_{l0} and E_{l1} in the computational region $\Omega_{l0} \cup \Omega_{l1}$ as shown in figure 4.13. It should be noted that they also include nodes at the interface of elements E_{l0}/E_{l1} and elements E_{tr} . The displacements ΔU^{l2B} on the other hand corresponds to nodes ($\text{nd}^{l2/tr}$) on the interfaces of elements E_{tr} and elements E_{l2} or to nodes ($\text{nd}^{l2/2}$) on the interfaces between two E_{l2} elements. Contributions to the stiffness matrix $[K]$ and load vector $\{F\}$ for elements in $\Omega_{l0} \cup \Omega_{l1}$ may be obtained as

$$(K_{\alpha j \beta}^{l0/1, l0/1})^i = \int_{\Omega_{l0}^{n+1} \cup \Omega_{l1}^{n+1}} \frac{\partial N_\alpha^G}{\partial x_i} \frac{\partial \Sigma_{ij}}{\partial e_{kl}} \frac{\partial N_\beta^G}{\partial x_l} d\Omega$$

$$(F_{i\alpha}^{l0/1})^i = \int_{\Omega_{l0}^{n+1} \cup \Omega_{l1}^{n+1}} f_i N_\alpha^G d\Omega + \int_{\Gamma_{l0}^{n+1} \cup \Gamma_{l1}^{n+1}} t_i N_\alpha^G d\Gamma - \int_{\Omega_{l0}^{n+1} \cup \Omega_{l1}^{n+1}} \Sigma_{ij} (\mathbf{u}_n + \Delta \mathbf{u}^i) \frac{\partial N_\alpha^G}{\partial x_j} d\Omega$$

α, β correspond to the node numbers and N_α are the shape functions of macroscopic elements. For the elements E_{tr} and E_{l2} belonging to Ω_{l2} , contributions to the stiffness matrix and load vectors are obtained by VCFEM calculations, together with static condensation. The transition

element facilitates continuous variation from microscopic to macroscopic elements without jumps or discontinuities. On the $E_{l0/l1}$ - E_{tr} interfaces, this is accomplished by constraining displacements at nodes \mathbf{nd}^{sc} to conform to displacement interpolation of the adjacent E_{l0} or E_{l1} elements. The constraints at the nodes \mathbf{nd}^{sc} are applied in terms of displacements at $\mathbf{nd}^{l01/tr}$ as

$$\{\Delta U^{sc}\} = [Q] \left\{ \Delta U^{l01/tr} \right\} \quad (4.38)$$

where $[Q]$ is the constraining matrix. For bilinear QUAD4 level-0/1 elements, each row of $[Q]$ consists of the inverse of the distance of the constrained node to the corner nodes. The interfaces with the E_{l2} elements, i.e. the E_{l2} - E_{tr} interfaces are treated in the same way as E_{l2} - E_{l2} interfaces.

The displacements ΔU^{l2B} in equation (4.37) correspond to those at the boundary nodes ($\mathbf{nd}^{l2/2}$, $\mathbf{nd}^{l2/tr}$, $\mathbf{nd}^{l01/tr}$ and \mathbf{nd}^{sc}) of level-2 elements that contain the microstructural VCFE model. To account for the contribution of the internal nodes (\mathbf{nd}^{l2I}), it is therefore necessary to use static condensation and recovery process for representing the VCFEM displacement solutions at the internal nodes ΔU^{l2I} in terms of the displacements at boundary nodes ΔU^{l2B} , where

$$\left\{ \Delta U^{l2B} \right\} = \begin{Bmatrix} \Delta U^{l2/2} \\ \Delta U^{l2/tr} \\ \Delta U^{l01/tr} \\ \Delta U^{sc} \end{Bmatrix} = \begin{bmatrix} I & 0 & 0 & 0 \\ 0 & I & 0 & 0 \\ 0 & 0 & I & 0 \\ 0 & 0 & 0 & Q \end{bmatrix} \left\{ \begin{array}{c} \Delta U^{l2/2} \\ \Delta U^{l2/tr} \\ \Delta U^{l01/tr} \\ \Delta U^{sc} \end{array} \right\} \quad (4.39)$$

where $[I]$ and $[Q]$ are the identity and constraint matrices respectively. In a VCFEM solution process the stiffness matrix and the load vector may be partitioned accordingly as

$$\begin{bmatrix} K^{l2B,l2B} & K^{l2B,l2I} \\ K^{l2I,l2B} & K^{l2I,l2I} \end{bmatrix} \left\{ \begin{array}{c} \Delta U^{l2B} \\ \Delta U^{l2I} \end{array} \right\} = \left\{ \begin{array}{c} \Delta F^{l2B} \\ \Delta F^{l2I} \end{array} \right\} \quad (4.40)$$

Static condensation of the internal degrees of freedom yields

$$\left[\left[K^{l2B,l2B} \right] - \left[K^{l2B,l2I} \right] \left[K^{l2I,l2I} \right]^{-1} \left[K^{l2I,l2B} \right] \right] \left\{ \Delta U^{l2B} \right\} = \left\{ \Delta F^{l2B} \right\} - \left[K^{l2B,l2I} \right] \left[K^{l2I,l2I} \right]^{-1} \left\{ \Delta F^{l2I} \right\} \quad (4.41)$$

These stiffness matrices and load vectors are then used in the assembly process of equation (4.37).

4.9 Adaptation Criteria for Various Levels

It is evident that appropriate criteria need to be established for transitioning the computational subdomains from one level to another. In addition to level transitions, element refinement by *h-adaptation* is also executed in level-0 and level-1 regions for reducing discretization error, identifying regions of high solution gradients and zooming in to reduce the scale gap between macroscopic and microscopic elements. The criteria used for element refinement and level transition are delineated below.

- **Level 0/1 h-adaptation** may be executed based on an error measure may be defined as

$$E_e = \|f(\mathbf{u} - \mathbf{u}_h)\| \quad (4.42)$$

where \mathbf{u} is the true solution, \mathbf{u}_h is its finite element approximation, f is any appropriate function of deformation e.g. energy, stresses, strains etc., and $\|\cdot\|$ denotes a norm of the function. Work on h-method of mesh refinement (see e.g. Zhu and Zienkiewicz (1988), Melosh and Marcal (1977), Demkowicz et. al. (1985)) have proposed various forms of f and norms to optimize the computational effort and improve reliability. In this work, elements are subdivided based on an element level parameter defined as

$$(E_e)_{cr} = q_i \frac{\|f(\mathbf{u}_h)\|}{\sqrt{NE}} \quad (4.43)$$

where $(E_e)_{cr}$ corresponds to a threshold element parameter, above which the element needs to be refined and q_i is a prescribed quality index. $\|f(\mathbf{u}_h)\| = \sum_{e=1}^{NE} \|f(\mathbf{u}_h)\|_e$ is the sum of element norms of any function for the entire computational domain and NE is the number of elements. Such error criteria is conventionally used to equi-distribute errors due to discretization by mesh refinement for relatively well behaved problems. However for mesh dependent problems with inherent localizations or singularities in the solutions, the above criteria may be used for signaling steep gradients in the solution variables and may be used for increasing the resolution in the region of high local gradients. In this work $\|f(\mathbf{u}_h)\|_e$ is taken to be the maximum difference in plastic work with neighboring elements. i.e.:

$$\|f(\mathbf{u}_h)\|_e = \text{Max} \left| \left(\int_{\Omega} \Sigma_{ij} \bar{\epsilon}_{ij}^p d\Omega \right)^e - \left(\int_{\Omega} \Sigma_{ij} \bar{\epsilon}_{ij}^p d\Omega \right)^{\text{adjacent}} \right|$$

with a value of $q_i=1.5$.

- **Level-0 to level-1 transition** of E_{l0} elements takes place in accordance with criteria based on macroscopic variables e.g. (Σ, \mathbf{e}) in the continuum model that are related to critical microscopic variables. Additionally, this transition is activated when the continuum level model in section 4.5.1 starts to digresses considerably from the results of two-scale homogenization. Different criteria are used for composite and porous materials.

A. For composite microstructure with inclusions:

$$(\Sigma_I) \geq \Sigma^{cr} = r * \sigma^{cr} \quad \text{and/or} \quad \frac{(\Sigma_{xx} + \Sigma_{yy})}{2} \geq \Sigma_h^{cr} \quad (4.44)$$

Here Σ_I is the maximum principal stress in E_{l0} , Σ^{cr} is a critical stress that is a pre-determined fraction r of the critical fracture stress (σ^{cr}) for microstructural inclusions. The fraction r is selected to be $\frac{1}{3}$ in this study. The second condition is established since the earliest digression from the homogenization results is observed for biaxial loading, and Σ_h^{cr} established from the results of section 4.5.4.

B. For porous microstructure with voids: Strain based criteria are deemed more important in the case of damage in porous materials and hence transition is activated when

$$(\bar{\epsilon}^p) \geq (\bar{\epsilon}^p)^{cr} = r * (\epsilon^p)^{cr} \quad \text{and/or} \quad \frac{(e_{xx} + e_{yy})}{2} \geq e_H^{cr} \quad (4.45)$$

where \bar{e}^p ($= \sqrt{\frac{1}{2} e_{ij}^p e_{ij}^p}$) is the macroscopic effective plastic strain in E_{l0} and $(\bar{e}^p)^{\sigma}$ is a pre-determined fraction r of a suitably assessed high microstructural plastic strain $(\epsilon^p)^{\sigma}$. Again e_H^{σ} is established from the limiting values of biaxial strain in section 4.5.4.

- **Level-1 to level-2 transition** of E_{l1} elements occur when a sufficiently high spatial resolution is attained by h-refinement and when the RVE is deemed to be on the verge of significant damage evolution. The adaptive criteria, which monitor the transition from elements E_{l1} to E_{l2} are prescribed in terms of topological evolution of microscopic damage as:

A. For composite microstructure with inclusions:

$$R_{damage} = \frac{NDP}{NP} \geq R_{cr} \quad (4.46)$$

B. For porous microstructure with voids:

$$R_{damage} = \frac{ADR}{AR} \geq R_{cr} \quad (4.47)$$

where R_{damage} is the ratio of the number of damaged inclusions (NDP) to the total number of inclusions (NP) for composites. For porous microstructures, it is the ratio of the damaged area corresponding to regions which have high plastic strains to the total RVE area. R_{cr} is a prescribed critical ratio and varies from problem to problem.

4.10 Numerical Examples with the Adaptive Multilevel Model

Numerical examples are solved to understand the effect of structural geometry and microstructural morphologies on the macroscopic and microscopic responses. In all examples, the inclusions are assumed to be linear elastic which can crack by the principal stress criterion and the matrix is elastic-plastic. In the first example, a RVE consisting of a single circular inclusion is modeled by level-1 and level-2 elements under applied uniaxial tension loading. In the first case the E_{l1} macroscopic element is coupled with the microscopically periodic RVE by asymptotic homogenization, while in the second case, the tension load is directly applied on one edge of the Voronoi cell element E_{l2} model of the RVE. The loading is continued beyond the level of inclusion cracking. This is represented by the loss of stress carrying capacity in the averaged stress-strain plot of figure 4.14a. Though the response is similar in the initial elastic phase, it diverges with the onset of plastic flow. The damage occurs earlier in the level-1 element due to the additional constraint of periodicity. The contour plots of inclusion maximum principal stress, normalized by the critical stress σ^{σ} , are compared at a macroscopic strain 2.1% in figure 4.14. This is just before cracking by the level-1 model. A considerably lower stress level is seen for the level-2 model. Such over-estimation of stresses with periodicity boundary condition near free boundaries necessitate the use of the proposed multi-level models.

4.10.1 Effects of inhomogeneity size (Scale effect)

Neglecting scale effects, that reflect the actual size of microstructural constituents, is a characteristic of homogenization with assumptions of statistical periodicity of a vanishingly small RVE.

While elements E_{l0} and E_{l1} conform to this restriction, the level-2 elements E_{l2} in this work depict the actual size of the microstructure through the multi-level coupling and hence scale effects prevail.

In this example the effect of particle or void size on the evolution of damage is investigated. The two different microstructural RVE's considered in figure 4.15b (i and ii) have identical distribution (square edge) and same particle or void area fraction of $V_f = 20\%$. But the RVE sizes are different in that, the size of the smaller RVE (i) is 0.5mm x 0.5mm while that of the larger RVE(ii) is 1mm x 1mm. The macroscopic structure is a square plate with a square hole, for which the initial level-0 mesh with dimensions is shown in figure 4.15a. Only a quarter of the plate is modeled from symmetry considerations. The smallest size of macroscopic element allowed in this analysis by $h - adaptation$ is set to 1mm. Thus the E_{l2} elements contain only one element in the VCFEM model for the larger RVE(ii) but four elements in the VCFEM model for the smaller RVE (i). The material properties for both composite and porous materials are as follows.

Aluminum matrix (Elastic-Plastic): Young's Modulus (E_m)=68.3 GPa, Poisson Ratio (ν_m)=0.30, Initial Yield Stress (Y_0)= 55 MPa, and Post Yield hardening law: $\sigma_{eqv} = Y_0 + 2.08\epsilon_{eqv}^{pl}$

Alumina particle (Elastic): Young's Modulus (E_c)= 344.5GPa, Poisson Ratio (ν_c)= 0.26, Critical particle cracking stress (σ^c)=0.3GPa

The load is applied in 20 equal increments upto a total displacement of 1 mm as shown in figure 4.15a.

For the composite microstructures, figure 4.16 depicts the evolved macroscopic and level-2 computational domains at the end of loading stages. The level-0, level-1, level-2 elements are shown in white, grey and black respectively for the adapted macroscopic mesh in 4.16a and b. The evolution of the levels and mesh with h-adaptation is provided in table 3. The effect of the microstructure size becomes more pronounced with increasing deformation. A larger level-2 domain (29 macroscopic elements) with a smaller level-0 domain is evidenced for the smaller RVE (i). The effect of RVE size on the pattern of particle cracking is very significant. The level-2 region shows 24 cracked particles for the RVE (i) as opposed to 6 cracked particles for the RVE(ii). The path of evolution of cracked particles is quite different for the two models. For the RVE(ii), the aggregate microscopic cracks is found to propagate perpendicular to the macroscopic loading direction and all the microcracks have the same orientation as the chain or macrocrack. For the smaller particles in RVE (i), the chain of microcracks or the macrocrack is observed to move at 45° to the loading direction with individual microcracks predominantly at 90° to the loading direction.

The contour plots of macroscopic and microscopic plastic strain distribution at the final loading stage are shown in figures 4.17 and 4.18 for the two microstructures. The macroscopic strain distribution for both models shows higher strain concentration at the corner of square hole with increased loading. While the macroscopic strains are not very different for the two RVE's, significantly larger local plastic strains are seen in the level-2 microstructure of RVE (i). A better representation of this difference is seen in the graphs of figures 4.19 and 4.20. The macroscopic (averaged) stress Σ_{xx} history at the critical corner in figure 4.19 does not indicate significant difference and hence exhibits little scale effect. The stress drops in this figure correspond to particle damage. The histogram

of the evolution of particle cracking however shows a considerably different pattern and a much higher rate of cracking for RVE (i).

The same problem is solved for porous microstructures with the two sized RVE's, but with a total displacement of 0.4mm. The evolved levels and meshes in the computational models at the end of loading are shown in figures 4.21a and b and the corresponding level-2 microstructures in figures 4.21c and d. The evolution of the computational domain is also charted in table 4. It is interesting to note that the difference in response for the two RVE's is insignificant this case. This may be attributed to lack of matrix damage or softening in the model. The plastically hardening matrix does not trigger adequate difference in the adaptation criteria as the particle cracking does for composites. A larger level-1 domain opens up with the adaptation criteria for elements which appear to be on the verge of strain localization, but subsequently do not make the transition to level-2. The contour plots of macroscopic and microscopic plastic strain distribution in figures 4.22 and 4.23, show similar macroscopic strain distributions, but higher strains for the microscopic model with smaller porosity RVE (i), due to the proximity of voids. This again shows the scale effect on the solution.

4.10.2 Homogenization vs. multi-level simulation

The effect introducing level-2 elements on both macroscopic and microscopic response is studied by comparing a pure level-1 simulation of the square composite plate in the previous example with a multi-level simulation. The results shown are for the larger particles in RVE(ii). The figure ?? shows the microstructure near the inside corner by the two models at the end of loading. The boxed RVE's in figure ??a symbolize their periodic repetition. The periodicity constraint results in a considerably large portion of the microstructure being damaged for the homogenized simulation. The direction of the damage evolution indicated by the homogenized model is also different from the level-2 simulations. The stress Σ_{xx} along the section A-B is plotted in figure 4.25 to evaluate the effect of homogenization on stress concentrations near the corner and free edge. The two models behave similarly upto the neighborhood of the corner. While the multi-level model predicts a higher peak near the corner, it subsides considerably to meet the traction free edge conditions. The corresponding microscopic level-2 stress variations for the multi-level model are shown in the inset.

4.10.3 Effect of heterogeneity distribution and shape

To illustrate the influence of particle distribution on the macro-microscopic damage response, two RVE's are selected with same volume fraction (20%), size (1.0mm) and number of particles (25). One has a hardcore distribution (figure 4.15b (iii)), which is a random distribution with a minimum permissible distance between particles, while the other has one cluster in a hardcore background. Proximity of particles within the cluster is known to initiate damage in discrete microstructures. The starting macroscopic mesh is the same as in the previous examples and a total displacement of 0.55mm is applied on the edge in equal increments. The smallest allowed size of macroscopic

elements by h-adaptation is set to 1mm such that each E_{l2} element consists of one RVE.

The evolved macroscopic models for the two RVE's, at the finish of the loading cycle, are shown in figures 4.26a and b. The level-2 region (black) for the clustered RVE is larger than that for the hardcore RVE. Within the E_{l2} elements, only one element for the hardcore distribution experiences particle damage as shown in figure 4.26d. However, several E_{l2} elements for the clustered microstructure exhibit particle damage, mainly within the cluster (figure 4.26e). While the macroscopic averaged plastic strains show very little difference for the different microstructures in figures 4.27a and 4.28a, the microscopic plots in figures 4.27b and 4.28b clearly depict the influence of distribution. Much higher levels of effective plastic strain values are observed within the cluster, compared to significantly lower levels in the hardcore RVE. Figure 4.30 shows the and evolution of macroscopic stress Σ_{xx} at the corner of the square hole and the number of damaged particles as a function of straining. The stress drops to lower values for the clustered RVE due to a larger damage microstructure. More than twice the number of particles are damaged for the clustered case as shown in the histogram.

To investigate the influence of shape, a RVE (see figure 4.15b (iv)) with the same volume fraction (20%), size (1.0mm) and number (25) is considered. The particles are elliptical with aspect ratio 3.0 and randomly distributed and oriented. The evolved macroscopic model in figures 4.26c shows a larger level-2 region compared with other two microstructures, with several E_{l2} elements exhibiting particle damage. The much larger number of cracked particles is also observed from the histogram of figure 4.30b. For this case, both macroscopic and microscopic plastic strains in figure 4.29 are also considerably larger. The macroscopic stress Σ_{xx} shows a larger drop due to the increased damage in the microstructure.

4.10.4 A heterogeneous plate with a macroscopic holes

A different macroscopic domain, viz. a plate with periodically repeated square diagonal array of circular holes is considered in this final example. The plate is incrementally loaded using prescribed displacement on the top and bottom surfaces to a total extension of 0.15 mm. Due to periodicity and symmetry, only a part of domain is modeled as shown in figure 4.31. The radius of the circular holes are 50mm for the 100 mm x 100 mm square plate as shown in figure 4.31. The microstructural RVE is a 20% volume fraction 0.4 mm x 0.4 mm square region with a single circular particle. The same material properties as in the previous example are used with the only exception being that the critical particle cracking stress $\sigma^c = 0.2 \text{ GPa}$.

The adapted multilevel computational domain is shown in figure 4.32 and the number of elements in each levels with increasing are tabulated in table 5. The level-2 elements are created along a clear path connecting the holes due to localization by particle cracking. Extended portions of the damaged microstructure in level-2 regions are shown in figure 4.32. The macroscopic plastic strain contour in figure 4.33a gives an indication of 'hot spots' of evolving damage near the central region. The microscopic strain plots in figure 4.33b show a large fraction of particles cracked and may be interpreted as the initiation of localization to cause failure between the holes.

4.11 An Example on Convergence of the Multi-level Method

To provide convergence characteristics of the multi-level model, an example problem of an elastic fibrous composite with a free-edge and loaded in the out of plane direction, is considered. This classical problem was proposed by Pagano and Rybicki (1974) to demonstrate the limitations of effective modulus or homogenization theory in predicting stress states in laminated composites, especially near the free-edge. The problem consists of a composite cross-section as shown in figure (4.34a). The upper half of the cross-section consists of n periodic rows of aligned cylindrical fibers, arranged in a square array, while the bottom half is the homogeneous matrix material. The ratio of fiber radius to edge length in the local RVE of figure (4.34b) is $\frac{r}{l} = 0.3$, corresponding to a local volume fraction of 28.2%. The body is subjected to a generalized plane strain loading with out-of-plane loading, prescribed as $\epsilon_{zz} = 1$. Due to symmetry in the xz and yz planes only one quarter of the laminate is modeled (figure 4.34a). Symmetric boundary conditions are employed on the surfaces $x = 0$ and $y = 0$, and the top and right surfaces are assumed to be traction free. The material properties for the boron fiber and epoxy matrix are prescribed as: $E_{boron} = 60 \times 10^6$ psi, $\nu_{boron} = 0.2$, $E_{epoxy} = 0.5 \times 10^6$ psi and $\nu_{epoxy} = 0.34$.

4.11.1 Microscale VCFEM Simulations

To establish convergence of solutions at the micro-scale, the adaptive Voronoi cell finite element model (AVCFEM) developed in Moorthy and Ghosh (1999) is coupled with the multi-level computational model. In AVCFEM, two error measures are introduced to measure the quality of the solution. They are (i) the traction reciprocity error, derived *a-posteriori* from solved traction discontinuity at the element boundary and matrix-inclusion/void interface, and (ii) the error in kinematic relationships that is equated to an error in the strain energy, in each of the element constituent phases. Displacement adaptations that minimize traction discontinuity, are implemented to approach 'optimal' directions for displacement fields on the boundary/interface. These directions optimize the virtual work due to traction discontinuity and are obtained as components of the traction discontinuity in directions, orthogonal to the original displacement field. It is achieved through h -adaptation by adding displacement degrees of freedom in the x - or y -directions on the boundary/interface. This is followed by polynomial or spectral p -enrichment of boundary element interpolation functions $[L]$. The error in kinematic relations may be minimized by enhancing the stress functions by polynomial enrichment or "enriched" p -adaptation in the matrix and inclusion phases. Since the enrichments are carried out simultaneously for all elements, the adaptation has elements of minimizing both local and pollution errors in the microstructure. Numerical analyses of several microstructures with different distributions, sizes and shapes of heterogeneities have shown a superior convergence rate with these adaptations.

The adaptive VCFEM of Moorthy and Ghosh (1999) is incorporated to reduce error in microstructural simulations, especially in level-2 elements. To illustrate the effect of microscale adaptation, a simplified form of the problem posed above, with 1 row of 4 fibers is considered. The mesh consists of 4 Voronoi cell elements as shown in figure 4.35a. The matrix stresses in the hybrid formulation are constructed from an Airy's stress function consisting of a 12 term 4-th order poly-

nomial expansion and a 36 term reciprocal function (see Moorthy and Ghosh (1996,1999)). The inclusion stresses are constructed using a 25 term, 6-th order polynomial function. Displacement fields corresponding to equation (4.22) are constructed with linear shape functions for element boundaries and quadratic shape functions for curved interface elements. The sequence of adaptations consists of two cycles of h - followed by a cycle of p - adaptation of displacement degrees of freedom, followed by a cycle of e^{nr} p -adaptation of the stress functions. The adapted mesh, showing added displacement degrees of freedom, is illustrated in figure (4.35a). The pre-adaptation nodes are marked with a \bullet , the x direction nodal adaptations are marked with a \square while those in the y direction are shown with Δ . The convergence of the VCFEM solutions is shown in figure (4.35b), only for the average traction reciprocity error or (*A.T.R.E.*) as a function of the total degrees of freedom. The *A.T.R.E.* is calculated as (see Moorthy and Ghosh (1999)):

$$A.T.R.E. = \frac{\sum_{\tilde{e}_E=1}^{\tilde{N}_E} e_T^E + \sum_{\tilde{e}_I=1}^{\tilde{N}_I} e_T^I}{\tilde{N}_E + \tilde{N}_I} \quad (4.48)$$

where \tilde{N}_E , \tilde{N}_I , e_T^E and e_T^I correspond to the total number of segments and the traction reciprocity error on the element boundary and interface elements respectively. The degrees of freedom (D.O.F.) correspond to the sum of the total number of nodal degrees of freedom and the number of β stress parameters, i.e. $D.O.F. = 2 * N_{nodes} + N_\beta$. Table 6 and figure 4.35b provide numerical details of *A.T.R.E* with added degrees of freedom due to each adaptation, on the boundary and interface only. Discrete points in the figure correspond to the different stages of adaptation. The first two drops are for the two consecutive cycles of h -adaptation and the third for p -adaptation. The traction reciprocity error reduces rather drastically in the h -adaptation cycles, i.e. a 90% change in *A.T.R.E.* is obtained with a 61% increase in D.O.F.. With the subsequent p -adaptation, and additional 4% change in *A.T.R.E.* is obtained with a further 13% increase in D.O.F.. Since very little *A.T.R.E.* reduction is gained beyond two cycles of boundary h -adaptations, only these are employed for the multi-scale simulations of this section.

A comparison study is made with the solutions in Pagano and Rybicki (1974) (the same results are also generated by the commercial code ANSYS). The ANSYS mesh, for which convergence is achieved has 4230 QUAD4 elements and 4352 nodes. The microscopic in-plane stress σ_{yy} plots along horizontal sections $y = h$ are compared for the unadapted VCFEM, adapted VCFEM and the ANSYS model in figure 4.36. It should be noted that the transverse stress σ_{yy} is approximately two orders lower compared to the leading order stress σ_{zz} and hence convergence is harder to achieve. Results of the adapted VCFEM results agree very well with those of the converged ANSYS model. This is therefore a strong attestation of the accuracy of the adaptive VCFEM solutions. The figure also shows the singular nature of the solution in the free edge region when effective modulus theory by homogenization is used. Since this is physically unattainable, detailed micromechanics solutions are needed in this region.

4.11.2 Multi-level Simulations

To test convergence of the overall model qualitatively, the composite problem with 40 ($n = 40$) rows of 6400 fibers is simulated by the multi-level code. The level-0/1 h-adaptation criterion is based on a traction jump criterion across adjacent element boundaries, stated as:

$$\text{Refine element if } E_i \geq C1 * E_{avg} \text{ where } E_{avg} = \frac{\sum_{i=1}^{NE} E_i}{NE}, E_i = \frac{\int_{\partial Y} ((|T_x|)^2 + (|T_y|)^2)^{1/2} d\partial Y}{\int_{\partial Y} d\partial Y} \quad (4.49)$$

where NE is the total number of level-0/1 elements. This criterion is intended for signaling and zooming in on regions high stress gradients. For level-0 to level-1, the transition is made based on element jump in the significant stress σ_{yy} , in addition to the traction jump condition of equation (4.49), stated as:

$$\text{Level - 0} \rightarrow \text{Level - 1} \text{ if } E_i \geq C2 * E_{avg} \text{ or } {}^y E_i \geq C2 * {}^y E_{avg} \text{ where } {}^y E_i = \frac{\int_{\partial Y} [|\sigma_{yy}|] d\partial Y}{\int_{\partial Y} d\partial Y} \quad (4.50)$$

where $C1, C2$ are prescribed constants. Finally, the level-1 to level-2 transition is made from observations made in the microstructural RVE's of level-1 elements. It is based on the ratio of local energy density (at each integration point of VC element) to the average energy density for the entire RVE (aggregate of VC elements). The procedure followed for determining this is:

- Solve the RVE problems with periodicity boundary conditions and four sets of applied macroscopic strains, viz. (i) $e_{xx} = 1, e_{yy} = 0, e_{xy} = 0, e_{zz} = 0$, (ii) $e_{xx} = 0, e_{yy} = 1, e_{xy} = 0, e_{zz} = 0$, (iii) $e_{xx} = 0, e_{yy} = 0, e_{xy} = 1, e_{zz} = 0$ and (iv) $e_{xx} = 0, e_{yy} = 0, e_{xy} = 0, e_{zz} = 1$.
- For all cases (i-iv) evaluate the energy densities at integration point of the matrix and inclusion phases as $U^{mat/incl} = S_{ijkl}^{mat/incl} \sigma_{ij} \sigma_{kl}$, where S_{ijkl} is the compliance tensor.
- Evaluate the energy density concentration factors:

$$R^{mat} = \frac{\text{Maximum } U^{mat} (= U_{max}^{mat})}{\text{RVE Averaged } U^{mat} (= U_{aver}^{mat})} \quad \text{and} \quad R^{incl} = \frac{\text{Maximum } U^{incl} (= U_{max}^{incl})}{\text{RVE Averaged } U^{incl} (= U_{aver}^{incl})}$$

- In the multi-level problem with actual strain components, the transition is made according to:

$$\text{Level - 1} \rightarrow \text{Level - 2} \text{ if } {}^{actual} U_{max}^{mat} \geq R^{mat} * {}^{actual} U_{aver}^{mat} \text{ or } {}^{actual} U_{max}^{incl} \geq R^{incl} * {}^{actual} U_{aver}^{incl} \quad (4.51)$$

at more than 1% of all integration points.

The initial mesh consists of 200 level-0 QUAD4 elements. To examine the dependence of results on adaptation parameters, two sets of parameters viz. ($C1 = 1.5, C2 = 2$) and ($C1 = 1.25, C2 = 1.5$) are experimented with. Figures 4.37a and b show the h-adapted level-0/level-1/level-2 meshes with the different adaptation parameters. The first set leads to 391 level-0 elements, 0 level-1 elements,

6 transition elements and 4 level-2 elements, while the second set has 475 level-0 elements, 4 level-1 elements, 9 transition elements and 6 level-2 elements. The microstructural RVE or unit cell is assumed to be of dimension $l = \frac{h}{80}$ and the level-2 elements are assumed to contain a single unit cell. The same problem is also solved using the commercial code ANSYS with a mesh of 30,000 elements, for which a 3×3 array of fibers near the free-edge and laminate interface are modeled explicitly (see 4.37c). In figure 4.38a the macroscopic response of level-0 elements, with homogenized effective moduli, is plotted. The figure shows the effect of mesh dependence in the solutions near the free-edge. With increasing cycles of adaptations the artificial stress singularity moves towards the free edge and gains intensity. In figure 4.38b the microscopic level-2 stresses are plotted in the vicinity of the free edge (indicated as L2 in figure 4.38a). It is clearly seen that the artificial singularity of homogenized solutions no longer exist and there is no mesh dependence near the free edge. The two multi-level meshes of figures 4.38 a and b and the ANSYS model all produce similar results. Thus, through this example, the convergence characteristics of the multi-level model is qualitatively verified and confidence is gained about its application.

4.12 Discussions and Conclusion

Adaptivity in the computational modules for multiple scale problems entails minimizing two types of errors, viz. the discretization error and the modeling error. In this work an adaptive multi-level method is proposed to primarily focus on reducing the modeling error and predicting the evolution of stresses, strains and damage at the structural and microstructural scales. The microstructural analysis is conducted with the Voronoi cell finite element model (VCFEM) for elastic-plastic constituents with particle cracking. VCFEM allows for continuous change in element topology due to progressive damage with high accuracy as shown in Moorthy and Ghosh (1999) and Ghosh and Moorthy (1998). The efficiency of the method, due to embedding micromechanics in FEM formulation, makes modeling of large microstructural regions relatively easy. A conventional displacement based elastic-plastic FEM code is developed for macroscopic analysis. Adaptive mesh refinement and level transition strategies are developed to create a hierarchy of computational sub-domains with varying resolutions. This differentiates between non-critical and critical regions and helps in increasing the efficiency of computations by preferential ‘zoom in’.

Three levels of hierarchy, viz. level-0, level-1 and level-2, evolve in the multi-scale model with progressive deformation. A piecewise continuous elastic-plastic constitutive law is developed for level-0 simulations. The specialty of this model is that since it is developed from rigorous micromechanical simulations with precise material morphology, it is sensitive to variations in the microstructural distribution. The constitutive relation leads to very high efficiency in simulations when compared with two-scale analysis by homogenization (e.g. Guedes and Kikuchi (1991)).

Level-0 simulations are accompanied by mesh-refinement using h-adaptation techniques, to reduce discretization error in the computational model and zoom in on regions of evolving localization due to microscopic non-homogeneity. The criteria for h-adaptation are based on gradients or jumps in plastic work or stresses. While these error criteria are effective in equi-distributing discretization

errors where solutions are relatively regular, they are also helpful in identifying regions of localization or singularity due to steep gradients in the solution variables. It should however be mentioned that the proposed refinement schemes and error criteria are by no means optimal. For example, it has been shown in Guo and Babuska (1986), Rank and Babuska (1987) the $h - p$ adaptation, which combines local mesh refinement with increase of the polynomial order of interpolants, enjoy exponential rate of convergence and excellent accuracy especially for problems with singularity. Additionally, it has been demonstrated in Oden and Feng (1996) and Babuska et. al. (1994), that local error estimation techniques are incapable of detecting pollution error particularly when singularities are present. A robust mesh adaptation procedure for reducing errors should therefore incorporate pollution error reduction criteria, as well as $h - p$ adaptation. Much of the ongoing and future efforts by the authors are focussed on introducing these techniques.

When imminent damage and localization are sensed by the code, the level-0 elements automatically switch to level-1 elements, which use computations both at the macroscopic and microscopic scales. The criteria for signaling such transition are nonunique and a number of them are considered in this study. Among those that yielded effective results are: (i) when the homogenized constitutive relation has reached its limit; (ii) when the maximum macroscopic principal stress or hydrostatic stress exceeds a certain fraction of the microscopic fracture stress or (iii) when the macroscopic effective plastic strain or the dilatation exceeds certain pre-determined values. With the rise in local gradients of macroscopic variables or with microstructural damage, the pre-assumed representative volume element in the microstructure are no longer effective and a shift to complete microscopic simulations is necessary. Extended portions of the microstructure are directly modeled by VCFEM in these level-2 elements. An adaptive VCFEM model (AVCFEM) is used to study convergence of the microstructural analysis model. In AVCFEM, traction reciprocity error and error in kinematic relationships are optimized through boundary/interface enrichment in the form of additional displacement degrees of freedom and interpolation orders, as well as through stress function enhancement. In Moorthy and Ghosh (1999), excellent convergence rate of AVCFEM has been established for elastic and elasto-plastic microstructural analysis. For the problem considered in this work, two cycles of boundary $h-$ adaptation is found to achieve desirable results in the level-2 elements.

Several numerical examples are conducted with the multi-level model to examine the effect of various microstructural morphologies on the multi-scale response of composite and porous structural components. Specifically scale effects, effects of microstructural distribution and shapes and structural geometry, on the mechanical and damage response are investigated. In conclusions, the multi-level model has addressed a number of difficult issues in solving multi-scale problems. However a number of avenues for further model enhancements remain. For example, the Newton-Raphson iteration scheme used for nonlinear problems struggle for convergence, as more and more level-2 elements with damage emerge. The migration of boundaries between different levels within each iteration loop has an adverse effect on convergence as well. Also for the level-1 elements, an iterative loop is necessary for convergence of steps (a), (b) and (c) in section 4.6. In addition, the issues of adaptivity mentioned above remain. These issues are currently being dealt with for

making this an effective tool in the prediction of structural failure.

Bibliography

- [1] Benssousan, A., Lions, J.L. and Papanicoulau, G. (1978). Asymptotic analysis for periodic structures, North Holland, Amsterdam.
- [2] Sanchez-Palencia, E. (1980). Non-homogeneous media and vibration theory, Lecture notes in Physics, **127**, Springer-Verlag, Berlin Heidelberg,
- [3] Parton, V.Z. and Kudryavtsev, B.A., (1993). Engineering mechanics of composite structure CRC Press
- [4] Bakhvalov, N. S. and Panasenko, G. P., (1984). Homogenization in Periodic Media. Mathematical Problems of the Mechanics of Composite Materials. Nauka, Moscow
- [5] Fish, J. and Belsky, V., (1995). Multigrid method for periodic heterogeneous media, part II: multiscale modeling and quality control in multidimensional case, *Comp. Meth. in Appl. Mech. and Engng.* **126**, 17-38.
- [6] Fish, J. and Wagiman, A., (1993). Multiscale finite element method for a locally nonperiodic heterogeneous medium, *Comput. Mech.* **12**, 164-180.
- [7] Guedes, J.M. and Kikuchi, N., (1991). Preprocessing and postprocessing for materials based on the homogenization method with adaptive finite element methods, *Comp. Meth. in Appl. Mech. Engng.*, **83**, 143-198.
- [8] Hollister, S.J. and Kikuchi, N., (1992). A comparison of homogenization and standard mechanics analysis for periodic microstructure, *Comput. Mech.* **10**, 73-95.
- [9] Suquet, P., (1985). Local and global aspects in the mathematical theory of plasticity, Plasticity Today- Modeling methods and Applications, Sawczuk, A. and Bianchi, G. (eds.), Elsevier, London,
- [10] Fish, J. , Shek,K., Pandheeradi, M. and Shephard, M. S.. (1997). Computational Plasticity for composite structures based on mathematical homogenization: Theory and Practice, *Comp. Meth. in Appl. Mech. and Engng.*, **148**, 53-73.
- [11] Guedes, J.M., (1990). Nonlinear computational model for composite material using homogenization, Ph. D. Dissertation, University of Michigan MI.

- [12] Cheng, C. -H., (1992). Modeling of the elasto-plastic behavior for composite materials using homogenization method, Ph. D. Dissertation, University of Michigan MI.
- [13] Lene, F., (1986). Damage constitutive relations for composite materials, *Engin. Frac. Mech.* **25**(5), 713-728.
- [14] Devries, F., Dumontet, H., Duvaut, G. and Lene, F., (1989). Homogenization and damage for composite structures, *Int. J. Num. Meth. in Engng.* **27**, 285-298.
- [15] Belytschko, T., Fish, J. and Bayliss, A., (1994). The spectral overlay on the finite element solution with high gradients, *Comput. Meth. Appl. Mech. Engng.* **81**, 71-89.
- [16] Robbins D.H. and Reddy, J.N., (1996). An efficient computational model for the stress analysis of smart plate structures, *Smart Mater. Struct.*, **5**:3, 353-360.
- [17] Hughes, T.J.R., (1995). Multiscale phenomena: Green's functions, the Dirichlet-to-Neumann formulation, subgrid scale models, bubbles and the origins of stabilized methods *Comput. Meth. Appl. Mech. Engng.*, **127**(1-4), 387-401.
- [18] Pagano, N.J. and Rybicki, E.F., (1974). On the significance of effective modulus solutions for fibrous composites, *Jour. Comp. Mat.* **8**, 214-228.
- [19] Fish, J., Nayak, P. and Holmes, M.H., (1994). Microscale reduction error indicators and estimators for a periodic heterogeneous medium, *Comput. Mech.*, **14**:4, 323-338.
- [20] Zohdi, T.I. , Oden, J.T. and Rodin, G. J., (1996). Hierarchical modeling of heterogeneous bodies, *Comput. Meth. Appl. Mech. Engng.* **138**, 273-298.
- [21] Oden. J.T. and Zohdi, T.I., (1997). Analysis and adaptive modeling of highly heterogeneous elastic structures, *Comput. Meth. Appl. Mech. Engng.* **148**, 367-391.
- [22] Oden, J.T., Vemaganti, K. and Moes, N., (1999). Hierarchical modeling of heterogeneous solids, *Comput. Meth. Appl. Mech. Engng.* **172**, 3-25.
- [23] Moorthy, S. and Ghosh, S., (1996). A model for analysis of arbitrary composite and porous microstructures with Voronoi cell finite elements, *Int. Jour. Numer. Meth. Engin.* **39**, 2363-2398.
- [24] Moorthy, S. and Ghosh, S., (1998). A Voronoi cell finite element model for particle cracking in composite materials, *Comp. Meth. Appl. Mech. Engin.* **151**, 377-400.
- [25] Ghosh, S. , Nowak, Z. and Lee, K., (1997). Quantitative characterization and modeling of composite microstructures by Voronoi cells, *Acta Metall. et Mater.*, **45**(6), 2215-2234.
- [26] Moorthy, S. and Ghosh, S., (2000). Adaptivity and convergence in the Voronoi cell finite element model for analyzing heterogeneous materials, *Comp. Meth. Appl. Mech. Engin.* (in press).

- [27] Ghosh, S., Lee, K. and Moorthy, S., (1995). Multiple scale analysis of heterogeneous elastic structures using homogenization theory and Voronoi cell finite element method, *Int. Jour. Solids Struct.*, **32**(1), 27-62.
- [28] Ghosh, S., Lee, K. and Moorthy, S., (1996). Two scale analysis of heterogeneous elastic-plastic materials with asymptotic homogenization and Voronoi cell finite element model, *Comp. Meth. Appl. Mech. Engin.*, **132**, 63-116.
- [29] Ghosh, S. and Moorthy, S., (1998). Particle fracture simulation in non-uniform microstructures of metal-matrix composites, *Acta Mater.*, **46**(3), 965-982.
- [30] Hill, R., (1965). A self consistent mechanics of composite materials, *Jour. Mech. Phys. Solids*, **13**, 213-222.
- [31] Suquet, P., (1987). Elements of homogenization theory for inelastic solid mechanics, Homogenization Technique for Composite Media, Sanchez-Palencia, E. and Zaoui, A. (eds.), Springer-Verlag, Berlin-Heidelberg-New York, 194-275.
- [32] Lee, K. , Moorthy, S. and Ghosh, S., (1999). Multiple scale computational model for damage in composite materials, *Comp. Meth. Appl. Mech. and Engng.*, **172**, 175-201.
- [33] Sun, C. T. and Chen, J. L., (1991). A micromechanical model for plastic behavior of fibrous composites, *Comp. Sci. Tech.*, **40** 115-129.
- [34] Xie, M. and Adams, D., (1995). A plasticity model for unidirectional composite materials and its applications in modeling composite testing, *Comp. Sci. and Tech.*, **54**, 11-21.
- [35] Bao, G., Hutchinson, J. W. and McMeeking, R. M., (1991). Plastic reinforcement of ductile matrices against plastic flow and creep, *Acta Metallur. et Mater.*, **39**.
- [36] Gurson, A.L., (1977). Continuum theory of ductile rupture by void nucleation and Growth-I, Yield criteria and flow rules for porous ductile media, *J. Engng. Mater. Technol.*, **99**, 2-15.
- [37] Tvergaard, V., (1982). On localization in ductile materials containing spherical voids *Int. Jour. of Frac.*, **18**(4) 237-251.
- [38] Terada, K. and Kikuchi, N., (1995). Nonlinear homogenization method for practical applications. Computational Methods in Micromechanics. ed. Ghosh, S. and Ostoja-Starzewski, M., ASME AMD **212**, 1-16.
- [39] Dvorak, G.J. and Benveniste, Y., (1992). On transformation strains and uniform fields in multiphase elastic media, *Proc. R. Soc. Lond.*, A 437, 291-310.
- [40] Hill, R., (1971). The mathematical theory of plasticity. Oxford Press.
- [41] Zhu, J. Z. and Zienkiewicz, O. C., (1988). Adaptive techniques in the finite element method, *Comm. Appl. Num. Meth.* **4**, 197-204.

- [42] Zhu, J. Z. and Zienkiewicz, O. C., (1992). The superconvergent patch recovery and a posteriori error estimates. Part 2: Error estimates and adaptivity, *Int. J. Num. Meth. Engng.* **33**(7), 1365-1382.
- [43] Melosh, R. J. and Marcal, P. V., (1977). An energy basis for mesh refinement of structural continua, *Int. J. Num. Methods Eng.* **11**(7), 1083-1092.
- [44] Demkowicz, L., Devloo, Ph. and Oden, J. T., (1985). On an h type mesh refinement strategy based on a minimization of interpolation error, *Comp. Meth. in Appl. Mech. Engng.*, **3** , 67-89.
- [45] Bass, J. M. and Oden, J. T., (1987). Adaptive finite element methods for a class of evolution problems in viscoplasticity, *Int. J. Engng. Sci.*, **25**(6) , 623-653.
- [46] Ladeveze, P. and Oden, J. T. (eds.), (1998). Advances in adaptive computational methods, *Studies in Applied Mechanics*, **47**, Elsevier.
- [47] Zhu, J. Z., Hinton, E. and Zienkiewicz, O. C., (1993). Mesh enrichment against mesh regeneration using quadrilateral elements, *Comm. Num. Meth. Engng.* **9**, 547-554.
- [48] Paulino, G.H., Menezes, I.F. M., Cavalcante Neto, J.B., Martha, L.F., (1999). A methodology for adaptive finite element analysis: Towards an integrated computational environment, *Comp. Mech.* **23**, 361-388.
- [49] Koh, B.C. and Kikuchi, N., (1987). New improved hourglass control for bilinear and trilinear elements in anisotropic linear elasticity, *Comp. Meth. Appl. Mech. Engng.* **65**, 1-46.
- [50] Guo, B. and Babuska, I., (1986). The h-p version of the finite element method, *J. Comput. Mech.* **1**, 21-42.
- [51] Rank, E. and Babuska, I., (1987). An expert system for the optimal mesh design in the hp-version of the finite element method, *Int. J. Numer. Methods Eng.* **24**, 2087-2106.
- [52] Oden, J. T. and Feng, Y., (1996). Local and pollution error estimation for finite element approximations of elliptic boundary value problems, *J. Comput. Appl. Math.*, **74**(1-2) , 245-293.
- [53] Babuska, I., Strouboulis, T., Mathus, A., and Upadhyay, C. S., (1994). Pollution error in the h-version of the finite element method and the local quality of a-posteriori error estimators, *Finite Elem. Anal. Design*, **17** , 273-321.

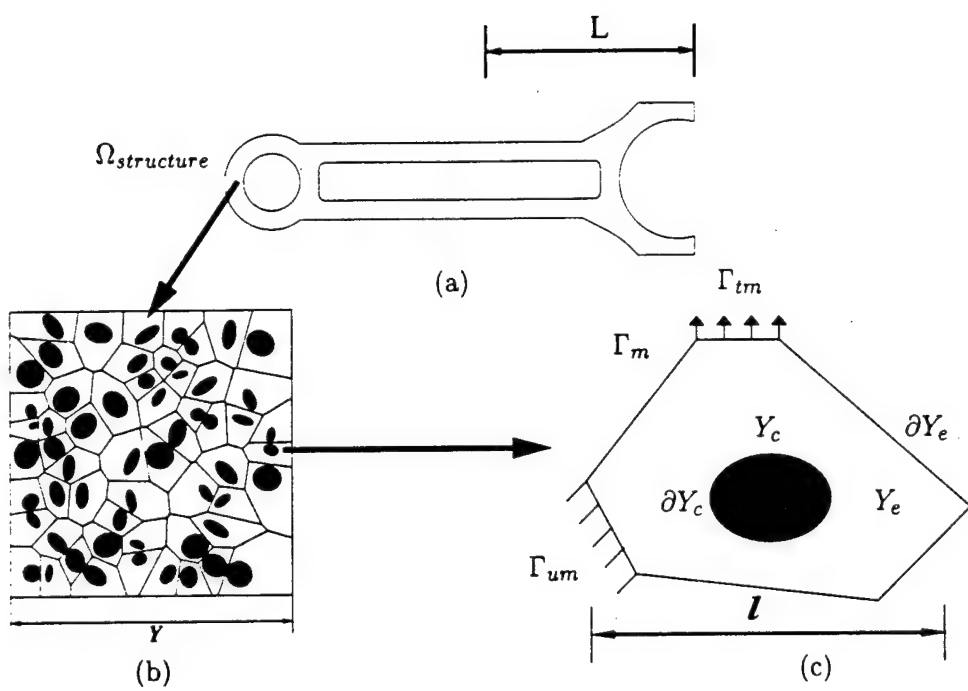
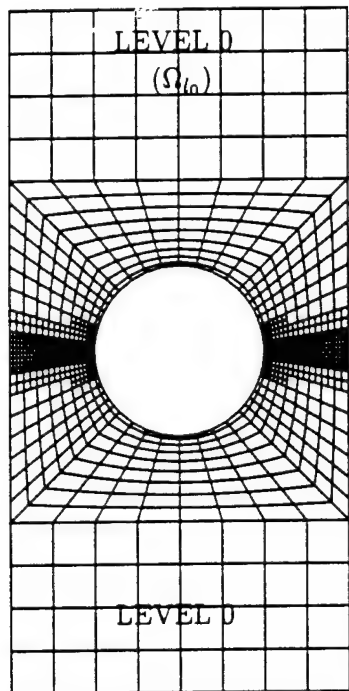
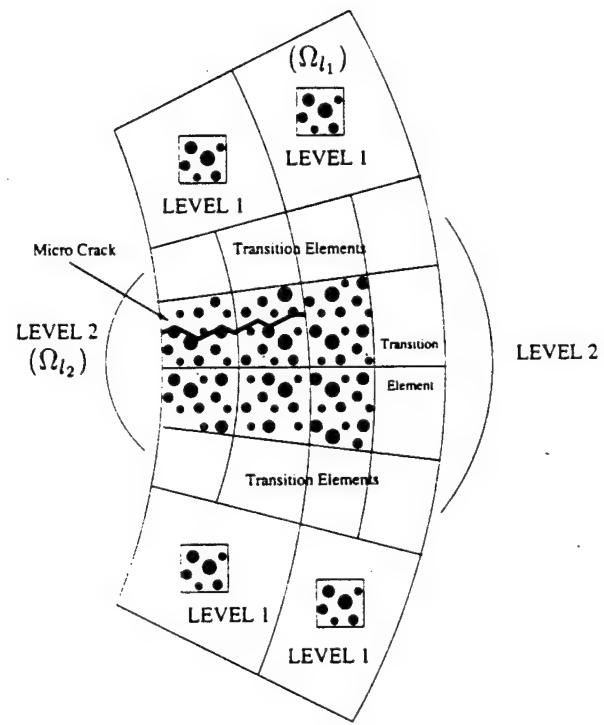


Figure 4.1: A heterogeneous structure showing various scales: (a) The structure at the macroscopic scale of applied loads (b) A representative volume element (RVE) at the microscopic scale with the VCFE model and (c) A Voronoi cell element at the scale of a single heterogeneity or basic structural element.



(a)



(b)

Figure 4.2: A hierarchical multi-level computational domain; Level-0 for macroscale continuum modeling (a) Level-1 for coupled macro-microscopic (RVE) modeling with asymptotic homogenization and (b) Level-2 for pure microscopic modeling

Figure 4.3: Flow chart of the sequence of operations in the multiple-scale model.

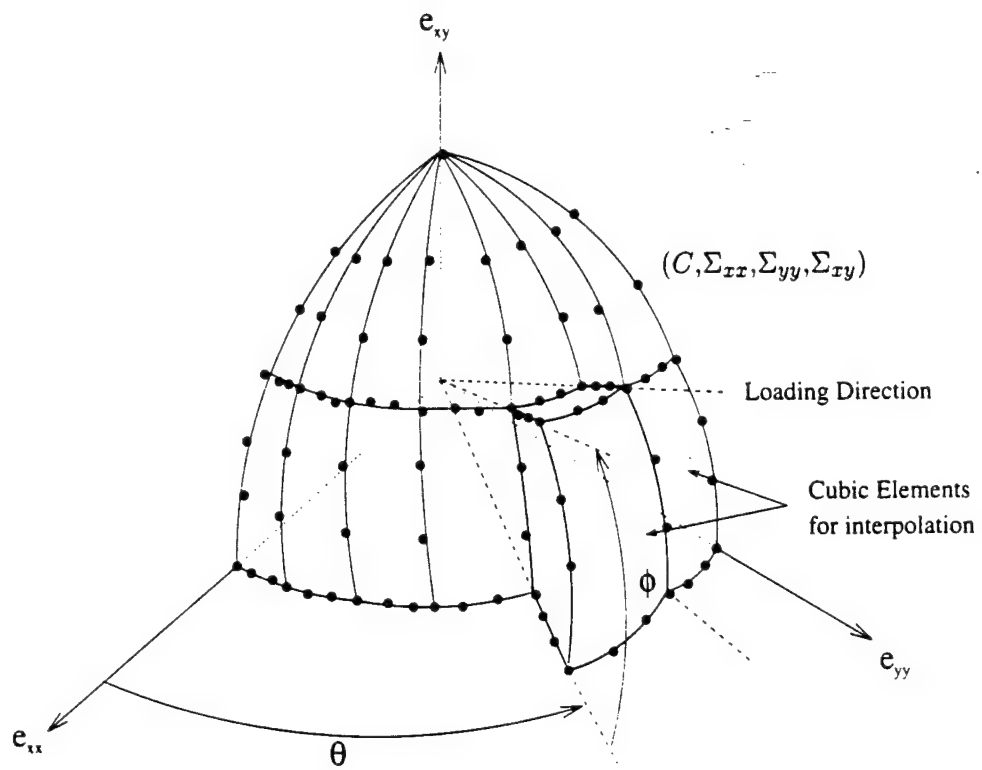


Figure 4.4: A $e_{xx} - e_{yy} - e_{xy}$ strain sub-space, discretized into cubic elements for interpolating constitutive model parameters. The nodal values of stresses and plastic work are numerically generated.

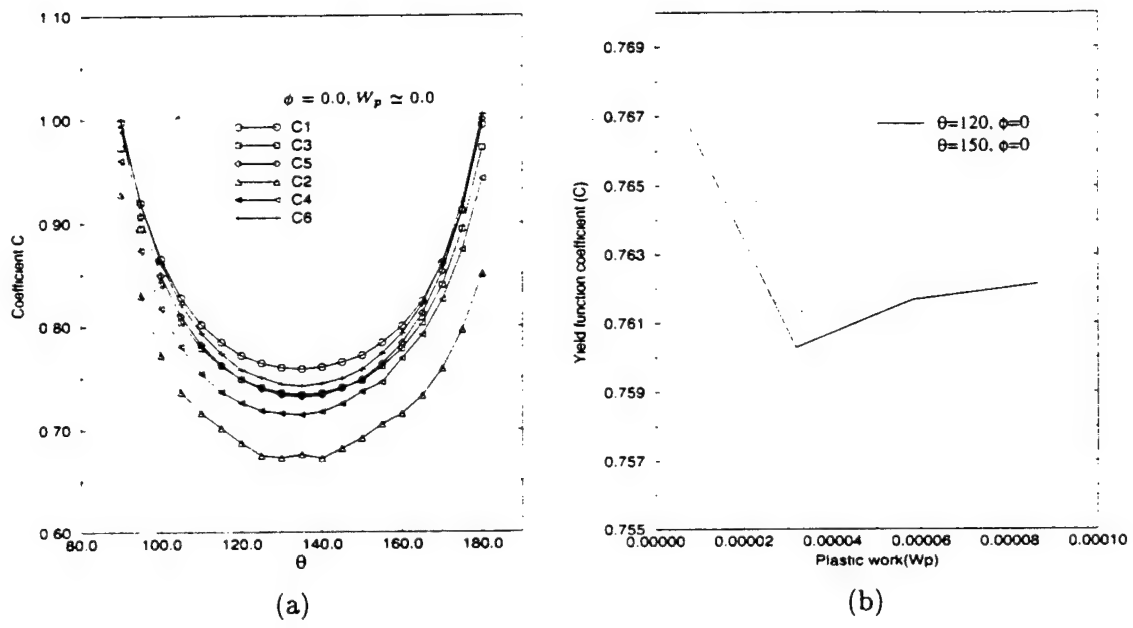
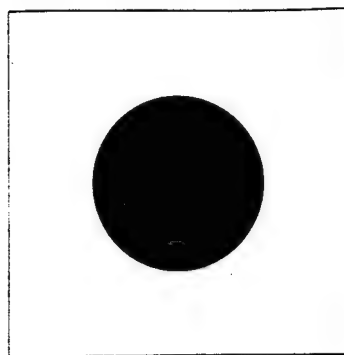
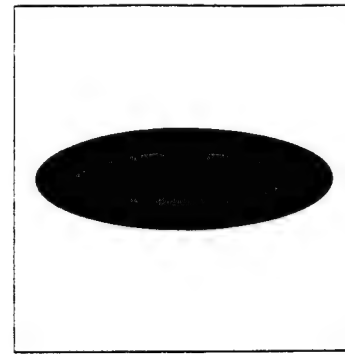


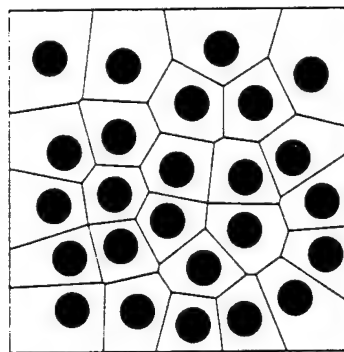
Figure 4.5: Variation of the yield function coefficient $C(e_{xx}, e_{yy}, e_{xy}, W_p)$, (a) as a function of θ or normal strains for different microstructures, (b) as a function of plastic work W_p .



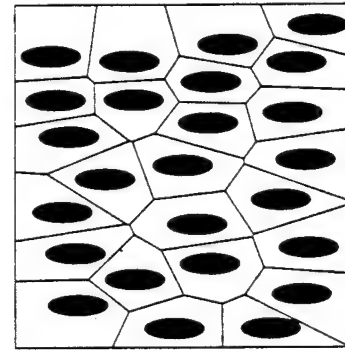
(C1,V1)



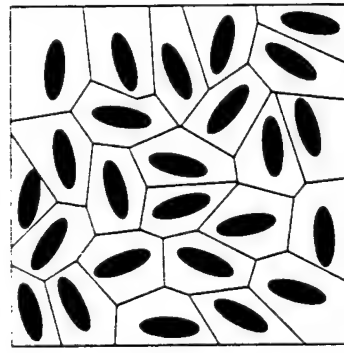
(C2,V2)



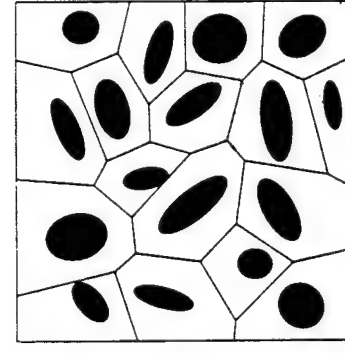
(C3,V3)



(C4,V4)



(C5,V5)



(C6,V6)

Figure 4.6: Microstructures with different shape, size, orientation and spatial distribution, for 20% volume fraction composite (C1,C2,C3,C4,C5,C6) and porous (V1,V2,V3,V4,V5,V6) materials.

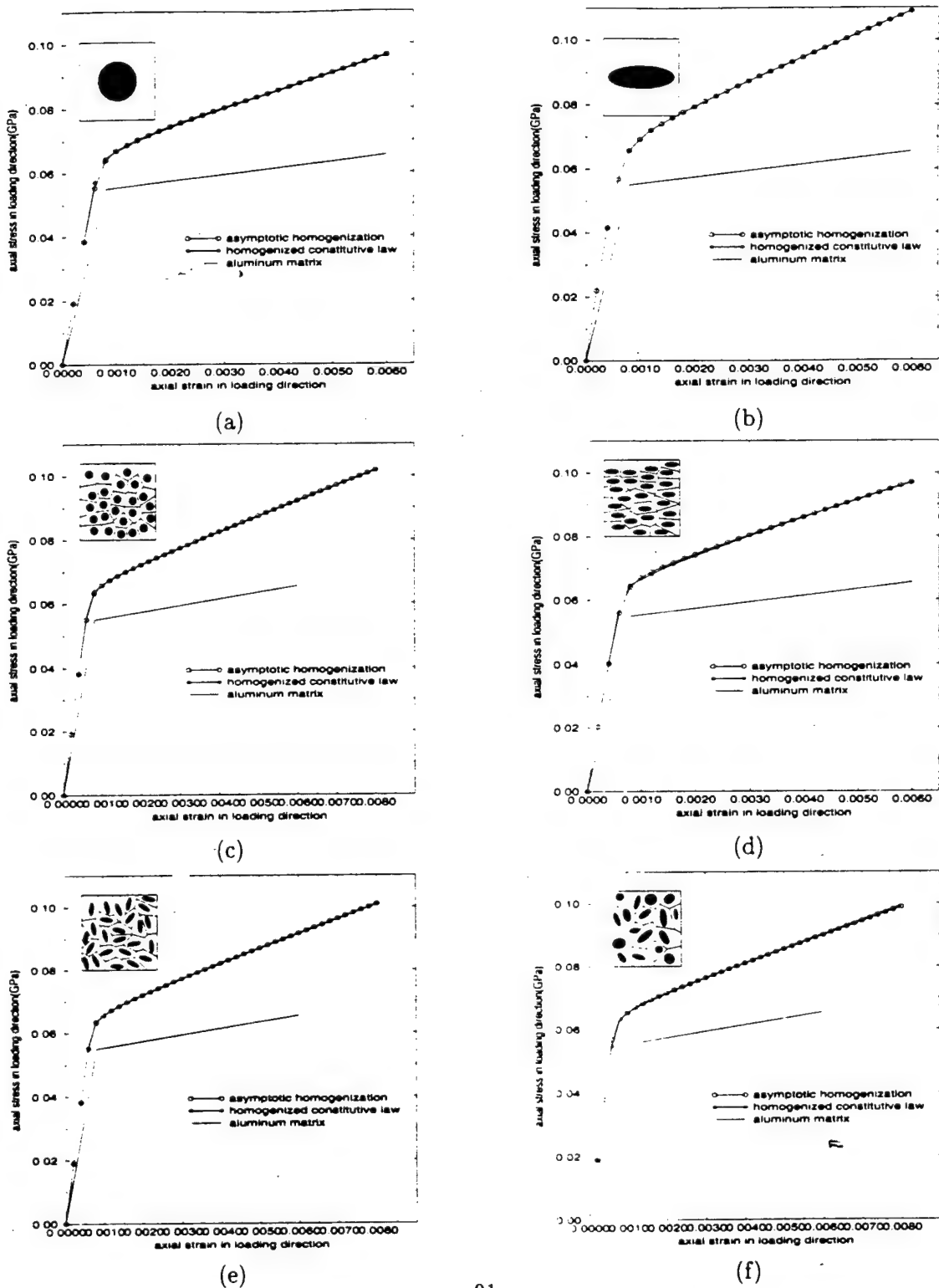


Figure 4.7: Comparison of the stress-strain results in the composite for the uniaxial loading test by (i) macroscopic analysis with the homogenized constitutive model and (ii) two-scale analysis with asymptotic homogenization model for: (a) C1, (b) C2, (c) C3, (d) C4, (e) C5 and (f) C6 microstructures.

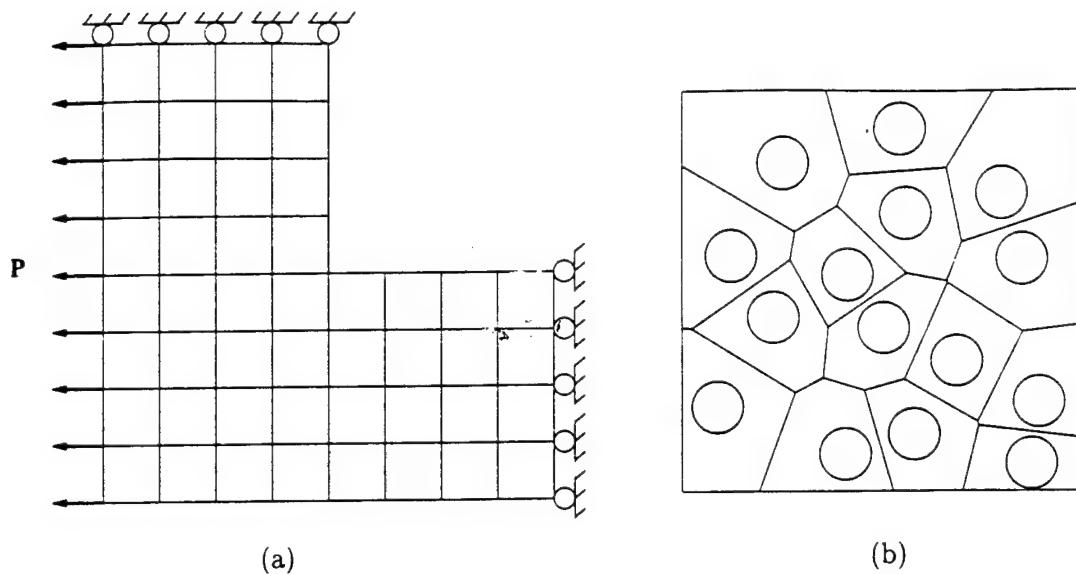


Figure 4.8: (a) Finite element model for a quarter of the square composite plate with square hole and (b) the VCFE model of the microstructural composite RVE.

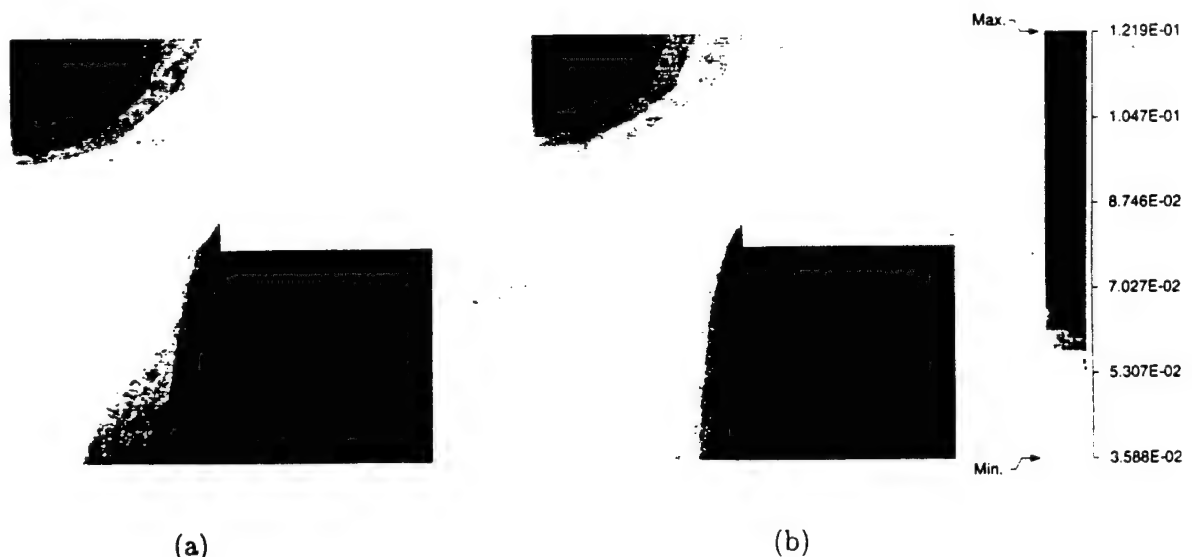
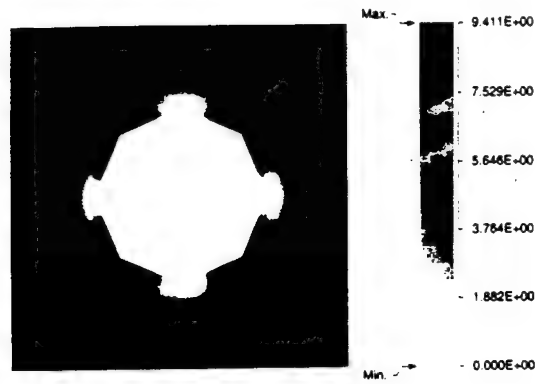
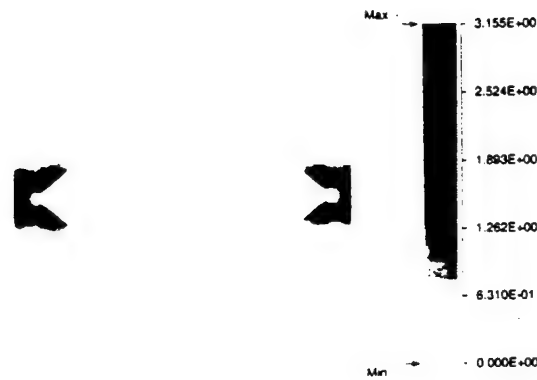


Figure 4.9: Comparison of macroscopic stress (Σ_{xx}) contours in composite material with (a) the homogenized constitutive model and (b) two-scale analysis with asymptotic homogenization.

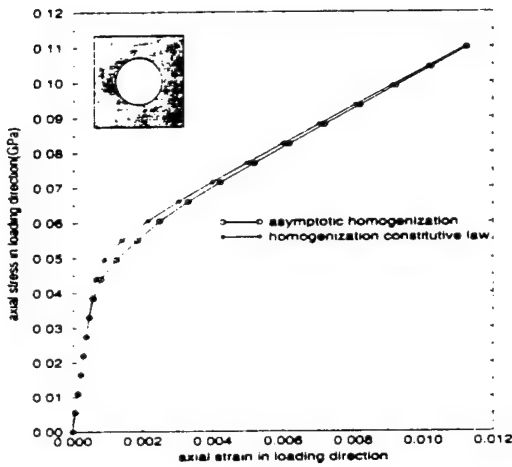


(a)

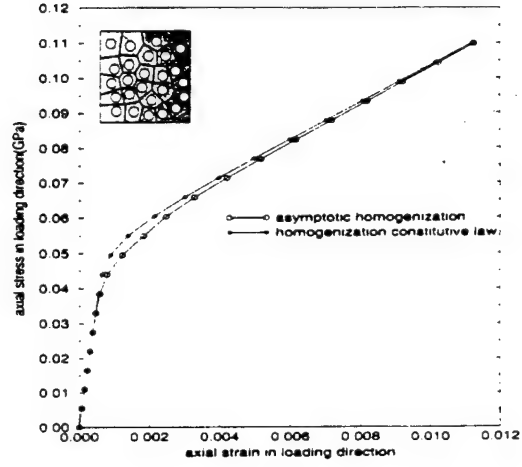


(b)

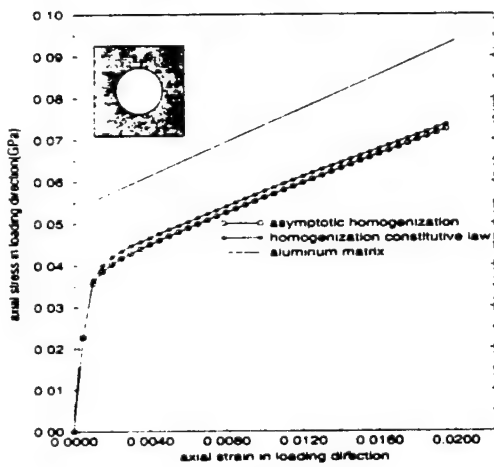
Figure 4.10: Contour plot of the microscopic plastic strain ϵ^p in the voided microstructures under pure shear loading condition, for (a) V1 (b) V2 microstructures.



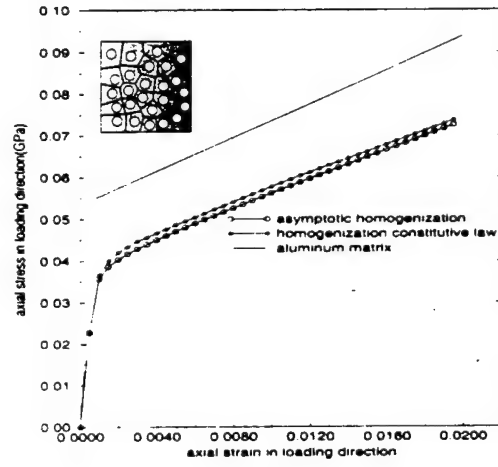
(a)



(b)



(c)



(d)

Figure 4.11: Comparison of the stress-strain results in the porous material for (a) bi-axial tension for V1 microstructure (b) bi-axial tension for V3 microstructure, (c) uniaxial tension for V1 microstructure and (d) uniaxial tension for V3 microstructure.

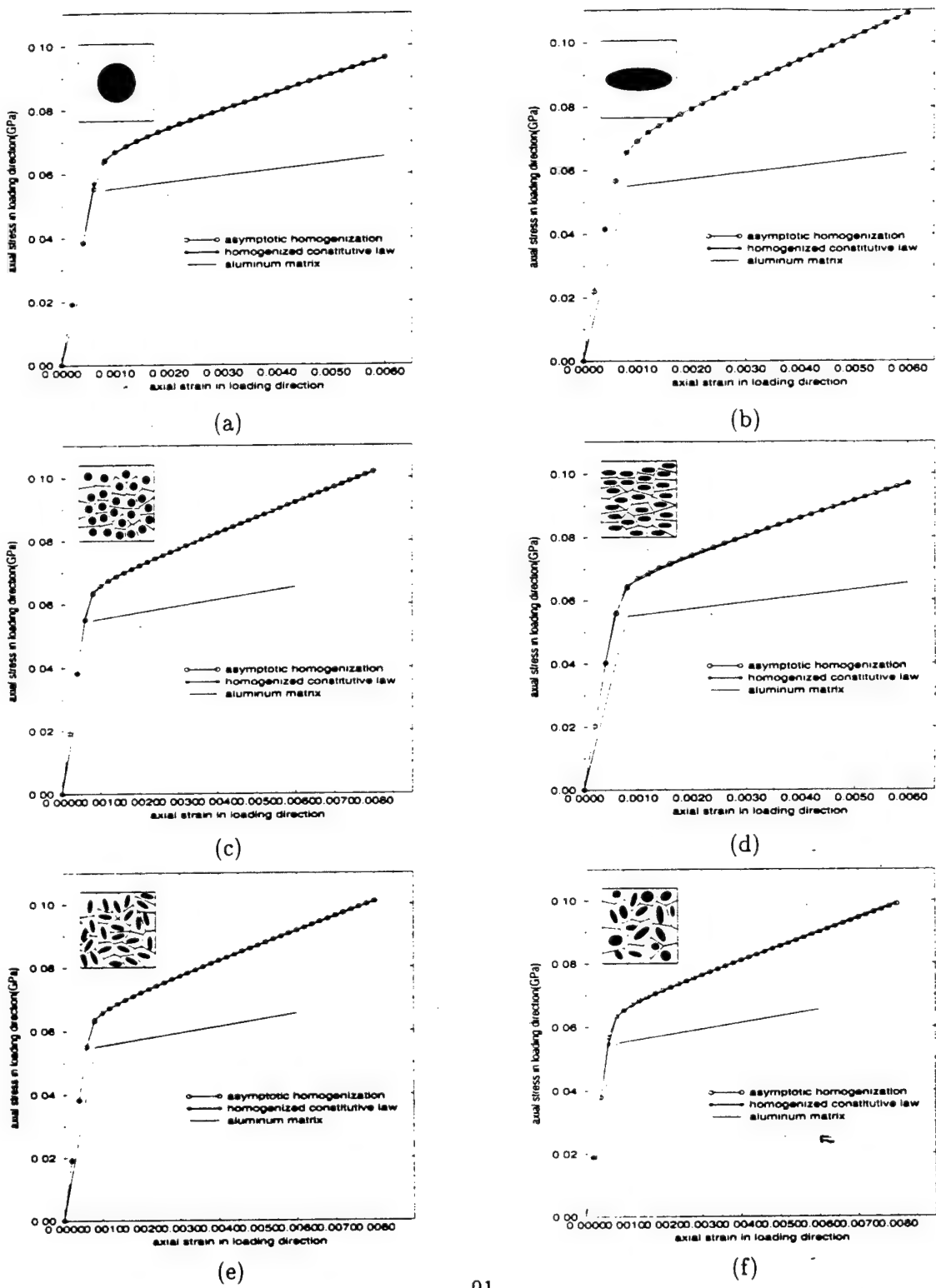


Figure 4.7: Comparison of the stress-strain results in the composite for the uniaxial loading test by (i) macroscopic analysis with the homogenized constitutive model and (ii) two-scale analysis with asymptotic homogenization model for: (a) C1, (b) C2, (c) C3, (d) C4, (e) C5 and (f) C6 microstructures.

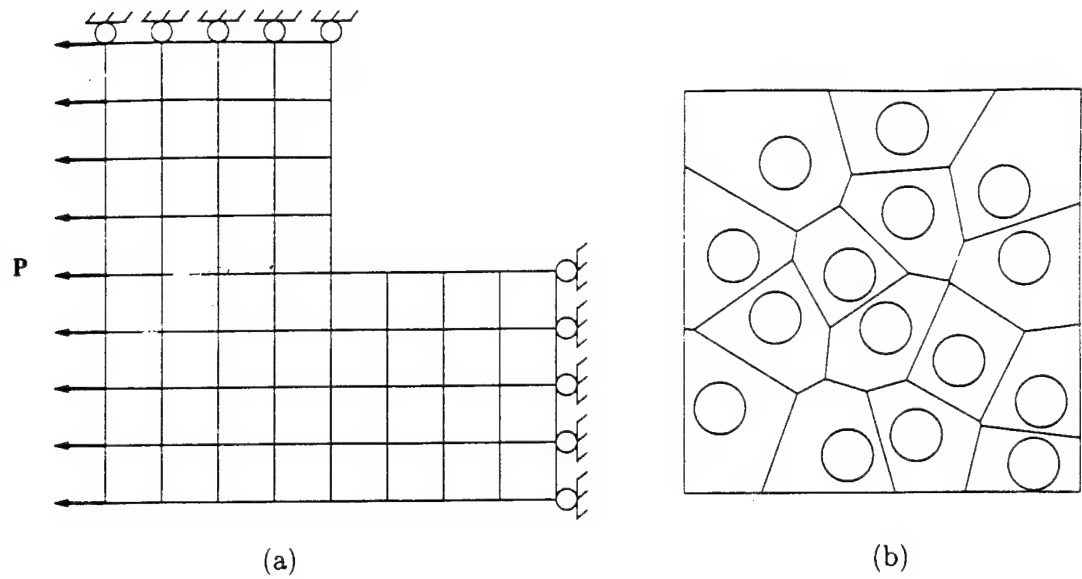


Figure 4.8: (a) Finite element model for a quarter of the square composite plate with square hole and (b) the VCSE model of the microstructural composite RVE.

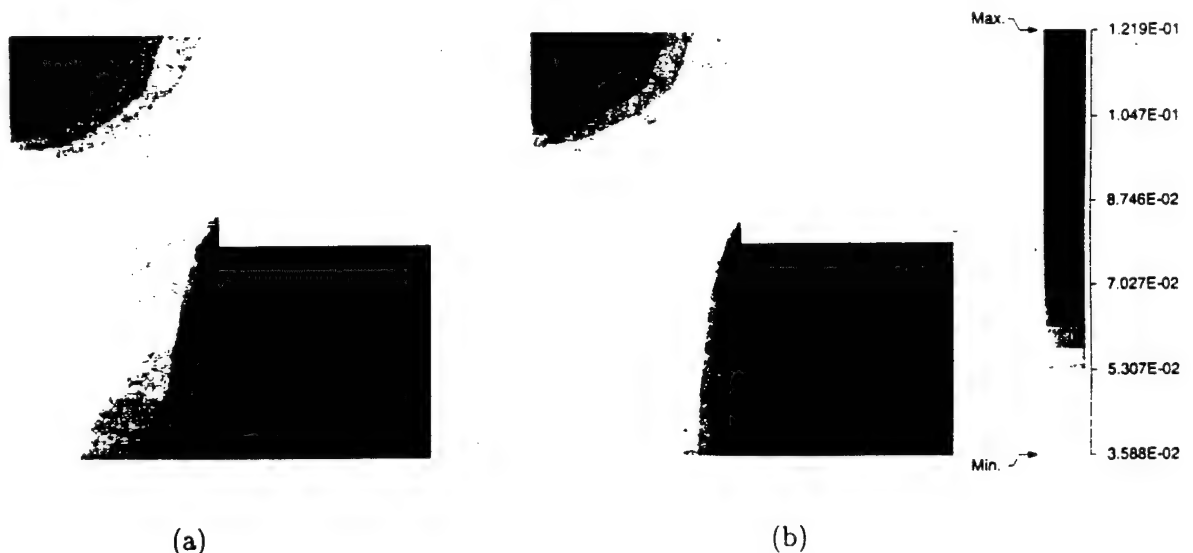
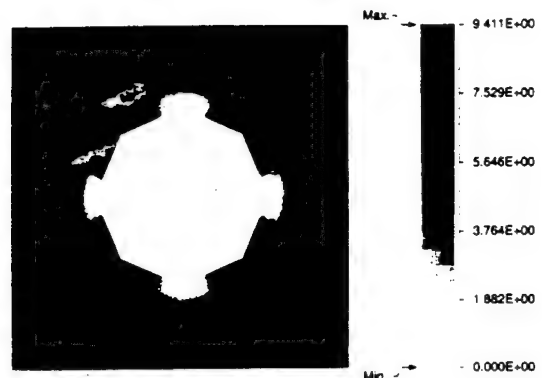
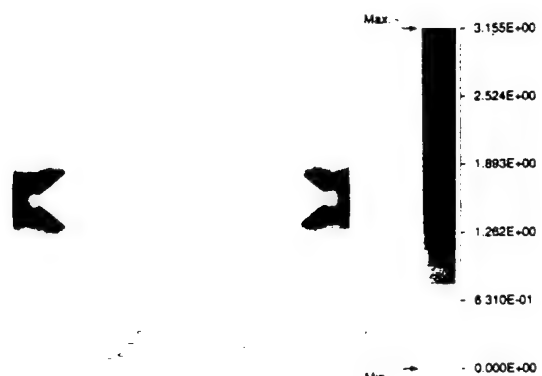


Figure 4.9: Comparison of macroscopic stress (Σ_{xx}) contours in composite material with (a) the homogenized constitutive model and (b) two-scale analysis with asymptotic homogenization.



(a)



(b)

Figure 4.10: Contour plot of the microscopic plastic strain ϵ^p in the voided microstructures under pure shear loading condition, for (a) V1 (b) V2 microstructures.

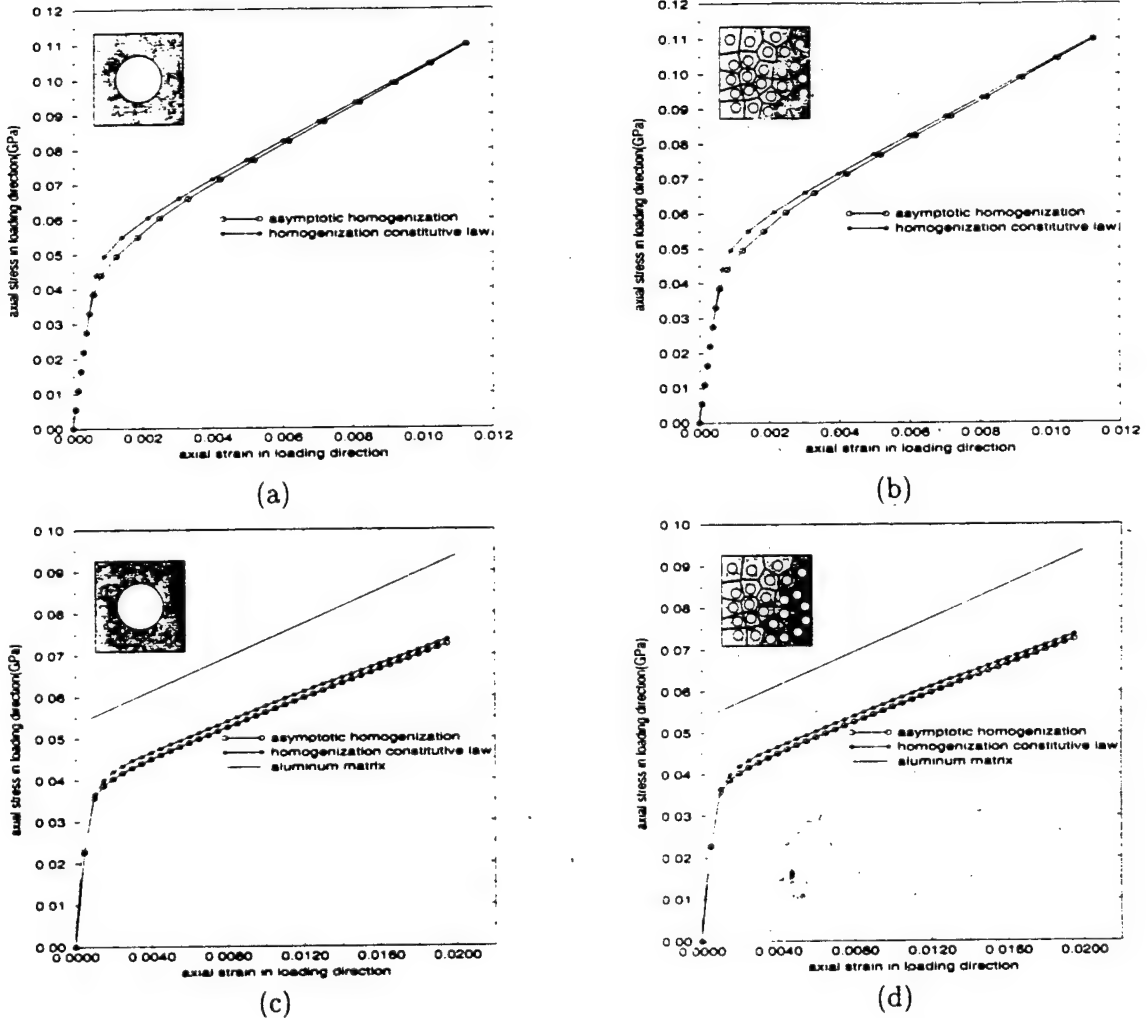


Figure 4.11: Comparison of the stress-strain results in the porous material for (a) bi-axial tension for V1 microstructure (b) bi-axial tension for V3 microstructure, (c) uniaxial tension for V1 microstructure and (d) uniaxial tension for V3 microstructure.

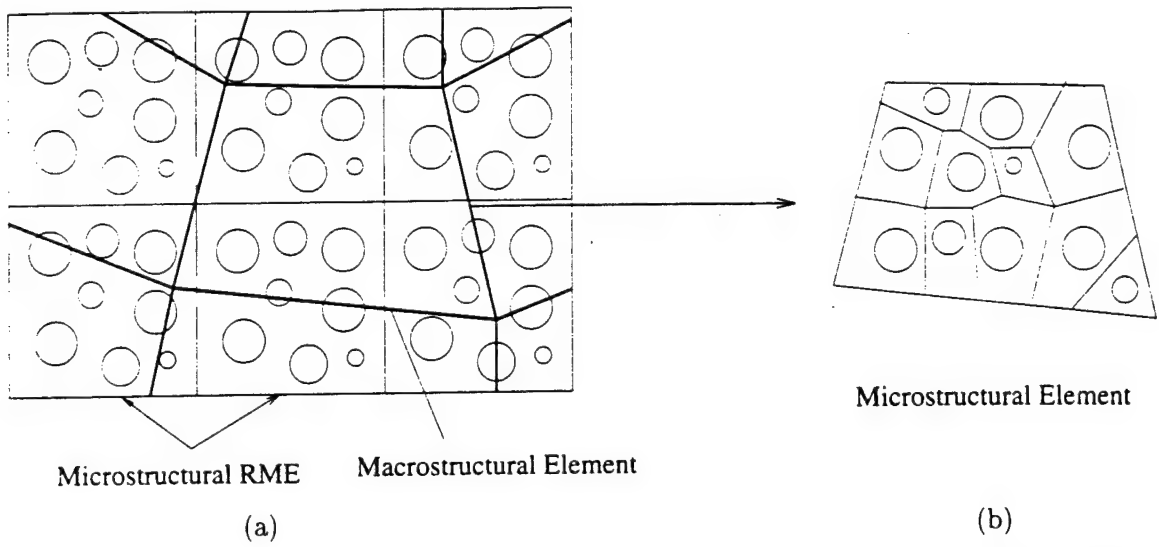


Figure 4.12: Creating extended microstructure; (a) a mesh of macroscopic elements with an underlying microstructure of repeated RVEs, (b) the extended microstructure by Voronoi tessellation.

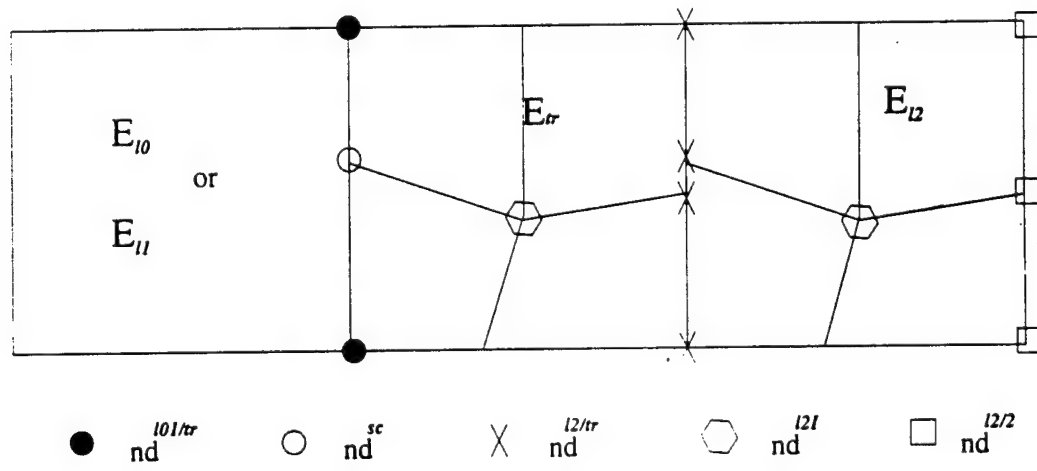
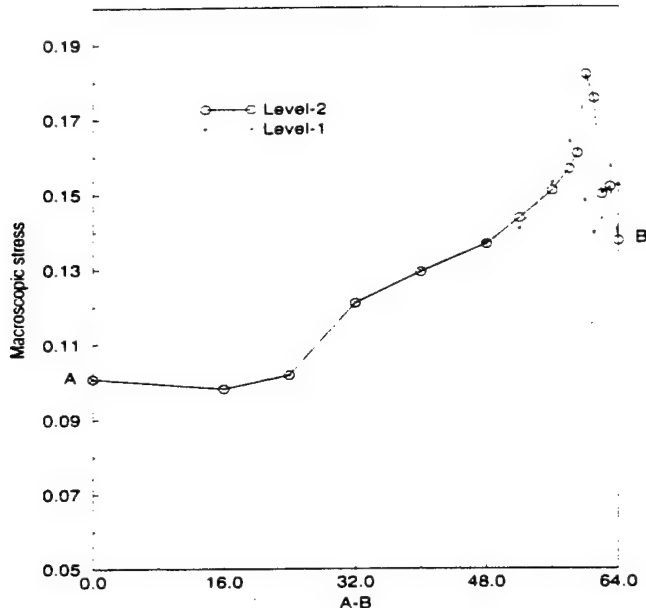
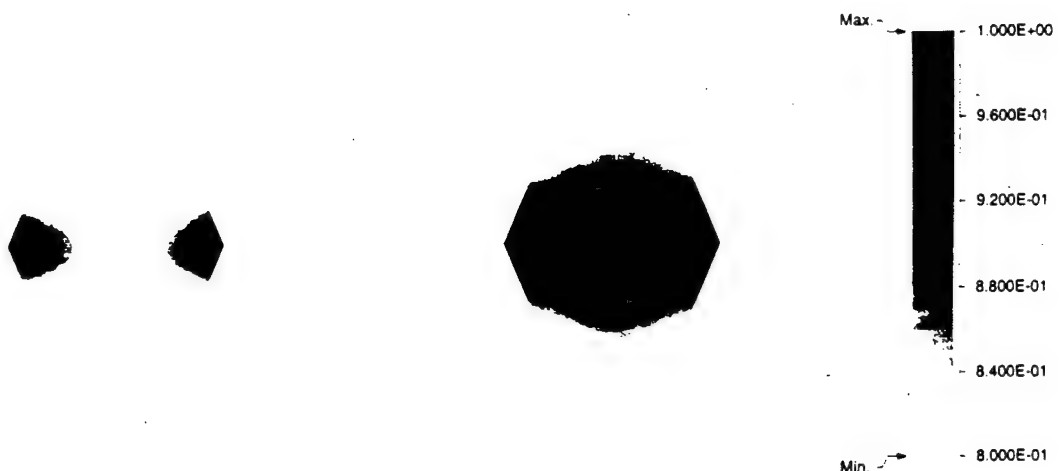


Figure 4.13: Interfaces between the level 0/1 E_{l0} and E_{l1} elements, transition E_{tr} elements and the level-2 E_{l2} elements.



(a)



(b)

(c)

Figure 4.14: (a) Macroscopic axial stress-strain plots for a single RVE in tension modeled by level-1 and level-2 elements; Maximum principal stress distribution in the inclusion by (b) level-2 element and (c) level-1 element.

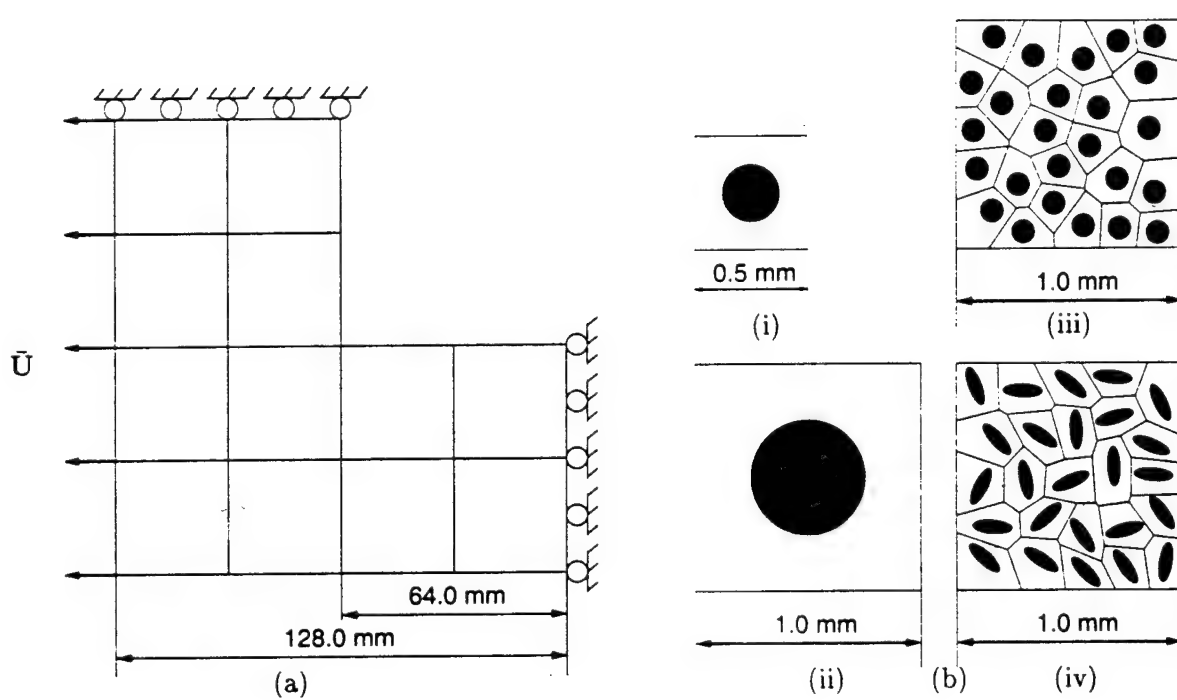
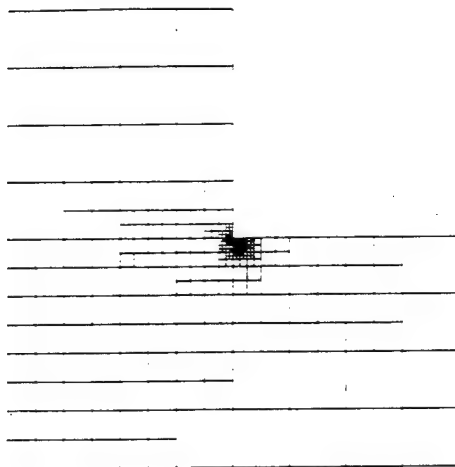
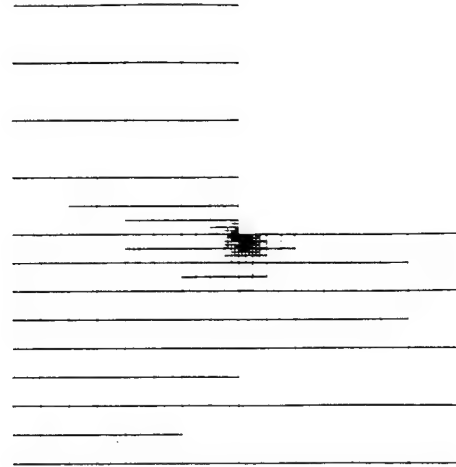


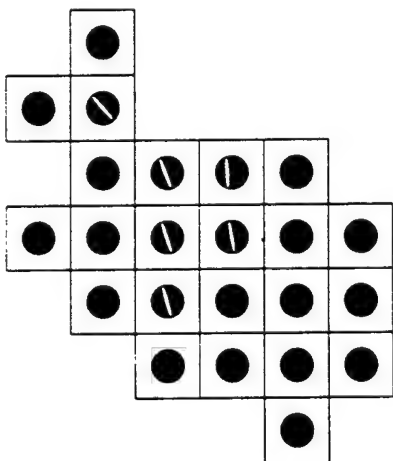
Figure 4.15: (a) A quarter of the level-0 starting macroscopic model of a square plate with a square hole. (b) four different microstructural RVE's for the plate model.



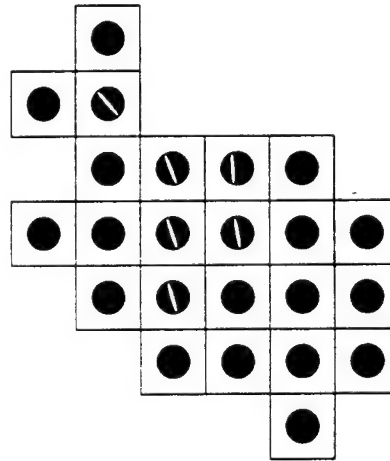
(a)



(b)



(c)



(d)

Figure 4.16: Macroscopic three level evolved mesh for the composite material at the end of the loading cycle for (a) the larger RVE (ii) and (b) smaller RVE (i); the corresponding level-2 region with the (c) the larger RVE (ii) and (d) smaller RVE (i). Level-0 is with white elements, level-1 is with grey elements and level-2 is with black elements.

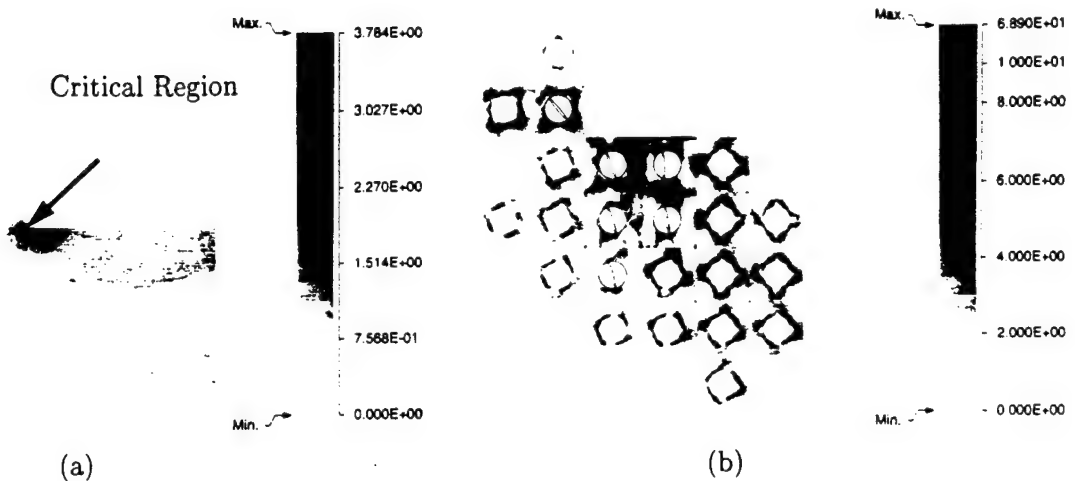


Figure 4.17: Contour plot of plastic strain $\bar{\epsilon}^p$ for the composite square plate: (a) the macroscopic averaged strain and (b) the level-2 microscopic strain at the critical region for the larger RVE (ii) model.

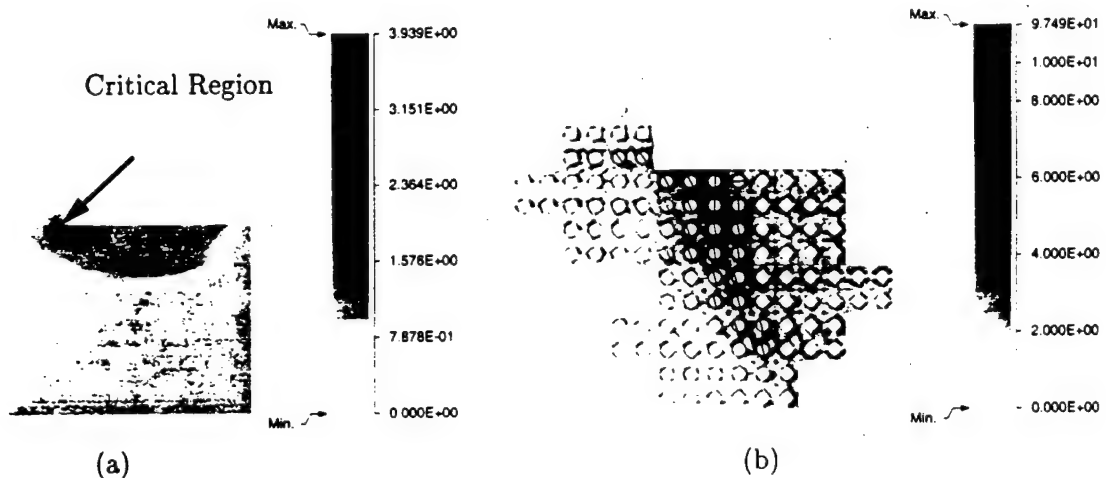


Figure 4.18: Contour plot of plastic strain $\bar{\epsilon}^p$ for the composite square plate: (a) the macroscopic averaged strain and (b) the level-2 microscopic strain at the critical region for the smaller RVE (i) model.

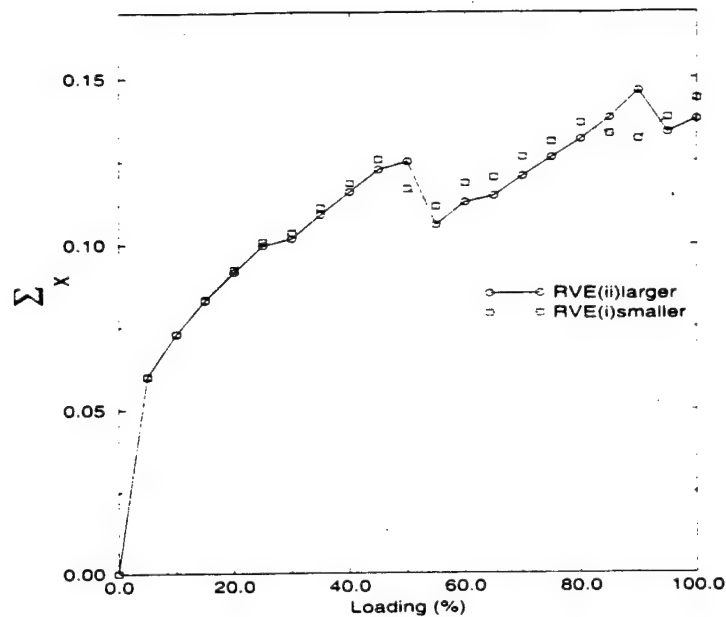


Figure 4.19: The evolution of Σ_{xx} at the corner node of square hole for the two microstructures.

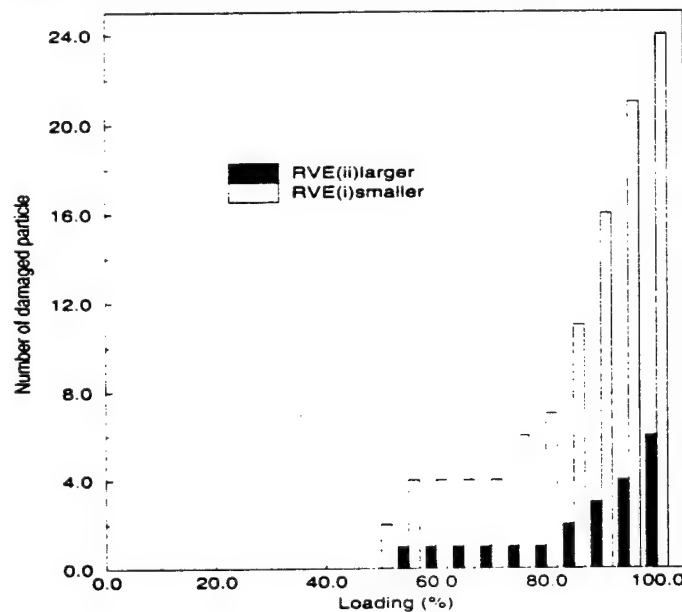
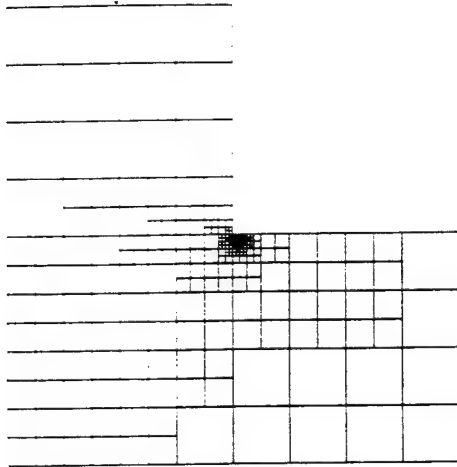
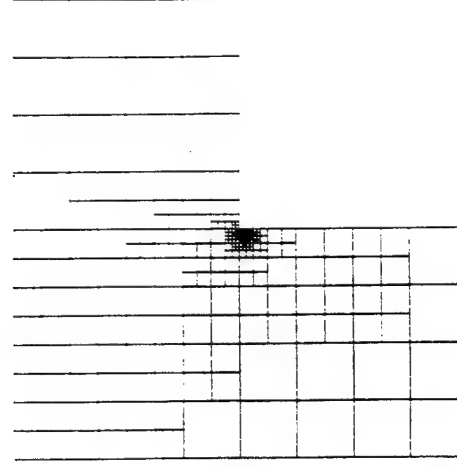


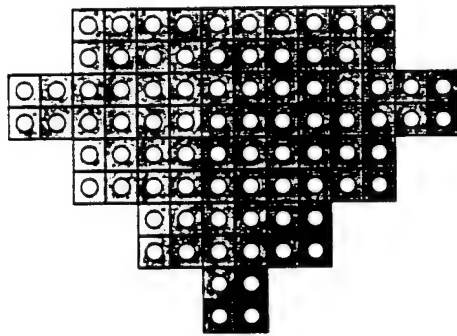
Figure 4.20: Histogram of the number of damaged particles as a function of straining.



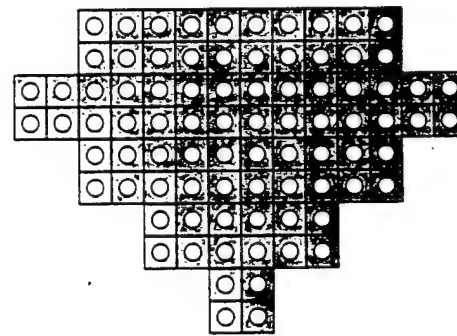
(a)



(b)



(c)



(d)

Figure 4.21: Macroscopic three level evolved mesh for the porous material at the end of the loading cycle, for (a) the larger RVE (ii) and (b) smaller RVE (i); The corresponding level-2 region with the (c) the larger RVE (ii) and (d) smaller RVE (i). Level-0 is with white elements, level-1 is with grey elements and level-2 is with black elements. 401

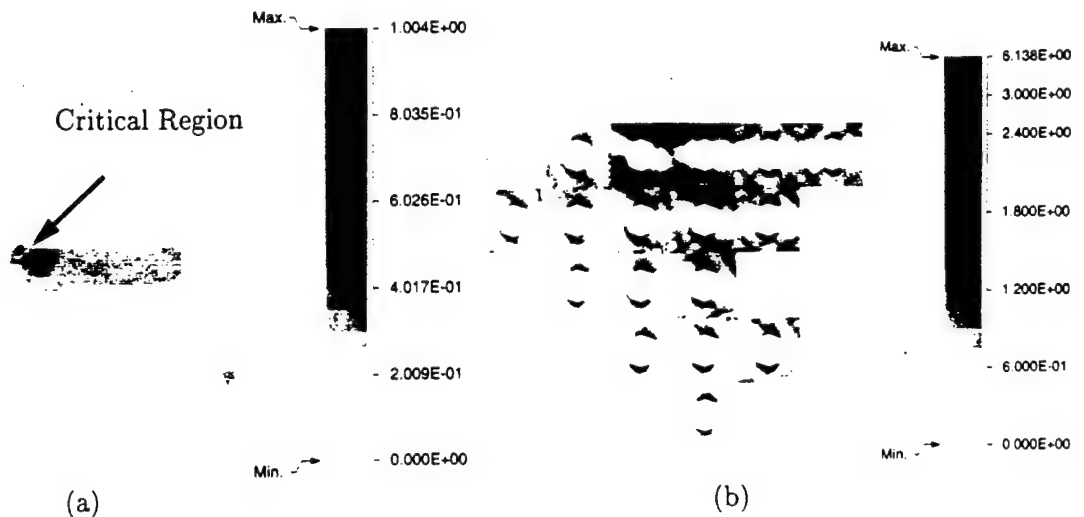


Figure 4.22: Contour plot of plastic strain $\bar{\epsilon}^p$ for the porous square plate: (a) the macroscopic averaged strain and (b) the level-2 microscopic strain at the critical region for the smaller RVE (ii) model.

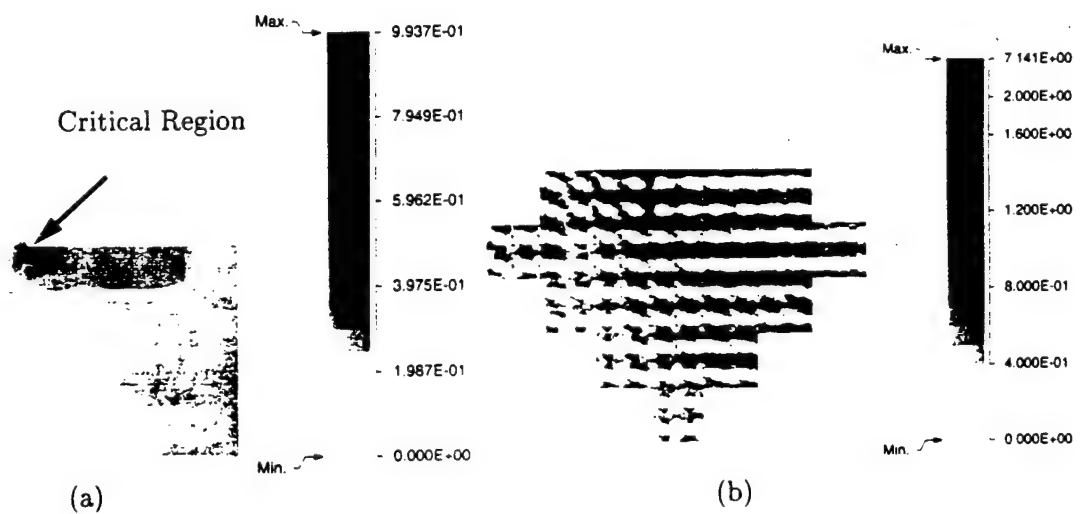


Figure 4.23: Contour plot of plastic strain $\bar{\epsilon}^p$ for the porous square plate: (a) the macroscopic averaged strain and (b) the level-2 microscopic strain at the critical region for the smaller RVE (i) model.

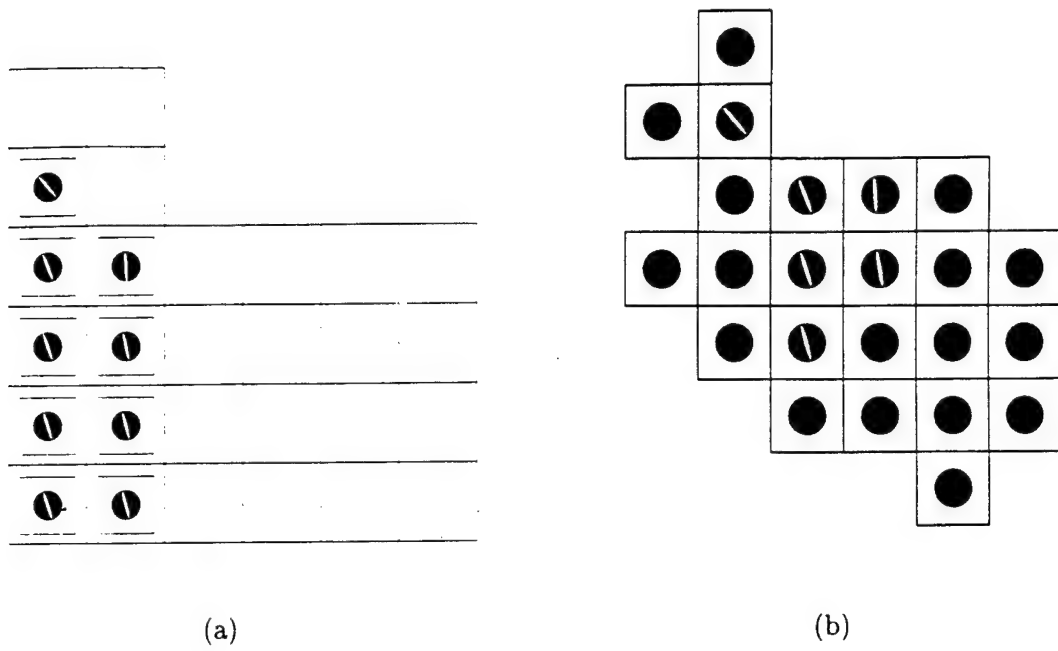


Figure 4.24: A comparison of the microstructural evolution near the inside corner by (a) complete level-1 analysis and (b) adaptive multi-level analysis.

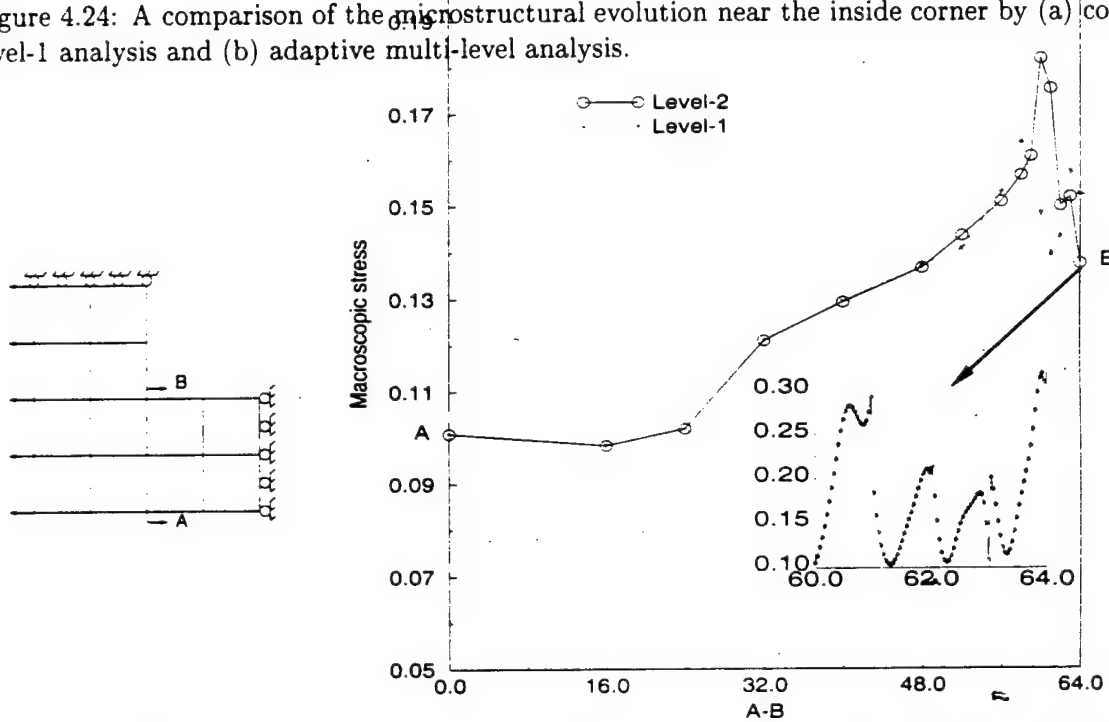


Figure 4.25: Comparison of macroscopic stress Σ_{xx} along section A-B by level-1 and multi-level analysis.

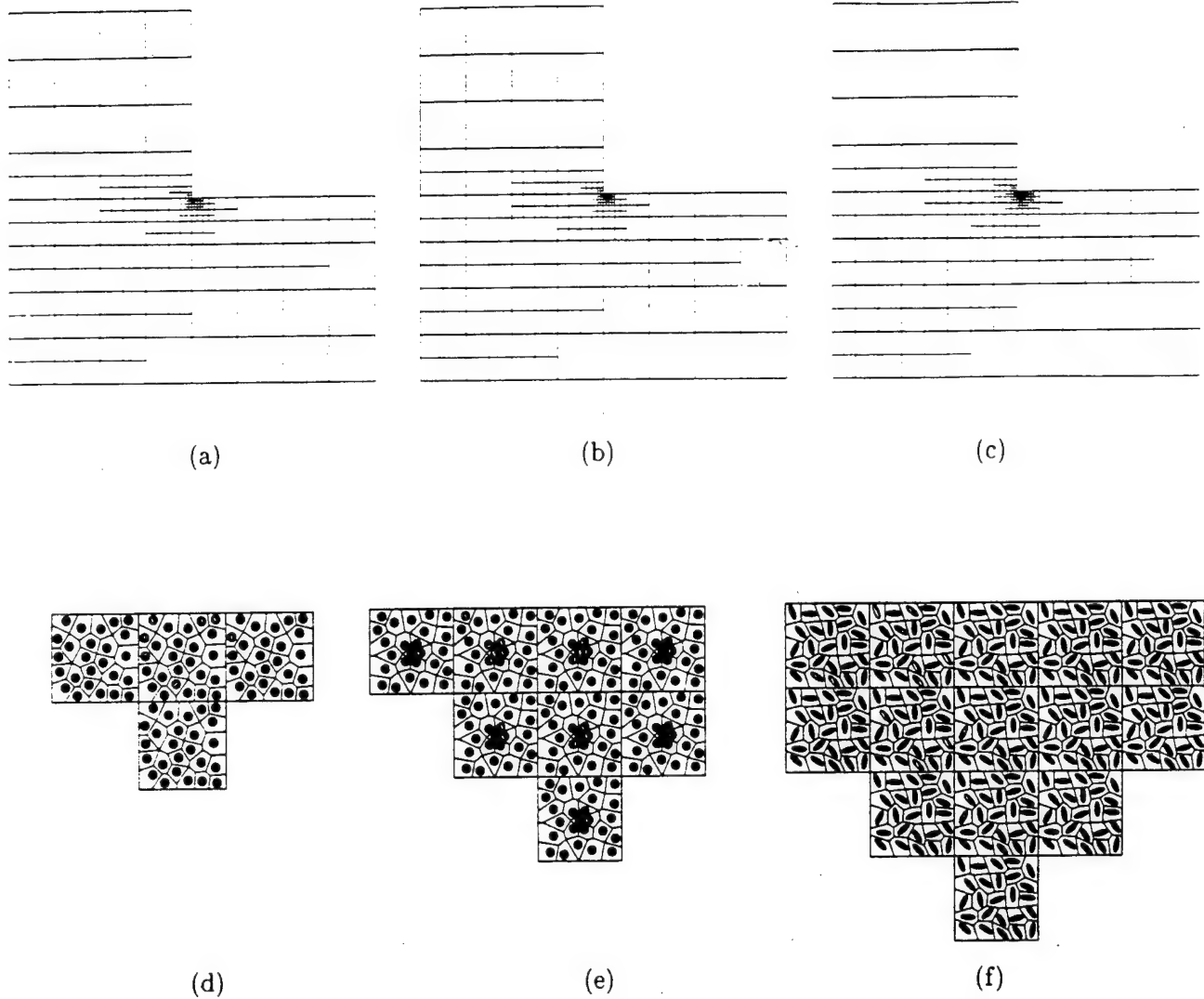


Figure 4.26: Macroscopic three level evolved mesh for the composite material at the end of the loading cycle for (a) hardcore distribution with circular particles, (b) clustered distribution with circular particles, and (c) hardcore distribution with elliptical particles; the corresponding level-2 microstructures for (d) hardcore (e) clustered and (f) elliptical RVE's.

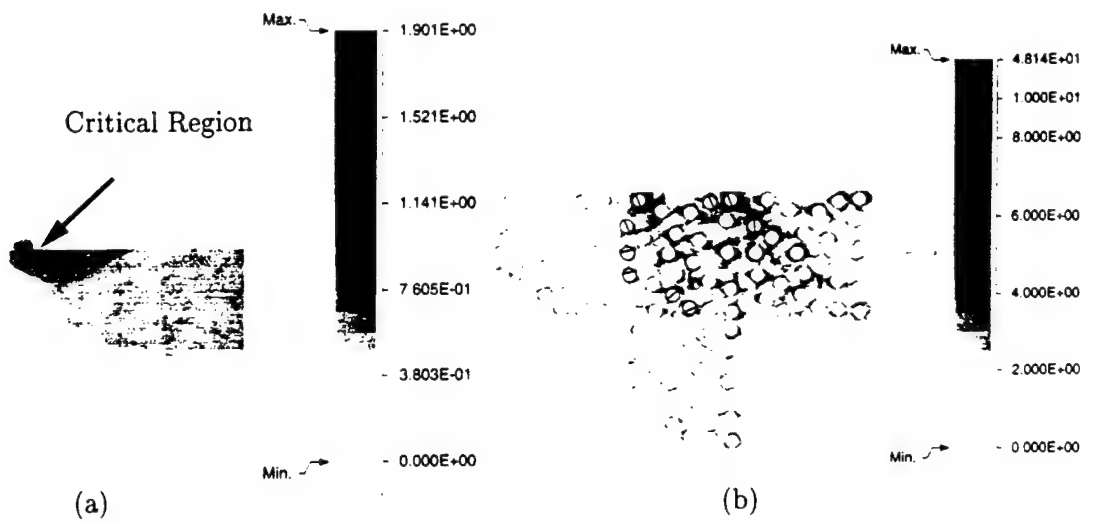


Figure 4.27: Contour plot of plastic strain $\bar{\epsilon}^p$ for the composite square plate: (a) the macroscopic averaged strain and (b) the level-2 microscopic strain at the critical region for the hardcore RVE model.

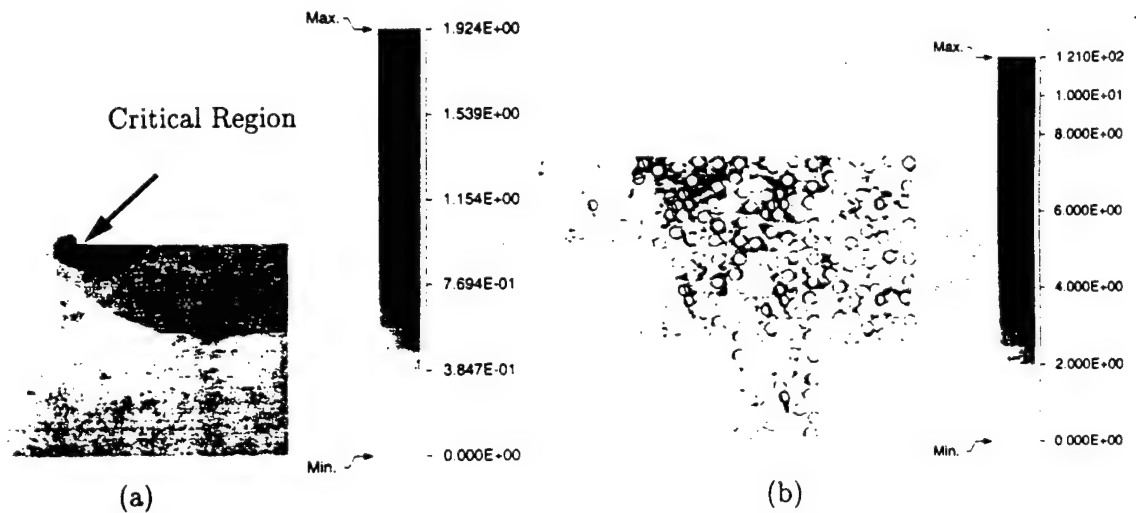


Figure 4.28: Contour plot of plastic strain $\bar{\epsilon}^p$ for the composite square plate: (a) the macroscopic averaged strain and (b) the level-2 microscopic strain at the critical region for the clustered RVE model.

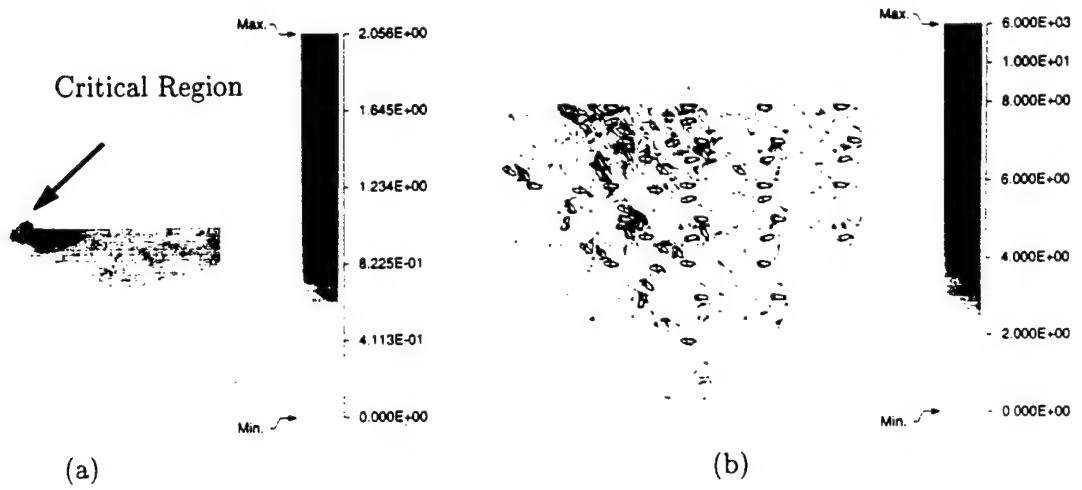


Figure 4.29: Contour plot of plastic strain $\bar{\epsilon}^p$ for the composite square plate: (a) the macroscopic averaged strain and (b) the level-2 microscopic strain at the critical region for the elliptical RVE model.

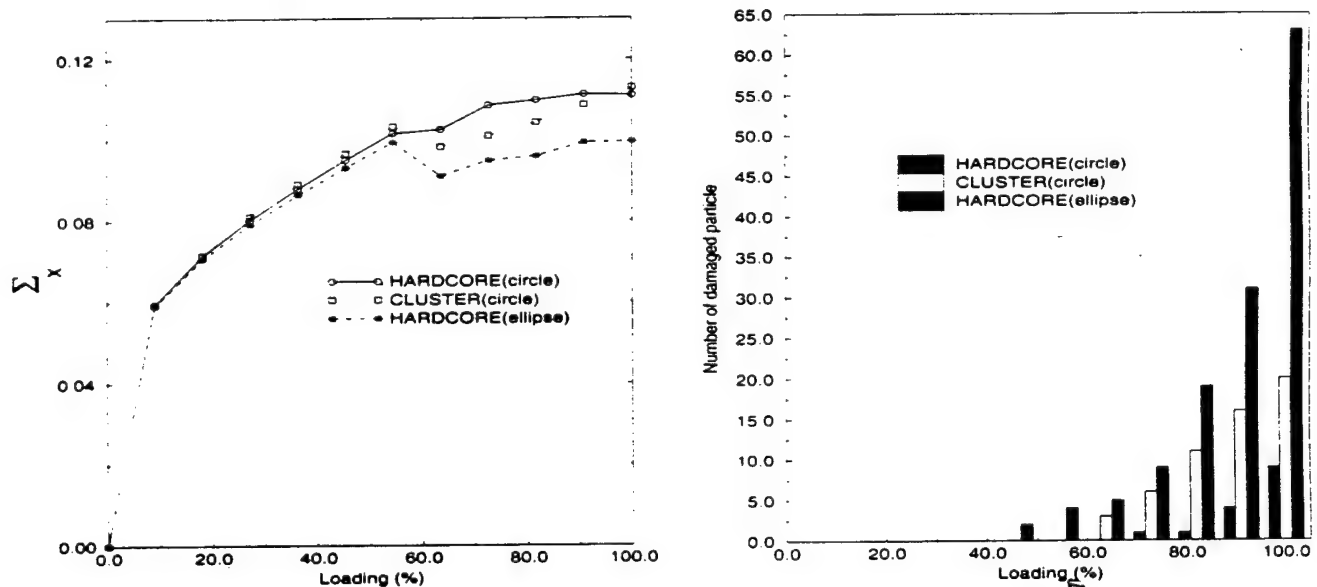


Figure 4.30: The evolution of (a) Σ_{xx} at the corner node of square hole and (b) the number of damaged particles for the three microstructures.

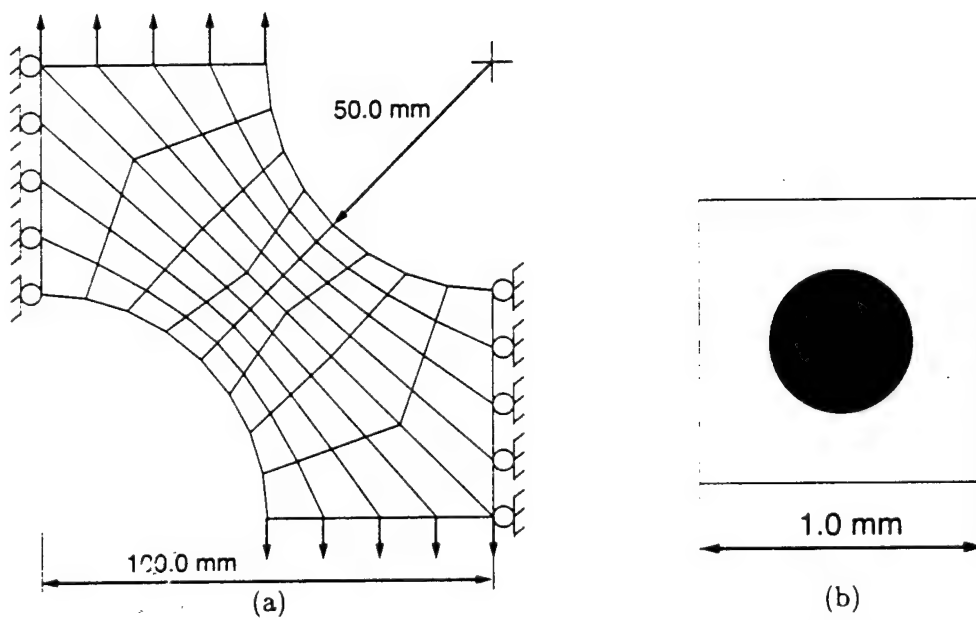


Figure 4.31: (a) Finite element model for a part of the composite plate with two circular holes and (b) the VCFE model of the microstructural composite RVE:

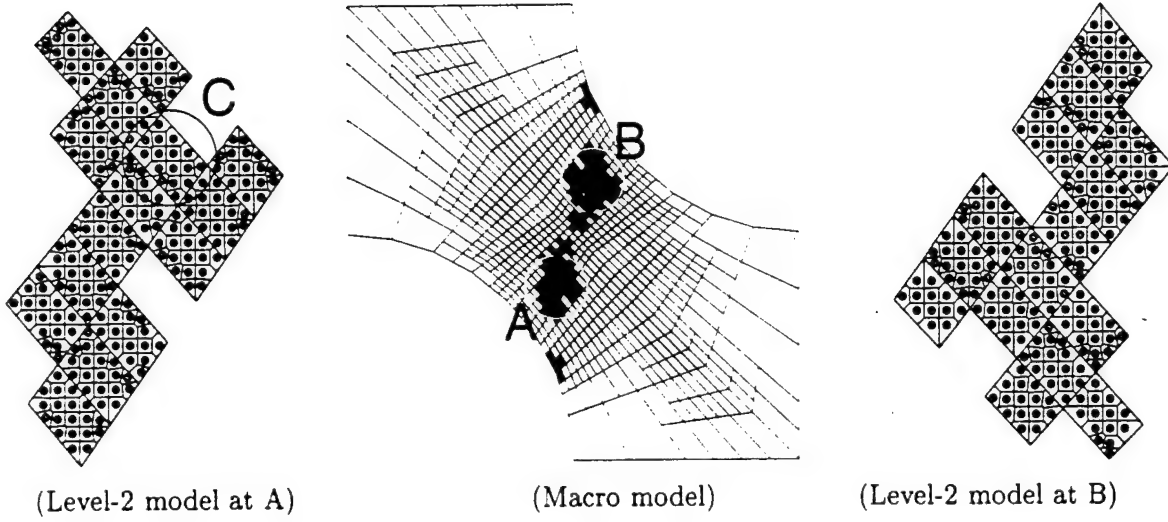


Figure 4.32: Macroscopic three level evolved mesh for the composite plate with two holes at the end of loading. The level-2 regions in the microstructure are shown at the two regions A and B.

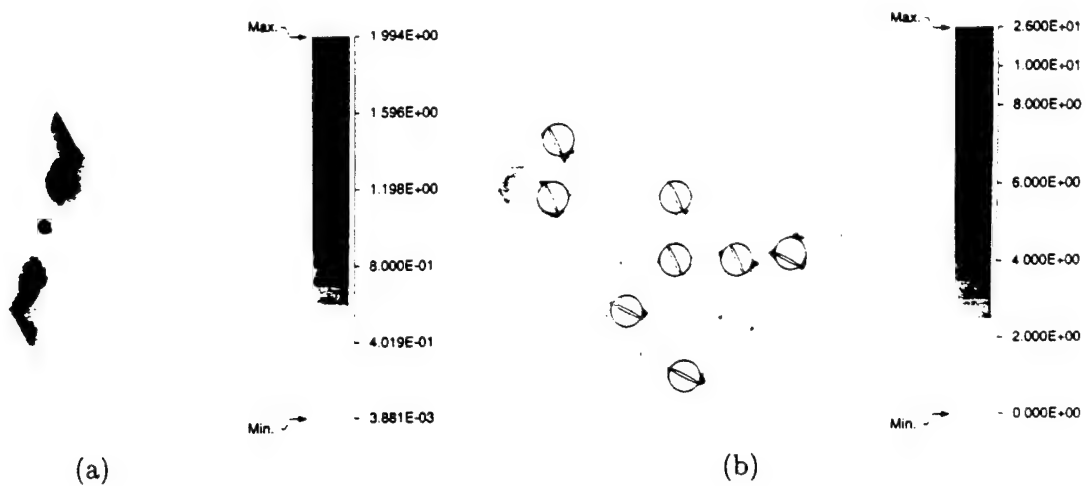


Figure 4.33: Contour plot of (a) the macroscopic plastic strain $\bar{\epsilon}^P$ and (b) level-2 microscopic plastic strain $\bar{\epsilon}^P$ at the region C of the microstructure in figure 4.32

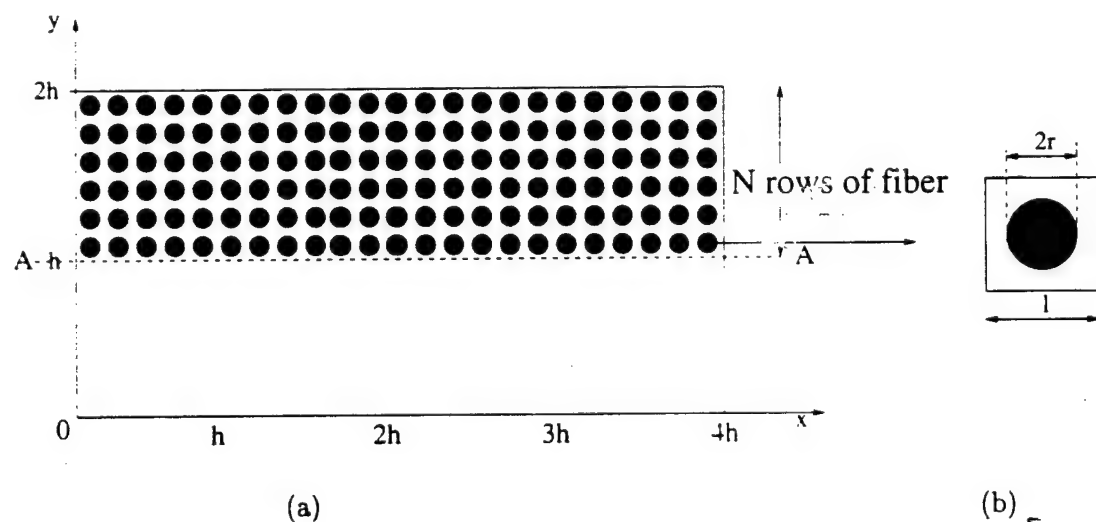


Figure 4.34: (a) A composite cross-section with n periodic layers of circular fibers, (b) a representative volume element for the effective medium theory calculations.

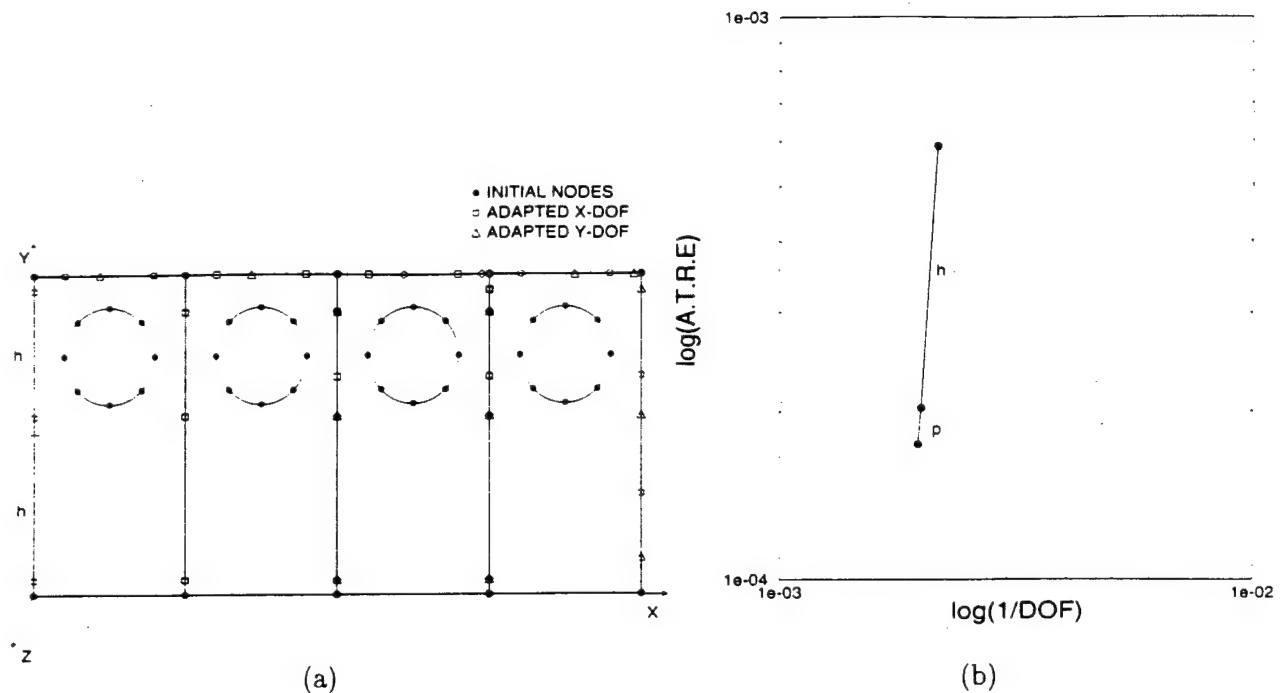


Figure 4.35: (a) A microstructural $h - p$ -adapted VCFEM mesh showing locations of the initial and added nodes with x - and y - D.O.F.; (b) solution convergence rate in terms of average traction reciprocity error (A.T.R.E.) as functions of inverse of effective modulus F .

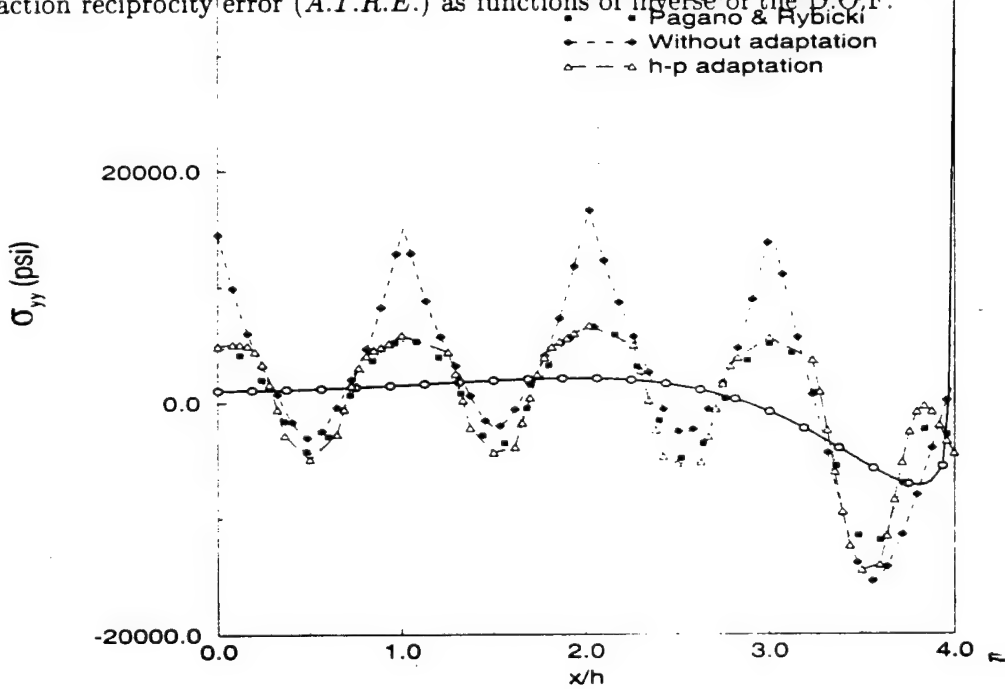
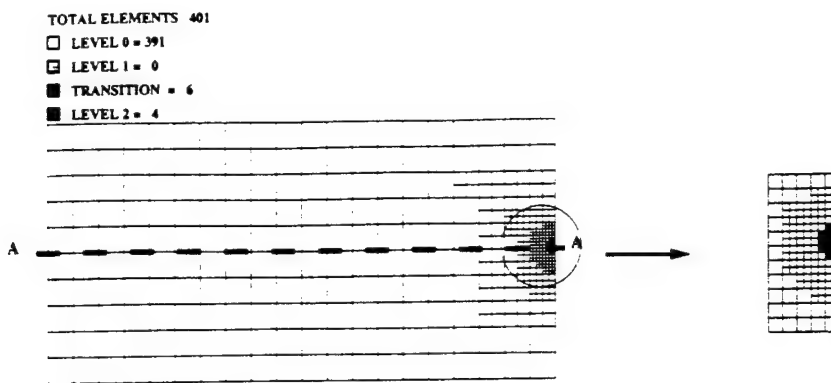
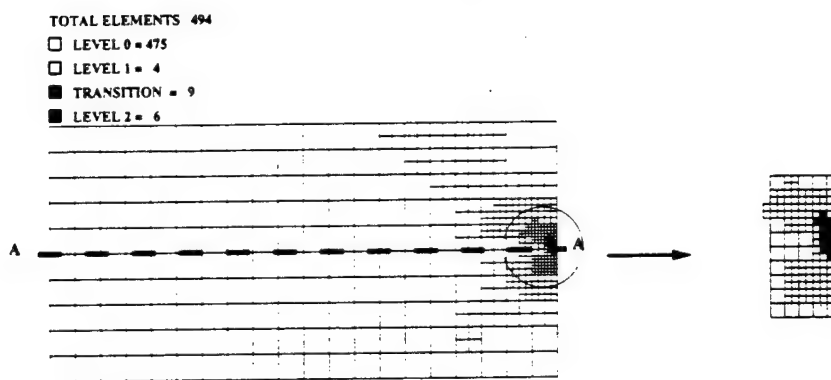


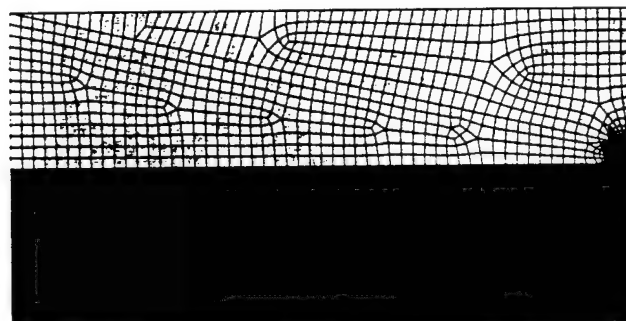
Figure 4.36: σ_{yy} distribution at section AA ($y=h$) for the composite section with 1 row of fiber



(a)

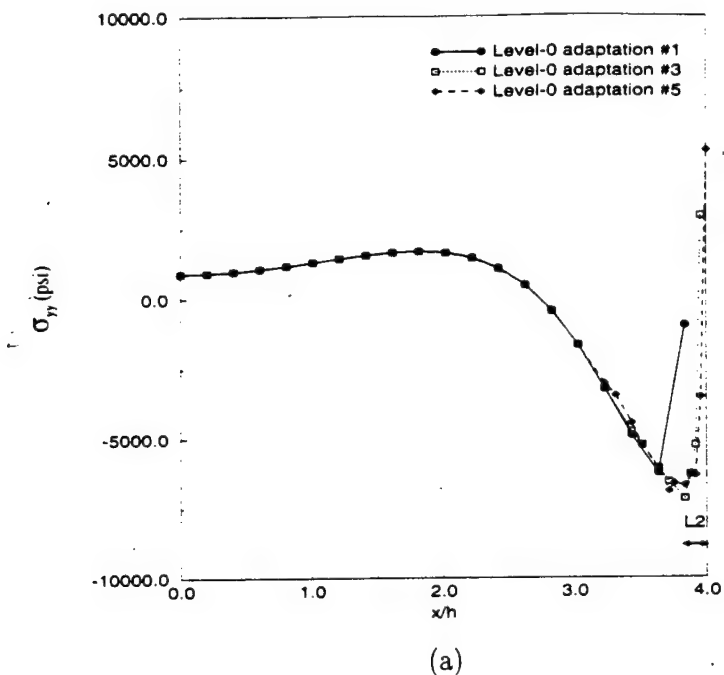


(b)

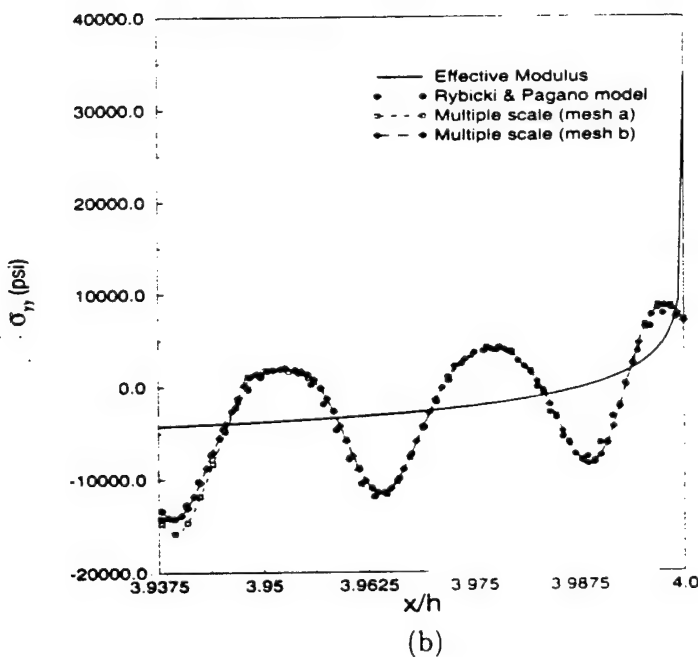


(c)

Figure 4.37: (a,b) H-adapted multi-level mesh showing level-0, level-1 and level-2 for two different parameters in transition criteria, and (c) a corresponding ANSYS mesh with detailed microstructure modeled near the free edge.



(a)



(b)

Figure 4.38: Convergence of stress σ_{yy} at the section A-A ($y = h$): (a) macroscopic stress plots using the homogenized moduli and level-0 elements, (b) microscopic level-2 stress plots near the critical free-edge region.

Chapter 5

Experimental-Computational Investigation Of Damage Evolution In Discontinuously Reinforced Aluminum Matrix Composite

5.1 Introduction

The commercial use of particle-reinforced metal matrix composites in automotive, aerospace and other engineering systems has increased in the last few decades due to their potentially superior mechanical properties, as well as their ability to reduce life-cycle costs through enhanced thermal stability and weight reduction. The property advantages of these materials are, however, often diminished by general degradation of failure properties like ductility and fracture toughness. Various experimental and numerical studies [1, 2, 3, 4, 5, 6, 7, 8, 9, 10] have been conducted to understand the influence of morphological factors such as volume fraction, size, shape and spatial distribution as well as constituent material and interface properties on the deformation and damage behavior. These studies have concluded that failure mechanisms are highly sensitive to local reinforcement distribution, morphology, size, interfacial strength etc.

Traditionally *unit cell* models [11, 12, 13, 14, 15] based on the finite element analysis have been used to predict the onset and growth of evolving damage in composite materials. While these models provide valuable insights into the microstructural damage processes, simple morphologies idealize actual microstructures for many engineering materials that bear little relationship to the actual stereographic features. These deficiencies have been circumvented in [16, 8, 17], where computational models of discontinuously reinforced materials with random spatial dispersion have been considered. Richmond and coworkers [18, 19] have investigated the effect of morphology on damage in composite, porous and polycrystalline materials by modeling actual geometries obtained from 2D micrographs. Using the Voronoi Cell finite element model, Ghosh et. al. [9, 10] have examined the effect of various spatial dispersions and particle shape and size on the damage initiation and

evolution process in ductile matrix composites.

Many characterization studies with 2-D microstructures e.g. [20, 21, 22, 23] have also been conducted to understand the relation between microstructural morphology and damage. Experimental research [25, 26, 27, 28, 29] has however pointed to the necessity of examining the full 3D characteristics for understanding the damage process. These studies infer that 2-D assessment can sometimes be misleading, especially in the presence of spatial clustering. Non-destructive evaluation methods, e.g. techniques based on ultrasonics e.g. [30], acoustic emission [4] and X-ray based computer tomography (CT) [31, 32] have emerged as potential methods for studying 3D damage. However many of these systems are thus far not capable of achieving spatial resolutions required to accurately capture microscopic particles and damage in the particle reinforced MMC's. Buffiere et. al [33] are developing a CT technology to yield tomographic images with a higher spatial resolution.

This work deals with a combined experimental-computational approach to study the evolution of microscopic damage to cause complete material failure in commercial SiC particle reinforced aluminum alloys or DRA's. Through a combination of 2D and 3D characterization and analysis models, it is intended to understand what aspects of microstructural morphology that are most critical for damage nucleation and evolution. Since it is difficult to identify the microcrack growth process once a material has failed completely, an interrupted testing technique is designed. Subsequently, sample microstructures in the severely necked region are microscopically examined in 3D using a serial sectioning method discussed in [24, 25, 26]. Computer simulated equivalent microstructures are tessellated into meshes of 2-D and 3-D Voronoi cells. Various characterization functions of geometric parameters are generated and a sensitivity analysis is conducted to explore the influence of morphological parameters on damage. 2D characterization functions are compared with 3D to evaluate the effectiveness of modeling the 2D micrographs. Modeling of the initiation and propagation of damage is conducted with Voronoi Cell Finite Element Method (VCFEM) [9, 10, 34, 35]. Each Voronoi cell element may consist of a matrix phase, an inclusion phase and a crack phase. Damage initiation by particle cracking is assumed to follow a maximum principal stress based Rankine criterion. The VCFEM for particle cracking has shown a significant promise in modeling large aggregates of heterogeneities. While the appropriateness of 3D analyses is recognized for this study, the 3D VCFEM (under development) does not currently have all necessary features. Due to enormous computing requirements of conventional 3D FEM models, various studies have resorted to simplified manifestations of complex geometries and properties e.g. [7, 41, 15]. This study is restricted to 2D in the form of VCFEM analyses of section micrographs. Finally, the effect of size and characteristic lengths of representative material element (RME) on the extent of damage in the model systems is also investigated.

5.2 Experiments for Damage Assessment

5.2.1 Interrupted tests

The material analyzed in this work is a discretely reinforced commercial aluminum that is fabricated by a powder metallurgy process [36]. It consists of extruded commercial X2080 aluminum alloy with 15% volume fraction SiC particles. The X2080 matrix has a nominal alloy composition with

weight percentages of 3.8% Cu, 1.8% Mg and 0.2% Zr, in addition to low impurity contents of Fe and Si. The precipitation hardened X2080 aluminum alloy system is naturally aged by heat treating for 4 hours at 930°F, followed by cold water quench and aging for 2 days at room temperature.

An important object in this failure study is to obtain adequate microstructural data that depict the growth of damage into a major failure path. In general, it is difficult to identify the dominant damage mechanisms and also the microcrack growth process, once a material has fractured completely. Thus an interrupted testing technique is designed where the load and deformation are halted in the material instability zone, following necking but prior to fracture. The tests assume that the major cracks are essentially prominent in this stage, and are helpful in understanding the linkage mechanism of microcracks or particle debonds to facilitate growth of the dominant damage. To initialize the testing, estimates of the necking and fracture strains are first obtained by observing the behavior of a tension test to failure. The uniaxial tension tests are executed on a MTS 810 material system with a HP 7044 X-Y recorder to monitor the loads and strains, and the critical strains are measured with a MTS 632.11 strain gauge extensometer. Following the initialization, strain controlled interrupted tests are carried out, in which the specimens are loaded to the instability region before the load is stopped.

Figure 5.1a shows a typical tension specimen for the naturally aged material. Data for six specimens of this material, viz. t1, t2, t3, t4, t5 and t6 are tabulated in table 1. The specimens t1, t2, t4 and t6 are obtained from the outer annulus region of the stock material while t3 and t5 are from the central core regions. The initialization of the test to study the entire material behavior and estimate the post-instability region is done with specimens t1 and t2. The material load-displacement curve is plotted in figure 5.1b, from which the necking strain is obtained from the peak load value. For the specimen t1, the test is conducted at a strain rate is $\dot{\epsilon} = 5 \times 10^{-4} \text{ sec}^{-1}$ and the necking strain and fracture strain are found to be $\epsilon_n = 9.15\%$ and $\epsilon_f = 9.40\%$ respectively. The short instability region in t1 prompts a reduced strain rate $\dot{\epsilon} = 3 \times 10^{-4} \text{ sec}^{-1}$ for specimen t2, for which $\epsilon_n = 9.05\%$ and $\epsilon_f = 9.20\%$.

In table 1, $\dot{\epsilon}$, ϵ_n and ϵ_f correspond to the strain rate, the necking strain and the interrupted strain respectively. The interrupted strain coincides with the fracture strain in the event that fracture precedes the load stoppage. This is indicated with F or I in the table. Load interruption is only possible for the specimens t3 and t6 due to the extremely short post-instability range of this material in comparison with the resolution of the loading mechanism. The necking strains for the specimens t1, t2, t4 and t6 are in the range of 9.00% ~ 9.30%, while those for specimens t3 and t5 are in the 9.80% ~ 10.20% range. This difference is possibly due to gradients created by the heat treatment at different locations in the stock material. The core cools slower and more uniformly than the surface. This results in the more uniform microstructure and larger necking and fracture strains for specimens (t3 and t5) located near the core of the stock material.

5.2.2 Damage examination and microscopic analysis

To examine the dependence of microstructural damage on the local morphology, serial sectioning of sample coupons extracted from the load-interrupted specimens t3 and t6, is invoked. This method, discussed in [24, 25, 26], involves gradual removal of material layers to obtain a series of scanning electron/optical micrographs, representing sections of a microstructure. It is a very

effective method for reconstructing 3D microstructures from a series of 2D sections of particulate reinforced composites, requiring a resolution of few microns. Prior to sectioning, locations are selected in figure 5.1a for cutting out the sample coupons. X-rays and acoustic microscopy with a AEROTECH UNIDEX 11 acoustic microscope with a resolution of about $50\mu m$ are used in this process to detect regions that contain major crack paths. Polished surfaces of these extracted samples are then examined by a Nikon optical microscope for major damage sites. For the specimen t3, shorter cracks passing through 2 ~ 3 particles at most are found. However, for the specimen t6, a larger crack passing through 5 ~ 6 particles is identified, and is consequently chosen for analysis. Coupons of approximate size $6\text{ mm} \times 6\text{ mm} \times 6\text{ mm}$ are subsequently prepared for the serial sectioning operation to sequentially expose parallel sections of the microstructure. As discussed in [24, 25, 26], parallel layers in a direction perpendicular to the straining direction (see figure 5.1a) are removed using a precision dimple grinder. The depth of material removal per step is selected such that each particle is sectioned at least once, ensuring that all particles of interest are adequately captured in the micrographs. For the DRA considered, the particle size range is approximately $3\text{-}25\mu m$, with an average size of $\sim 9.2\mu m$ and the standard deviation is $3.891\mu m$. The section to section step size is chosen to be $2\mu m$, corresponding to a total traversed thickness of $36\mu m$ for 18 sections. Two typical micrographs showing damage are depicted in figures 5.2, for which the horizontal corresponds to the loading direction. The micrographs are then serially stacked using a graphic software [37] to yield 3D microstructures as shown in figure 5.3a. The precise 3D location, shape, size and orientation of each particle can be obtained at a fairly high resolution by this method.

5.2.3 Major observations

The micrographs of serial sections 3 and 5 in figure 5.2, perpendicular to the middle plane of the tensile specimen, provide important information on the evolution of the dominant damage path in the material. A dominant damage path is clearly seen in the boxed regions. The damage size progressively diminishes with increasing sections, indicating the end of the cracked particles. The particle area fraction (AF), total number of particles (NP) and total number of cracked particles (NCP) for each section micrograph are presented in table 2. Generally speaking, sections with large AF and NCP are found to contain the larger cracks. The 3D image by assembling 2D micrographs in figure 5.3a also shows the dominant damage path in the boxed region.

From the microscopic observation results, it is found that for the naturally aged material, the main mode of damage is by particle cracking. Large particles in particle rich regions are more susceptible to cracking than those in particle sparse regions. Microcracks in the particle rich areas link up to form paths of dominant damage. The linkage and evolution of these larger cracks lead to the overall failure of the material. These paths are approximately perpendicular to the tensile loading direction. Thus, spatial distribution of particles plays a more important role in damage than particle size for this material.

5.3 Equivalent Microstructure & Mesh Generation

The actual 3D geometry of particles, as seen in figure 5.3a, can be quite complex and an exhaustive database is required to store all geometric details. To avert this, equivalent microstructures that closely approximate the actual morphology but are computationally less demanding, are generated. In this process, each particle and an associated crack are replaced by equivalent ellipses (in 2D) or ellipsoids (in 3D). This method economizes the image analysis and characterization process by way of well known geometric properties. For obtaining equivalent microstructures, digitized image data is first transferred into a binary format to distinguish between the particle, matrix and crack phases. The 0th (I_0), 1st (I_x, I_y) and 2nd (I_{xx}, I_{yy}) order geometric moments are then computed for each particle by adding contributions from each voxel (in 3D) or pixel (in 2D) that lies within the particle boundary. For 2D microstructures the computed moments are equated to the moment formulae for ellipses to evaluate the centroidal coordinates (x_c, y_c), half major and minor axis lengths (a, b), and orientation θ of the major axis from:

$$\begin{aligned} x_c &= \frac{I_y}{I_0}, \quad y_c = \frac{I_x}{I_0}, \quad a = \sqrt{\frac{1}{2}(C_1 + \sqrt{C_1^2 - 4C_2})}, \quad b = \sqrt{\frac{1}{2}(C_1 - \sqrt{C_1^2 - 4C_2})} \\ \theta &= \frac{1}{2}\cos^{-1}\left(\frac{4}{a^2 - b^2}\right)\left(\frac{I_{yy} - I_{xx}}{I_0} - \frac{I_y^2 - I_x^2}{I_0^2}\right) \end{aligned} \quad (5.1)$$

where $C_1 = 4 * \left(\frac{I_{xx} + I_{yy}}{I_0} - \frac{I_x^2 + I_y^2}{I_0^2}\right)$ and $C_2 = \frac{I_0^2}{\pi^2}$. For 3D microstructures, the centroidal coordinates (x_c, y_c, z_c) of the equivalent ellipsoid are first evaluated from the 0th and 1st order moments as: $x_c = \frac{I_y}{I_0}, \quad y_c = \frac{I_x}{I_0}, \quad z_c = \frac{I_z}{I_0}$. The principal directions (or orientations of the three axes) for the ellipsoids are obtained from the eigen-values of the 2nd order moments I_{ij} ($i = 1..3, j = 1..3$). The major (2a), intermediate (2b) and minor (2c) axes of the equivalent ellipsoids are then obtained from the principal moments I_1, I_2, I_3 as:

$$a = \sqrt{\frac{5}{I_0}(I_2 + I_3 - I_1)}, \quad b = \sqrt{\frac{5}{I_0}(I_1 + I_3 - I_2)}, \quad c = \sqrt{\frac{5}{I_0}(I_1 + I_2 - I_3)} \quad (5.2)$$

A simulated 3D microstructure with particles (grey) and cracks (black) is shown in figure 5.3b. The microstructures are then tessellated into a mesh of 2D and 3D Voronoi cells, by surface based algorithms detailed in [25, 26]. In figure 5.3c, the mesh of Voronoi cells is created based on the morphology of particles, while in figure 5.3d the mesh is due to tessellation based on the geometry of particle cracks. Tessellation into a mesh of Voronoi cells plays an important role in developing geometric descriptors for quantitative characterization. They represent regions of immediate influence for each heterogeneity and also define neighbor of each heterogeneity from individual faces or edges of the Voronoi cells. This facilitates easy evaluation of parameters like local area fractions, near neighbor and nearest neighbor distances and orientations.

5.4 Microstructure and Damage Characterization

The morphology of particles and associated damage or microcracks can be characterized by various functions of size, shape, orientation and spatial distribution. A number of these classifier functions

have been used by the authors and others in [24, 25, 26, 34, 35, 20, 21, 22, 6] to characterize various aspects of microstructural morphology. In this section, some of these functions are considered for the 3D microstructure and 2D micrographs to investigate the relation between morphological characteristics and the path of dominant damage in the material. The specimen t6 with a large microcrack is considered for this study.

In the first exercise, a sensitivity analysis is done with the simulated 3D microstructure in figure 5.3b to reveal the dependence of damage on microstructural variables. Two damage parameters, viz. the number fraction of cracked particles (nf) and the volume fraction of cracked particles (vf) are chosen to manifest the damage level in the DRA. Six microstructural parameters are considered, viz. (i) particle equivalent size (diameter); (ii) nearest neighbor distance computed as the distance between particles that share a common Voronoi cell edge; (iii) local volume fraction measured as a ratio of the particle size to that of the associated Voronoi cell; (iv) particle shape or ellipsoid aspect ratio; (v) nearest neighbor orientation, measured as the angle between a line joining the centers of particle and its nearest neighbor, and the loading direction; and (vi) particle orientation with respect to the loading direction. The cracked particle fractions are plotted as functions of these parameters in figure 5.4. A linear interpolation, obtained by a least square fit, yields the corresponding overall gradient or slope.

While both the nf and vf plots coincide for the particle size plot (i), large differences are noted for nearest neighbor distances (ii) and aspect ratios (iv). Largest slopes of these plots are observed with particle size, nearest neighbor distance and local volume fraction. This infers that the strongest influence on particle cracking comes from the size and local spatial distribution. Particle shape has a relatively smaller effect on damage initiation. Sensitivity of damage to particle orientation and nearest neighbor orientation is found to be minimal for this material.

The characteristics of particles forming the dominant damage path (within the marked box in 5.3a) are compared with those for all cracked particles in the histograms of figure 5.5. The dotted lines correspond to all cracked particles while the shaded areas are for cracked particles in the dominant damage region only. The histograms are with respect to three variables that are found to play important roles in the damage process, viz. the particle size, nearest neighbor distance and orientation with respect to the loading direction. While the range of sizes for all cracked particles is $4 \sim 13\mu m$, that for the particles forming the dominant damage path is $5.7 \sim 13\mu m$. This reveals that larger particles generally contribute to dominant damage path. The plot for nearest neighbor clearly exhibits the influence of particle rich areas (clustering or alignment) on the preferential growth of damage. The nearest neighbor distance for particles in the dominant damage path are in the range $0.4 \sim 3.7\mu m$ when compared with the range $0.4 \sim 12.3\mu m$ for all cracked particles. The histogram of cracked particles as a function of the orientation with respect to the loading direction reveals that particles with major axis along the loading direction (0° and 180°) are generally susceptible to cracking. This is much more pervasive for particles in the dominant damage path, due to the smaller cross-sectional areas normal to loading. In conclusion, particles in the dominant damage path generally have larger size, are in particle rich areas, and are oriented in loading direction.

Finally, it is of interest to identify discriminating characteristics of 2D micrographs that may be helpful in making dominant damage predictions for the actual 3D microstructures. Two repre-

sentative micrographs, viz. section 1 which contains a dominant damage and section 14 without any dominant damage, but only scattered particle cracks are compared with the 3D microregion. Four important characterization functions viz. (a) the probability density function of particle equivalent size (diameter), (b) the probability density function of the nearest neighbor distance, (c) the probability density function of the local area/volume fraction and (d) a transformation function $L(r)$ of a second order intensity function $K(r)$, are plotted in figure 5.6 for 2D and 3D micrographs. The second order intensity function $K(r)$ and its transformed functions ($L(r) = (\frac{K(r)}{\pi})^{\frac{1}{2}}$ in 2D, and $L(r) = (\frac{3}{4\pi}K(r))^{\frac{1}{3}}$ in 3D) capture second order statistics of spatial distributions are used as a graphical tool for detecting departures from a homogeneous Poisson process [34, 35, 25, 26]. The plot of $L(r)$ vs. r is a 45° straight line for a pure Poisson distribution.

The plots distinctly reveal a few important features of the micrographs. The particle size distribution for the two 2D micrographs are similar and the tails are significantly shorter than 3D. As is expected, 3D particle sizes are larger than 2D particle section sizes due to sectioning along non-principal planes. However the probabilities of both the nearest neighbor distances and local area fractions in figures 5.6b and c yield a distinguishing characteristic. The micrograph with dominant damage has peaks and valleys, as well as tails that are very similar to that for 3D. The peaks which reflect particle rich regions and the tails which reflect sparse areas are both found to be important discriminants. Deviation from the $L(r) = r$ function or the 45° line represents a bias towards clustering. The section with the dominant damage has a larger deviation from the random distribution in comparison with the section without major cracking, and is closer to the 3D response. In summary, it may be concluded that when analyzing 2D sections, the likelihood of better representation of dominant damage are for those sections that have higher peaks at lower near neighbor distances with longer tails and have higher deviation from the Poisson distribution. Similar observations have also been made in [5, 1, 38, 29].

5.5 Damage Simulation by Voronoi Cell FEM

Two dimensional plane strain/stress simulations of the microstructural damage evolution is conducted by the Voronoi cell finite element model (VCFEM) described in [9, 10, 34, 35]. The current 2D VCFEM only accommodates particle cracking, and hence matrix cracking is ignored in the simulations. The simulations are useful in understanding the damage evolution process by a sequence of particle cracking. Rectangular $195\mu\text{m} \times 155.018\mu\text{m}$ micrographs as shown in figure 5.8a,b are analyzed with monotonically increasing strains. Periodicity boundary conditions are imposed by requiring edges to remain straight and parallel to the original direction throughout deformation as:

$$\begin{aligned} u_x &= 0 \text{ (on } x = 0\text{)} , u_y = 0 \text{ (on } y = 0\text{)} , u_x = u_{ap} \text{ (on } x = L_x\text{)} , u_y = D_y^* \text{ (on } y = L_y\text{)} \\ T_y &= 0 \text{ (on } x = 0/L_x\text{)} , T_x = 0 \text{ (on } y = 0/L_y\text{)} \end{aligned} \quad (5.3)$$

where u_{ap} is an applied displacement and D_y^* is determined from the average force condition $\int_X T_x dx = 0$ on $y = L_y$. The reinforcing phase of SiC particles are assumed to be brittle and is modeled with the linear elastic properties: Young's modulus $E = 427$ GPa, Poisson's ratio $\nu = 0.17$. The aluminum matrix material is assumed to be ductile and is modeled by small deformation isotropic hardening J_2 elasto-plasticity theory with properties: Young's modulus $E = 72$

GPa, Poisson's ratio $\nu = 0.33$ and the post yield elastic-plastic behavior is obtained from [39] as shown in figure 5.7. Microstructural damage by particle cracking is assumed to be governed by a maximum principal stress or Rankine criterion. In this criterion, a crack is initiated when the maximum principal stress in tension exceeds a critical fracture stress σ_{cr} at a point. The crack is oriented at right angle to the principal stress direction. The critical stress σ_{cr} is also influenced by the particle size due to the existence of microcracks. To account for the size effect in σ_{cr} , a Weibull distribution based criterion is used, where the probability of particle fracture $P_f(A, \sigma)$ is related to the particle volume/area v and the maximum principal stress σ_I as:

$$P_f(v, \sigma_I) = 1 - \exp\left[-v\left(\frac{\sigma_I}{\sigma_0}\right)^m\right] \quad (5.4)$$

where σ_0 and m are two material parameters in the Weibull distribution that are calibrated from experiments.

5.5.1 Calibration of Weibull parameters σ_0 and m

In the two parameter Weibull model, the fraction of fractured particles may be obtained (see [41, 42, 26]) from a known probability distribution of particle volumes $p(v)$, as:

$$\rho(v) = \int_{V_{min}}^{V_{max}} p(v) P_f(v, \sigma_I) dv \approx \sum_{i=1}^N p(v_i) \left(1 - \exp\left[-\frac{v_i}{v_0} \left(\frac{\sigma_I^i}{\sigma_0}\right)^m\right]\right) \Delta v_i \quad (5.5)$$

where $p(v_i)$ is the probability density distribution of particle volume/area v_i . The entire area is divided into N intervals such that $\Delta v_i = v_i - v_{i-1}$, σ_I^i is the average particle maximum principal stress for particles with size in the range of $[v_{i-1}, v_i]$ and v_0 is a reference area taken to be the average area. The fraction of cracked particles ρ is readily obtained from the experimental micrographs. Again, the section micrographs 2, 8 and 14 are used to calibrate the Weibull parameters. The fractions of cracked particles and the average particle area for these three sections are 31.78%, 24.76%, 28.57% and 53.43, 48.91 and 52.67 μm^2 respectively. The maximum principal stress σ_I^i for each particle is obtained from VCFEM simulation prior to the onset of particle cracking at a true strain of $\epsilon = 8.88\%$. From the experimental observations it is assumed that no major damage has initiated at this strain. The Weibull parameter m is assumed to take integer values between 1 and 8 following [42, 26] and the corresponding values of σ_0 are given in table 3.

The Weibull parameters are also calibrated using a 3D ABAQUS model simulation of a cubic unit cell with a single, 15% volume fraction, spherical particle as described in [26]. The 1x1x1 unit cell model has a particle of radius $R = 0.66$. A modified form of equation 5.5 is used to account for the shape variability of the particles as

$$\rho(\alpha, v) = \int_{\alpha_{min}}^{\alpha_{max}} \int_{V_{min}}^{V_{max}} p(\alpha)p(v) P_f(v, \sigma_I) dv \quad (5.6)$$

where α corresponds to the particle aspect ratio. The particle size and shape distribution functions $p(v)$ and $p(\alpha)$ are calculated from the computer simulated representation of the actual 3D microstructure shown in figure 5.3. This average particle volume and the fraction of cracked particle

are directly computed from figure 5.3 as $\bar{v} = 642.0 \mu\text{m}^3$ and $\rho = 45.48\%$. The average particle stress at a macroscopic strain $\epsilon = 8.88\%$ is obtained from the ABAQUS simulation as $\sigma_p = 862.60 \text{ MPa}$. Results of calibration with and without shape effects are documented in table 3. It is found that the best agreement in σ_0 for all 2D sections and 3D is obtained for m between 4 and 5. Consequently the parameter is chosen to be $m = 4.2$. The corresponding value of σ_0 for section 2 is 3.04 GPa , for section 8 is 3.19 GPa , for section 14 is 2.79 GPa and the average of these sections is $\sigma_0 = 3.01 \text{ GPa}$.

Results of VCFEM analysis of the simulated micrographs of sections 1, 3, 5 and 9 are provided in table 4. The number of cracked particles at a macroscopic strain of 8.88% by VCFEM are compared with experimental results. While the general agreement is quite good, it is seen that the concurrence is particularly favorable when the simulation is conducted with a σ_0 that is obtained from a section that is near to the one being analyzed. For example, the results of sections 1 and 3 are very good when $\sigma_0 = 3.01 \text{ GPa}$, which is obtained from section 2. This concurrence may be attributed to the similarity in the distribution of heterogeneities in neighboring sections, and suggests that spatial distribution has a strong effect on the Weibull parameters.

Microscopic Damage Analysis

Various results for section 1 which contain a dominant damage path are generated by VCFEM simulation and compared with experimental observations in this section. The macroscopic stress-strain plot for plane strain and plane stress assumptions are compared with experimental results in figure 5.7a. The overall yield strength is better predicted by the plane stress model. However, the post yield behavior with plane strain conditions is much closer to the experimental results. The initial higher yield strength is expected with plane strain due to the plastic constraint caused by the $\epsilon_z = 0$ condition. A shifted stress-strain plot (modified plane strain VCFEM result in figure 5.7a) where the stresses are reduced by the initial difference in yield stress shows a very good match between experiments and simulation. Thus plane strain assumptions are used in subsequent computations. Figure 5.7b is intended to predict the onset of plastic instability by the model and compare it with actual fracture observed in the experiments. The use of the Considere criterion to predict the onset of plastic instability has been suggested by Llorca [2, 41] in the absence of dilatational strain associated with reinforcement fracture. In this criterion, the average stress $\bar{\sigma}$ is related to the strain hardening rate $\frac{d\bar{\sigma}}{d\epsilon}$ as

$$\bar{\sigma} = \frac{d\bar{\sigma}}{d\epsilon} \quad (5.7)$$

The strain derived from this relation corresponds to the lower bound of the tensile ductility since it controls the composite load bearing capacity. Three sets of curves are plotted in the figure 5.7b corresponding to the matrix material, the VCFEM results in plane strain and the experimental results. It is seen that the Considere criterion (junction of the two curves) predicts the experimental point corresponding to the onset of fracture rather well. Additionally the 2D prediction of the plane strain simulation is also quite good and can be used with reasonable confidence. \approx

Microstructural results of the simulation are compared with experiments in figure 5.8. The computed micrograph with evolved damage for section 1 is compared with the experimental micrograph at 8.88% strain in figure 5.8a and b. The damaged particles are shown with the contained

crack. Most damaged particles in the simulation coincide with the experimental results, with the box indicating the dominant damage path. The damage path is approximately perpendicular to the tensile loading direction. Figure 5.8b also shows the contour plot of effective plastic strain in the ductile matrix and indicates the path of damage linkage. The plastic strain is higher and localized between cracked particles and this is expected to cause matrix cracking. The number fraction of cracked particles in different size ranges are plotted in figure 5.8c. Very good agreement is seen between simulation and experimental results. Figure 5.8d is a contour plot of the particle fracture probability at 8.88% strain. The black shade corresponds to the highest probability and fractured particles are illustrated in white with a crack. Similar plots (not shown) at earlier stages of deformation show that several particles with higher probability at the smaller strain have cracked with deformation. The number fraction of cracked particles as a function of straining are plotted for sections 1, 5 and 9 together with the experimental observation in figure 5.9. At lower strains the number fraction of cracked particles for sections 1 and 5 with particle rich regions are higher than that for section 9. This is due to higher stress concentrations particle rich areas that are enough to fracture some particles even at low strains. With increasing strains more particles start to crack in the section 9 and exceeds that for section 5 which has less particles in the clustered regions. The 2D simulations however exhibit less cracked particles than that in the actual 3D microstructure.

5.6 Characteristic Size of Microstructures

The influence region of local morphology on the mechanical response is characterized by a microstructural representative material element (RME) that is critical in delineating length scales. The RME depicts a region which is assumed to be representative of the entire microstructure. Functions that distinguish between variations in stress/strain distributions for local disturbances in microstructural patterns can provide important insight on microstructure-property relations. Marked correlation functions, discussed in [22, 10, 35, 26] for multivariate characterization of patterns, are evaluated to characterize length scales or RME size in the presence of damage. A mark may be identified with an appropriate microstructural variables, e.g. in this case a variable that related to quantification of damage. The marked correlation function for a heterogeneous domain W of volume V containing N heterogeneities is mathematically expressed as [22, 23, 10]:

$$M(r) = \frac{[\frac{dH(r)}{dr}]/(4\pi r^2)}{g(r)}; \quad H(r) = \frac{1}{m^2 N^2} \sum_{i=1}^N \sum_{k=1}^{k^i} m_i m_k(r) \quad \text{and} \quad g(r) = \frac{1}{4\pi r^2} \frac{dK(r)}{dr} \quad (5.8)$$

where $K(r)$ is the second order intensity function defined in [34, 35], $g(r)$ is the pair distribution function and $H(r)$ is the mark intensity function. The $H(r)$ function reduces to the $K(r)$ function if all heterogeneities have the same mark. A mark associated with the i^{th} heterogeneity is denoted as m_i . k^i is the number of heterogeneities which have their centers within a sphere of radius r around i^{th} heterogeneity, for which the mark is m_k , and m is the mean of all marks. By definition $M(r)$ establishes a relation between the location and associated variables for heterogeneities. Two marks are considered in this study. The first corresponds to particle cracks and are designated as $m_i = 1$ for a cracked particle and $m_i = 2$ for an intact particle. The second corresponds to the probability

of particle fracture, which signifies the propensity to advance the microstructural damage state. The $M(r)$ function statistically stabilizes at near-unit values at a distance r_{inter} at which the local morphology ceases to have any significant influence on evolving variable. Values of $M(r) > 1$ show positive correlation, while $M(r) < 1$ indicates repulsion between marks. This distance r_{inter} is an indication of the physical range of interaction and is significant in making decisions about length scales and the RME size.

The marked correlation functions corresponding to cracked particles and probability of fracture, are plotted in figures 5.11a and b from the simulation of the entire micrograph of section 1 (termed as RME 0) with dimensions $195\mu m \times 155\mu m$. The dotted line corresponds to the unit $M(r)$ for uniform distribution of spherical heterogeneities with identical marks. Contour plots of the equivalent plastic strain in the simulated micrograph with cracked particles are shown in figure 5.10a. The particle area fraction for this micrograph 18.37% and the total number of particles and cracked particles are 105 and 34 respectively. The plots are made with only upto 40% of the entire micrograph, or $80\mu m$ to avoid boundary effects in $M(r)$. The $M(r)$ functions in both figures approximately stabilize at near-unit values at a distance r_{inter} of about $60 \mu m$. At this distance, the local morphology is expected to have a significantly reduced influence on the evolving variables. The slower attenuation of $M(r)$ for particle fracture at shorter range indicates the strong effect of the local morphology on damage evolution. Next, a smaller region (RME 1) is selected for damage simulation corresponding to the stabilized region in the $M(r)$ plots. Since the stable region is $60\mu m$, the dimension of the micrograph is chosen to be $150\mu m \times 155\mu m$, incorporating the scaling factor, i.e. $\frac{60}{4} = 150$. This is shown with the box in figure 5.10a. Again the contour plots of plastic strain with cracked particles by VCFEM simulation are shown in figure 5.10b.. The dominant crack behavior is quite similar to that for RME 0, even though there is some difference near the boundary. Also the plastic strain contours and limiting values are similar. The particle area fraction for RME 1 is 18.13% with the total number of particles and cracked particles at 84 and 28 respectively. The $M(r)$ plots in figure 5.11c and d show that the functions may still be assumed to stabilize at around $60\mu m$. A smaller subset (RME 2), with dimensions $116\mu m \times 115\mu m$ is next simulated and the plastic strain is depicted in figure 5.10c. Significantly different plastic strains and cracking pattern is observed for this microstructure. The particle area fraction for this micrograph is 18.68% with a total of 51 particles of which 18 are cracked. The plots of $M(r)$ function do not stabilize in the domain of the simulation window. Through this analysis the size effect of microstructure, needed for adequate representation and analysis in the presence of evolving damage is demonstrated.

5.7 Conclusions

In this work, a combination of experimental and computational methods are utilized to characterize and understand the evolution of microscopic damage that cause failure in naturally aged commercial SiC particle reinforced DRA's. The main mode of damage for the naturally aged material is found to be particle cracking. Larger particles in particle rich regions are more susceptible to cracking than those in particle sparse regions. Spatial distribution of particles plays a more important role in damage than particle size for this material. A sensitivity analysis with respect to microstructural

parameters infers that the strongest influence on particle cracking comes from the size and local spatial distribution. Particle shape, orientation and nearest neighbor orientation have relatively smaller effect on damage initiation. Histograms of particles forming the dominant damage path in comparison with all cracked particles reveal that larger particles oriented in loading direction and in relatively rich areas are more susceptible to contribute to a dominant crack in the microstructure. In an attempt to identify discriminating characteristics of 2D micrographs that may be of helpful in making dominant damage predictions for the actual 3D microstructures, probability density functions of particle size nearest neighbor distance, and second order intensity function $K(r)$ of spatial distribution are plotted. Better representation of damage is possible with those sections that have higher peaks at lower near neighbor distances and longer tails, as well as have propensity towards clustering.

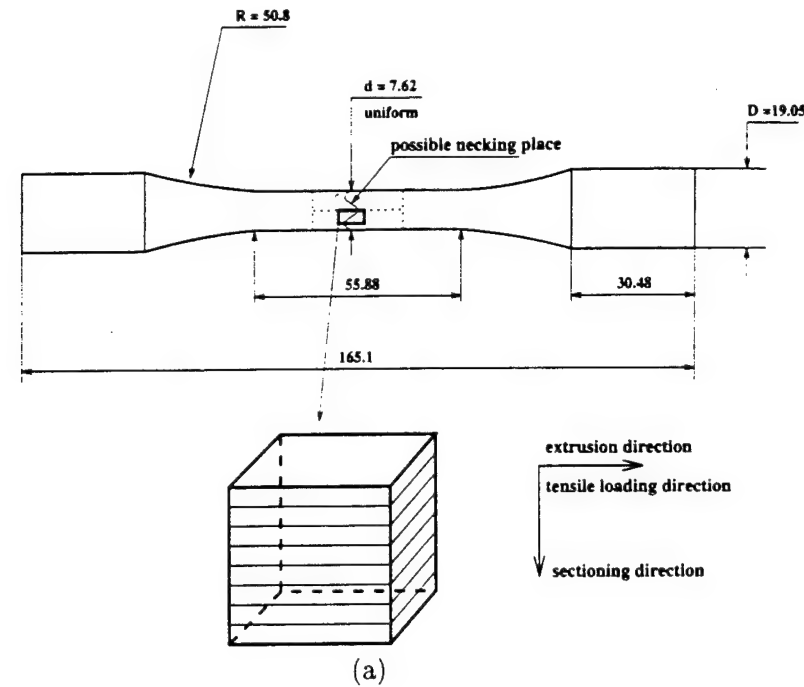
Next the two dimensional Voronoi cell finite element model is used to simulate microstructural damage evolution in computer generated equivalent micrographs. Both macroscopic and microscopic variables obtained by the VCFEM simulation are compared with experimental observations. The macroscopic stress-strain plot for the plane strain analysis is found to yield quite good match with experiments if the difference in the initial yield strength due to plastic constraint is subtracted. Prediction of the onset of plastic instability by the Considere criterion is also found to be in reasonably good agreement with the experimental results. For the microstructural results with number of cracked particles in different size ranges, the Weibull model is found to give better concurrence with experiments. A plot of the number fraction of cracked particles as a function of straining shows that at lower strains sections with particle rich regions damage rapidly, but the rate slows down with additional deformation. Finally, the marked correlation functions are evaluated to characterize length scales and representative material element size in the presence of damage. Particle cracks and the probability of particle fracture are chosen to be the marks. The study reveals that a significantly large portion of the microstructure should be analyzed for reasonable accuracy in the presence of damage. The correlation functions do not stabilize below a certain length scales and this keeps growing with increased damage. In summary, various important characteristics of growing damage are investigated in this work to understand the role of microstructure in the material failure process.

Bibliography

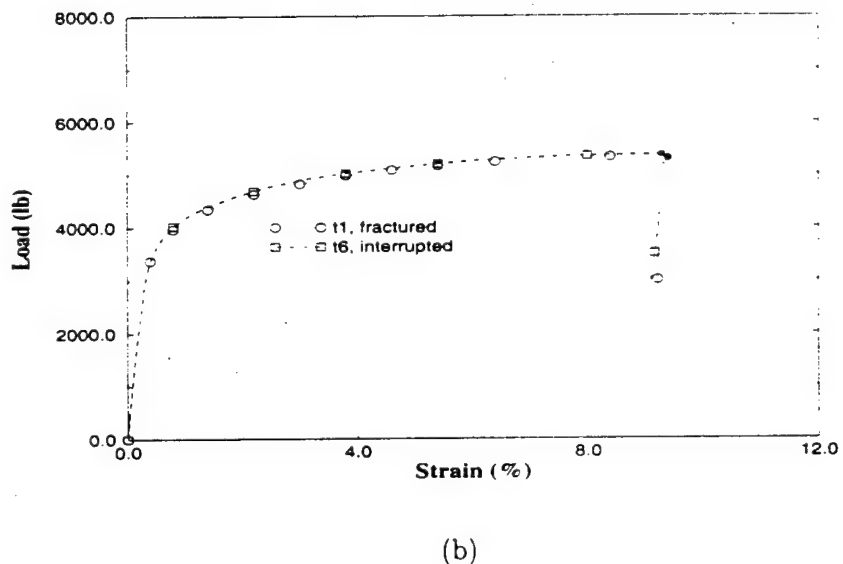
- [1] P.M. Singh and J.J. Lewandowski, *Metall. Trans. A*, **26A**, 2911 (1995).
- [2] J. Llorca and C. Gonzalez, *J. Mech. Phys. Solids*, **46**, 1 (1998).
- [3] A.B. Pandey, B.S. Majumdar and D.B. Miracle, *Processing and Fabrication of Advanced Materials, Proc. of TMS Conf.*, ed. by T.S. Srivatsan and J.J. Moore, 185 (1995).
- [4] P.M. Mummery, B. Derby and C.B. Scruby, *Acta Metall. Mater.*, **41**, 1431 (1993).
- [5] Y. Brechet, J.D. Embury, S. Tao and L. Luo, *Acta Metall. Mater.*, **39**, 1781 (1993).
- [6] W.H. Hunt, *Ph.D Thesis*, Carnegie Mellon University, (1992).
- [7] J. Llorca and M. Elices, *Intrinsic and Extrinsic Fracture Mechanisms in Inorganic Composite Systems*, ed. by J.J. Lewandowski and W.H. Hunt, a publication of the Minerals, Metals & Materials Society, 15 (1995).
- [8] T. Christman, A. Needleman and S. Suresh, *Acta Metall. et Mater.*, **37**, 3029 (1989).
- [9] S. Moorthy and S. Ghosh, *Comp. Meth. Appl. Mech. Eng.*, **151**, 377 (1998).
- [10] S. Ghosh and S. Moorthy, *Acta Metall. et Mater.*, **46**, 965 (1998).
- [11] A. Needleman, *J. Appl. Mech.*, **54**, 525 (1987).
- [12] V. Tvergaard, *Jour. Mech. Phys. Solids*, **41**, 1309 (1991).
- [13] G. Bao, *Acta Metall. et Mater.*, **40**, 2547 (1992).
- [14] C.L. Hom, P.A. Mataga and R. M. McMeeking, *Int. Jour. Numer. Meth. Engrg.*, **27**, 233 (1989).
- [15] M. Finot, Y.-L. Shen, A. Needleman and S. Suresh, *Metall. Mat. Trans. A*, **25A**, 2403 (1994).
- [16] J.R. Brockenbrough, S. Suresh and W.A. Weincke, *Acta Metall. et Mater.*, **39**, 735 (1991).
- [17] P.E. McHugh, R.J. Asaro and C.F. Shih, *Acta Metall. et Mater.*, **41**, 1461 (1993).
- [18] J.R. Brockenbrough, W.H. Hunt Jr. and O. Richmond, *Scripta Metall.*, **27**, 385 (1992).

- [19] R. Becker and O. Richmond, *Model. Simul. Mater. Sci. Eng.*, **2**, 439 (1994).
- [20] W.A. Spitzig, J.F. Kelly and O. Richmond, *Metallography*, **18**, 235 (1985).
- [21] P.J. Wray, O. Richmond and H.L. Morrison, *Metallography*, **16**, 39 (1983).
- [22] R. Pyrz and B. Bochenek, *Sci. Engrg. Comp. Mat.*, **3**, 95 (1994).
- [23] R. Pyrz, *Mater. Sci. Eng.*, **A177**, 253 (1994).
- [24] M. Li, S. Ghosh, T.N. Rouns, H. Weiland, O. Richmond and W. Hunt, *Mater. Characterization*, **41(2-3)**, 81 (1998).
- [25] M. Li, S. Ghosh, O. Richmond, H. Weiland and T.N. Rouns, Part I, *Mater. Sci. Engin. A*, (in press).
- [26] M. Li, S. Ghosh, O. Richmond, H. Weiland and T.N. Rouns, Part II, *Mater. Sci. Engin. A*, (in press).
- [27] W.H. Hunt, *Intrinsic and extrinsic fracture mechanisms in inorganic composite systems*, ed. by J.J. Lewandowski and W.H. Hunt, A Publication of the Minerals, Metals & Materials Society, 31 (1995).
- [28] J.J. Lewandowski, C. Liu, W.H. Hunt, Jr., *Powder Metallurgy Composites*, ed. by P. Kumar, K.M. Vedula and A.M. Ritter, TMS-AIME, Warrendale, PA, 117 (1987).
- [29] D.J. Lloyd, *Acta Metall. Mater.*, **39**, 59 (1991).
- [30] S.I. Rokhlin, W. Huang and Y.C. Chu, *Ultrasonics*, **33**, 351 (1995).
- [31] P. Potet, C. Bathias and B. Degrigny, *Mater. Eval.*, **46**, 1050 (1988).
- [32] B. London, R.N. Yancey and J.A. Smith, *Mater. Eval.*, **48**, 604 (1990).
- [33] J.-Y. Buffiere, E. Maire, C. Verdu, P. Cloetens, M. Pateyron, G. Peix and J. Baruchel, *Mater. Sci. Eng.*, **A234-236**, 633 (1997).
- [34] S. Ghosh, Z. Nowak and K. Lee, *Acta Mater.*, **45**, 2215 (1997).
- [35] S. Ghosh, Z. Nowak and K. Lee, *Comp. Sci. & Tech.*, **57**, 1187 (1997).
- [36] W.H. Hunt, Jr., T.M. Osman and J.J. Lewandowski, *J.O.M.*, **45(1)**, 30 (1993).
- [37] *SPYGLASS Slicer, Quick Tour and Reference*, Version 1.0, Spyglass Inc., Champaign, IL 61826 (1994).
- [38] P.M. Singh, J.J. Lewandowski, in: *Intrinsic and Extrinsic Fracture Mechanisms in Inorganic Composite Systems*, ed. by J.J. Lewandowski and W.H. Hunt, a publication of the minerals, metals & materials Society, 1995, pp.57.

- [39] W.H. Hunt, C.R. Cook and R.R. Sawtell, *SAE paper*, 910834 (1991).
- [40] C.W. Nan and D.R. Clarke, *Acta Mater.*, **44**, 3801 (1996).
- [41] C. Gonzalez and J. Llorca, *Scripta Materialia*, **35**, 91 (1996).
- [42] J. Llorca, *Acta metall.mater.*, **43**, 181 (1995).

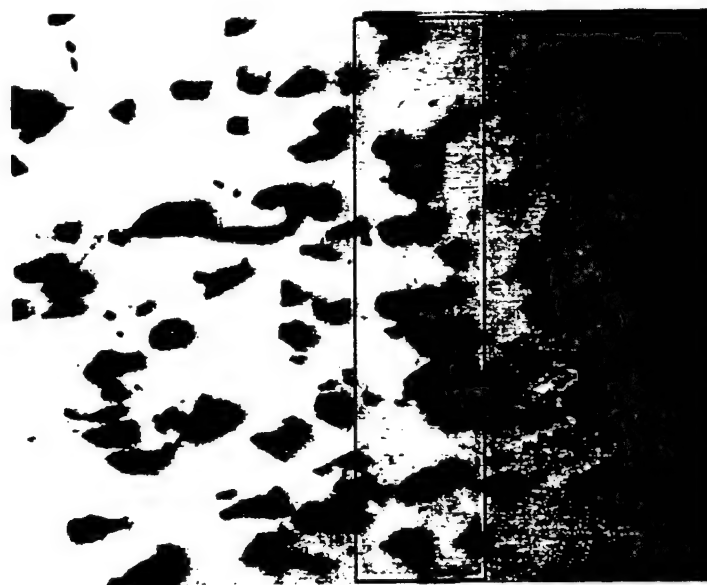


(a)



(b)

Figure 5.1: (a) Interrupted uniaxial tensile test specimen for naturally aged material and sample coupon for serial sectioning (unit in mm); (b) Load-strain plots for two specimens of naturally aged DRA. Dark points indicate where the loading is interrupted or where the specimen is fractured.



(a)

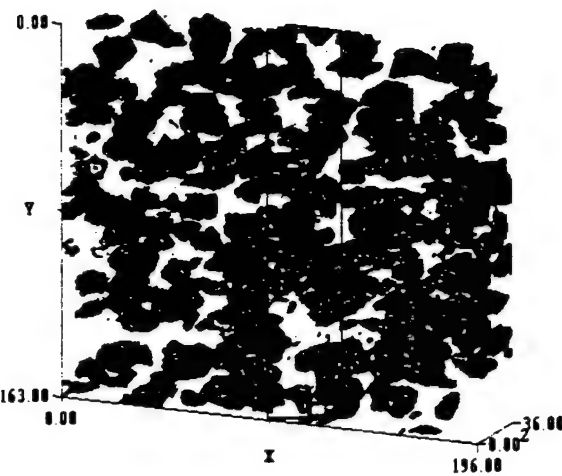
→
→
→ loading
direction



(b)

→
→
→ loading
direction
→
→
→

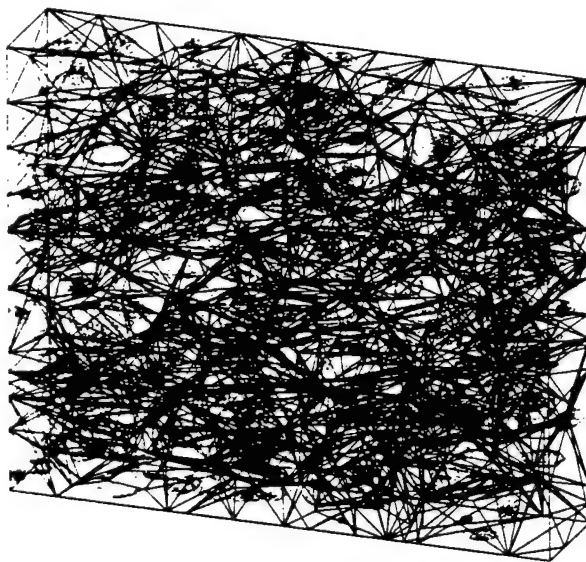
Figure 5.2: Micrographs of different sections of the t6 specimen showing cracked particles; (a) section 3, (b) section 5.



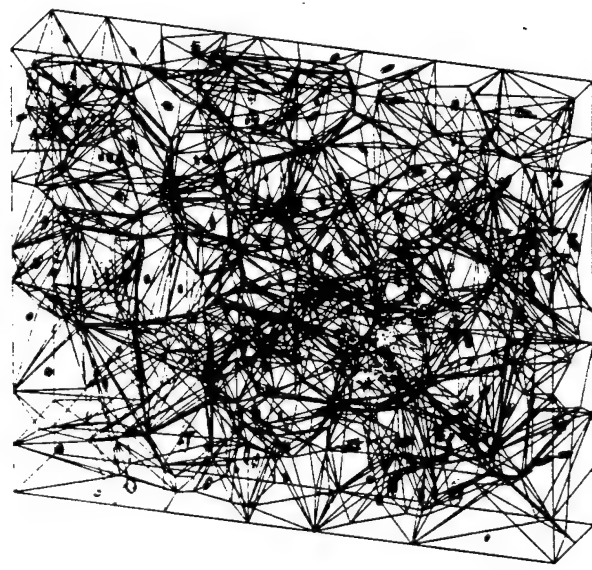
(a)



(b)



(c)



(d)

$50 \mu\text{m}$

Figure 5.3: 3D microstructure for SiC particle reinforced DRA after interrupted test (units in μm): (a) A computer created image by serially stacking section micrographs, (b) Simulated microstructure of ellipsoidal particles and cracks. Tessellation for 2D and 3D microstructures, (c) 3D tessellation based on particle morphology and (d) 3D tessellation based on microcrack morphology.

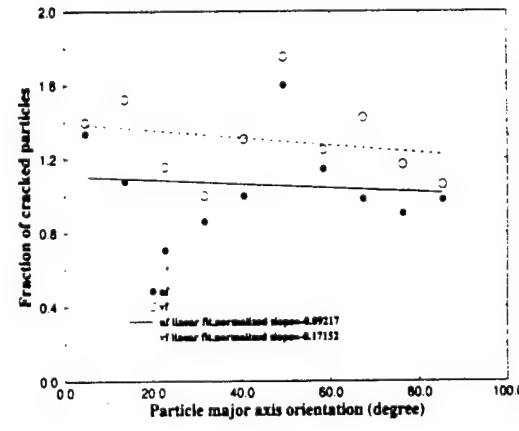
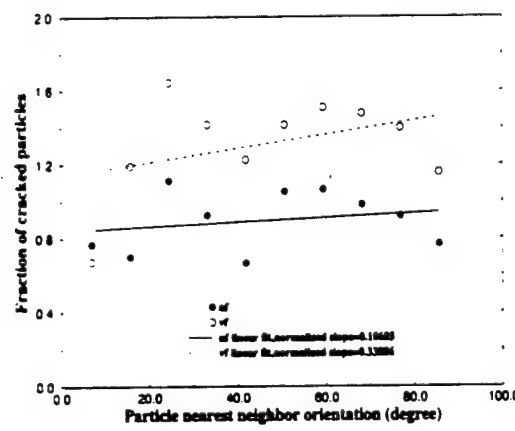
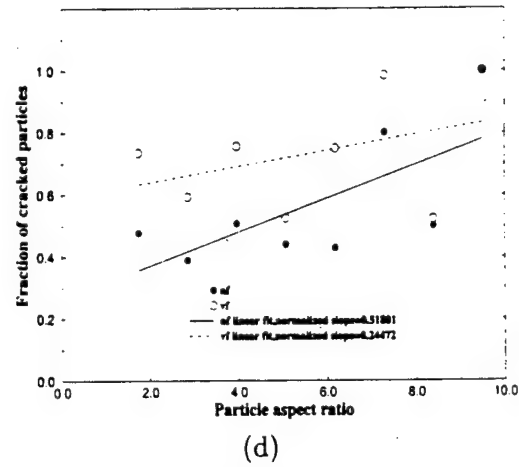
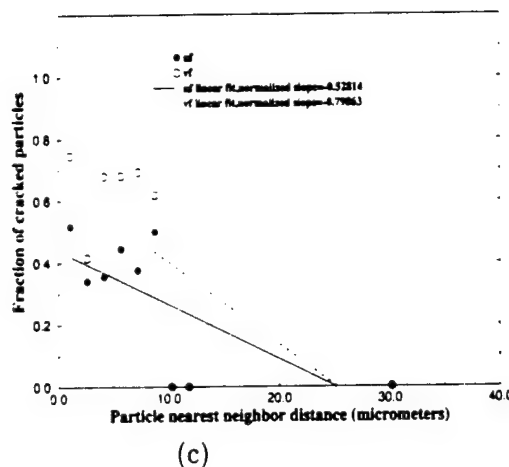
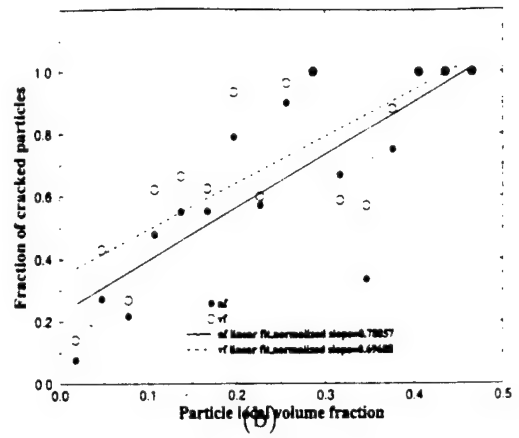
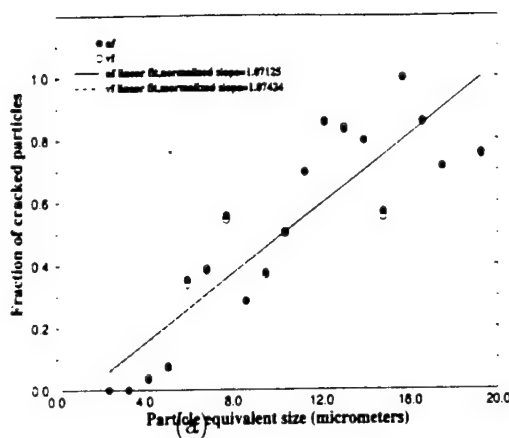
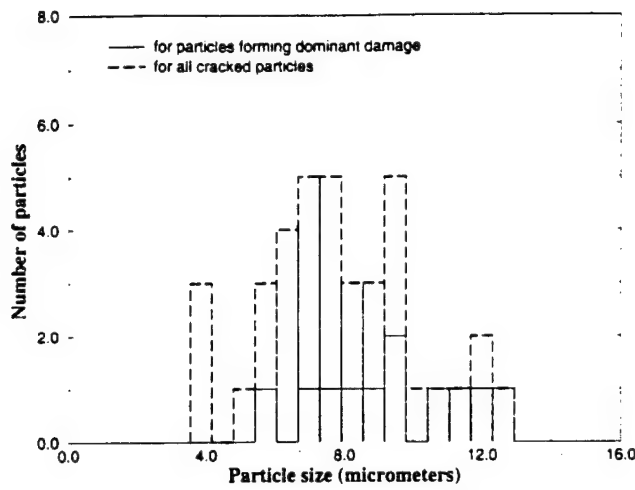
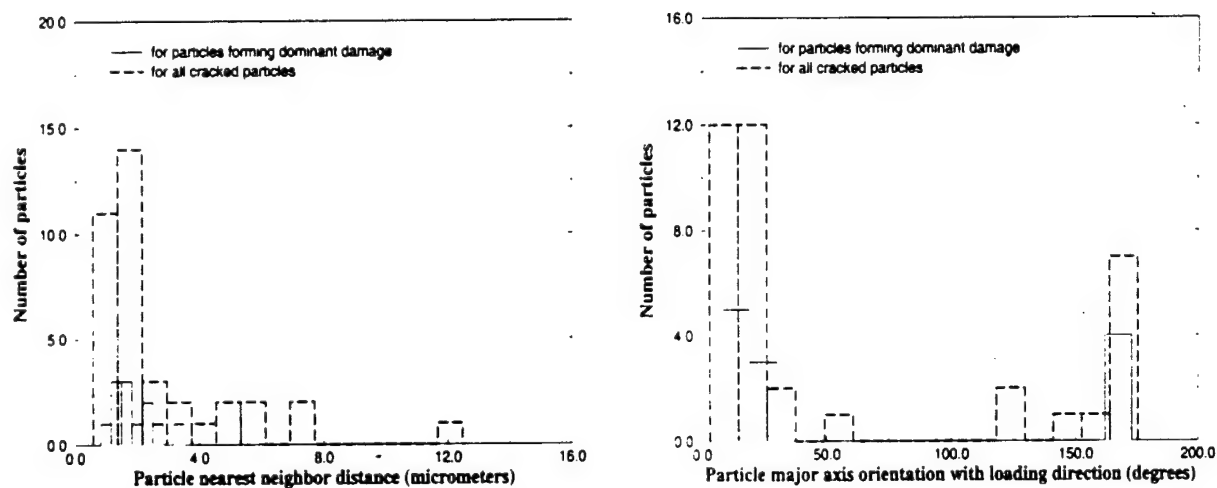


Figure 5.4: Sensitivity of damage to various microstructural variables



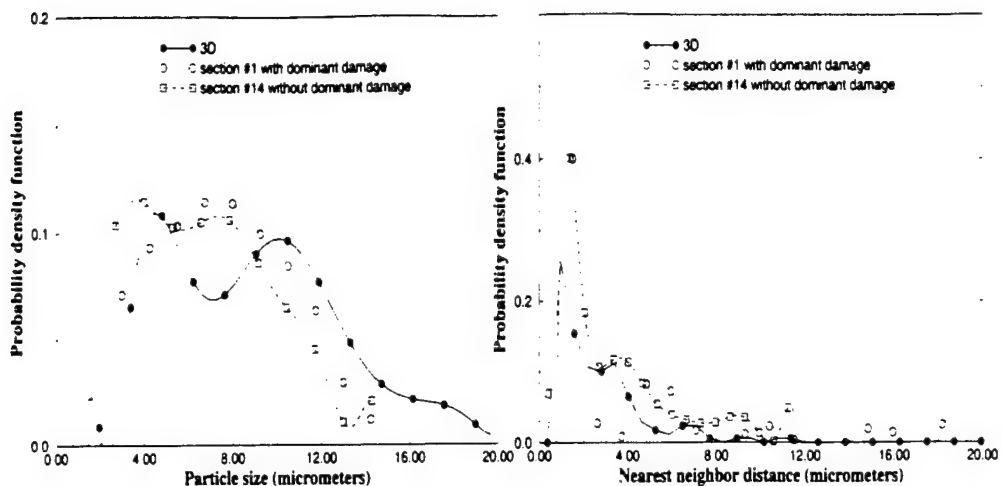
(a)



(b)

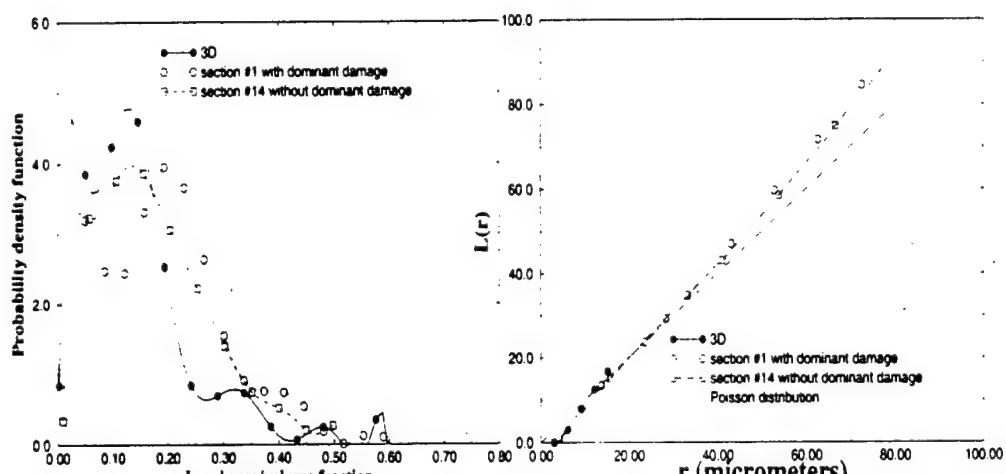
(c)

Figure 5.5: Histograms comparing characteristics of particles with dominant damage with all cracked particles



(a)

(b)



(c)

(d)

Figure 5.6: Characterization functions for 2D sections and 3D microstructure.

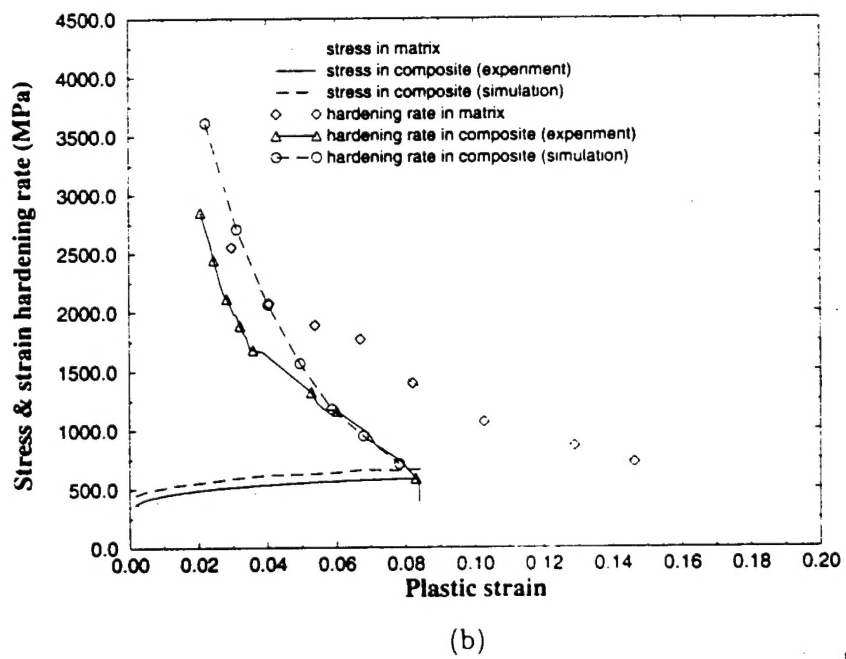
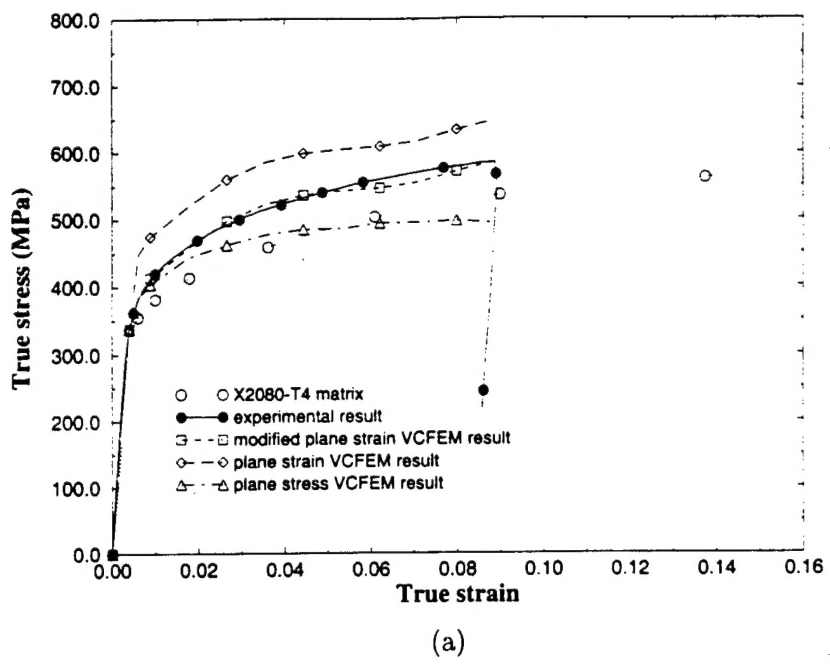
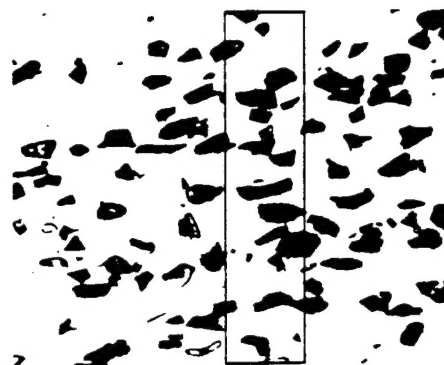
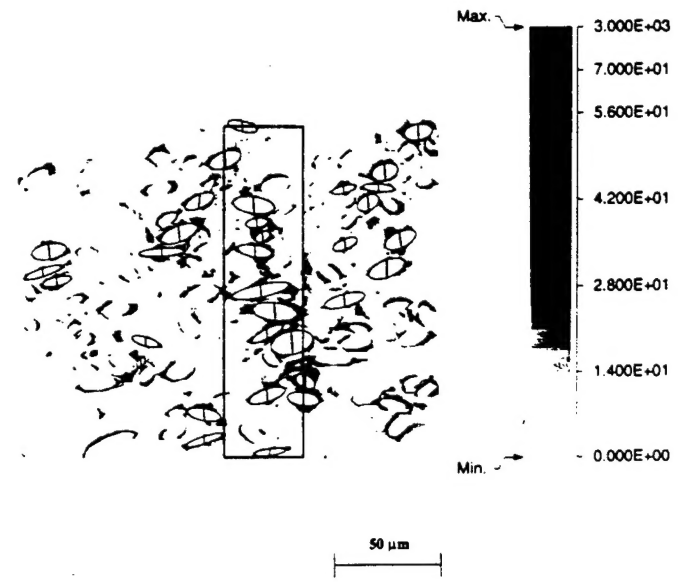


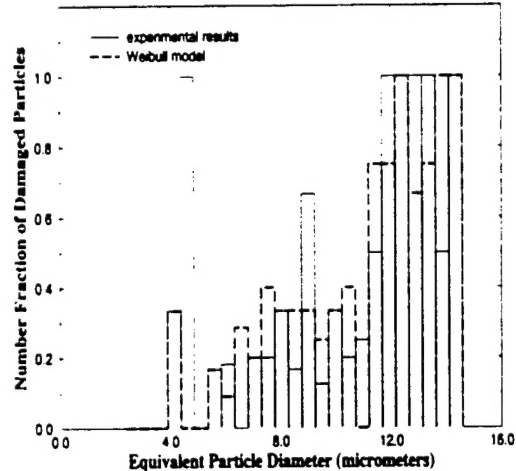
Figure 5.7: (a) Macroscopic stress-strain response by plane strain and plane stress VCFEM simulation, (b) Stress-strain hardening rate plots for the Considere condition.



(a)



(b)



(c)



(d)

Figure 5.8: (a) Experimental micrographs, (b) VCFEM simulated micrograph showing damage and contour plot of effective plastic strain at 8.88% strain in section 1, (c) histogram of number fraction of cracked particles as a function of particle size by Weibull based probabilistic criterion, and (d) contour plot of particle fracture probability of section 1 at 8.88% strain.

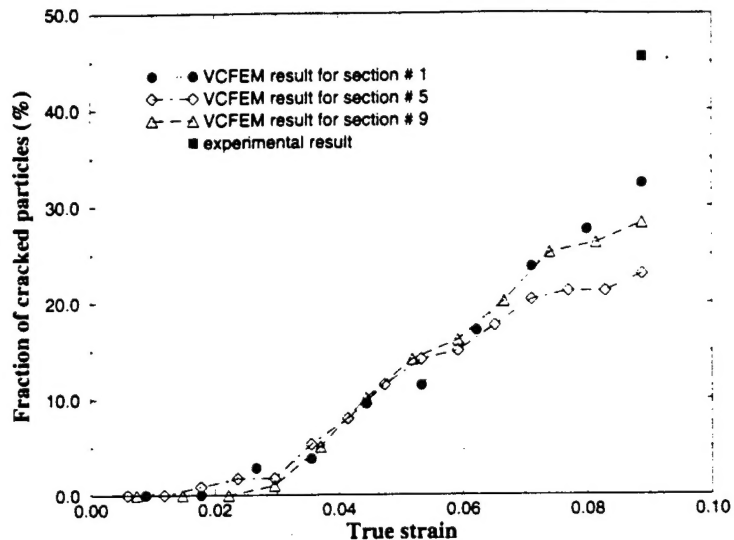


Figure 5.9: Number fraction of cracked particles as a function of straining.

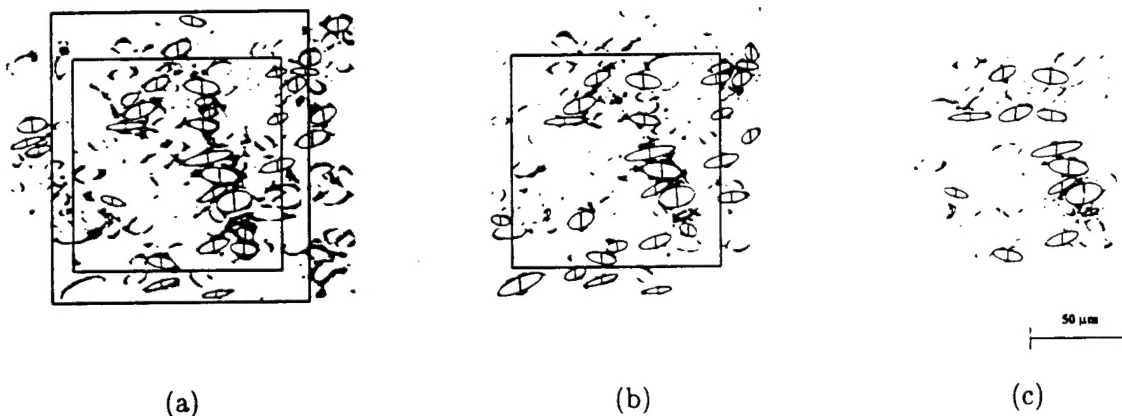


Figure 5.10: Simulations showing effective plastic strain(%) and cracked particles in three different subsets of the entire micrograph of section 1, (a) RME 0 with dimension $195\mu m \times 155\mu m$ (b) RME 1 with dimension $150\mu m \times 155\mu m$ and (c) RME 2 with dimension $116\mu m \times 115\mu m$.

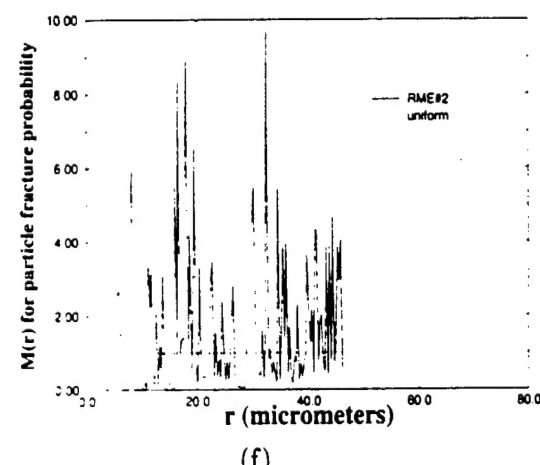
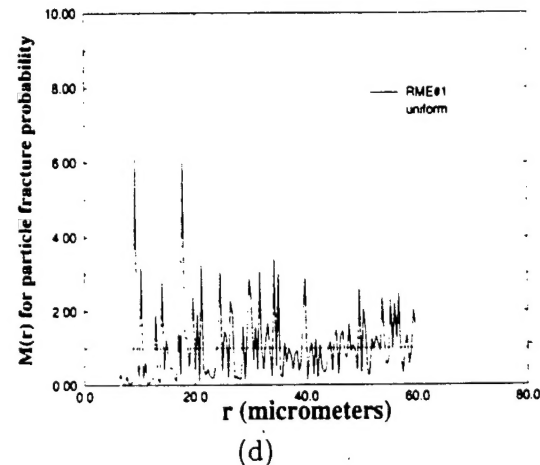
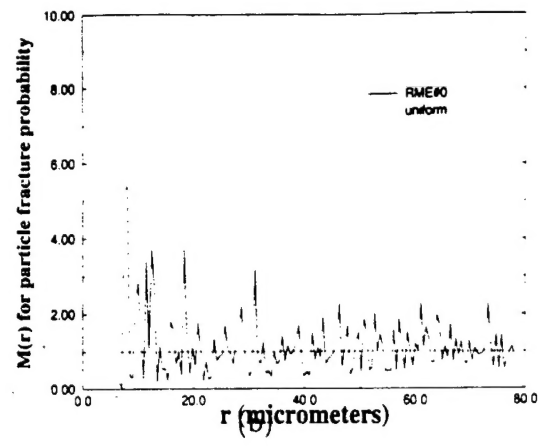
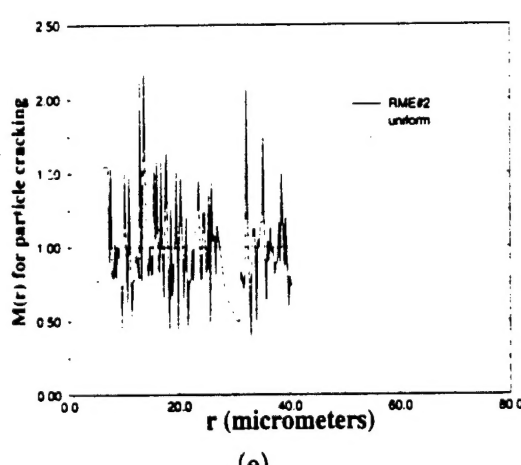
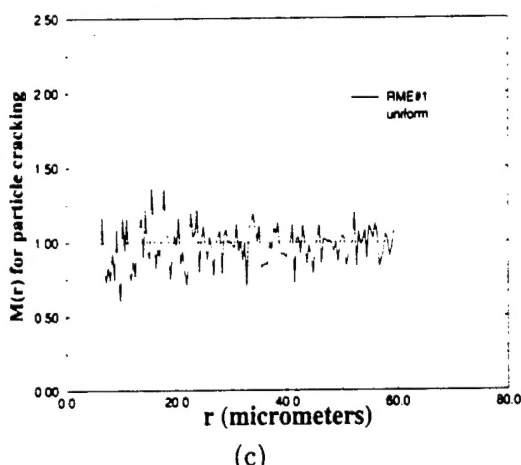
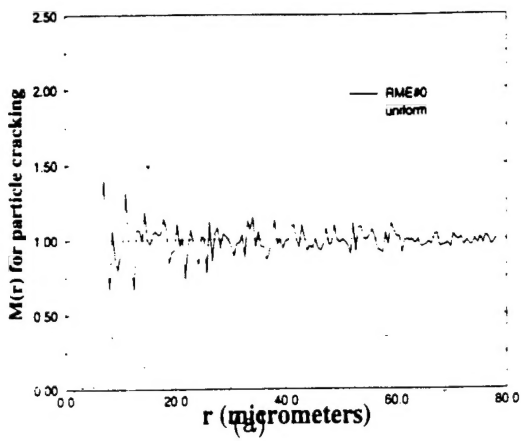


Figure 5.11: Marked correlation function as a function of radial distance; (a) cracked particles as marks and (b) probability of cracking as makr for RME 0; (c) cracked particles as marks and (d) probability of cracking as makr for RME 1; (e) cracked particles as marks and (f) probability of cracking as makr for RME 2.